Etude des biomarqueurs de réponse aux traitements systémiques et identification de nouvelles cibles thérapeutiques dans les cancers de vessie et de l'uretère

Luc Cabel

To cite this version:

Luc Cabel. Etude des biomarqueurs de réponse aux traitements systémiques et identification de nouvelles cibles thérapeutiques dans les cancers de vessie et de l'uretère. Cancer. Université Paris sciences et lettres, 2022. Français. NNT : 2022UPSLS069 . tel-04416279

PSL
UNIVERSITÉ PARIS

THÈSE DE DOCTORAT
DE L'UNIVERSITÉ PSL

Préparée à L'institut Curie
UMR144 - Biologie cellulaire et cancer

Etude des biomarqueurs de réponse aux traitements systémiques et identification de nouvelles cibles thérapeutiques dans les cancers de vessie et de l'uretère

Soutenue par
Luc Cabel
Le 14/12/2022

Ecole doctorale n° 582
Cancérologie – Biologie – Médecine – Santé

Spécialité
Sciences de la vie et de la santé

Confidentiel jusqu'au 31/12/2023

Composition du jury :

Nadine, HOUÉDÉ Pr, Institut de Cancérologie du Gard - CHU Caremeau	*Présidente, Rapporteur*
Murielle, LE ROMANCER DR, Centre Léon Bérard	*Rapporteur*
Elisabetta, MARANGONI CR, Institut Curie	*Examinatrice*
Rémy NICOLLE CR, Centre de Recherche sur l'Inflammation	*Examinateur*
François RADVANYI DR, Institut Curie	*Directeur de thèse*
Isabelle, BERNARD-PIERROT CR, Institut Curie	*Co-Directrice de thèse*

institut Curie

A Soumeya et Naël

Résumé en Français

Le cancer de vessie est responsable de 212 536 décès en 2020 dans le monde. Il est constitué de tumeurs n'infiltrant pas le muscle (TVNIM, à risque de récidives locales), et infiltrant le muscle (TVIM, à risque de disséminations métastatiques et de décès). 95% sont des cancers urothéliaux alors que 5% sont des cancers épidermoïdes. Au niveau moléculaire, ces tumeurs sont caractérisées principalement par des tumeurs luminales (incluant des Luminales-papillaires) ou basales (Ba/Sq). Le traitement en 2022 est principalement basé, pour les stades avancés, sur la chimiothérapie (incluant les anticorps drogues conjugués), l'immunothérapie par inhibiteur de point de contrôle immunitaire (IPI, anticorps anti-PD-1/L1) et les inhibiteurs de FGFR en cas d'altérations génomiques *FGFR2/3*. Ces traitements ont néanmoins une efficacité modérée.

Les objectifs de cette thèse étaient dans les TVIM de rechercher des biomarqueurs de sensibilité ou de résistance aux traitements ainsi que de rechercher de nouvelles pistes thérapeutiques.

Concernant la recherche de biomarqueurs de réponse ou de résistance dans les TVIM nous avons pu montrer que :

- les structures lymphoïdes tertiaires, mesurées par l'expression du gène *CXCL13*, sont un biomarqueur prédictif majeur de réponse aux anticorps anti-PD-L1, et sont enrichies dans le type Ba/Sq, (étude réalisée via l'analyse de cohortes publiques comme IMVIGOR210) ;
- les cellules plasmatiques semblent également un biomarqueur de réponse aux IPI dans les TVIM métastatiques (conclusion basée sur des résultats préliminaires des données de séquençage de noyaux uniques de la cohorte MATCH-R avant et pendant le traitement par IPI) ;
- une combinaison thérapeutique par anti-FGFR (erdafitinib) + anti-EGFR (erlotinib) est efficace dans des PDXs (patient-derived xenografts) mutés pour *FGFR3*, cette efficacité étant probablement due à une surexpression d'*ERBB2-3* et d'*EGFR* sous inhibiteur de FGFR ;
- les tumeurs sarcomatoïdes présentaient une expression/activité plus faible d'EGFR et un switch vers FGFR1, responsable d'une moindre réponse à un inhibiteur d'EGFR par rapport aux autres TVIM Ba/Sq ;
- les PDXs étaient hétérogènes au niveau moléculaire et protéique, et les TVIM pouvaient présenter un changement phénotypique de Ba/Sq à luminal lors de la greffe chez la souris.

Nous avons pu identifier de nouvelles pistes thérapeutiques dans les lignées cellulaires de cancers urothéliaux :

- RARγ, partenaire de RXRα, cible identifiée dans la base publique de criblage par CRISPR-Cas9 de lignées cellulaires (DepMap). RARγ est activé dans les TVIM en particulier dans les sous-types Ba/Sq et Luminales-papillaires, et son inhibition semble intéressante en particulier dans le sous type Ba/Sq.

- Le birinapant (XIAP/cIAP1/2 inhibiteur, Smac-mimétique) qui est efficace dans certaines lignées de cancer de vessie selon les données de DepMap. L'efficacité du birinapant a été confirmée *in vitro et in vivo* au laboratoire dans les lignées UMUC14 et SCaBER, avec comme biomarqueur de sensibilité potentiel l'amplification de *BIRC2* ou la surexpression de *RIPK1*.
- FGFR1 qui est une nouvelle piste thérapeutique dans les cancers de vessie de type sarcomatoïde.

Remerciements

Je tiens en premier lieu à remercier l'équipe d'Anesthésie-Réanimation de l'Hôpital Tenon, sans qui ce travail n'aurait pas eu de sens.

Je remercie François Radvanyi et Isabelle Bernard Pierrot de m'avoir accueilli dans le laboratoire et m'avoir initié à la complexité de l'oncologie moléculaire.

Un grand merci à Florent et Hélène qui m'ont permis de mieux comprendre la biologie et le Wet lab, et à Clarice puis Clément qui m'ont initié à la bio-informatique, toujours dans un esprit prêt à aider.

Merci à ceux qui étaient présents au labo pendant le COVID, période où il était important de pouvoir croiser des collègues.

Merci à Yohann et à Ronan pour m'avoir permis de commencer à travailler sur la cohorte MATCH-R de l'IGR.

A ma famille et mes amis qui m'ont soutenu, malgré leur incompréhension de mon parcours.

A Soumeya qui m'a permis de traverser les différentes phases de la thèse, du COVID mais aussi de la paternité, 3 éléments intriqués de ce travail.

Merci à la Fondation pour la Recherche Médical (FRM) et à l'Institut Curie qui m'ont permis de financer cette thèse, ainsi qu'aux donateurs.

1 Table des matières

1 Table des matières

12 Articles Annexes

Abréviations

Anticorps drogues conjugués : ADC

Basal/squameux : Ba/Sq

Carcinome in situ : CIS

Fibroblast Growth Factor Receptor : FGFR

Immunohistochimie : IHC

Inhibiteurs de points de contrôle immunitaires : IPI

Luminal papillary : LumP

Luminal Unstable : LumU

Luminal Non-Specified : LumNS

Macrophages associés à la tumeur : TAM

Xénogreffes dérivés de patients : PDX

Séquençage ARN des cellules uniques : scRNA-seq

Séquençage ARN des noyaux uniques : snRNA-seq

Structures lymphoïdes tertiaires : SLT

TVIM : Rumeur vessie infiltrant le muscle

TVNIM : Tumeurs de vessie n'infiltrant pas le muscle

1 Cancer urothélial de vessie et de l'uretère

1.1 Généralités

Le cancer de vessie est le 10e type de cancer le plus fréquent dans le monde, avec une estimation de 573 278 nouveaux cas et 212 536 décès en 2020 [1–3].

Les facteurs de risque de développer un cancer de la vessie sont le sexe masculin, le tabagisme, les antécédents personnels ou familiaux de cancer de la vessie, les radiations pelviennes, les expositions environnementales/professionnelles (en particulier aux amines aromatiques), l'exposition à certains médicaments, l'infection ou l'irritation chronique des voies urinaires et certaines comorbidités telles que l'obésité ou le diabète [4].

Les tumeurs de vessie n'infiltrant pas le muscle (TVNIM) vésical représentent la majorité de ces cancers (~80%) (**Figure 1**), sont localisées et présentent fréquemment des rechutes locales. A l'inverse les tumeurs de vessie infiltrant le muscle (TVIM, ~20%) présentent un risque important de dissémination métastatique (50% de rechute métastatique après chirurgie) et de décès.

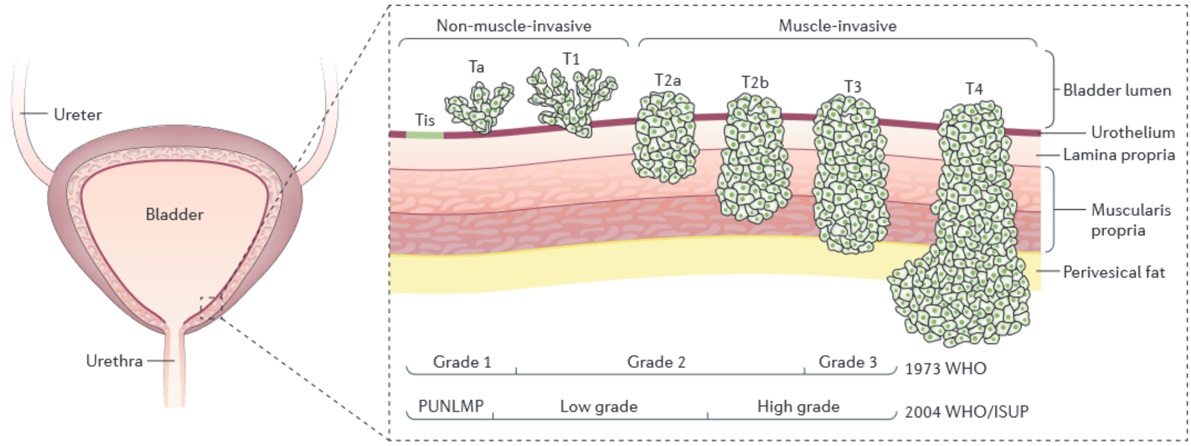

Nature Reviews | Disease Primers

Figure 1 : Evolution des tumeurs de vessie du stade non-infiltrant à infiltrant le muscle vésical. [4] La stadification selon le système TNM est ici présentée. Les TVIM sont classées T2 en cas d'invasion isolée du muscle , T3 en cas d'invasion de la graisse péri-vésicale et T4 des organes avoisinants (prostate, utérus, vagin, intestin…). La distinction bas grade et haut grade (WHO 2004) est un facteur pronostic majeur sur le risque d'invasion, important dans la prise en charge des TVNIM.

Les données cliniques, pathologiques et moléculaires chez l'homme indiquent que le carcinome urothélial se développe selon deux voies distinctes – **Figure 2** [4]:

- celle des TVNIM papillaires, tumeurs le plus souvent peu invasives, se limitant au stade pTa et ne se transformant généralement pas en TVIM. Les TVNIM papillaires présentent de manière fréquente une mutation de *FGFR3* et une délétion du chromosome 9,

- celle des lésions non papillaires et des carcinomes *in situ* (CIS) qui peuvent fréquemment évoluer en TVIM. Ces tumeurs sont associées à l'inactivation d'un ou de plusieurs gènes suppresseurs de tumeurs (*TP53*, *RB1*, *PTEN*).

Du fait de la présence d'urothélium au niveau de l'uretère et du bassinet, il existe également des tumeurs malignes du bassinet et de l'uretère qui sont habituellement des carcinomes urothéliaux. Le syndrome de Lynch est une prédisposition génétique à plusieurs cancers dont celui de l'uretère.

Au niveau histologique, les cancers de vessie et de l'uretère sont généralement des carcinomes urothéliaux (>90%), mais il existe dans ~5% des cas des carcinomes épidermoïdes. Parmi les carcinomes urothéliaux, il peut exister différents variants (épidermoïde, sarcomatoïde, plasmocytoïde, micropapillaire, neuroendocrine...).

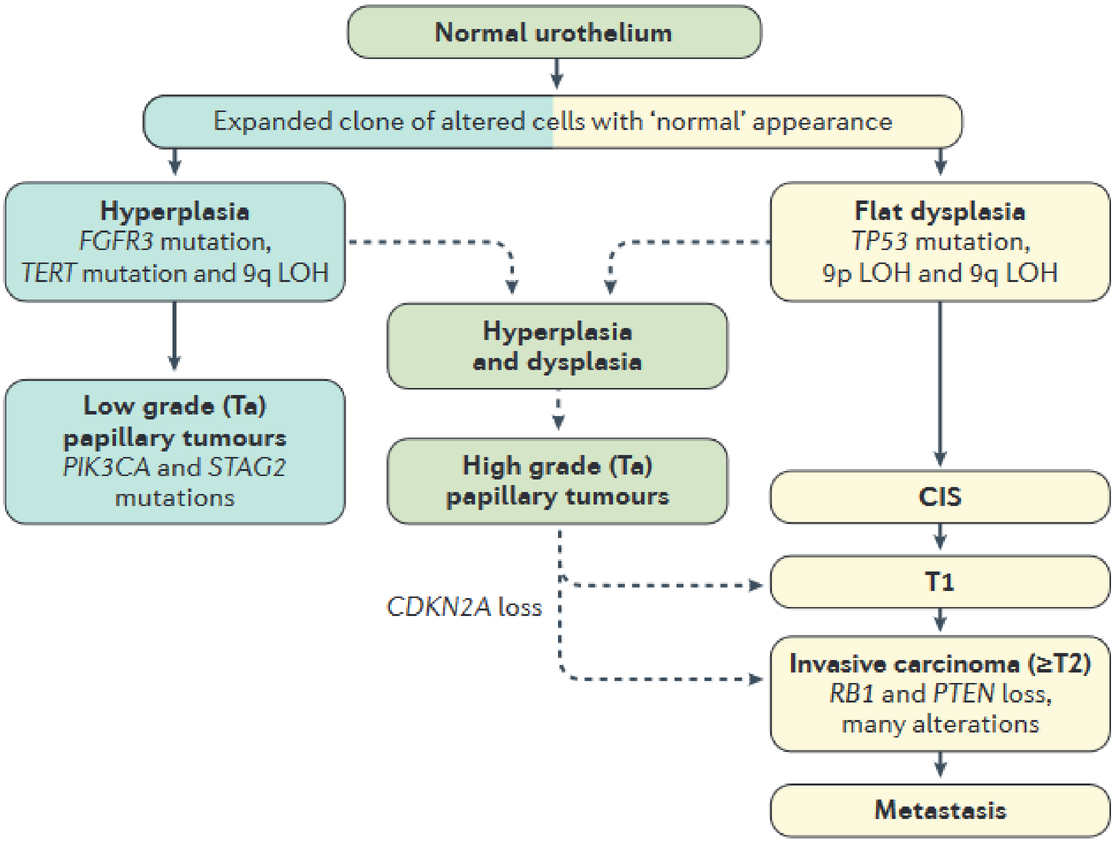

Nature Reviews | Disease Primers

Figure 2 : Deux grandes voies de développement des cancers de vessie. Hyperplasie/Tumeurs papillaires versus dysplasie/carcinome *in situ* et cancer infiltrant le muscle.[4] Les TVNIM de bas grade (Ta) sont souvent peu invasives et ne se transforment généralement pas en TVIM. Elles présentent de manière fréquente une mutation de *FGFR3* et une délétion du chromosome 9. Les TVIM évoluent à partir de carcinome in situ ou de lésions non papillaires, et sont associées à l'inactivation d'un ou de plusieurs gènes suppresseurs de tumeurs (*TP53*, *RB1*, *PTEN*).

1.2 Traitement

La prise en charge est conditionnée au type TVNIM ou TVIM.

- Le traitement des TVNIM repose sur une résection trans-urétrale de vessie, qui peut être complétée par des instillations locales de mitomycine-C (chimiothérapie) ou de BCG [2,5].
- Les TVIM non métastatiques sont traitées généralement par chimiothérapie néoadjuvante puis cystectomie.
- Les TVIM métastatiques sont traitées de manière palliative par chimiothérapie, immunothérapie ou thérapie ciblée (inhibiteur de FGFR) (**Figure3**).

1.3 Chimiothérapie

La chimiothérapie est le principal traitement systémique utilisé jusqu'à récemment dans les TVIM localisées ou métastatiques. En particulier les associations à base de sels de platine + gemcitabine sont devenus le standard en 1ère ligne métastatique (cisplatine en cas de fonction rénale normale, sinon carboplatine), alors qu'en situation localisée une chimiothérapie néoadjuvante (cisplatine et gemcitabine ou MVAC (Méthotrexate. vinblastine, doxorubine, cisplatine)) est indiquée pour 4-6 cycles, avec une toxicité importante.

En 2022, l'indication de chimiothérapie en pratique clinique n'est conditionnée sur aucune analyse moléculaire, mais sur le stade clinique tumoral et l'état général du patient.

1.4 Anticorps drogue conjugué

Les anticorps drogues conjugués (ADC) sont une nouvelle classe thérapeutique récente alliant l'immunothérapie et la chimiothérapie et ont démontré une efficacité importante dans des nombreux cancers[6]. L'un des aspects les plus importants du développement des ADC pour le cancer est l'identification de la cible antigénique unique de l'anticorps, devant être exprimée le plus fortement et spécifiquement possible sur les cellules tumorales et non sur les cellules saines, comme pour TROP2 et NECTIN4. Le choix de la chimiothérapie liée à cet anticorps, leur nombre ainsi que le « linker », liant l'anticorps aux drogues, sont également des éléments clés d'efficacité de ces traitements.

Récemment, deux ADC ont montré leur efficacité dans les cancers urothéliaux avancés, le Sacituzumab Govitecan (anticorps anti-TROP2, dont la chimiothérapie fait partie de la classe des inhibiteurs de topoisomérase 1) [7,8] et l'Enfortumab Vedotin (6) (anticorps anti-NECTIN4, dont le vedotin est un agent cytotoxique antimicrotubule) [9].

Il a été suggéré que l'expression de NECTIN4 et TROP2 était variable et pouvait être liée à leur activité, et que l'expression de NECTIN4 était plus élevée dans les tumeurs luminales [10,11].

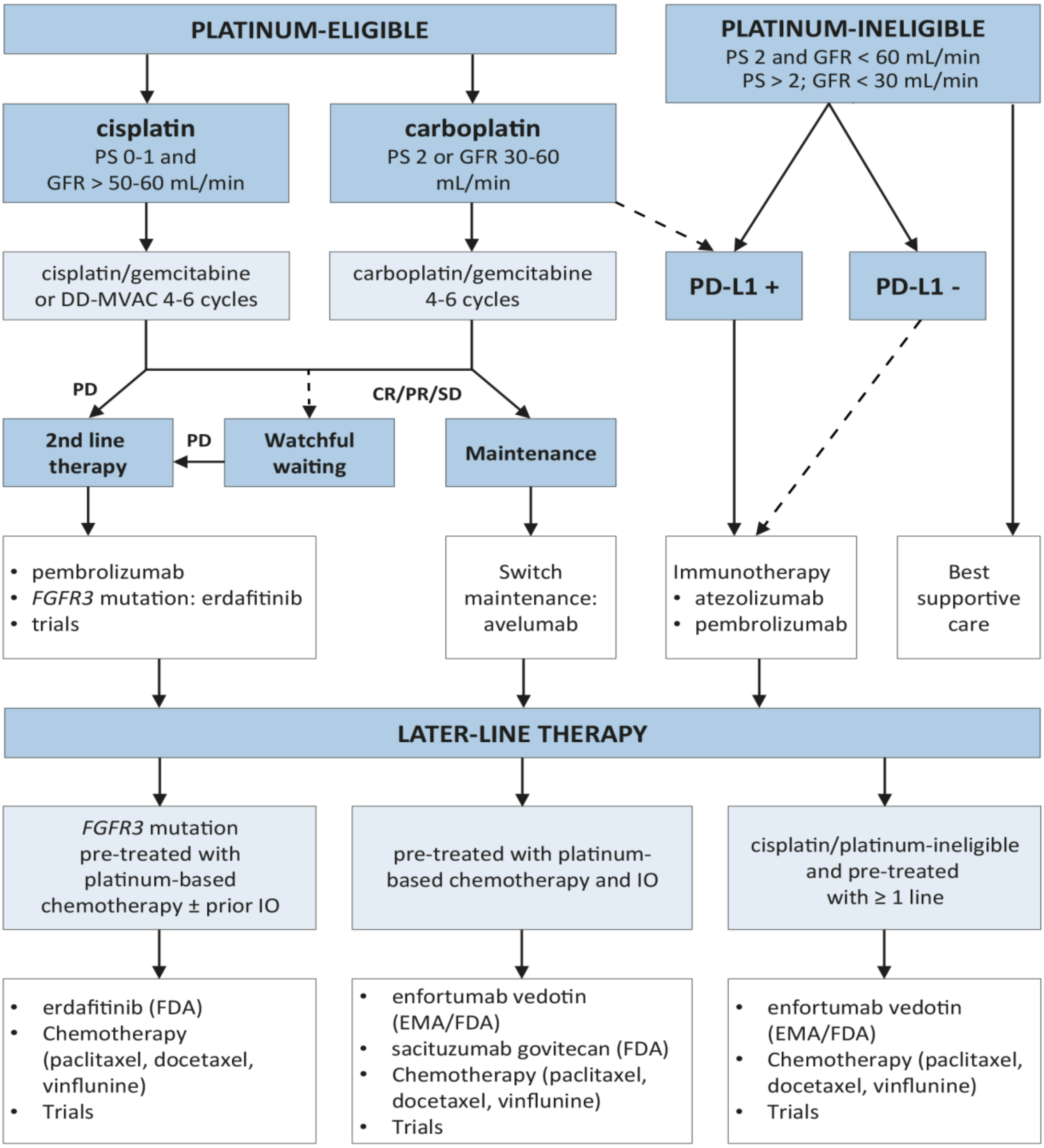

Figure 3 Résumé de la prise en charge des cancers de vessie métastatique

L'éligibilité au cisplatine est basée sur la fonction rénale et l'état général
BSC : best supportive care, CR : complete response, DD-MVAC : dose dense methotrexate vinblastine doxorubicin cisplatin, EMA : European Medicines Agency, EV : enfortumab vedotin, FDA : US Food and Drug Administration, FGFR : fibroblast growth factor receptor, GFR : glomerular filtration rate, IO : immunotherapy
PD : progressive disease, PR : partial response, PS : performance status, SD : stable disease
https://uroweb.org/guideline/bladder-cancer-muscle-invasive-and-metastatic/

1.5 Immunothérapie

L'oncologie a connu ces dernières années une révolution thérapeutique avec la mise sur le marché des inhibiteurs des « checkpoints » immunitaires. Ces derniers sont principalement représentés à l'heure actuelle en pratique clinique par les anticorps anti CTLA-4 (Cytotoxic T-Lymphocyte Associated Protein 4) et des anticorps anti PD-1 (Programmed cell death 1) ou PD-L1 (Programmed death-ligand 1).

Le mécanisme d'action de ces thérapeutiques est de réactiver l'immunité lymphocytaire cytotoxique anti-tumorale, inhibée au cours de la progression tumorale [12]. PD-1 est exprimé au niveau membranaire par le lymphocyte T et induit en cas d'activation du récepteur un signal d'inhibition du lymphocyte. PD-L1 est lui exprimé par plusieurs types cellulaires dont les cellules présentatrices de l'antigène, ainsi que par certaines cellules du microenvironnement tumoral comme les cellules endothéliales [12]. PD-L1 est le ligand de PD-1 et a un effet activateur du récepteur (et donc inhibiteur du lymphocyte T).

Alors que la chimiothérapie à base de sels de platine restait le traitement principal des cancers de vessie localement avancés/métastatiques, l'immunothérapie par anticorps anti-PD-1 (ex. pembrolizumab, nivolumab) ou PD-L1 (ex. atezolizumab, durvalumab, avelumab) a démontré une efficacité chez les patients ayant une contre-indication à celle-ci [13,14], ou en cas de progression sous/après chimiothérapie [15–17]. Dans cette dernière indication le pembrolizumab a été approuvé en 2018 sur les résultats d'une phase 3 démontrant un gain en survie globale de 3 mois en valeur absolue [15]. Néanmoins, et en cohérence avec les autres essais cliniques testant des anticorps anti-PD-1/PD-L1, le taux de réponse tumorale reste faible (environ 20%) dans une population non sélectionnée, avec des traitements coûteux. Plus récemment, un traitement d'entretien par avelumab après chimiothérapie de première ligne a démontré une amélioration de la survie globale et est devenu le standard thérapeutique[18].

L'expression de PD-L1 (tumorale et/ou stromale) est le principal biomarqueur prédictif évalué et utilisé en pratique clinique, mais reste imparfait pour sélectionner les patients qui bénéficieront d'une immunothérapie [19].

1.6 FGFR3

Du fait des altérations génomiques de la voie FGFR, en particulier des altérations de *FGFR3* (translocation/mutation), plusieurs thérapies ciblées anti-FGFR ont été développées dans le cancer de vessie.

L'erdafitinib (pan inhibiteur FGFR1-4) a une autorisation d'utilisation pour son utilisation chez les patients atteints d'un carcinome urothélial localement avancé ou métastatique, avec des altérations génétiques de *FGFR3* ou *FGFR2*, après progression post- chimiothérapie. Dans l'essai de phase II évaluant l'erdafitinib, le taux de réponse tumorale était de 40%, avec une durée moyenne de réponse de 5,6 mois, correspondant à une durée d'efficacité plus faible que d'autres thérapies ciblées comme les inhibiteurs d'EGFR dans le cancer du poumon *EGFR* muté (9-12 mois). [20,21]. Ce délai plus court de réponse suggère l'apparition rapide d'une résistance secondaire et/ou d'une résistance primaire plus fréquente. De plus, il existait des effets indésirables non négligeables (46% de toxicités de grade 3 ou plus, 16 % d'arrêt pour toxicités)[20].

En conclusion de cette partie, il est donc nécessaire de découvrir de potentielles nouvelles thérapies dans les tumeurs de vessie et de l'uretère, ainsi que d'améliorer l'efficacité des thérapies existantes, en particulier les inhibiteurs de FGFR3.

2 Cancer de vessie : aspects moléculaires

Les classifications moléculaires des différents cancers permettent de mieux comprendre l'hétérogénéité inter-tumorale et de regrouper les tumeurs en groupe ayant une biologie similaire, pouvant bénéficier de traitements stratifiés.

Nous allons décrire dans cette partie la classification moléculaire des TVIM, en particulier basée sur le transcriptome, puis décrire certains gènes importants dans le contexte du cancer de vessie et de ce projet de thèse, comme *FGFR3, EGFR, RXRA/PPARG* et *AHR*.

2.1 Classification moléculaire TVIM/TVNIM

2.1.1 Transcriptome

Plusieurs classifications moléculaires des TVIM basées sur des données transcriptomiques ont été proposées ces dernières années (CIT Curie [22], Lund [23], MDA [24], Baylor [25], UNC [26], TCGA[27]), retrouvant plusieurs sous types que nous allons décrire (ex TCGA avec 5 sous types décrits, **Figure 4).**

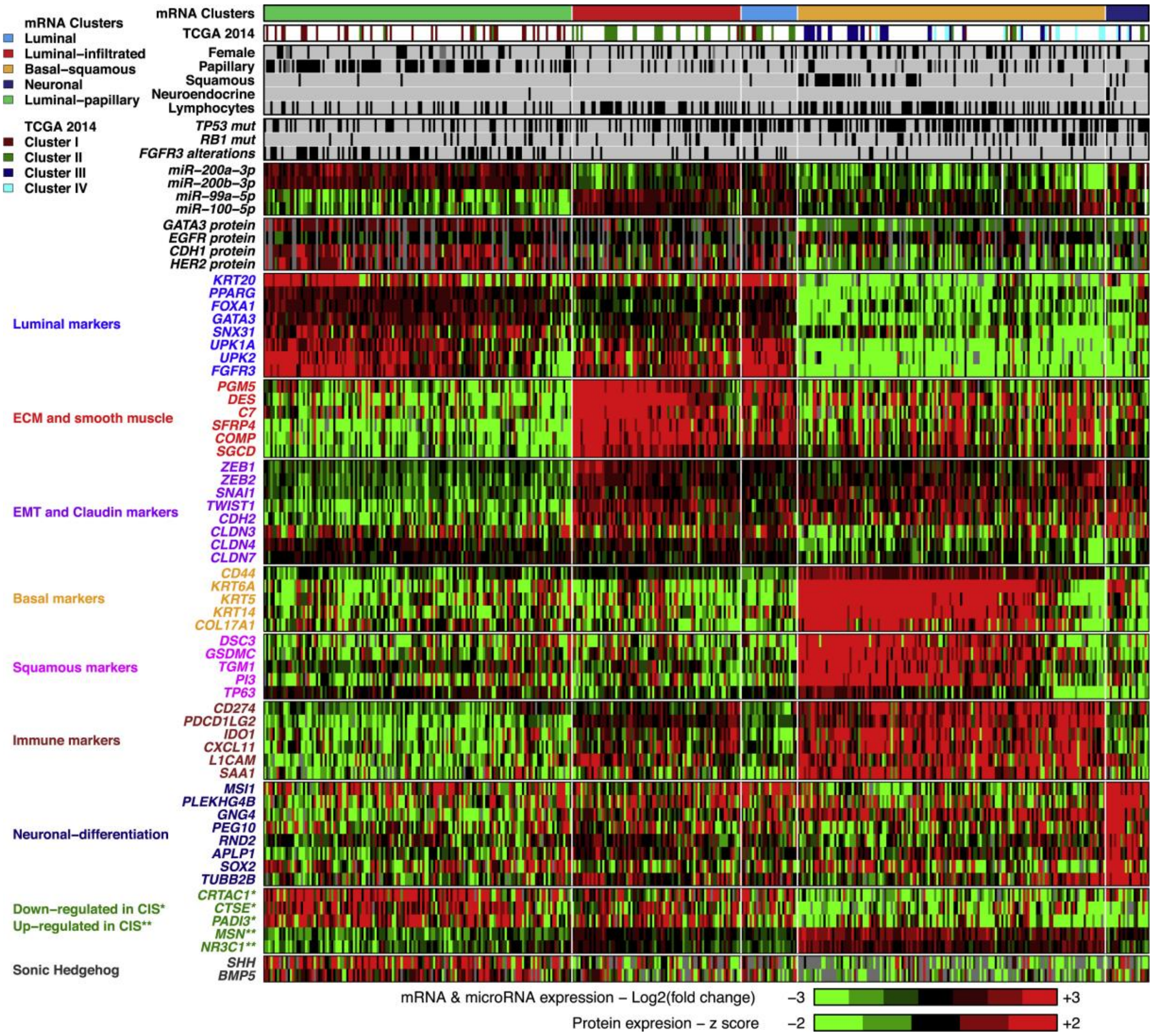

Figure 4 : Expression des principaux gènes selon le sous type Moléculaire dans la cohorte du TCGA.[27] Cette classification basée sur l'expression ARN (RNA-seq) comporte 5 sous types moléculaires (de gauche à droite : Luminal-papillaire, Luminal-infiltré, Luminal, Basal-Squameux et Neuronal).

Une classification consensus des TVIM a été proposée en 2020 en utilisant les données de plusieurs équipes, dont celle du laboratoire, pour permettre d'homogénéiser la classification dans les études cliniques et moléculaires sur ces cancers.

Cette classification consensus obtenue à partir du transcriptome sur 1750 TVIM, individualise 6 sous-types : 3 sous-types luminaux (LumP- Luminal papillary, LumU – Luminal Unstable, LumNS – Luminal Non-Specified), un sous-type basal/squameux (Ba/Sq), un sous-type neuroendocrine (NE-like) et un sous-type riche en stroma (Stroma-rich). Chaque sous-type a été caractérisé sur le plan moléculaire (mutations, altérations génomiques, voies de signalisation activées), histologique et clinique, avec plusieurs messages clés :

- Le sous-type le plus fréquent est le Ba/Sq (35%) suivi du sous type LumP 24%, alors que sous type NE-like est rare (<3%).
- Le sous-type luminal (comprenant LumP, LumU et LumNS) est caractérisé par une signature de différenciation urothéliale, incluant KRT20, uroplakines UPK1A/2 et PPARG/GATA3/FOXA1, alors que le sous type Ba/Sq est caractérisé par l'expression de marqueurs basaux de type KRT5/6/14, CD44 et EGFR.
- Parmi les sous-types luminaux, les LumP présentait un enrichissement des signatures d'activation de la voie Ta et de FGFR3, les LumNS celui d'une signature transcriptomique stromale en particulier de fibroblastes, et les LumU un enrichissement d'une signature de cycle cellulaire.
- Le sous-type stroma-rich présente une signature transcriptomique d'infiltration stromale élevée, en particulier de cellules musculaires lisses, de cellules endothéliales et de fibroblastes/myofibroblastes.

2.1.2 Génomique

Les altérations génomiques les plus fréquentes retrouvées dans les TVIM sont les altérations génomiques de *TP53, RB1*, *FGFR3*, *CDKN2A*, *PPARG*, *ERBB2*, *E2F3*, ainsi que de nombreuses altérations des gènes impliquées dans les régulations épigénétiques *(KDM6A, ARI1A, KMT2C/D).* [28]

Le sous type LumP est particulièrement enrichi en mutations de *FGFR3* (33%) et *KDM6A* (38%) (**Figure 5A et Figure 5B**).

Le groupe luminal est enrichi en amplification de *PPARG*.

Les sous-types Ba/Sq et neuroendocrine sont enrichies en mutation *TP53* (61%/100%) et *RB1* (25%/61%).

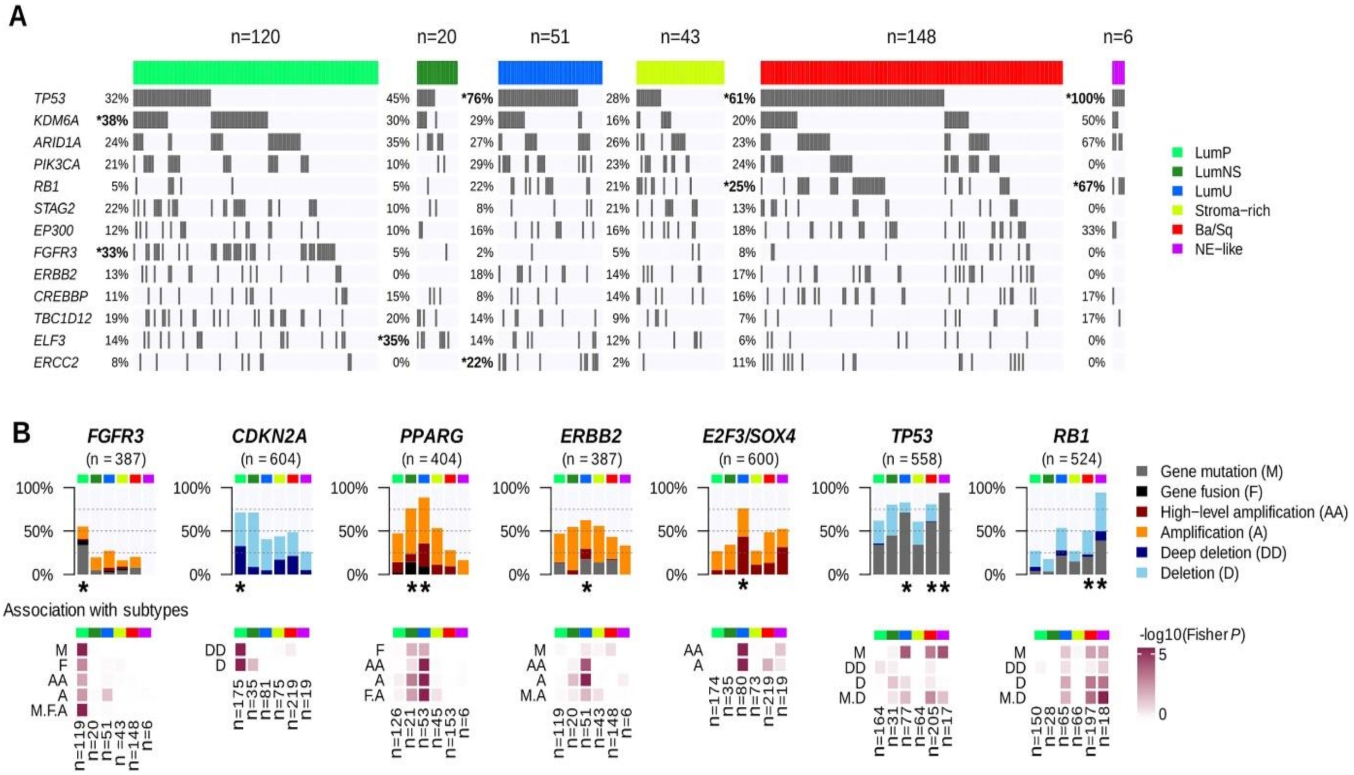

Figure 5 : Principales altérations génomiques selon le sous type moléculaire de cancer de vessie dans la classification consensus. [28]**.**

A Altérations génomiques selon le sous type moléculaire (n=388 exomes de TVIM).

B Panel haut : combinaison des altérations génomiques pour 7 gènes principaux des TVIM. Panel bas : association entre le sous type moléculaire consensus, et le type d'altération génétique (amplification, mutation, et délétion) pour un gène donné.

Les gènes marqués d'une * sont significativement enrichies en altérations génomiques dans le sous-type considéré.

2.1.3 Régulons

2.1.3.1 Principe du régulon

L'activité protéique d'un gène n'est pas toujours bien corrélée avec son expression au niveau ARN ou protéine, du fait en particulier des modifications post traductionnelles. Une protéine activée, en particulier un facteur de transcription, module l'expression de différents gènes. Il est donc possible par inférence de mesurer une activité protéique selon l'expression des différents gènes cibles modulés par cette protéine, facteur de transcription ou non [29].

Pour connaitre les gènes cibles d'un facteur de transcription/d'une protéine, il est possible d'inférer un réseau de régulation transcriptionnel bio-informatiquement sur des données en particulier transcriptomique à l'aide de différentes méthodes (information mutuelle - ARACNE [30], arborescence [31]).

2.1.3.2 *Régulon inféré par données transcriptomiques*

L'inférence des principaux régulons du cancer de vessie, en utilisant un algorithme basé sur l'information mutuelle, retrouve une activité régulon élevée de PPARG, GATA3, ERBB2-3 et FOXA1 dans les tumeurs luminales, de RXRA, RARG, FGFR3 dans le sous type LumP, et de EGFR, STAT3, HIF1A, FOXM1, KLF4 et GATA6 dans les Ba/Sq (**Figure 6**).

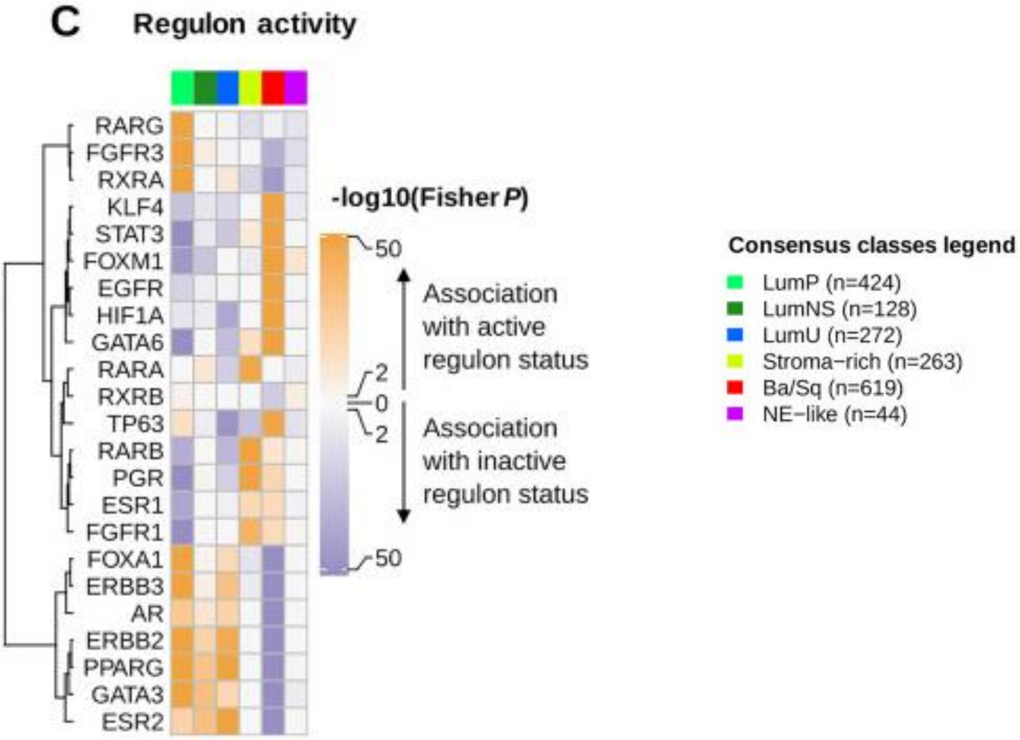

Figure 6 : Activité de protéines (régulon) impliquée dans les cancers de vessie [28]. L'activité de 23 régulons (protéines) a été inférée en utilisant les données transcriptomiques. L'association entre cette activité régulon et le sous type moléculaire (test de Fisher) est ici présentée pour chacun de ces 23 gènes. Par exemple, les activités régulons de PPARG, ERBB2 et ERBB3 sont ainsi élevées dans les TVIM luminales, et l'activité régulon d'EGFR dans les Ba/Sq.

2.1.4 Impact pronostique

En dehors de la compréhension des mécanismes moléculaires en jeu dans les TVIM, la classification moléculaire consensus a également une signification pronostique sur la survie globale (**Figure 7**). En effet les patients ayant une tumeur LumP ont un meilleur pronostic (médiane de survie globale à 4 ans), alors que les patients ayant une tumeur Ba/Sq ont un mauvais pronostique (survie médiane à environ 1.2 an).[28].

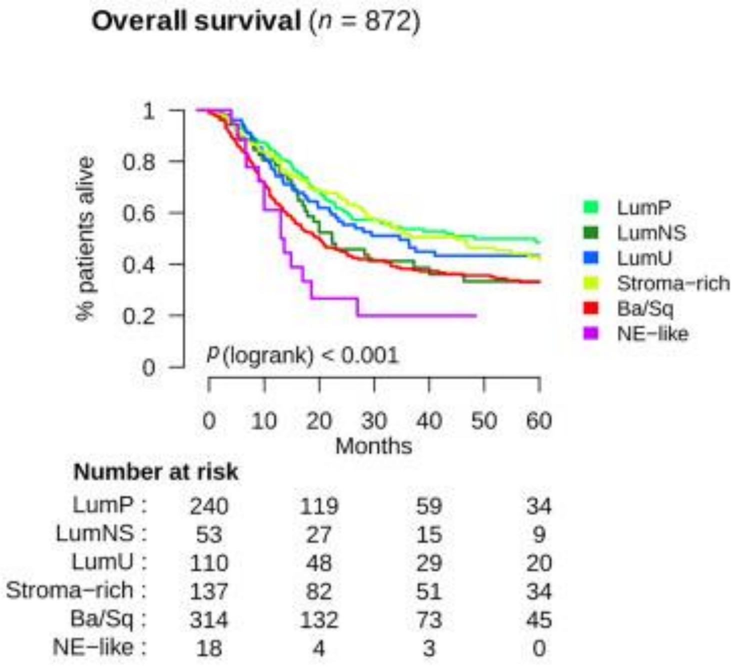

Figure 7 : Survie globale selon le sous type moléculaire de TVIM [28].
Les courbes de Kaplan-Meier ont été générées à partir de 872 patients dont les données de survie étaient disponibles (les patients qui avaient reçu une chimiothérapie néoadjuvante ont été exclus).

En résumé, il a été proposé pour la classification consensus un schéma présentant les principales caractéristiques selon le sous type moléculaire des TVIM (**Figure 8**).

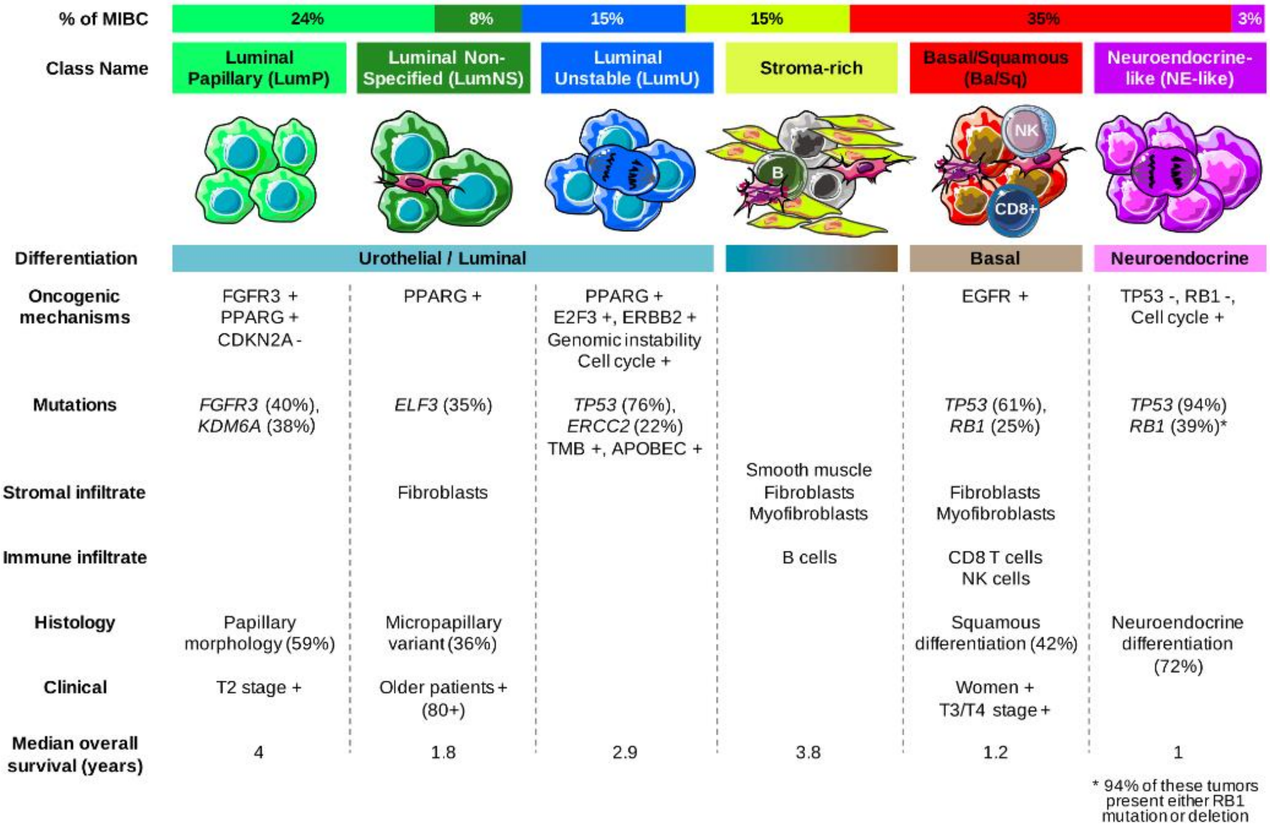

% of MIBC	24%	8%	15%	15%	35%	3%
Class Name	Luminal Papillary (LumP)	Luminal Non-Specified (LumNS)	Luminal Unstable (LumU)	Stroma-rich	Basal/Squamous (Ba/Sq)	Neuroendocrine-like (NE-like)
Differentiation	Urothelial / Luminal				Basal	Neuroendocrine
Oncogenic mechanisms	FGFR3 + PPARG + CDKN2A -	PPARG +	PPARG + E2F3 +, ERBB2 + Genomic instability Cell cycle +		EGFR +	TP53 -, RB1 -, Cell cycle +
Mutations	*FGFR3* (40%), *KDM6A* (38%)	*ELF3* (35%)	*TP53* (76%), *ERCC2* (22%) TMB +, APOBEC +		*TP53* (61%), *RB1* (25%)	*TP53* (94%) *RB1* (39%)*
Stromal infiltrate		Fibroblasts		Smooth muscle Fibroblasts Myofibroblasts	Fibroblasts Myofibroblasts	
Immune infiltrate				B cells	CD8 T cells NK cells	
Histology	Papillary morphology (59%)	Micropapillary variant (36%)			Squamous differentiation (42%)	Neuroendocrine differentiation (72%)
Clinical	T2 stage +	Older patients + (80+)			Women + T3/T4 stage +	
Median overall survival (years)	4	1.8	2.9	3.8	1.2	1

* 94% of these tumors present either RB1 mutation or deletion

Figure 8 : Principales caractéristiques des sous-types consensus des TVIM [28]. Ce tableau résume les principales caractéristiques cliniques, génomiques, du microenvironnement et histologiques observées pour chaque sous type moléculaire.

2.2 FGFR3

FGFR3 (Fibroblast Growth Factor Receptor 3) appartient à une famille de quatre récepteurs tyrosine kinase (FGFR1-4) structurellement apparentés, et joue un rôle essentiel dans la régulation de la prolifération, de la différenciation et de l'apoptose de certaines cellules, en particulier durant l'embryogénèse et le développement du squelette.

Dans le carcinome urothélial, le rôle oncogène des mutations *FGFR3* est médié par la voie RAS-MAPK[32,33]. Des mutations somatiques activatrices du *FGFR3* ont été détectées dans 50 à 70 % des carcinomes urothéliaux papillaires [27,33–35]. Ces mutations, généralement faux-sens sont regroupées en trois points chauds (exons 7, 10 et 15), et entrainent une substitution d'acides aminés dans les régions externe, transmembranaire ou intracellulaire du récepteur. La mutation la plus fréquente (jusqu'à 70 % des tumeurs présentant des mutations du FGFR3) est la S249C dans l'exon 7. Les mutations ayant comme conséquence le remplacement d'un acide aminé par une cystéine conduisent à une dimérisation, une autophosphorylation et une activation du récepteur indépendantes du ligand. Les mutations activatrices du récepteur à activité tyrosine kinase FGFR3 , ont été identifiées il y a 20 ans [36] ; plus récemment, les protéines de fusion FGFR3-TACC3 et FGFR3-BAIAP2L1 ont été mises en évidence dans les tumeurs de vessie [37,38].

Bien que les propriétés oncogéniques du récepteur FGFR3 altéré par mutation ou fusion génique aient été démontrées [38–42], les voies de signalisation qui lui sont associées dans les tumeurs de vessie sont encore peu caractérisées même si des efforts ont été faits en ce sens [43,44].

Les altérations génomiques de *FGFR3* sont très enrichies dans les TVNIM de bas grade, et dans le sous type moléculaire de type LumP des TVIM.

Il existe des thérapies ciblées dans le contexte de tumeurs métastatiques de vessie avec altération génomique de *FGFR3*, et plus rarement de *FGFR2*, décrites dans la partie clinique ci-dessus.

2.3 EGFR

EGFR est un récepteur de tyrosine kinase bien connu dans le domaine de la cancérologie, et bénéficiant de traitements en pratique clinique dans les cancers du poumon mutés pour EGFR et les cancers du côlon non mutés pour KRAS.

Malgré la forte expression et les preuves de l'activation de l'EGFR dans les tumeurs Ba/Sq [22], les résultats des essais cliniques utilisant des traitements anti-EGFR dans les cancers de vessie, qu'il s'agisse d'anticorps ou de petites molécules, ont été décevants [45–47].

Plusieurs mécanismes de résistance primaire et acquise aux inhibiteurs de l'EGFR, non limités aux tumeurs basales, ont été proposés, notamment dans les cancers du poumon et colorectaux : mutations au sein de la voie de l'EGFR incluant des mutations de résistance de l'EGFR, changement phénotypique des cellules cancéreuses (comme une transition épithéliale à mésenchymateuse), activation d'un récepteur alternatif, comme MET, IGF1R ou IFNAR [48–51].

EGFR est donc un récepteur important dans les cancers Ba/Sq, et semble inhibé par PPARγ selon les données du laboratoire, où j'ai effectué une partie des analyses.

2.4 PPARG/RXRA

2.4.1 Récepteurs nucléaires

La famille des récepteurs nucléaires comporte 48 membres, comprenant les récepteurs RXR, PPAR et RAR. Les récepteurs RXR (RXRα, RXRβ, and RXRγ) forment des homo/hétérodimères avec de nombreux membres de la superfamille des récepteurs nucléaires, notamment les PPAR, les RAR, les FXR, les LXR, les TR, les CAR, les NURR1 et les récepteurs de la vitamine D3 (VDR) [52] (**Figure 9**). Les récepteurs PPAR et RAR ont également plusieurs isoformes (PPAR-β/δ/*γ, RAR*-α/β/*γ)*, ayant chacune une localisation et fonction différente selon le type cellulaire.

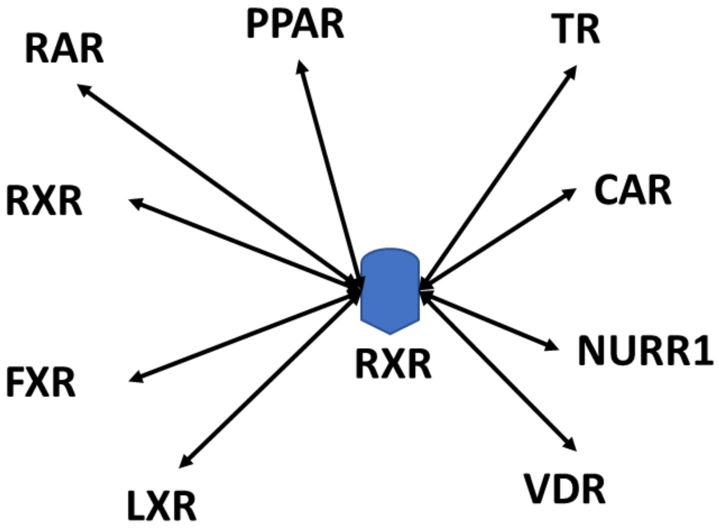

Figure 9 : Partenaires potentiels d'hétéro/homodimères des RXR. Les récepteurs RXR (RXRα, RXRβ, and RXRγ) forment des homo/hétérodimères avec de nombreux membres de la superfamille des récepteurs nucléaires, notamment les PPAR, les RAR, les FXR, les LXR, les TR, les CAR, les NURR1 et les récepteurs de la vitamine D3 (VDR).

2.4.2 PPARγ et RXRα : oncogènes dans les cancers urothéliaux

Dans le cancer de vessie, les récepteurs PPAR*γ et* RXRα ont récemment montré un rôle oncogénique notable. De manière physiologique, PPAR*γ* est un récepteur nucléaire impliqué dans le métabolisme cellulaire, en régulant le stockage des acides gras et le métabolisme du glucose, dans la différenciation et prolifération cellulaire, via majoritairement une hétérodimérisation avec le récepteur RXRα [53]. PPAR*γ* a un rôle dans de nombreux types cellulaires comme les adipocytes ou les macrophages. Alors que *PPARG* a été suggéré comme gène suppresseur de tumeurs au cours des dernières années dans de nombreux sous types tumoraux [53], dont le sous type basal des cancers de vessie comme démontré par notre équipe [54], un rôle inverse, protumorigénique, de PPAR*γ* a été mis en évidence dans les tumeurs luminales de vessie[55].

Au niveau épidémiologique, plusieurs études montrent qu'un traitement des patients diabétiques par la pioglitazone, un ligand de PPAR*γ*, entraine une augmentation du risque de développer un cancer de la vessie [56]. Au niveau fonctionnel, notre laboratoire a montré que la viabilité des modèles de lignées cellulaires de carcinomes de vessie exprimant *PPARG* dépend de l'expression de ce gène[27,57,58], par analogie avec le récepteur aux œstrogènes dans le cancer du sein luminal[59]. L'inhibition de *PPARG* en préclinique inhibe la prolifération tumorale des cancers luminaux de la vessie ([55,57,60]), ce qui fait de PPARγ une cible thérapeutique particulièrement intéressante dans ces cancers, actuellement non développée en recherche clinique.

PPARγ a un rôle sur la cellule tumorale, comme le montrent les expériences *in vitro*, mais également sur le microenvironnement. En effet, l'activation de l'hétérodimère RXRα/ PPARγ a été montrée comme responsable d'une répression des chimiokines pro-inflammatoires et de l'infiltration réduite tumorale des cellules T CD8+, pouvant conduire à une résistance à l'immunothérapie par inhibiteur de checkpoint immunitaire actuellement utilisé en pratique clinique (anticorps anti-PD1)[61].

Cette activation était fréquemment associée à des gains/amplifications et une surexpression de *PPARG* ~20%)[24,27,57] et/ou à des mutations ponctuelles activatrices de *RXRA* (2-5%) [61,62].

Un séquençage systématique de *PPARG* dans 384 tumeurs de vessie et une analyse des données de séquence de *PPARG* publiées (n = 455) avait permis d'identifier des mutations récurrentes de *PPARG* associées aux tumeurs luminales de vessie, la mutation la plus fréquente étant la mutation T475M [55]. Des analyses fonctionnelles de 7 des 8 mutants identifiés ont montré une activité transcriptionnelle augmentée de 6 des 7 mutants par rapport à la forme sauvage de la protéine). Il a également été montré dans le laboratoire la dépendance pour le mutant T475M d'une lignée cellulaire tumorale de vessie présentant cette mutation confirmant l'activation et l'activité protumorale du récepteur muté.

Des études structure-fonction des mutations dans le domaine de liaison au ligand réalisées en collaboration avec notre laboratoire ont permis d'identifier les éléments structuraux responsables des gains de fonction. L'identification de mutations récurrentes activatrices de PPARG dans les tumeurs luminales apporte une preuve génétique supplémentaire du rôle protumorigénique de PPARγ et renforce l'importance de la voie PPARγ/ RXRα dans ce groupe de tumeurs[55].

Concernant les mutations de RXRα (S427F/Y), des études structure-fonction indiquent que cette mutation de *RXRA* régule de manière allostérique le domaine AF2 de PPAR, et active donc de manière préférentielle PPARγ par rapport aux autres partenaires de RXR[62].

2.4.3 PPARγ : rôle de gène suppresseur de tumeurs dans les cancers urothéliaux

Parallèlement aux altérations génétiques conduisant à une activation de PPARγ dans les tumeurs luminales de vessie, il a été observé une perte d'activité de PPARγ dans les tumeurs basales suggérant un possible rôle de suppresseur de tumeurs de *PPARG* dans ce sous-type. Parmi les mutations non récurrentes de *PPARG* identifiées [55], certaines étaient associées à des tumeurs basales, et ont été confirmées comme inactivatrices [54].

Il a par ailleurs été identifié un enrichissement dans les tumeurs basales en délétions hémizygotes de *PPARG*, une hyperméthylation du promoteur et la présence de la marque répressive H3K9me3 dans cette région associée à la perte d'expression de PPARG. En outre, l'expression induite de *PPARG* ou l'activation de *PPARG* dans les lignées de cellules cancéreuses de la vessie de type basal a diminué la viabilité cellulaire, alors qu'elle n'a montré aucun effet sur la viabilité cellulaire des cellules de type luminal[54].
Enfin, il a été montré par des techniques de ChIP-Seq et d'étude de gènes différentiellement exprimés après la modulation de l'activité de *PPARG*, dont j'ai effectué une partie des analyses bio-informatiques, que l'activité suppressive de *PPARG* dans les tumeurs basales pourrait au moins partiellement reposer sur l'inactivation de la voie de l'EGFR dont dépendent les cellules basales [22].

PPARγ / RXRα sont des récepteurs nucléaires majeurs dans le cancer de vessie, avec un rôle dual pour PPARγ oncogénique/suppresseur de tumeurs selon le sous type moléculaire de cancer[63], et un rôle de RXRα principalement connu comme étant associé à PPARγ plutôt qu'à d'autres de ses partenaires.

2.5 AHR

AHR est un facteur de transcription, localisé au niveau du cytoplasme lorsqu'inactif, faisant parti d'un complexe protéique (HSP-90, p23, AIP et SRC). Après activation par un ligand, endogène tel que la kynurénine ou ITE ((2-(1' H-indole-3'-carbonyl)-thiazole-4-carboxylic acid methyl ester), ou exogène tel que FICZ (6-formylindolo[3,2-b]carbazole) ou TCDD (2,3,7,8-tetrachlorodibenzo-p-dioxin), le complexe AHR est activé [64,65] (**Figure 10A**).

Cette activation conduit à une translocation dans le noyau avec une libération des protéines chaperonnes et formation d'un hétérodimère avec ARNT. L'hétérodimère AHR-ARNT peut permettre la modulation de la transcription de gènes via le domaine « xenobiotic response elements » (XRE), mais aussi d'autres gènes par interaction avec d'autres récepteurs nucléaires tel que le récepteur aux œstrogènes [66]. Les gènes cibles classiques d'AHR sont *CYP1A1*, *CYP1B1, AHRR et TIPARP*. En dehors de son rôle transcriptomique, AHR peut exercer un rôle une fois activé en libérant la protéine SRC, ou en se liant à une ubiquitine-ligase (CUL4B), pouvant moduler la dégradation de protéines telles que MYC et PPARγ (**Figure 10B**).

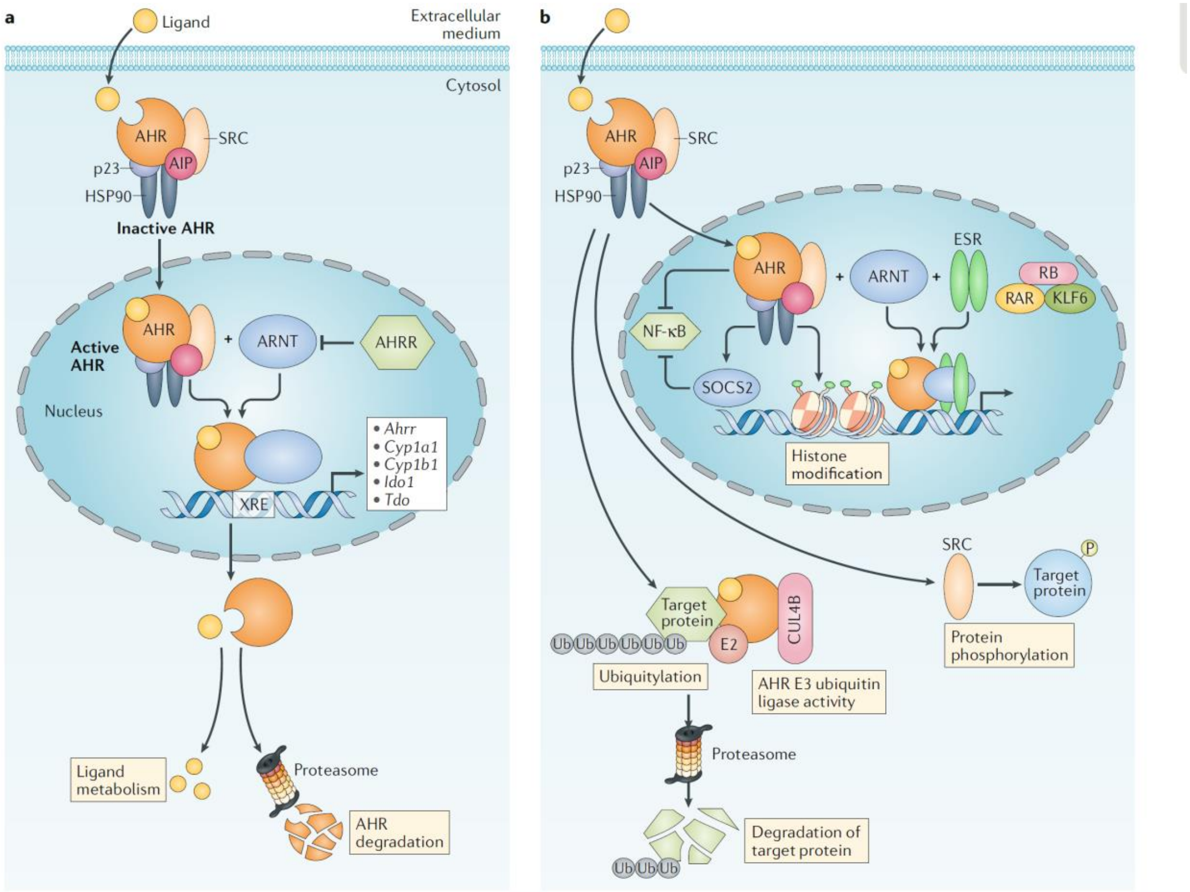

Figure 10 : Mécanismes d'action intracellulaire d'AHR (a) transcriptionnelle (b) cytoplasmique.[67]

A AHR inactif est associé à HSP90, AIP, p23 et SRC. Son activation par un ligand d'AHR conduit à sa translocation dans le noyau et à la formation d'un hétérodimère avec ARNT. L'hétérodimère AHR-ARNT peut permettre la modulation de la transcription de gènes via le domaine « xenobiotic response elements » (XRE).

B Le complexe AHR/ARNT peut également interagir avec d'autres facteurs de transcription et ainsi moduler leurs activités (ex : ESR1, NF-κB). En dehors de son rôle transcriptomique, AHR peut exercer un rôle cytoplasmique une fois activé en libérant la protéine SRC, ou en se liant à une ubiquitine-ligase (CUL4B), pouvant moduler la dégradation de protéines telles que MYC et PPARγ.

Concernant le rôle d'AHR, il a historiquement été montré comme ayant un rôle dans le métabolisme des xénobiotiques (principalement des hydrocarbures aromatiques, dont les dioxines ou PCB "polychlorobiphényles"), qui ont été les premiers ligands découverts d'AHR [68]. En dehors de ce rôle majeur, de nombreux rôles dépendant du contexte d'AHR ont été décrit : invasion et adhésion cellulaire, prolifération, rôle dans la reproduction, le développement vasculaire, neurologique ou hématopoïétique [68].

Le rôle d'AHR dans le cancer a été étudié depuis de nombreuses années, avec un rôle surtout décrit comme tumeur suppresseur mais également oncogénique selon le type de cancer [64,69–72]. En particulier AHR, qui a pour ligand potentiel la Kynurénine, a un rôle majeur dans l'immunité anti tumoral, avec un effet global immunosuppresseur [65].

Dans le cancer de vessie, notre équipe a montré récemment qu'il existait des mutations d'*AHR* (Q383H) qui étaient dues à un processus mutationnel de type APOBEC et spécifiques au cancer de vessie. AHR présentait par ailleurs une signature d'activation plus élevée (signature basée sur des gènes dont l'expression est corrélée à AHR et CYP1A1, et modulés par des siRNA ciblant AHR dans une lignée de cancer du sein MCF7) dans les cancers luminaux de vessie, avec une sensibilité de lignées cellulaires luminales à un inhibiteur d'AHR à forte concentration (CH-223191). [73].

AHR a donc été suggéré comme un oncogène dans le cancer de vessie, dont le rôle est mal connu actuellement.

2.6 Réseau de régulation des tumeurs luminales ou basales

Il a été proposé qu'il existait des « master regulators » ou point de contrôle tumoraux, protéines cruciales regroupées en réseau et participant au maintien du phénotype cellulaire tumorale et à l'identité de la cellule [74,75] (**Figure 11**).

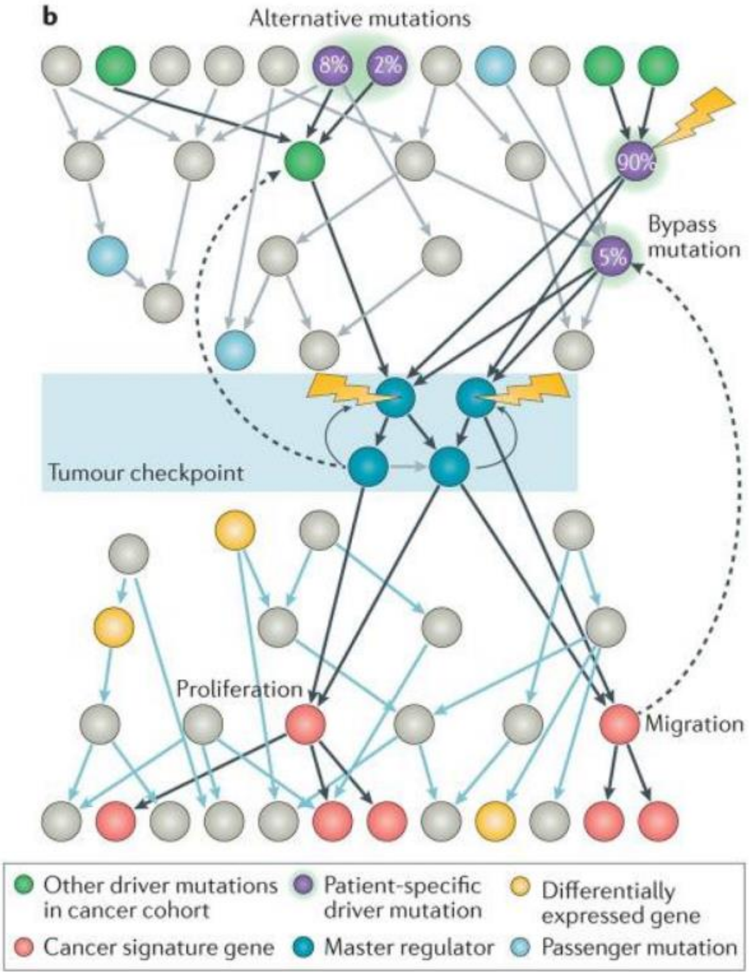

Figure 11 : Schéma représentant le concept de « points de contrôle tumoraux » dans la cellule tumorale, protéines clés regroupées en réseau et participant au maintien du phénotype tumoral [74]. Les points de contrôles tumoraux représentent un ensemble de protéines regroupées en réseau, nécessaires et suffisantes pour le maintien du phénotype tumoral. Leur activité aberrante est induite par des gènes en amont, mutés de manières variables selon le patient. Ceci peut expliquer que différentes altérations génétiques dans différents gènes peuvent conduire au même phénotype tumoral. En aval, il est ainsi possible de déterminer des signatures d'expression spécifiques de ce phénotype tumoral.

Il a été montré dans des lignées de cancers urothéliaux qu'il existait un réseau de régulation entre FOXA1, GATA3 et PPARG pour permettre l'expression de gènes luminaux et que leur activation pouvait trans-différencier une lignée basale (5637) en phénotype luminal[76]. Ces 3 gènes peuvent donc être considérés comme des points de contrôle tumoraux dans les cancers de vessie luminaux, en particulier dans la lignée cancéreuse 5637, vu qu'ils sont nécessaires et suffisants pour orienter le phénotype (**Figure 12**). Néanmoins, il est important d'identifier les autres gènes impliqués dans les points de contrôle tumoraux des tumeurs luminales, ainsi qu'identifier ceux impliqués dans les tumeurs Ba/Sq de vessie.

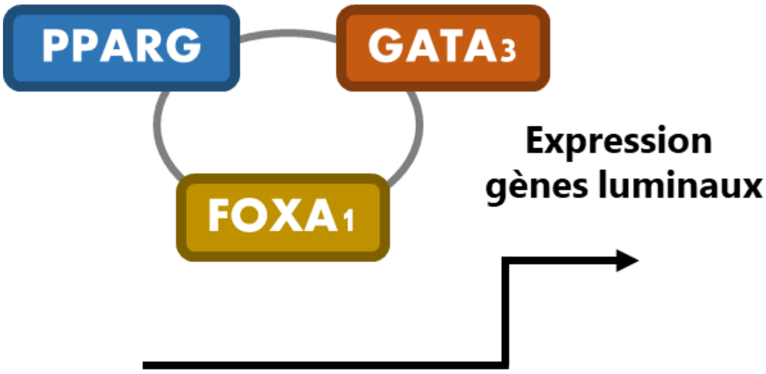

Figure 12 : PPARG, GATA3, FOXA1 sont des points de contrôles tumoraux des tumeurs luminales. Ces 3 facteurs de transcriptions agissent en coopération pour induire l'expression des gènes luminaux, et sont nécessaires pour l'obtention du phénotype luminal.

]

2.7 Hétérogénéité des cancers de vessie

L'hétérogénéité intra-tumorale est un phénomène maintenant bien connu en cancérologie, mécanisme majeur de résistance aux traitements et qui s'observe également dans les tumeurs de vessie [77–79].

Grâce à un double marquage GATA3/KRT5/6 par immunohistochimie (IHC), il a été identifié 83 tumeurs basales (GATA3 - et KRT5/6+) parmi une série de 331 TVIM incluses en paraffine[80]. 19 tumeurs présentaient un marquage hétérogène et des zones différentes ont ensuite été analysées au niveau transcriptomique et génomique. Dans 2/3 de ces tumeurs hétérogènes, les différentes zones montrent le même sous-type transcriptomique et les mêmes altérations génomiques, et dans le tiers restant elles correspondent à des sous-types transcriptomiques et altérations génomiques différentes.

Une étude ayant comparé la classification moléculaire observée chez des patients entre la TVIM et une métastase ganglionnaire a montré une discordance avec une hétérogénéité observée surtout dans les tumeurs basales (~50% des cas) [81].

Ces travaux, ainsi que d'autres [79], soulignent l'importance de considérer cette hétérogénéité intra-tumorale lors du diagnostic, pour orienter les choix thérapeutiques dans le cadre d'une médecine de précision mais également pour mieux appréhender les mécanismes de progression tumorale[82]. Cette hétérogénéité peut maintenant également s'observer avec les analyses de cellules uniques [83] et en transcriptomique spatiale.

3 Microenvironnement tumoral et cancer urothéliaux

3.1.1 Environnement immunitaire péritumoral : Généralités

Le microenvironnement tumoral comprend un nombre varié de types cellulaires : lymphoïdes (lymphocyte T, B, NK), myéloïdes (monocytes/macrophages, cellules dendritiques, neutrophiles, mastocytes), fibroblastes, et cellules endothéliales (**Figure 13**). Les cellules immunitaires peuvent également être classées entre cellules de l'immunité innée (neutrophiles, monocytes/macrophages, NK, mastocytes, cellules dendritiques et cellules lymphoïdes innées) et adaptative (lymphocyte T, B).[84]

La tumeur peut libérer des antigènes, capter principalement par les cellules présentatrices d'antigènes (cellules dendritiques principalement), qui vont migrer au niveau des ganglions pour activer les lymphocytes T CD8 cytotoxiques qui vont eux migrer au niveau du site tumoral et pouvoir exercer une activité anti tumorale. Les lymphocytes B vont également pouvoir être activés et devenir des cellules plasmatiques productrices d'anticorps. Les lymphocytes CD4 naïfs vont également pouvoir se différencier en lymphocytes CD4 (Th1, Th2 ou Th17), qui vont permettre de potentialiser l'activation des LT CD8+ par la production de cytokines et chimiokines (en particulier Lymphocytes CD4 Th1, production IL2/IFN-y).

Dans le cadre de la progression tumorale, un phénomène d'immuno-évasion va se mettre en place permettant à la cellule tumorale d'échapper à la réaction immunitaire anti-tumorale [84,85] et impliquant diverses cellules immunitaires et du stroma. Au cours du temps, un environnement immunosuppresseur va se mettre en place, comprenant des macrophages associés à la tumeur (TAM) de type M2, des cellules myéloïdes suppressives (Myeloid-derived suppressor cell), des lymphocytes T-reg (T régulateurs).

Cet environnement se met en place par la sécrétion de cytokines et chimiokines comme IL-10 et TGF-B. Les lymphocytes T régulateurs vont, en dehors de la production de cytokines immunosupressives (et un captage d'IL2), inhiber les cellules dendritiques via l'expression membranaire de CTLA4 et au final conduire à l'inactivation des lymphocytes T [86]. Secondairement au caractère chronique de l'inflammation et de cet environnement immunosuppresseur, les lymphocytes T CD8+ cytotoxiques vont alors présenter un phénomène d'« épuisement » (exhausted T cells) et être inhibé, phénotypiquement caractérisé par l'expression de CTLA-4, TIGIT, TIM3 et LAG3 [87].

Le développement de l'analyse de cellules uniques (décrit **Chapitre 4**), a permis ces dernières années une compréhension bien plus fine de ces différents acteurs et de leur interactions, du fait de l'observation qu'il existe à l'intérieur d'un même type cellulaire (exemple lymphocyte T, fibroblaste ou macrophage) des phénotypes très variés avec des fonctions diverses voire antagonistes.

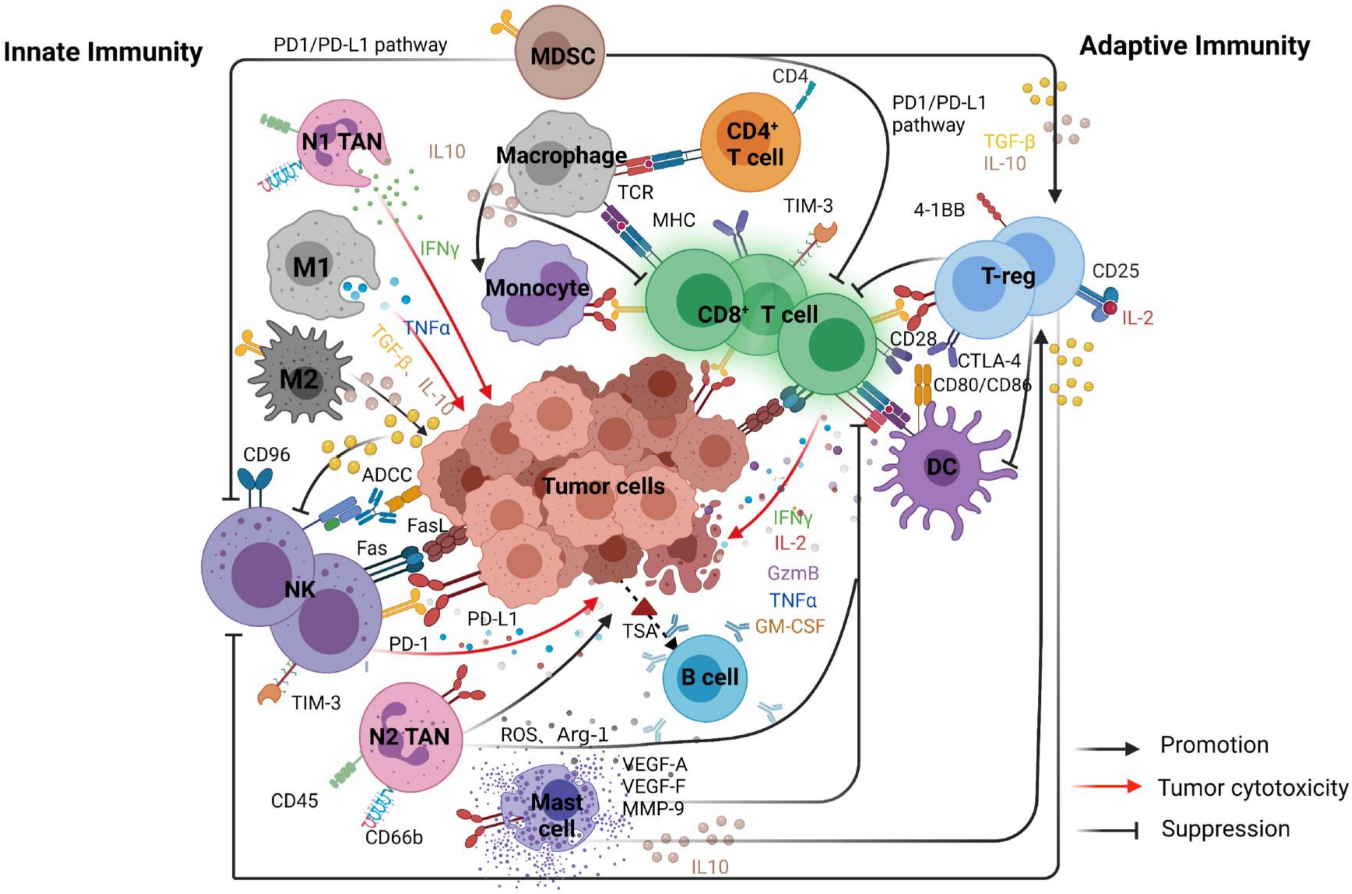

Figure 13 : Principales interactions entres les cellules tumorales et les cellules immunitaires du microenvironnement [84]. Les cellules tumorales sont en interaction avec de nombreuses cellules présentes dans le micro environnement, immunitaires comme les lymphocytes (T/B/NK) et les cellules myéloïdes (monocytes/macrophages, cellules dendritiques, neutrophiles, mastocytes) et non immunitaires (non présentes sur ce schéma) comme les fibroblastes, et les cellules endothéliales.

3.1.2 Structures lymphoïdes tertiaires : généralités

Les structures lymphoïdes tertiaires (SLT) sont des formations lymphoïdes ectopiques qui se forment dans un tissu non lymphoïde (**Figure 14**). Elles partagent des caractéristiques structurelles et fonctionnelles avec les structures lymphoïdes secondaires telles que les ganglions lymphatiques et peuvent contenir des follicules de cellules B et des centres germinatifs entourés d'une région de cellules T.

Ces structures lymphoïdes tertiaires existent dans différents niveaux de maturation (agrégats puis organisation en follicules).

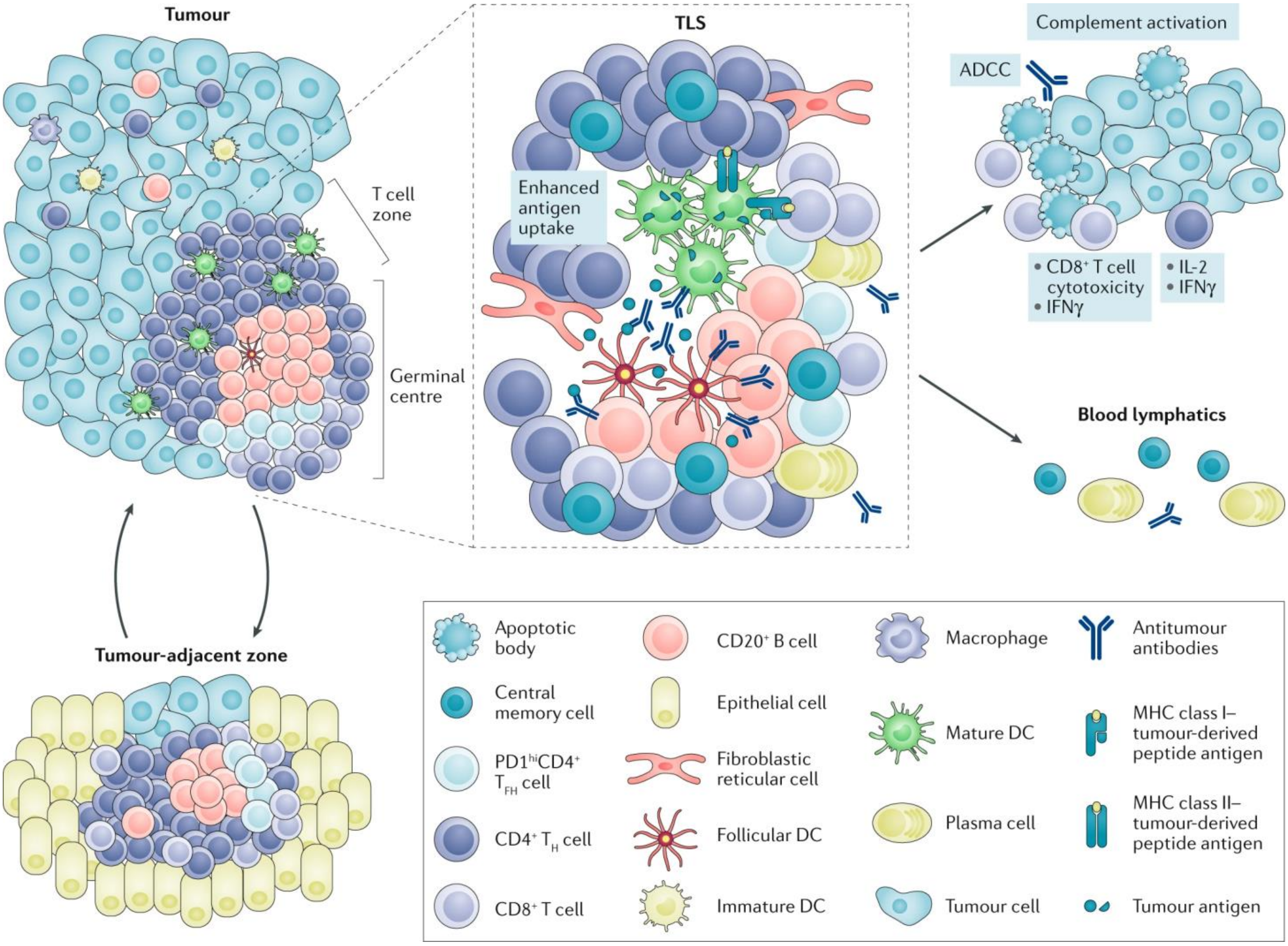

Figure 14 : Représentation schématique des structures lymphoïdes tertiaires [88]. Cette représentation montre la présence d'une SLT au sein d'une tumeur (haut/gauche) ou à distance (gauche/bas). Cette SLT (centre) est composée de lymphocytes B, cellules plasmatiques, lymphocytes T CD4+ et CD8+ ainsi que de cellules dendritiques. Les SLT permettent la diffusion sanguine de cellules plasmatiques, anticorps antitumoraux ou de cellules mémoires, ainsi qu'une action antitumorale locale via différents mécanismes (cytotoxicité des LT CD8, activation du complément, cytotoxicité cellulaire dépendante des anticorps – ADCC- et la production de cytokines comme IL2/IFNy.

3.1.3 Micro-environnement tumoral et cancer de vessie

Il est possible en utilisant des algorithmes de déconvolution d'estimer la présence et la proportion de cellules immunitaires ou du stroma à partir d'analyse de transcriptome (tissulaire ou de cellules uniques, certains marqueurs étant spécifiques de chacun de ces types cellulaires, ex : CD8A pour les lymphocytes T CD8+) (**Figure 15**) [28].

A partir de ces analyses, il a été montré que le type moléculaire Stroma-Rich et Ba/Sq était caractérisé par une infiltration par le microenvironnement, alors que les tumeurs

LumP ou LumU présentaient peu d'infiltration. En particulier, les tumeurs Stroma-Rich et Ba/Sq présentent une infiltration en fibroblastes et en cellules myéloïdes, et les tumeurs Ba/Sq une infiltration en lymphocytes T cytotoxiques et de la lignée monocytaire.

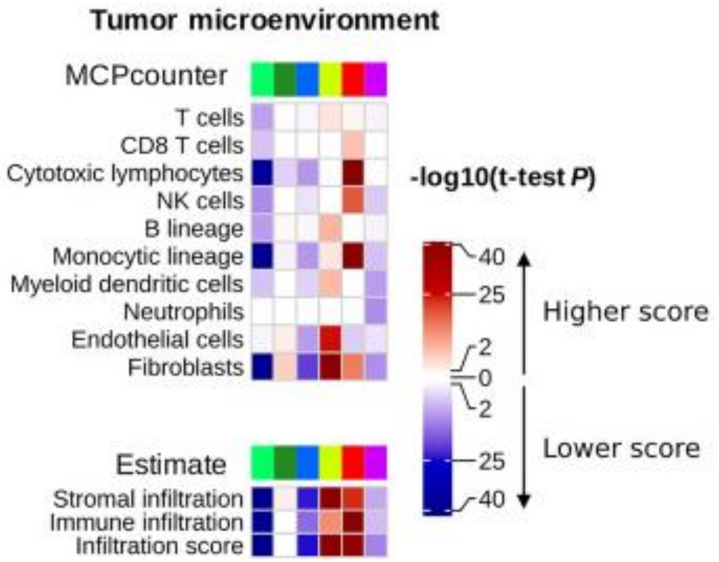

Figure 15 : Qualification et quantification du micro-environnement tumoral des TVIM par données transcriptomiques[28]**.** Utilisation de 2 outils bio-informatiques (Estimate/MCPcounter) pour quantifier/qualifier les cellules du microenvironnement dans un échantillon en utilisant les données transcriptomiques, via des marqueurs transcriptomiques biologiquement validés de sous-populations spécifiques de cellules immunitaires et stromales.

Du fait du mauvais pronostic observé chez les patients atteints d'une tumeur Ba/Sq, la présence de cellules myéloïdes ou fibroblastes sont généralement également associés à un mauvais pronostic.

Le lien entre ce microenvironnement tumoral et la réponse aux immunothérapies est également un sujet d'étude majeur, décrit dans la partie Biomarqueurs de réponse aux traitements.

4 Analyses Single cell - de Cellule unique

4.1 Généralités

Les analyses biologiques de cellule unique (« single-cell ») ont révolutionné la recherche dans le cancer ces dernières années [83,89] (**Figure 16**).

En effet, les principales analyses à large échelle auparavant étaient réalisées sur un échantillon dont les cellules étaient mélangées, que cela soit pour la recherche d'altérations génomiques ou pour les analyses du transcriptome, des altérations épigénétiques ou du protéome. Les analyses par cytométrie en flux (FACS) ou les analyses histologiques permettaient d'analyser l'hétérogénéité d'échantillons mais sur peu de marqueurs et en utilisant pour la cytométrie du tissu frais.

Ces analyses globales (« bulk) ont permis de réaliser, comme décrits plus haut, des classifications moléculaires des cancers, mais ne peuvent que partiellement appréhender l'hétérogénéité intra-tumorale, et de déterminer les différents sous types présents dans le micro-environnement.

Les analyses de cellule unique permettent théoriquement d'analyser individuellement les cellules d'un échantillon, selon la technique sur leur expression (single-cell RNA), épigénétique (ex ATAC-seq), génomique (single cell DNA) ou protéique.

L'inconvénient de ces analyses de séquençage de cellule unique est leur coût qui limite généralement la constitution de cohortes à large échelle, limitant la puissance statistique des analyses, mais aussi la nécessité de disposer de prélèvements frais, problème résolu avec le séquençage de noyau unique.

L'autre inconvénient majeur est le « drop out », c'est-à-dire le fait qu'un gène soit observé à un niveau d'expression modéré ou élevé dans une cellule, mais n'est pas détecté dans une autre cellule similaire, par un défaut de capture et non à cause d'une réalité biologique. Néanmoins, le fait de regarder simultanément un grand nombre de gènes permet de déterminer des clusters de types cellulaires.

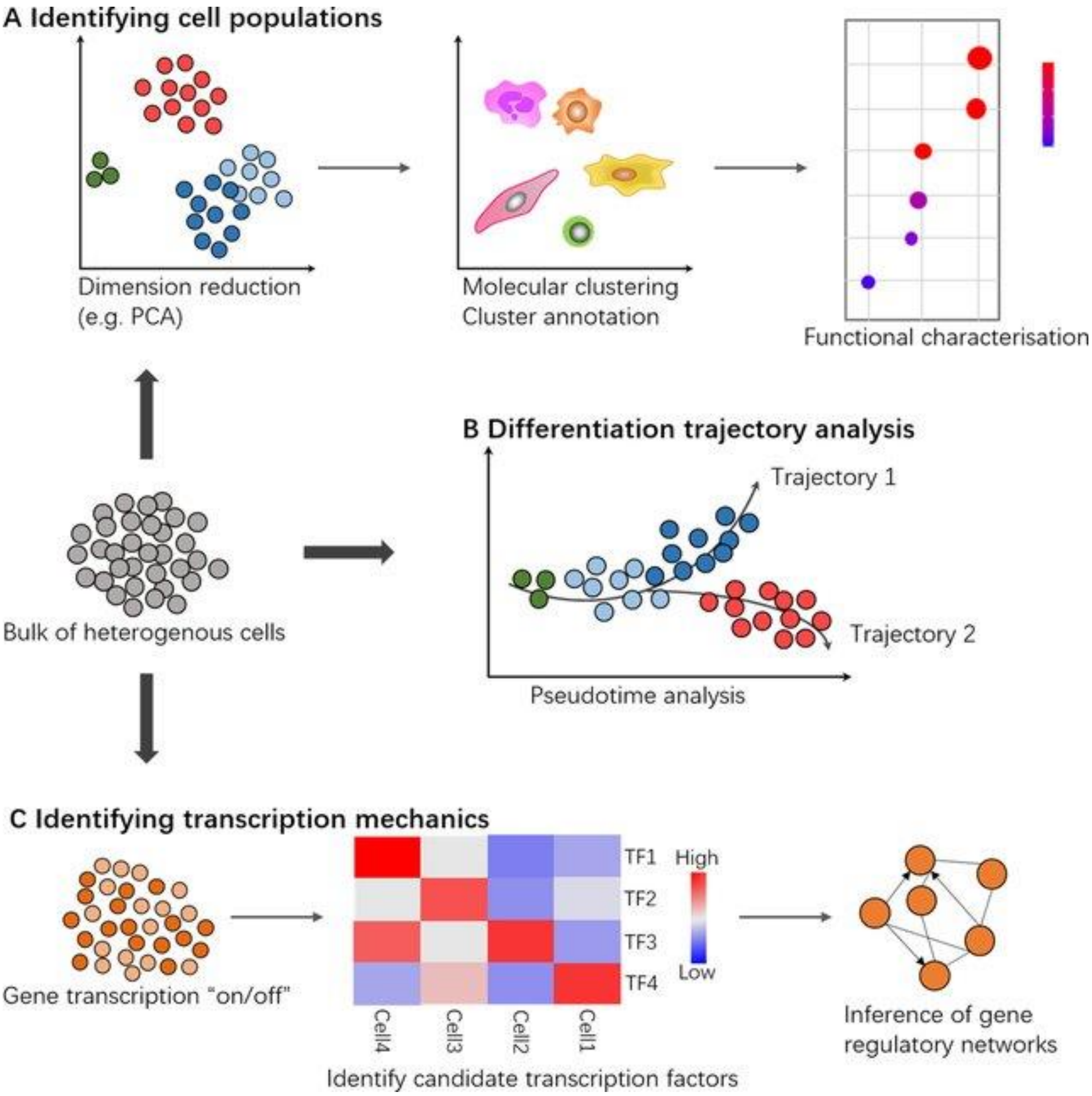

Figure 16 : Applications des analyses de séquençage de cellule unique dans le cancer [90]**.** Applications classiques : A) Identification des populations cellulaires. Les ensembles de données scRNA-Seq sont traités par des techniques de réduction de la dimension pour faciliter la visualisation. Le regroupement – « clustering » moléculaire permet d'identifier des sous-types cellulaires hétérogènes et de nouvelles populations. Les clusters peuvent être annotés selon leur profil d'expression. B) Analyse de la trajectoire de différenciation. L'analyse pseudo temporelle basée sur les ensembles de données scRNA-Seq ordonne une cellule unique le long de l'axe "série temporelle" qui représente les transitions dynamiques de l'état cellulaire, comme la différenciation ou les réponses de signalisation à un stimulus externe, pouvant identifier les groupes de gènes qui permettent cette transition d'état cellulaire. C) Identifier les mécanismes de transcription et inférer un réseau de régulation de gènes selon les variations d'expression entre les cellules ou des altérations génomiques.

Récemment, les techniques d'analyse de séquençage de noyau unique ont permis d'utiliser des prélèvements congelés plutôt que des prélèvements frais, permettant d'analyser certaines types tumoraux non analysables auparavant, ou de plus facilement permettre l'analyse de cohortes, avec une bonne corrélation entre les 2 analyses [91].

4.2 Cancer de vessie

Depuis 2020 ont été publiées quelques études concernant les tumeurs de vessie résumées dans la **Table 1**.

Ces différentes études ont pu confirmer qu'il existait une infiltration stromale hétérogène dans les tumeurs de vessie, composée selon les tumeurs de lymphocytes (T CD4/CD8, NK, B), fibroblastes, cellules myéloïdes (monocytes/macrophages, cellules dendritiques..), ainsi qu'une hétérogénéité du contingent épithélial.

Il est à noter que l'ensemble de ces études a étudié des tumeurs primaires de vessie et qu'aucune donnée sur des échantillons de métastases ne sont actuellement disponibles.

Technique	N Cells	N patients	Conclusions principales	References
scRNA-seq + TCR-Seq	CD4 19842 CD8 10762	7 (4 anti-PD-L1, 1 chimiothérapie, 2 Normaux	Les cellules T CD8+ ne sont pas différentes dans les tumeurs par rapport aux tumeurs non malignes. Les tumeurs de vessie humaine contiennent plusieurs états de cellules T CD4+ cytotoxiques Les cellules T CD4+ cytotoxiques exercent leur effet anti-tumoral de manière dépendante du CMH de classe II. Les cellules T régulatrices peuvent inhiber l'activité des cellules T CD4+ cytotoxiques. Une signature génétique des cellules CD4+ cytotoxiques permet de prédire la réponse à l'anti-PD-L1 dans le cancer de la vessie	[92]
scRNA-seq	19708	10 (7 Tumeurs, 3 Normaux)	Les signatures globales transcriptomiques de la réponse immunitaire adaptative et de l'inflammation pro-tumorogénique sont apportées par des types cellulaires différents dans le microenvironnement . Ces signatures sont liées plus au phénotype cellulaire qu'au type cellulaire (ex la signature pro-tumorogénique est liée à un certain type de macrophage)	[93]
scRNA +ATAC-Seq	54971 (37400 RNA, 17,571 ATAC)	13	La sous-population de cellules souches cancéreuses est enrichie lors de la récidive du cancer de la vessie avec une expression élevée d'EZH2. EZH2 maintient la répression du gène *NCAM1* médiée par H3K27me3, inhibant le programme transcriptionnel de la transition épithélio-mésenchymateuse dans les échantillons cliniques TCF7 favorise la transition épithélio-mésenchymateuse	[94]
scRNA-seq	36619	7	Les cellules tumorales de type basal possèdent des caractéristiques de transition épithélio-mésenchymateuse	[95]

			(enrichissement en gènes associés à la transition épithélio-mésenchymateuse). Les cellules de type basal présentaient la capacité de générer des cellules luminales, ce qui en fait des précurseurs possibles de l'invasion locale. Des propriétés de cellules souches ont été observées dans une TVIM.	
snRNA	71832	25	Une population tumorale CDH12+ est associée à un mauvais pronostic chez les patients traités par chirurgie et par chimiothérapie néoadjuvante à base de platine. La population CDH12+ prédit un meilleur pronostic et des taux de réponse plus élevés aux anti-PD-L1.	[96]
scRNA-seq	52721	8 (+ 3 para-tumoral)	19 types de cellules différentes identifiées dans le microenvironnement des TVIM, avec une forte hétérogénéité inter-tumorale. Les cellules tumorales avaient une expression diminuée de molécules du CMH-II, pouvant favoriser un micro-environnement immunosupresseur. Les monocytes subissent une polarisation M2 dans la région de la tumeur et se différencient. Le sous-groupe de cellules dendritiques LAMP3+ peut être capable de recruter des cellules Treg participant à la formation d'un micro-environnement immunosuppressif. Identification de iCAF impliqué dans la progression tumorale, de mauvais pronostic, ainsi que leur réseau de régulation.	[97]
scRNA-seq	26792	4	La voie de la biosynthèse des N-glycanes était activée dans les tumeurs de haut grade. Le microenvironnement tumoral des différents échantillons montre une grande hétérogénéité.	[98]
scRNA-seq	133,953	23 (+3 Normaux)	Les cellules tumorales TM4SF1+ conduisent à une hétérogénéité intra-tumorale.	[99]

Table 1 : Résumé des principales études de séquençage de cellules uniques dans les tumeurs de vessie

scRNA-seq : séquençage d'ARN de cellule unique, snRNA-Seq: séquençage d'ARN de noyau unique, CAF : « Cancer-associated fibroblast »

5 Biomarqueurs de réponse aux traitements systémiques

5.1 Chimiothérapie

Plusieurs études ont recherché des biomarqueurs de réponse à la chimiothérapie.
L'impact de la classification moléculaire consensus sur la réponse a montré des résultats variables selon les études [100–103]. Par exemple, Seiler *et al* ont montré que le sous type basal était associé à une meilleure réponse à la chimiothérapie [101], alors que Sjödhal *et al* ont montré une meilleure réponse dans un sous type luminal-like [102], et une autre étude une moins bonne réponse dans les basales [103]. Ceci étant en partie lié à la difficulté de distinguer un biomarqueur comme pronostic ou prédictif, en l'absence de bras contrôle sans traitement.
Taber *et al* ont montré en combinant une analyse génomique, transcriptomique, épigénétique et protéomique que les biomarqueurs génomiques principaux de réponse à la chimiothérapie étaient une instabilité génomique (haut niveau d'altérations chromosomiques, une signature mutationnelle « 5 » (signature enrichie en cas de mutations *ERCC2* et dans de nombreux types de cancer dus au tabagisme) et/ou des mutations somatiques de *BRCA2* [103]. D'autres études ont montré que les gènes impliqués dans la réparation de l'ADN sont des biomarqueurs de réponse à la chimiothérapie [104] (exemple mutations de *ERCC2* [105] et faible expression de ERCC1 [106] pour la sensibilité au cisplatine).

5.2 Inhibiteurs de points de contrôle immunitaires (IPI)

De très nombreux travaux ont étudié les mécanismes de sensibilité ou de résistance aux anti-PD-1/L1 (**Figure 17**). Ces biomarqueurs peuvent être au niveau de la zone tumorale (cellules tumorales ou du microenvironnement tumoral), dans les fluides (principalement le sang), les selles et les marqueurs liés à l'hôte [107]. J'avais proposé avant ma thèse une revue sur l'utilisation de l'ADN tumoral circulant comme biomarqueur pouvant être utilisé dans le cadre des IPI [108].

5.2.1 Biomarqueurs de réponse aux IPI : généralités

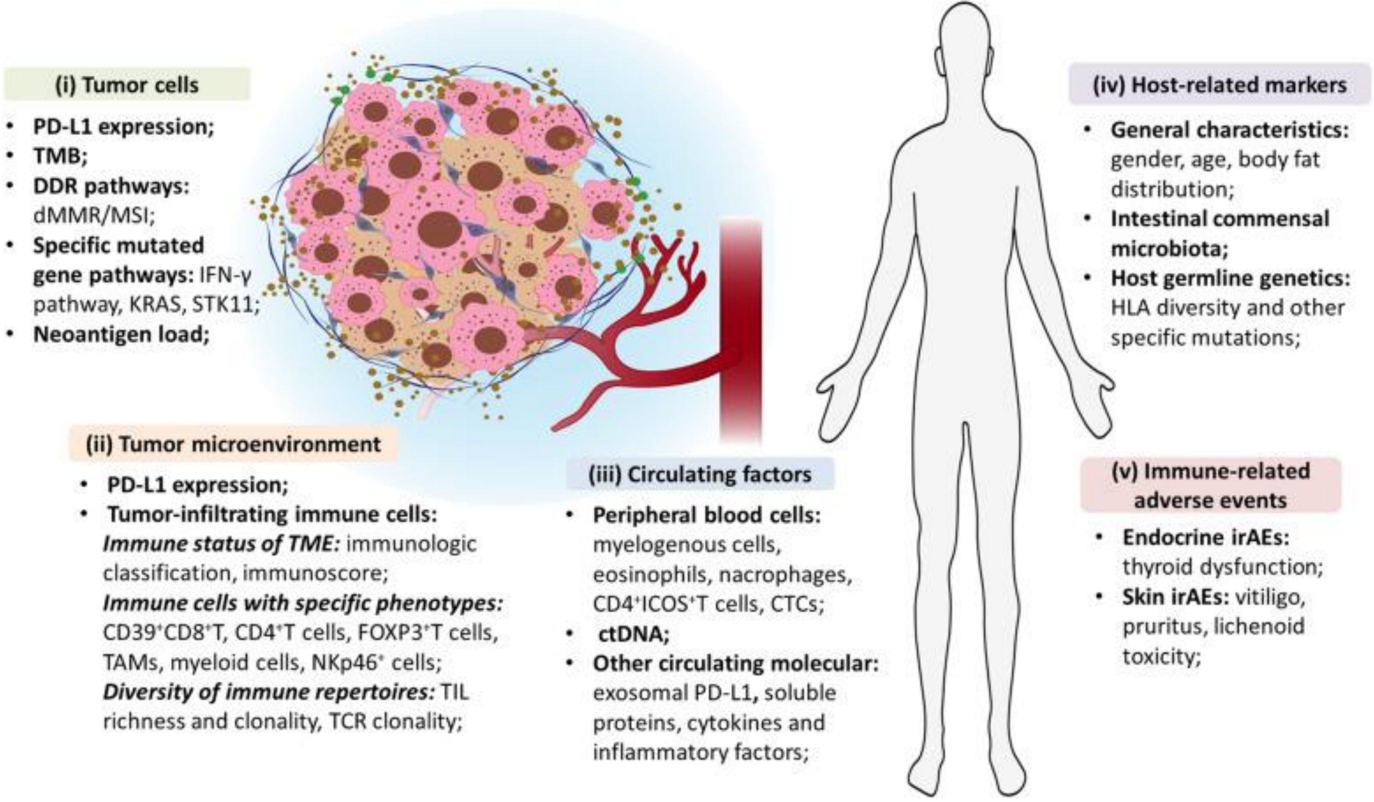

Figure 17 : Résumé des biomarqueurs de réponses à l'immunothérapie [107]. Il existe de nombreux biomarqueurs de réponse aux IPI pouvant être liés aux cellules tumorales, aux cellules du microenvironnement, à des facteurs circulants ou à des marqueurs liés à l'hôte et à sa réponse immunitaire.

5.2.1.1 Biomarqueurs tumoraux : charge mutationnelle et néoantigènes

Il a été montré par plusieurs études qu'une charge mutationnelle élevée était un biomarqueur de réponse aux IPI, ceci retrouvé dans une large méta-analyse pan cancer [109], avec un cut-off du nombres de mutations par Mb variable selon les études pour considérer une tumeur comme ayant une charge mutationnelle élevée (>10-20 mutations/Mb). Une charge mutationnelle élevée est associée à un taux de néo-antigène élevé, ce taux de néo-antigène étant également un biomarqueurs prédictif de réponse aux IPI car certains d'entre eux peuvent être reconnus par les lymphocytes [110].

Certaines caractéristiques moléculaires tumorales ont également été retrouvées comme des biomarqueurs de réponse aux IPI : le phénotype microsatellite-instable ou les mutations de POLE/POLD1 [111,112], les mutations inactivatrices de *PBRM1* (cancer du rein), alors que certaines altérations génomiques sont associées à une moins bonne réponse aux IPI, comme les mutations *EGFR* ou les translocations impliquant *ALK* dans les cancers du poumon non à petites cellules [113,114].

5.2.1.2 Biomarqueurs du microenvironnement

5.2.1.2.1 PD-L1

L'expression de PD-L1, pouvant être présent au niveau de la cellule tumorale ou de certaines cellules du microenvironnement (macrophages, cellules dendritiques) est le principal biomarqueur utilisé en clinique pour conditionner la prescription d'IPI, selon le contexte et le type de cancer. Dans les cancers du poumon non à petites cellules, seule l'expression de PD-L1 tumorale est considérée comme pronostique, alors que l'expression de PD-L1 dans les cancers du sein est principalement observée au niveau du stroma [115,116].

5.2.1.2.2 Infiltration globale immune du microenvironnement

Il a été montré que l'on pouvait schématiser le microenvironnement en 3 grandes classes : « immune-inflamed », « immune-excluded » and « immune-desert ». Les tumeurs « immune-inflamed » comprennent une infiltration importante en lymphocyte T CD4 et CD8, ainsi que l'expression des molécules de points de contrôle immunitaires. Ces tumeurs sont associées à une meilleure réponse aux IPI [117]. A l'inverse, les tumeurs « immune-excluded », où il existe une infiltration lymphocytaire mais qui est à distance de la tumeur, et « immune-desert « , où il n'y a pas ou très peu d'infiltrat lymphocytaire, sont associées à une résistance globale aux IPI.

De nombreuses signatures transcriptomiques ont été validées pour prédire l'efficacité des ICI, celles-ci étant généralement basées sur un certain nombre de gènes immuns, en particulier liés à une activation de lymphocytes T CD8 cytotoxiques activés (ex signature TGE8 : IFNG, CXCL9, CD8A, GZMA, GZMB, CXCL10, PRF1 and TBX21). Ces signatures sont associées au statut infiltré/désert ou exclu des tumeurs [118]

5.2.1.2.3 Cellules immunitaires avec des phénotypes spécifiques

L'étude globale du microenvironnement est un biomarqueur de réponse ou de résistance aux IPI, mais la variété importante des types cellulaires et de des phénotypes observés nécessitent une étude plus fine de ces composantes pour apprécier les mécanismes de résistance ou de réponse.

Par exemple, tous les lymphocytes T CD8+ ne reconnaissent pas les néo-antigènes tumoraux, et il a été montré que la clonalité observée des lymphocytes T CD8 était un biomarqueur de réponse aux IPI [119].

Il a également été montré que en dehors des lymphocytes, les autres types cellulaires pouvaient également influencer la réponse, par exemple les cellules myéloïdes de type macrophages, les cellules myéloïdes suppressives, ou les neutrophiles pouvaient être associées à une résistance aux IPI [120].

Il devient nécessaire de prendre en compte de multiples paramètres pour mieux comprendre la composition du microenvironnement, l'interaction entre ses composantes et la prédiction de la réponse immunitaire. Un article récent dans la revue

Cell a proposé un atlas de 69 états cellulaires, s'intégrant dans 10 écosystèmes, basés sur des données transcriptomiques bulk ou par cellule unique (**Figure 18**) [121].

Chacun de ces écosystème, appelé écotype, présente des caractéristiques propres en terme de biologie, pronostique et réponse aux traitements. Ils ont pu montrer que l'écotype 9, (infiltré en lymphocyte T CD8, signature IFNy) était un biomarqueur de réponse aux IPI, avec une meilleure prédiction de la réponse que d'autres marqueurs comme la charge mutationnelle, des signatures transcriptomiques couramment utilisées ou la prise en compte individuel de chaque population.

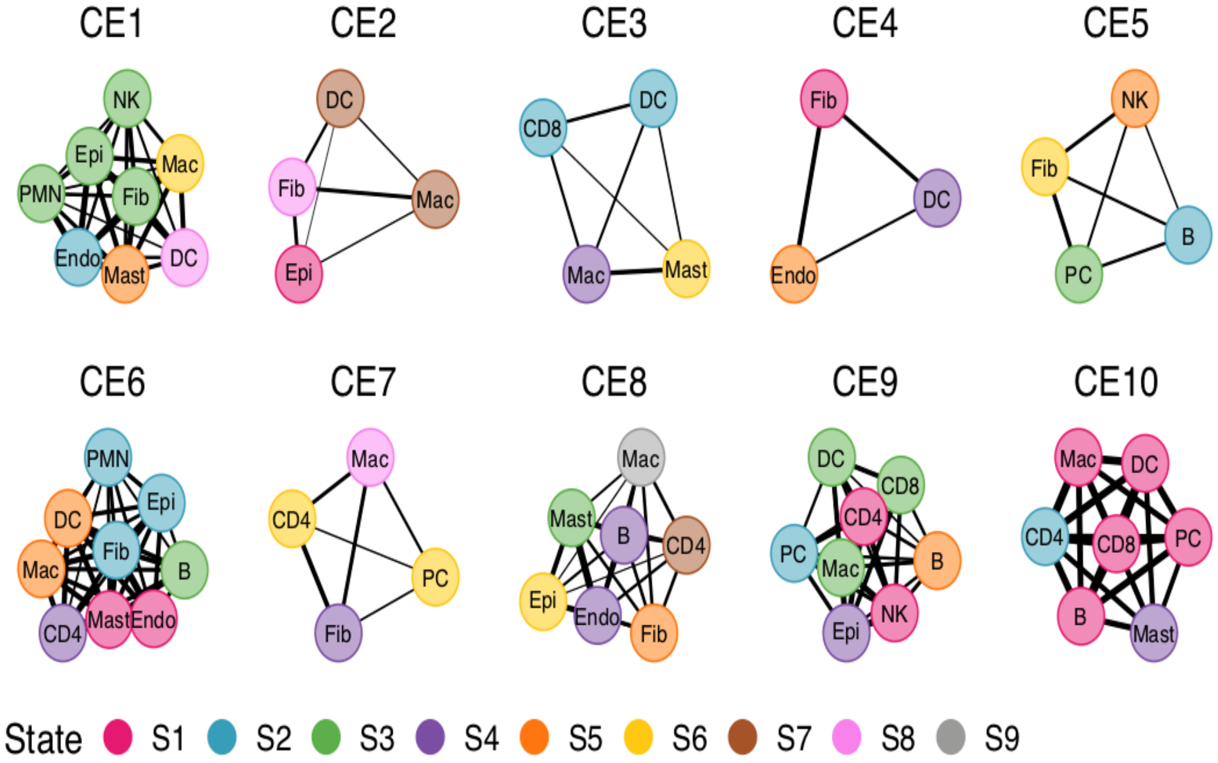

Figure 18 : 10 écotypes de cancer (CE) basés sur une analyse de données transcriptomiques pancancer [121]. L'analyse de 16 types de cancer a permis d'identifier dans cette étude 10 écotypes, chacun de ces écotypes correspondant à un réseau de différents types cellulaires (ex écotype 4 : fibroblastes, cellules dendritiques et cellules endothéliales), chacun de ces types cellulaires correspondant également à un état cellulaire (ex écotype 4 : composé de fibroblastes dans un état cellulaire S1, cellules dendritiques S4 et endothéliale S5).

5.2.2 Biomarqueurs de réponse aux IPI : cancers urothéliaux

Dans le cancer de vessie, des études translationnelles basées sur les données publiques issues d'essais cliniques d'anticorps anti-PD-1/PD-L1 ont proposé plusieurs biomarqueurs pronostics et/ou prédictifs de réponse aux immunothérapies [118,122–125].

L’étude de la cohorte IMVIGOR (patients ayant un TVIM métastatique traités par atézolizumab) avec analyse génomique et transcriptomique a retrouvé que la charge mutationnelle tumorale et certaines signatures transcriptomiques immunitaires (en particulier liée à une infiltration de lymphocyte T CD8 cytotoxiques) étaient des biomarqueurs de réponse à l’atézolizumab, alors que l’expression de TGF-B était un biomarqueur de résistance [118].

Une autre étude très récente, publiée durant la conduite de la thèse, a retrouvé les mutations *ARID1A* et la présence de structures lymphoïdes tertiaires (STL) comme biomarqueur de réponses [122].

L’étude des biomarqueurs de réponse à l’avelumab en maintenance (à partir des données d’immunohistochimie, de séquençage exome-entier et de RNA-seq) a retrouvé plusieurs biomarqueurs associés à la réponse à l’immunothérapie : expression de PD-L1 par les cellules tumorales, charge mutationnelle tumorale, signatures mutationnelles liées à APOBEC, expression de gènes liés à l'activité immunitaire innée et adaptative et au nombre d'allèles codant pour des variants à haute affinité des récepteurs Fcγ activateurs [126].

6 Modèles d'études des cancers

6.1 Lignées cellulaires, PDX

Il est nécessaire pour tester de nouvelles drogues et leurs mécanismes de résistance de disposer de modèles tumoraux précliniques. Plusieurs modèles de complexités différentes existent, du modèle le plus simple (lignée cellulaire en 2D) à des modèles plus complexes non-animal (3D, « Tumor on Chip »), à des modèles animaux (ex patient-derived xenograft – PDX)[127].

Il a été montré que les modèles les plus complexes reflètent mieux l'efficacité d'un traitement retrouvé en clinique que des modèles plus simples comme les lignées cellulaires 2D. Néanmoins, ces dernières de par leur facilité d'utilisation, leur coût plus faible, et leur large caractérisation moléculaire permettent souvent une première sélection de drogues avant de passer à des modèles plus complexes.

Bien que quelques études aient rapporté le développement de modèles PDX de TVIM, aucune n'a effectué une large caractérisation génomique, transcriptomique et pharmacologique intégrée d'une banque de PDX reflétant la diversité biologique des TVIM [128–130]. Récemment, une banque de 17 PDX d'UTUC a été rapportée [131] mais aucun modèle n'existe pour les tumeurs épidermoïdes, pour lesquelles le traitement standard est mal codifié.

L'inconvénient des PDX est leur coût, l'utilisation d'animaux, ainsi que l'absence de stroma tumoral humain. Le taux de prise est également un facteur limitant, toutes les tumeurs prélevées sur les patients ne se développant pas après xénogreffes.

Il y a également toujours le risque lors de la xénogreffe de sélectionner un clone non représentatif de l'hétérogénéité tumorale initiale (clone surreprésenté dans le prélèvement ou prolifération d'un clone plus adapté aux conditions de culture).

6.2 Données publiques de screening de viabilité cellulaire à large échelle

La découverte d'une nouvelle cible thérapeutique passait auparavant par une inhibition de quelques gènes ou protéines dans un nombre limité d'échantillons, souvent des lignées cellulaires humaines dans un premier temps, avant de tester les drogues sur des modèles biologiques plus représentatifs de la complexité tumorale, telles les PDX, ou des tumeurs induites sur des modèles animaux comme décrit ci-dessus.

Les développements technologiques biologiques ont permis de réaliser des criblages cellulaire à large échelle sur des lignées cellulaires de cancer humaines [132,133].

Des efforts de différents consortiums ont permis l'étude de l'effet sur la prolifération cellulaire d'une inhibition de gènes, par siRNA (Demeter2[134] ou CRISPR-Cas9 (Achilles) [135,136], ou de l'effet de drogues (PRISM [137], CTRP [138]) (**Figure 19**).

En parallèle, ces lignées cellulaires ont pu également être caractérisées sur le plan moléculaire, avec disponibilité de leurs données génomiques, transcriptomiques, de méthylation et protéiques. L'association de ces données permet la découverte de gènes essentiels pour une cellule cancéreuse (au moins *in vitro*), la découverte de nouvelles létalités synthétiques, avec éventuellement des biomarqueurs associés.

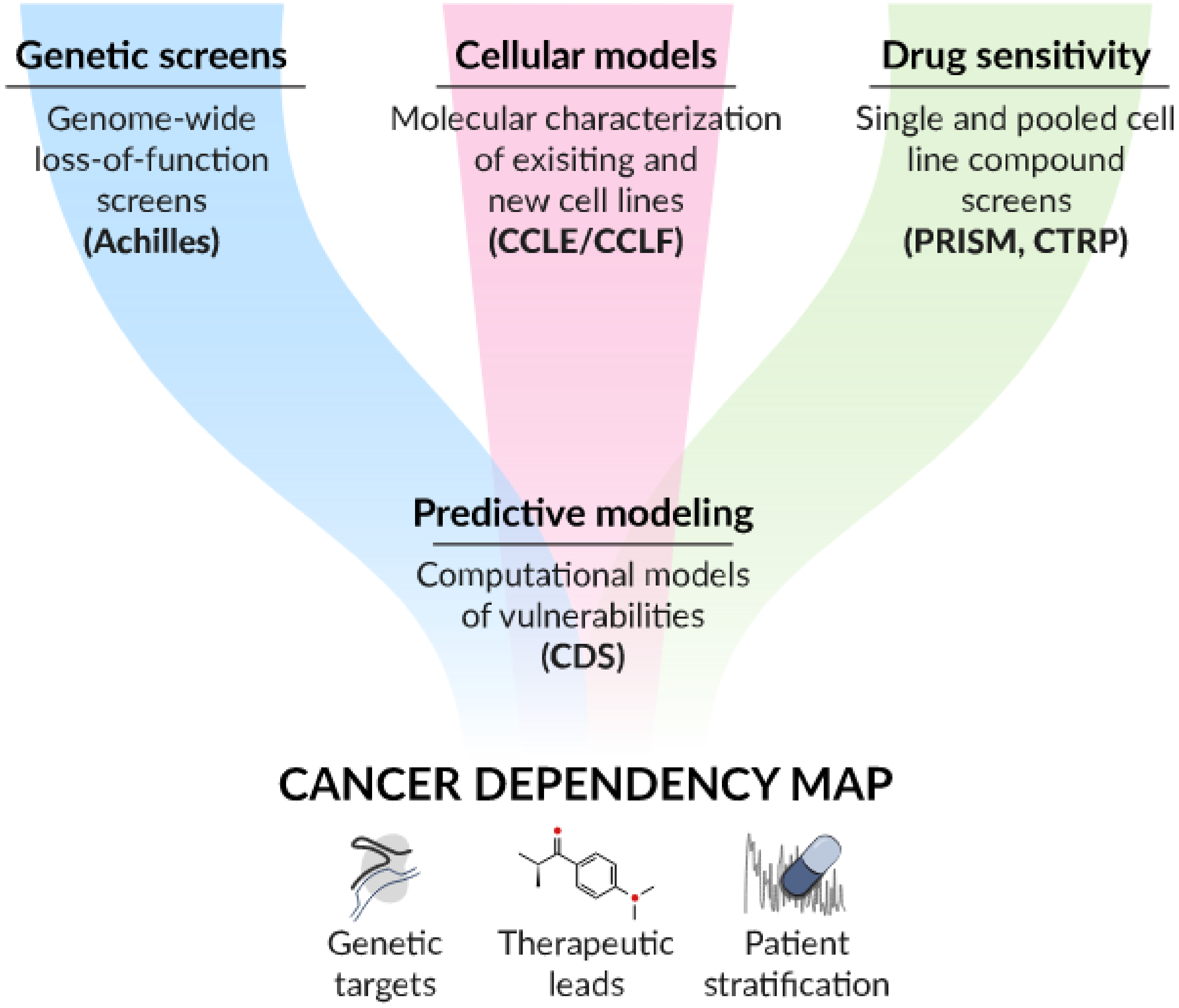

Figure 19 : Carte de dépendance des cancers du Broad Institute (tirée de leur site internet). La carte de dépendance « Cancer Dependency Map » est constituée de plusieurs bases de données soit de criblage génomique (siRNA ou CRISPR-Cas9), de criblage de drogues (PRISM, CTRP), ou de caractérisation moléculaire des lignées cellulaires (au niveau transcriptomique, protéomique, épigénétique, génomique).

Ces bases sont principalement étudiées sur un angle pan-cancer, du fait du nombre plus importants de lignées permettant des conclusions statistiques plus robustes. Néanmoins, il existe des cibles spécifiques de certains tissus d'origine, du fait de la biologie propre de chaque tissu (ex ESR1 dans les cancers exprimant le récepteur aux œstrogènes, sensibilité à l'inhibition de BRAF plus importante dans les mélanomes que dans les autres cancers mutés pour BRAF).

Achilles, basée sur une inhibition de gènes par CRISPR-CAS9, est actuellement la base la plus large, avec pour la 22Q2 plus de 1086 lignées analysées et plus de 17386 gènes inhibés individuellement dans chacune de ces lignées. Il n'existe pas pour le moment de recherche spécifique sur les données DepMap dans les lignées cellulaires cancéreuses de tumeur urothéliale, qui sont au nombre de 31 dans cette base. [135,136]

L'exploration de ces bases de données, en particulier de DepMap qui est la plus large actuellement, peut permettre de découvrir des gènes essentiels dans le cancer de vessie, pouvant être de futures cibles thérapeutiques.

7 TNFR/cIAP1/BIRC2, cIAP/XIAP inhibiteurs

Un rappel de la voie biologique du TNF-récepteur et des SMAC-mimétiques dans les cancers est présenté ici (**Figure 20**, décrite ci-dessous), pour aider à la compréhension des résultats.

7.1 Voie du récepteur TNF et rôle de BIRC2-cIAP1

La liaison du TNF au TNFR1 induit le recrutement de TRADD, RIPK1, TRAF2, et de cIAP1 et 2 pour former le complexe I au niveau de la membrane plasmique [139].

BIRC2 (=cIAP1) se lie à TRAF2, au sein du complexe I, les cIAP1 et 2 s'auto-ubiquitinyle et permettent l'ubiquitinylation d'autres composants du complexe I tels que RIPK1.

L'ubiquitinylation médiée par les cIAP des composants du complexe I conduit au recrutement du complexe d'assemblage de chaîne d'ubiquitine linéaire (LUBAC, comprenant HOIL-1L, HOIP -RNF31-, and Sharpin), qui à son tour va ubiquitinyler plusieurs composants du complexe I, y compris TNFR1, TRADD, RIPK1 ou NEMO. Les chaînes d'ubiquitine servent de sites d'accueil pour TAB2/3/TAK1 et la sous-unité IKK NEMO.

TAK1 (MAP3K7) phosphoryle IKK2 et les MAPK kinases, conduisant à la transcription de gènes NFκB-dépendants et MAPK-dépendants qui conduisent à un rôle généralement protumoral ainsi qu'à une inflammation.

D'un autre côté, l'ubiquitinylation de RIPK1 et sa dégradation l'empêche de former un complexe avec FADD et la caspase 8, appelé le complexe II qui est pro apoptotique, ainsi qu'avec RIPK3-MLKL pour former le complexe nécrosome (ripoptosome), entrainant une nécroptose.

L'activation du TNF récepteur entraine donc l'activation de NFkB, des MAPK, et une inhibition de l'apoptose et de la nécroptose.

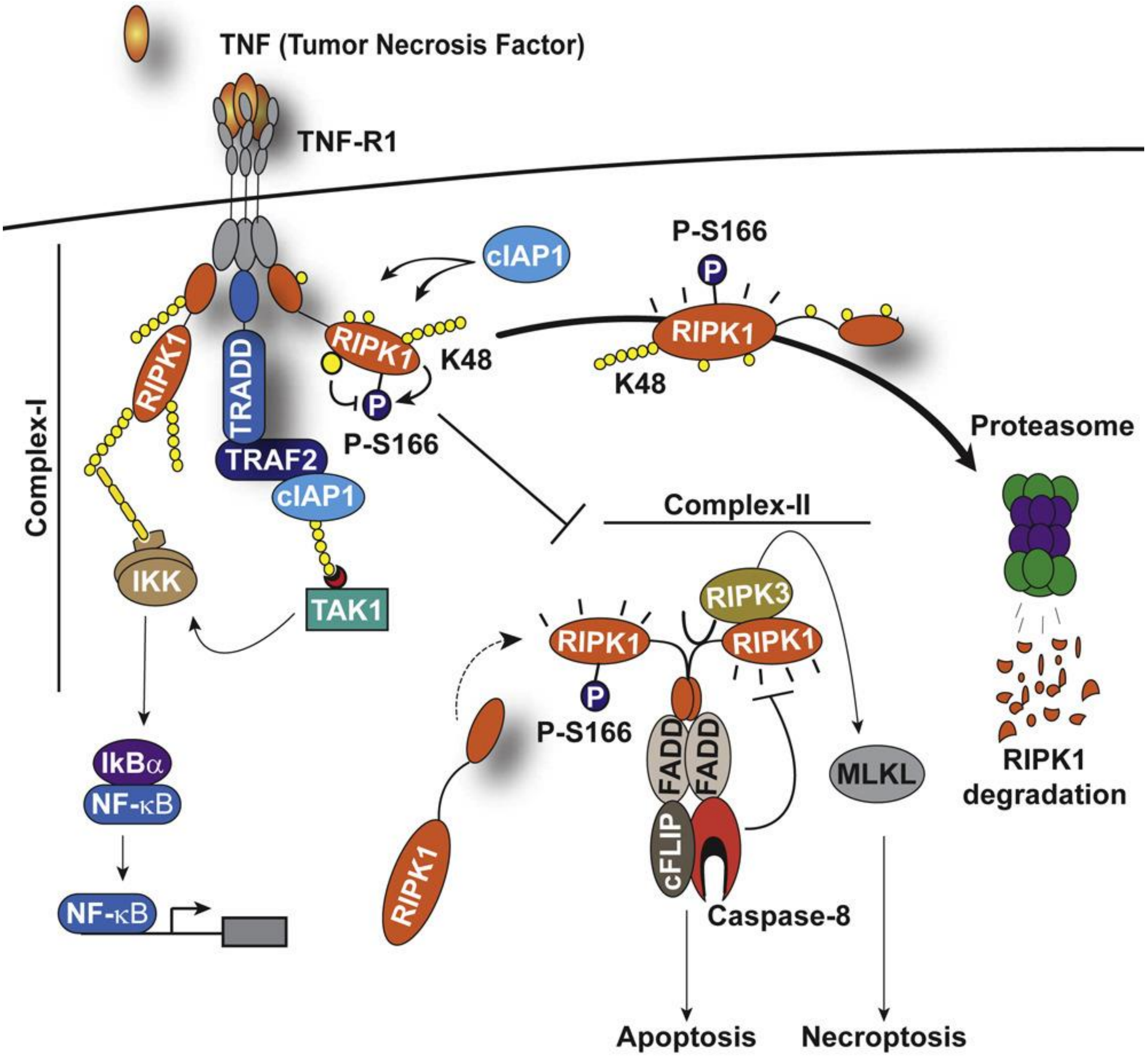

Figure 20 : Voie de signalisation du récepteur TNFR1, avec activation des voies NFkB, MAPK et inhibition de l'apoptose et de la nécroptose. 139

7.2 SMAC-mimétique

Les protéines IAP peuvent être neutralisées par leurs antagonistes endogènes, tels que SMAC/DIABLO, Omi/HtrA2 [86], ARTS (apoptosis-related protein in the TGFβ signaling pathway), et XAF1 (XIAP associated factor 1) 140.

SMAC est libéré des mitochondries dans le cytosol lors d'une stimulation apoptotique par clivage, et SMAC clivé se dimérise et peut se lier à XIAP et à cIAP1/cIAP2 pour les inhiber.

Plusieurs drogues SMAC-mimétiques ont été développées depuis plusieurs années (birinapant, LCL161, GDC0152) [141]. Dans les modèles pré cliniques, l'activité des SMAC mimétiques a été observée entre autres dans les cancers du sein [142–144], ovaire [145,145,146], estomac [147], et colorectal [148].

Cependant, dans les lignées cellulaires urinaires, une étude n'a trouvé que 1/6 des lignées cellulaires sensibles au birinapant (lignée J82 sensible, lignées résistantes T24/TCCSUP/HT1376/UC3/RT4)[142] , alors qu'une autre a décrit les RT112 comme modérément sensibles [149].

Il a été démontré que cette activité préclinique passe par une augmentation de l'apoptose.[144,150], une augmentation de l'expression du TNF-a et au rôle de NFkB.

En clinique, du fait de leur capacité à entrainer l'apoptose, et leur activité modeste en monothérapie, les SMAC-mimétiques ont particulièrement été développées en combinaison avec un agent permettant d'entrainer l'apoptose, en particulier en combinaison avec la chimiothérapie dans des phases I/II. Néanmoins, dans une population non sélectionnée, l'activité reportée est modeste [141,151], avec une étude clinique ayant retrouvée l'expression de RIPK1 en particulier comme potentiel biomarqueur d'efficacité.

8 Objectifs

La prise en charge actuelle des cancers de vessie métastatiques repose principalement sur la chimiothérapie, les IPI, et les inhibiteurs de FGFR (en cas d'altérations génomiques *FGFR2/3*), pour lesquels peu de biomarqueurs prédictifs de réponse existent et sont utilisés en pratique clinique.

La chimiothérapie, bien qu'efficace chez environ la moitié des patients au stade avancé n'est efficace que transitoirement, comme les thérapies anti-FGFR dans les TVIM métastatique avec altération de *FGFR2/3* (~10% des patients). Les traitements par IPI sont utilisés en maintenance sur le seul critère de réponse, et après la 1ère ligne chez tous les patients ou basés sur l'expression de PD-L1, qui est un biomarqueur imparfait, avec un faible taux de réponse tumorale.

Les objectifs de cette thèse étaient de :

1) Rechercher des biomarqueurs de sensibilité ou de résistance aux traitements dans le cancer de vessie aux thérapies ciblées ou IPI.
2) Rechercher de nouvelles pistes thérapeutiques, en utilisant principalement les données publiques de screening de lignées cellulaires de cancer de vessie à grande échelle par drogue ou par inhibition de gènes par CRISPR-Cas9.

Concernant la recherche de biomarqueurs de réponse ou de résistance dans les TVIM, les résultats de la caractérisation d'une banque de PDX de cancer de vessie et de l'uretère, certaines traitées par anti-FGFR et ou anti-EGFR, sont présentées **Article 1** (Frontiers in Oncology, co-1er auteur). Nous avons pu montrer que :

- une combinaison thérapeutique par anti-FGFR (erdafitinib) + anti-EGFR (erlotinib) est efficace dans des PDXs (patient-derived xenografts) mutées pour *FGFR3*, cette efficacité étant probablement due à une surexpression d'*ERBB2-3* et d'*EGFR* sous inhibiteur de FGFR.
- les tumeurs sarcomatoïdes présentent une expression/activité plus faible d'EGFR et un switch vers FGFR1, responsable d'une moindre réponse à un inhibiteur d'EGFR par rapport aux autres TVIM Ba/Sq.
- les PDXs étaient hétérogènes au niveau moléculaire et protéique, et les TVIM pouvaient présenter un changement phénotypique de Ba/Sq à luminal lors de la greffe chez la souris.

Concernant les biomarqueurs de sensibilité aux IPI, nous avons pu montrer que :

- Les structures lymphoïdes tertiaires, estimées par l'expression du gène *CXCL13*, sont un biomarqueur prédictif majeur de réponse aux anticorps anti-PD-L1, et sont enrichies dans le type Ba/Sq, via l'analyse de cohortes publiques comme IMVIGOR210 (patients traités par atezolizumab) (**Article 2**).

- Les cellules plasmatiques pourraient être également un biomarqueur de réponse aux IPI dans les TVIM métastatiques, sur des résultats préliminaires des données de séquençage de noyaux uniques de la cohorte MATCH-R avant et pendant le traitement par IPI (**Chapitre 10.2**).

Recherche de nouvelles pistes thérapeutiques, nous avons pu identifier :

- RARγ, partenaire de RXRα, cible identifiée dans la base publique de criblage par CRISPR-Cas9 de lignées cellulaires (DepMap). RARγ est activé dans les TVIM en particulier dans les sous-types Ba/Sq et Luminales-papillaires, et son inhibition semble intéressante en particulier dans le sous type Ba/Sq (**Article 3 – en préparation**).
- Le birinapant (XIAP/cIAP1/2 inhibiteur, Smac-mimétique) qui est efficace dans certaines lignées de cancer de vessie selon les données de DepMap. L'efficacité du birinapant a été confirmée *in vitro* et *in* vivo au laboratoire (en utilisant les lignées UMUC14, SCaBER), avec comme biomarqueur de sensibilité potentiel l'amplification de *BIRC2* ou la surexpression de *RIPK1* (**Article 3**).
- FGFR1 comme nouvelle cible thérapeutique potentielle des TVIM de type sarcomatoïde (3^{e} auteur**, Article 4** en révision dans The Journal of Pathology).
- J'ai recherché des cibles thérapeutiques en aval de PPARγ dans une lignée PPARG-dépendante, mais cela n'a pas permis d'identifier une cible prometteuse (**Chapitre 11.3**).

En annexe sont présentés des travaux collaboratifs dans lesquels j'ai participé, de la caractérisation d'un réseau de régulation des cancers de vessie de type luminal ou basal (**Article 5 en révision**), de FGFR3 comme oncogène dans un modèle murin (**Article 6, European Urology**).

9 Biomarqueurs de réponses aux thérapies ciblées

9.1 Introduction

Les modèles *in vivo* permettent de tester des traitements (actuels ou nouveaux) et d'étudier les mécanismes de sensibilité ou de résistance à ces traitements. J'ai pu, dans l'article ci-dessous dont j'ai écrit le manuscrit, réaliser l'analyse bio-informatique d'une cohorte de 31 PDXs de cancer de vessie ou de l'uretère, et participer à sa caractérisation au niveau histologique, moléculaire et pharmacologique (par chimiothérapie et thérapie ciblée). Ce travail entre donc dans les 2 objectifs principaux de la thèse (biomarqueurs de sensibilité/résistance aux thérapies ciblées et identification de nouvelles cibles thérapeutiques).

Dans l'article ci-dessous, nous avons pu montrer que :

- Les tumeurs sarcomatoïdes bien que basales semblent être résistantes aux anti-EGFR, car elles présentent un faible niveau d'expression et d'activité régulon d'EGFR, ici montré via une PDX sarcomatoïde. Ceci complémente ce qui a été montré dans l'**Article 4** ou nous avons pu montrer un switch phénotype d'EGFR à FGFR1 dans les tumeurs basales devenant sarcomatoïdes.

- Les traitements anti-FGFR sont efficaces *in vivo*, mais parfois avec une faible activité. Il a été observé dans l'essai clinique de phase II de l'erdafitinib que les anti-FGFR ne présentaient que 40% de taux de réponse tumorale, avec une durée moyenne d'efficacité assez modérée (<6 mois) chez les répondeurs, suggérant des mécanismes de résistance primaires, ou secondaires d'installation rapide. Nous avons pu constater rapidement après mise sous anti-FGFR une augmentation de l'expression d'ERBB2-3 et d'EGFR, et qu'une combinaison de traitement par anti-FGFR et anti-EGFR permettait dans les PDX d'augmenter la réponse anti-tumorale dans les 3 PDXs mutées pour *FGFR3*.

- Nous avons pu montrer qu'il existait des tumeurs et PDXs hétérogènes au niveau moléculaire et histologique pour le phénotype luminal et basal, pouvant entrainer un switch phénotype de basal à luminal lors de la greffe de la tumeur à la PDX. Ces tumeurs/PDX hétérogènes au niveau moléculaire pouvaient être mixtes sur le phénotype luminal ou basal soit de manière spatiale en immunohistochimie (présence de zones distinctes luminales ou basales en utilisant les marqueurs KRT5/6 pour le phénotype basal et GATA3 pour le phénotype luminal), soit coexprimant dans les mêmes cellules les marqueurs caractéristiques des 2 sous types.

9.2 Article 1 : Integrated molecular and pharmacological characterization of patient-derived xenografts from bladder and ureteral cancers identifies new potential therapies

frontiers | Frontiers in Oncology

TYPE Original Research
PUBLISHED 11 August 2022
DOI 10.3389/fonc.2022.930731

Integrated molecular and pharmacological characterization of patient-derived xenografts from bladder and ureteral cancers identifies new potential therapies

Hervé Lang[1†], Claire Béraud[2†], Luc Cabel[3,4†], Jacqueline Fontugne[3,5,6], Myriam Lassalle[2], Clémentine Krucker[3,4,5], Florent Dufour[3,4,7], Clarice S. Groeneveld[3,4,8], Victoria Dixon[3,4,5], Xiangyu Meng[3,4,9], Aurélie Kamoun[8], Elodie Chapeaublanc[3,4], Aurélien De Reynies[8], Xavier Gamé[10], Pascal Rischmann[10], Ivan Bieche[11], Julien Masliah-Planchon[11], Romane Beaurepere[11], Yves Allory[3,5,6], Véronique Lindner[12], Yolande Misseri[2], François Radvanyi[3,4], Philippe Lluel[2*], Isabelle Bernard-Pierrot[3,4*‡] and Thierry Massfelder[13‡]

[1]Department of Urology, New Civil Hospital and Fédération de Médecine Translationnelle de Strasbourg (FMTS), Strasbourg, France, [2]Urosphere, Toulouse, France, [3]Institut Curie, Centre National de la Recherche Scientifique (CNRS), UMR144, Molecular Oncology team, PSL Research University, Paris, France, [4]Sorbonne Universités, Université Pierre-et-Marie-Curie (UPMC), Univ Paris, Paris, France, [5]Department of Pathology, Institut Curie, Saint-Cloud, France, [6]Université de Versailles-Saint-Quentin-en-Yvelines (UVSQ), Paris-Saclay University, Versailles, France, [7]Inovarion, Paris, France, [8]La Ligue Contre Le Cancer, Paris, France, [9]Department of Urology, Zhongnan Hospital of Wuhan University, Wuhan, China, [10]Department of Urology, Rangueil Hospital, Toulouse, France, [11]Department of Genetics, Institut Curie, Paris, France, [12]Department of Pathology, New civil Hospital, Strasbourg, France, [13]INSERM (French National Institute of Health and Medical Research) UMR_S1260, Université de Strasbourg, Regenerative Nanomedicine, Centre de Recherche en Biomédecine de Strasbourg, Strasbourg, France

EDITED BY
Alfredo Berruti,
University of Brescia, Italy

REVIEWED BY
Ning Li,
Fourth Affiliated Hospital of China Medical University, China
Takeshi Yuasa,
Japanese Foundation for Cancer Research, Japan

*CORRESPONDENCE
Isabelle Bernard-Pierrot
ibernard@curie.fr
Philippe Lluel
philippe.lluel@urosphere.com

†These authors have contributed equally to the work

‡These authors co-supervised the study

SPECIALTY SECTION
This article was submitted to Genitourinary Oncology, a section of the journal Frontiers in Oncology

RECEIVED 28 April 2022
ACCEPTED 08 July 2022
PUBLISHED 11 August 2022

CITATION
Lang H, Béraud C, Cabel L, Fontugne J, Lassalle M, Krucker C, Dufour F, Groeneveld CS, Dixon V, Meng X, Kamoun A, Chapeaublanc E, De Reynies A, Gamé X, Rischmann P, Bieche I, Masliah-Planchon J, Beaurepere R, Allory Y, Lindner V, Misseri Y, Radvanyi F, Lluel P, Bernard-Pierrot I and Massfelder T (2022) Integrated molecular and pharmacological characterization of patient-derived xenografts from bladder and ureteral cancers identifies new potential therapies. *Front. Oncol.* 12:930731.
doi: 10.3389/fonc.2022.930731

Background: Muscle-invasive bladder cancer (MIBC) and upper urinary tract urothelial carcinoma (UTUC) are molecularly heterogeneous. Despite chemotherapies, immunotherapies, or anti-fibroblast growth factor receptor (FGFR) treatments, these tumors are still of a poor outcome. Our objective was to develop a bank of patient-derived xenografts (PDXs) recapitulating the molecular heterogeneity of MIBC and UTUC, to facilitate the preclinical identification of therapies.

Methods: Fresh tumors were obtained from patients and subcutaneously engrafted into immune-compromised mice. Patient tumors and matched PDXs were compared regarding histopathology, transcriptomic (microarrays), and genomic profiles [targeted Next-Generation Sequencing (NGS)]. Several

PDXs were treated with chemotherapy (cisplatin/gemcitabine) or targeted therapies [FGFR and epidermal growth factor (EGFR) inhibitors].

Results: A total of 31 PDXs were established from 1 non-MIBC, 25 MIBC, and 5 upper urinary tract tumors, including 28 urothelial (UC) and 3 squamous cell carcinomas (SCCs). Integrated genomic and transcriptomic profiling identified the PDXs of three different consensus molecular subtypes [basal/squamous (Ba/Sq), luminal papillary, and luminal unstable] and included *FGFR3*-mutated PDXs. High histological and genomic concordance was found between matched patient tumor/PDX. Discordance in molecular subtypes, such as a Ba/Sq patient tumor giving rise to a luminal papillary PDX, was observed (n=5) at molecular and histological levels. Ten models were treated with cisplatin-based chemotherapy, and we did not observe any association between subtypes and the response. Of the three Ba/Sq models treated with anti-EGFR therapy, two models were sensitive, and one model, of the sarcomatoid variant, was resistant. The treatment of three FGFR3-mutant PDXs with combined FGFR/EGFR inhibitors was more efficient than anti-FGFR3 treatment alone.

Conclusions: We developed preclinical PDX models that recapitulate the molecular heterogeneity of MIBCs and UTUC, including actionable mutations, which will represent an essential tool in therapy development. The pharmacological characterization of the PDXs suggested that the upper urinary tract and MIBCs, not only UC but also SCC, with similar molecular characteristics could benefit from the same treatments including anti-FGFR for FGFR3-mutated tumors and anti-EGFR for basal ones and showed a benefit for combined FGFR/EGFR inhibition in FGFR3-mutant PDXs, compared to FGFR inhibition alone.

KEYWORDS

urothelial carcinoma, squamous cell carcinoma, upper-urinary tract carcinoma, luminal tumors, basal tumors, tyrosine kinase receptor, molecular subtypes, tumor heterogeneity

Introduction

Bladder cancer (BCa) is the ninth most common cancer type worldwide with an estimated 549,000 new cases in 2018 (1). Histologically, 90%–95% of BCa are urothelial cell carcinomas (UCs) and 5% are squamous cell carcinomas (SCCs) (2). Although less frequent, UC may also develop in the upper urinary tract (2%–5% of UCs). Muscle-invasive BCas (MIBCs) are of very poor outcome, with an overall 5-year survival of 50%–60% and less than 10% for patients with localized disease or distant metastasis, respectively. Localized UC/SCC-MIBC and high-risk upper tract urothelial carcinoma (UTUC) are treated by radical cystectomy and radical nephroureterectomy, respectively, with the addition of adjuvant or neoadjuvant chemotherapies (2, 3). In advanced-setting UC, immune checkpoint or fibroblast growth factor receptor (FGFR) inhibitors (for tumors presenting *FGFR2/3* genetic alterations) may also be proposed (2, 4), while there is no standard-of-care treatment for SCC. Recently, two antibody–drug conjugates (ADCs) have shown efficacy in urothelial cancers, sacituzumab govitecan (5) (anti-TROP2) and enfortumab vedotin (6) (anti-Nectin4). Notably, the expression of NECTIN4 and TROP2 is variable across BCas, with NECTIN4 expression higher in luminal tumors (7, 8), which could impact the efficacy of these drugs. We also find in PDX transcriptomic analysis a heterogeneity of NECTIN4 and TROP2 expression, with a

---

Abbreviations: PDXs, patient-derived xenografts; NMIBC, non-muscle-invasive bladder cancer; MIBC, muscle-invasive bladder cancer; FGFR, fibroblast growth factor receptor; EGFR, epidermal growth factor; SCC, squamous cell carcinoma; UC, urothelial cell carcinoma; UTUC, upper urinary tract urothelial carcinoma.

higher expression of NECTIN4 in luminal tumors. However, despite these treatments, the outcome remains poor, and the identification of new therapies is still needed. The development of relevant preclinical models is critical to reach this objective.

MIBCs constitute a heterogeneous group of tumors at the morphological and molecular levels. With the aim to improve the prediction of the clinical outcome and treatment response, an international consortium has recently reached a consensus molecular classification based on transcriptomic data, for MIBC, including six subtypes, facilitating interstudy comparisons (9). These subtypes can be divided into broad luminal (differentiated) and basal/squamous (Ba/Sq) groups. Although current systemic treatments are not based on molecular classification, some subtype features are associated with treatment response. For example, Ba/Sq tumors have worse prognosis than luminal-papillary (LumP) tumors [5], which commonly show the genetic alterations of FGFR3 (10). These subtypes have also been suggested to have a different sensitivity to chemotherapies, although results are currently inconsistent between studies (11–14). The Ba/Sq subtype and bladder SCC are associated with EGFR activation and sensitivity to anti-EGFR treatments in preclinical models (9, 15–18). UTUCs are molecularly comparable to MIBCs but have some distinct features, such as a higher prevalence of microsatellite instability (MSI) (19).

The molecular heterogeneity of MIBCs and UTUC and their divergent therapy sensitivities entails the need for a representative panel of preclinical models for unbiased therapeutic evaluation. Therapeutic testing in PDXs is highly effective in predicting the efficacy of both chemotherapies and targeted therapies (20, 21). Although few studies have reported the development of PDX models from MIBC, none have performed integrated genomic, transcriptomic, and pharmacological characterization of a bank of PDX reflecting the biological diversity of MIBC (22–24). Recently, a bank of 17 PDXs from UTUC has been reported (25) but no model exists for SCC, for which no standard of care is established.

In the present report, we describe the development and characterization of a bank of 31 PDXs, which maintain the characteristics of patient tumors and reflect the diversity of the molecular subtypes of bladder and upper urinary tract cancers. The evaluation of pharmacological responses to standard of care and targeted therapies suggests that non-sarcomatoid Ba/Sq tumors, notably SCC, could benefit from anti-EGFR therapies. In *FGFR3*-mutated tumor PDXs, an anti-FGFR and anti-EGFR combination therapy improves tumor response compared to FGFR inhibition alone.

Materials and methods

Animals

Four- to five-week-old immunodeficient mice (male) were purchased from Charles River Laboratories (L'Arbresle, France). Mice were maintained under specific pathogen-free conditions. Their care and housing were conducted in accordance with the European Community Council Directive 2010/63/UE and the French Ministry for Agriculture, Agrifood and Forestry Decree 2013-118. Experimental protocols were reviewed by CEEA-122 Ethical Committee for Protection of Animals used for Scientific Purposes and approved by French Ministry for National Education, Higher Education and Research under the number *APAFIS#14811-2018042316405732 v4*. The animal facility was maintained under artificial lighting (12 h) between 7:00 a.m. and 7:00 p.m. at a controlled ambient temperature of 22 ± 2°C and the relative humidity rate maintained at 55 ± 10%.

Specimen acquisition

From January 2009 to October 2019, patient tumors and matched normal tissues were obtained from 153 patients treated for bladder or ureteral cancers undergoing surgery either at the Hospital of Strasbourg (France) (n=135) or the Hospital of Toulouse (France) (n=18) in accordance with all relevant guidelines and regulations. All patients provided written informed consent. The incoming material of every donor patient was anonymized by receiving a chronological unique number, subsequently used to identify the corresponding PDX model. The specimens were examined, sectioned, and selected by pathologists for histological analyses and xenografts. Clinical and demographic information were obtained prospectively.

Patient-derived xenograft establishment

The PDX models of MIBC were generated by engrafting tumor tissues directly obtained from patients. Viable tumor tissue was macrodissected, and tumor pieces were then prepared for implantation. The NMRI nude (Rj : NMRI-Foxn1$^{nu/nu}$) immunodeficient mice strain was used for tissue implantation. Grafts were implanted into the interscapular fat pad. When s.c. xenograft tumors reached ~1,000–1,500 mm^3, they were serially transplanted for expansion into new mice. In addition, harvested xenograft material was cryopreserved for future implantations and/or fixed in 4% formalin for 24 h before paraffin embedding and/or stored at -80°C for subsequent analyses. A model was defined as established when stable growth over at least three passages and regrowth after a freeze–thaw cycle could be observed. The take rate (the proportion of mice developing tumors after the transplantation of the PDX) and passage time were recorded for every model and every individual passage. Tumor growth was determined weekly by a two-dimensional measurement with a caliper. The tumor volume was calculated as: TV (mm^3) = [length (mm) × width (mm)^2]*π/6, where the length and width are the longest and shortest diameters of the tumor, respectively.

Animals were sacrificed when the tumor volume reached 2,000 mm^3.

Histopathology and immunohistochemistry

For all PDX models, primary and passaged tumors preserved in formalin for 24 h were paraffin-embedded, sectioned into 4-µm-thick cuts, and placed on glass slides. The analysis of hematoxylin and eosin (H&E)-stained slides was performed by two experienced uropathologists.

RNA/DNA/protein extraction

Each frozen PDX fragment was ground to powder and subdivided for triple RNA, DNA, and protein extraction. RNA isolation was performed using TRIzol, while phenol/chloroform/isoamyl alcohol extraction was used for DNA isolation. See "Western blot" section for the protein extraction method.

Real-time reverse transcription–quantitative PCR

Reverse transcription was performed on 1 µg of total RNA using a high-capacity cDNA reverse transcription kit (Thermo Fisher Scientific, Illkirch, France). cDNAs were amplified by PCR in a Roche real-time thermal cycler, with the Roche Taqman master mix (Roche) and Taqman probe/primer pairs as follows:

Gene	Primer Forward	Primer Reverse
EGFR	GATCCAAGCTGTCCCAATG	GCACAGATGATTTTGGTCAGTT
ERBB2	CAACTGCACCCACTCCTGT	GCAGAGATGATGGACGTCAG
ERBB3	GGGAACCTTGAGATTGTGCT	CCTGTCACTTCTCGAATCCAC

Sanger sequencing

The coding exons and splice junctions of *PPARG* were amplified from genomic DNA by PCR with gene-specific primers available on request and sequenced by the Sanger method as described (26).

Weighted *in silico* pathology

WISP (Weighted *In Silico* Pathology; https://cit-bioinfo.github.io/WISP/) is an approach to assess intratumoral heterogeneity from bulk molecular profiles. Based on predefined pure molecular or histological populations for a particular cancer type, this approach gives a fine description of each tumor in a standardized way. The methodology is based on non-negative least squares regression and quadratic programming optimization for estimating the mixed proportions of distinct populations for a tumor sample. It can be applied on transcriptomic or methylation data. The output is the mixing proportion estimations for all samples.

For this analysis, we classified the samples from the MIBC CIT cohort (15) into a luminal or basal subtype according to the BASE47 classifier (27) to refine pure samples and calculate pure population centroid profiles, using standard parameters. Then, we estimated the mixed proportions of pure populations for each of our patient tumor and PDX samples, without scaling.

Short tandem repeat signature

Patient tumors and corresponding PDX DNA samples were subjected to STR using the Authentifiler PCR amplification kit (Thermo Fisher Scientific, Illkirch, France) that amplifies nine unique STR loci and the amelogenin gender-determining marker, according to the manufacturer's instructions. PCR products were separated by capillary electrophoresis on ABI PRISM 3100, and results were analyzed using the GeneMapper software.

Genomic alterations detection: mutations, copy number variant detection, variant calling, and tumor mutational burden

Patient tumors and PDX were sequenced with a targeted NGS panel (called "DRAGON") that has been developed by the genetics department of Institut Curie (Paris, France) and can detect mutations, copy number alterations (CNA), tumor mutational burden and microsatellite instability. It is composed of 571 genes of interest in oncology for diagnosis, prognosis, and theragnostics (Supplementary Table 1). NGS primers were selected based on their specificity on the human genome. The whole method is described in Supplemental Method Dragon.

Deleterious genomic alterations were defined as follows: (i) for oncogenes, only gain-of-function mutations were considered (i.e., hotspot missense mutations, in-frame insertions/deletions/splicing described as oncogenic), (ii) for tumor suppressor genes, only loss-of-function mutations were considered (i.e., biallelic truncating alterations—non-sense mutations, frameshift insertions/deletions/splicing—or monoallelic truncating alterations associated with heterozygous deletion detected by copy number analysis).

Gene expression analysis

Gene expression arrays/transcriptomic data/consensus class

The RNA of 31 PDX and patient tumors samples were hybridized in three batches in Affymetrix Human Genome U133 plus 2.0 Array Plates (Santa Clara, CA) according to Affymetrix standard protocols. Raw CEL files were RMA-normalized (28) using R statistical software. PCA confirmed that no batch effect was observed. The arrays were mapped to genes with a Brainarray Custom CDF (Human EntrezG version 24) (29).

Molecular consensus classes were determined with the "consensusMIBC" R package (v1.1.0, https://github.com/cit-bioinfo/consensusMIBC) using the RMA-normalized transcriptomic data. For WISP, we used a previously published dataset (15), which contains human MIBC samples (n = 85) also hybridized with Affymetrix Human Genome U133 plus 2.0 according to Affymetrix standard protocols. The raw CEL files used here are available from ArrayExpress (http://www.ebi.ac.uk/arrayexpress/) under accession number E-MTAB-1803.

Raw CEL files were RMA-normalized using R statistical software. The arrays were mapped to genes with a Brainarray Custom CDF (Human EntrezG version 23) (29)

In both datasets, we obtained a log2-transformed expression matrix with one value per gene.

Regulatory networks

The regulatory network was reverse-engineered by ARACNe-AP (30) from human urothelial cancer tissue datasets profiled by RNA-Seq from TCGA (n=414). The RNA-seq data was downloaded from the TCGA data portal using the TCGAbiolinks package (R). Raw counts were normalized to account for different library sizes, and the variance was stabilized with VST function in the DESeq2 R-package (31)

ARACNe was run with 100 bootstrap iterations using all probe-clusters mapping to a set of 1,740 transcription factors. The parameters used were standard parameters, with the mutual information p-value threshold of 10^{-8}.

Regulon activity—VIPER

The VIPER algorithm tests for regulon enrichment based on gene expression signatures (32), using the regulatory network obtained from ARACNe on urothelial cancer, and we computed the enrichment of each regulon on the gene expression signature using different implementations of the analytic rank-based enrichment analysis algorithm.

Dual-staining immunohistochemistry

Dual immunostaining for GATA3 and KRT5/6 on Formalin-Fixed, Paraffin-Embedded (FFPE) samples was performed to screen for homogeneous or heterogeneous luminal or Ba/Sq tumors at the immunohistochemical level. Automated sequential dual-staining immunohistochemistry (IHC; Discovery, Roche/Ventana, Tucson, AZ, USA) was used according to the manufacturer's instructions. Tissue sections cut at 3 µm were dewaxed and subjected to antigen retrieval, then incubated first with a GATA3-specific rabbit monoclonal antibody (1:300, clone ZR65 Diagomics, Blagnac, France), followed by an HRP-conjugated anti-rabbit IgG secondary antibody (MP-7401, Vector). The antigen–antibody reaction was detected using an ImmPACT DAB reagent (SK-4105, Vector), producing brown staining in positive nuclei. In the second sequence, a primary rabbit monoclonal antibody against KRT5/6 (1:100, clone EP24/EP67; Diagomics, Blagnac, France) was incubated, followed by alkaline phosphatase–conjugated anti-rabbit IgG secondary antibody (ENZ-ACC110-0150, Enzo). The antigen–antibody reaction was revealed using ImmPACT red reagent (Vector), producing red staining in positive cytoplasm. A normal urothelium was used as a positive control. The staining for GATA3 and KRT5/6 was evaluated by one blinded pathologist (JF), providing respective quick scores (QSs) calculated as intensity (0–3) multiplied by the percentage of stained tumor cells and normalized to [0;1]. Immunohistochemical thresholds for Ba/Sq tumors (IHC-Ba/Sq) defined as QS(KRT5/6) >0.14 and QS(GATA3) <0.02, or luminal QS(GATA3) >0.14 and QS(KRT5/6) <0.02, were used (33). Tumors showing IHC-Ba/Sq and non-Ba/Sq areas were defined as having intratumoral heterogeneity.

In vivo efficacy studies

Erlotinib (EGFR inhibitor) was purchased from MedChemExpress (Sollentuna, Sweden) and administered orally (gavage) 5 days per week during 4 weeks at a dose of 30 or 90 mg/kg (0.5% carboxymethylcellulose in PBS).

Erdafitinib (pan-FGFR inhibitor) was purchased from MedChemExpress (Sollentuna, Sweden) and administered orally (gavage) 6 days per week during 4 weeks at a dose of 10 or 30 mg/kg (20% 2-hydroxypropyl β-cyclodextrin in distilled water).

BGJ398 (pan-FGFR inhibitor) was purchased from LC Laboratories and administered orally (gavage) 6 days per week during 4 weeks at a dose of 30 mg/kg.

Cisplatin and gemcitabine were purchased from Sigma (St. Quentin Fallavier, France). Both drugs were administered intraperitoneally at a dose of 60 mg/kg (NaCl 0.9%) once a week (D0, D7, D14) and 4 mg/kg (NaCl 0.9%) once every 3 weeks (D1), respectively.

For efficacy studies, mice were implanted as described above. Tumor fragments were transplanted into 6-week-old NMRI mice. When the tumor reached a volume comprised between 60 and 270 mm^3, mice were randomly assigned to the vehicle or treatment groups (n= 7–10). The tumor volume was calculated as: TV (mm^3) = [length (mm) × width (mm)^2]*π/6, where the length and width are the longest and shortest diameters of the tumor, respectively. Tumor volumes were then reported to the initial volume as relative tumor volume (RTV). The means of the RTV in the same treatment group were calculated. Growth curves were generated using the GraphPad Prism software.

Western blot

Frozen PDX samples were resuspended in Laemmli lysis buffer [50-mM Tris-HCl (pH 6.8), 2-mM DTT, 2.5-mM EDTA, 2.5-mM EGTA, 2% SDS, 5% glycerol with protease inhibitors and phosphatase inhibitors (Roche)], and the resulting lysates were clarified by centrifugation. The protein concentration of the supernatants was determined with the BCA protein assay (Thermo Scientific, Illkirch, France). Proteins (10–50 µg) were resolved by SDS-PAGE in 10% polyacrylamide gels, electrotransferred onto Bio-Rad nitrocellulose membranes, and analyzed with antibodies against β-actin (Sigma-Aldrich #A2228, used at 1/25,000), or the extracellular domain of FGFR3 (Abcam, # ab133644, 1/5,000). Anti-mouse IgG, HRP-linked, and anti-rabbit IgG, HRP-linked antibody (Cell Signaling Technology # 7076 and # 7074, used at 1/3,000, Saint-Cyr-L'École, France) were used as secondary antibodies. Protein loading was checked by the Amido Black staining of the membrane after electrotransfer.

Statistical and bioinformatic analysis

Comparisons between PDX treatment responses were done using the Mann–Whitney test.

Bioinformatics analyses was performed with R (4.0.2).

Results

Establishment of urothelial PDXs

We successfully obtained 31 PDXs from 153 tumors (global engraftment rate ~20%, median latency 27.5 days with a range of 10–70 days) from January 2009 to October 2019. The main clinicopathological characteristics of the patients and patient tumors are summarized in Table 1 (additional clinical data from patients are presented in Supplementary Table 2). As expected, the majority of PDXs was derived from male patients (84%), with bladder as the primary site (84%) and were urothelial carcinomas (90%). The frequency of squamous cell carcinomas (SCC, 3/31, 10%) was higher than the known frequency of these tumors, potentially owing to a higher engraftment success rate (n=4/10, with one of the four that could not be further analyzed due to patient serology). One PDX was derived from a non-muscle-invasive BCa (NMIBC). Four patients had received systemic or radiotherapy treatment before the establishment of the PDX.

Histological and genomic characterization of PDXs

A histopathological analysis of the H&E-stained slides of patient tumors and PDXs was performed by two pathologists (VL, JF), based on the current WHO Classification of Tumors of the Urinary System (34). High histological concordance between patient tumors and PDXs was observed (Figure 1A) with the exception of three PDXs showing distinct histology compared to the matched patient tumors (M1030 and BLCU-011 lost the variant observed in the tumor, while a more squamous variant was observed in R1056, Supplementary Table 2). We confirmed by short tandem repeat (STR) profiling the concordant genetic identity between patient tumor and derived PDXs (Supplementary Table 3), with 85%–100% of conserved STR for the different models, as an example for L987 in Figure 1B. We characterized genomic alterations for 571 cancer-related genes (Supplementary Table 1 and Supplementary Table 4) in all 31 PDXs using a targeted next-generation sequencing assay, allowing the detection of mutations, the estimation of copy number alterations (CNA), tumor mutational burden (TMB), and MSI status (Figure 1C**).** As anticipated, the most frequent genomic alterations were mutations in *TERT* (68%) and *TP53* (61%) and the homozygous deletion of *CDKN2A/B* (~50%). We also identified activating mutations in potentially actionable genes such as *PIK3CA* (19%), *ERBB2* (19%), *FGFR3* (13%), *BRAF* (6%), *ERBB3* (3%), *KRAS G12C* (3%), and truncating mutations in the epigenetic genes *KDM6A* (19%), *ARID1A* (23%), *KMT2D* (19%), *KMT2A/B/C* (3% each), and *ARID2* (3%). One UTUC PDX displayed microsatellite instability associated with a bi-allelic deletion of *MSH2*, and this alteration was also observed in the parental tumor. To determine whether the PDXs retain the genomic alterations of the matched patient tumor, we sequenced five patient tumor/PDX pairs. The overall concordance of observed genomic alterations was high (90%–100%) (Figure 1D), except for the MSI-high PDX (B521) that harbored high TMB (40%). PPARG pathway activation, through PPARG amplifications or RXRA- and PPARG-activating mutations, is a known key feature of luminal tumors and a potential therapeutic target (16, 26, 35–37). We did not observe any *RXRA* mutation in our sequencing analyses. Since *PPARG* was not in our targeted panel, we performed a Sanger sequencing of the hotspot region within the ligand-binding domain of *PPARG* (26) and

TABLE 1 Clinicopathological characteristics of the samples used for patient-derived xenograft.

Variables	All patients
Total	31
Median age, years (IQR)	75 (52–88)
Gender	
Male	26 (84%)
Female	5 (16%)
Primary site	
Bladder	26 (84%)
Upper tract	5 (16%)
Histology	
Urothelial	28* (90%)
Conventional	17
Squamous differentiation	7
Sarcomatoid	2
Plasmacytoid	1
Glandular differentiation	1
Micropapillary	1
Poorly differentiated	5
Squamous	3 (10%)
Prior Treatment	
No	19 (61%)
BCG	3 (10%)
Cisplatin-based CT	3 (10%)
Radiotherapy + cisplatin-based CT	1 (3%)
NA	5 (16%)
pT Stage	
<pT2 (non-MIBC)	1 (3%)
≥pT2	30 (97%)
pN Stage	
pN0	7 (23%)
pN+	10 (32%)
pNx	14 (45%)
Associated CIS	
Yes	4 (13%)
No	27 (87%
Relapse (Yes)	4 (13%)

CT, chemotherapy.
*Variant total is above n=31 as some tumors have multiple variants.

identified one patient tumor/PDX pair (B521) harboring the T475M-activating mutation (n=1/23 tested PDX) and one patient tumor/PDX pair (M559) harboring the non-characterized and non-recurrent L339F mutation (26).

PDXs recapitulate the molecular subtypes and intratumoral heterogeneity

We then sought to determine whether PDX models recapitulate the molecular subtypes of patient tumors. In total, transcriptomic data using Affymetrix U133plus2 array were available for 22 patient tumor/PDX pairs and 8 individual PDXs. Unsupervised clustering analysis using the top 200 most variant genes did not highlight any segregation in PDXs by the primary site or histological tumor (Supplementary Figure 1, with the exclusion of the NMIBC PDX for the transcriptomic subtype analysis). We therefore considered all patient tumors/PDX similarly and stratified them into six subtypes by applying the molecular consensus classifier (9) (Figure 2A). We observed 15 Ba/Sq (52%), 11 LumP (38%), and 3 luminal-unstable (LumU) (10%) PDXs. All three SCC patient tumors/PDXs were classified as Ba/Sq. In contrast to genomic and histological characteristics, transcriptomic profiles were less stable between patient tumor/PDX pairs. Specifically, eight patient tumors gave rise to a PDX with a distinct molecular subtype (36%) including five Ba/Sq patient tumors to LumP PDX, one LumP to LumU, one stroma-rich to LumU, and one LumNS to the LumP subtype. We also stratified patient tumors and PDXs according to the BASE47 classifier (27) (Figure 2A). Among the 16/22 patient tumors that were classified as basal, 6 gave rise to a luminal PDX. In contrast, all luminal tumors formed luminal PDXs. For six matched tumor-PDX pairs, for which we did not have transcriptomic data, we performed GATA3 (luminal) and KRT5/6 (basal) dual immunostaining to assign molecular subtypes using previously defined thresholds for each marker (33) and we did not observe a difference in the subtype between tumors and PDXs (Figure 2A). To explore whether the basal- to-luminal discordance could be related to intratumoral heterogeneity, we evaluated the molecular heterogeneity in both patient tumors and PDXs using the WISP algorithm (Figure 2A). We observed the admixed proportions of luminal and basal subtypes in 59.1% of patient tumors and 41.4% of PDXs, including all six cases with discordant BASE47 subtypes. The high molecular heterogeneity found in the six basal tumors that gave rise to luminal PDXs was conserved in most of the matched PDXs. These findings suggest an intrinsic plasticity of these tumors, leading to a shift in subtype rather than a sampling bias of an area of a given subtype within a molecularly heterogeneous patient tumor (Figure 2A, lower panels).

Using defined biomarkers of luminal and basal differentiation (9, 10), we confirmed that PDXs were globally separated between luminal, differentiated tumors and basal tumors (Figure 2B and Supplementary Figure 1). Concerning NECTIN4 and TROP2, which could be targeted by drug-conjugated antibodies (5, 6), we also found in the PDX transcriptomic analysis a heterogeneity of NECTIN4 and TROP2 expression, with a higher expression of NECTIN4 in luminal tumors (Supplementary Figure 2).

To further explore the transcriptomes of our PDXs, we inferred the activity of 22 major regulons, as defined in TCGA analysis (10) (Figure 2C). Using this approach, we observed a perfect separation of luminal and basal PDXs in clustering analysis, independently of the primary site of patient tumor. Similar to patient tumors from TCGA, we observed a higher *EGFR* regulon activity in basal PDXs and a higher *PPARG/*

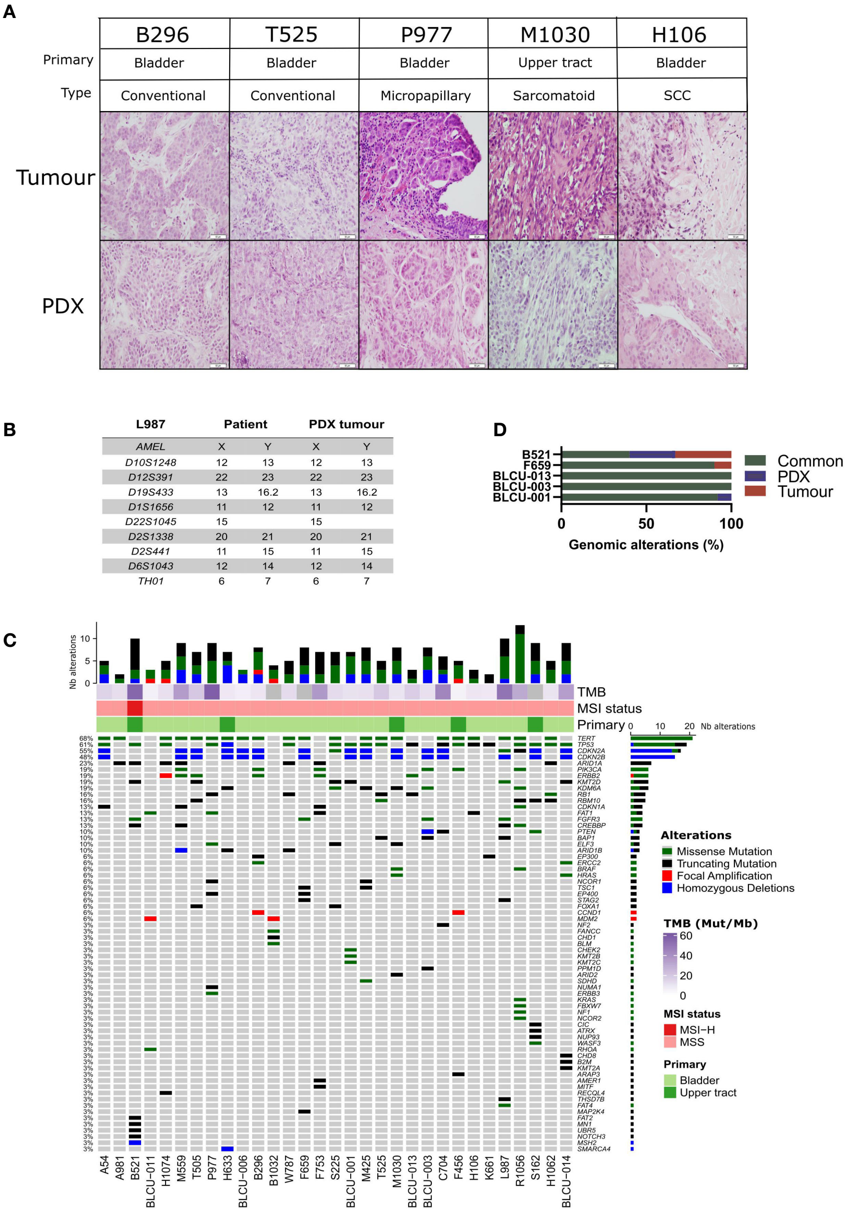

L987	Patient		PDX tumour	
AMEL	X	Y	X	Y
D10S1248	12	13	12	13
D12S391	22	23	22	23
D19S433	13	16.2	13	16.2
D1S1656	11	12	11	12
D22S1045	15		15	
D2S1338	20	21	20	21
D2S441	11	15	11	15
D6S1043	12	14	12	14
TH01	6	7	6	7

FIGURE 1
Histological and genomic characteristics of patient tumors and paired derived patient-derived xenografts (PDXs). **(A)** Histology of bladder/ureteral patient tumors and corresponding PDX models demonstrated similar histological features as assessed by hematoxylin and eosin (H&E) staining. Scale bar corresponds to 50 µm. H&E slides of a section of each patient tumor and matching PDX were reviewed by a board-certified pathologist, and representative pictures for the different histologies or variants are shown. **(B)** Short tandem repeat signature of a patient specimen and PDX tumor, an example of the L987 case. **(C)** Somatic genomic landscape of 31 bladder and ureteral PDXs analyzed using an in-house targeted sequencing assay (571 cancer-related genes, Supplementary Tables 2, 3), the tumor mutational burden per megabase (TMB, indicated in the log2 scale for each sample), and microsatellite instability–high (MSI-H) versus a microsatellite-stable (MSS) status. **(D)** Concordance of genomic alterations in five pairs tumor/PDX.

ERBB2/ERBB3 regulon activity in luminal PDXs (10). Of note, *FGFR3* mutations are enriched in LumP tumors (9) and we observed *FGFR3* mutations not only in two LumP PDXs, including one derived from UTUC, but also in two Ba/Sq PDXs, including one derived from an SCC tumor (Figures 2B, C) (9). As expected, high FGFR3 regulon activity was observed in tumors bearing *FGFR3* mutations.

To validate the intratumoral molecular subtype admixture inferred from the transcriptomic data *in situ*, we performed dual IHC staining combining a luminal (GATA3) and a basal marker

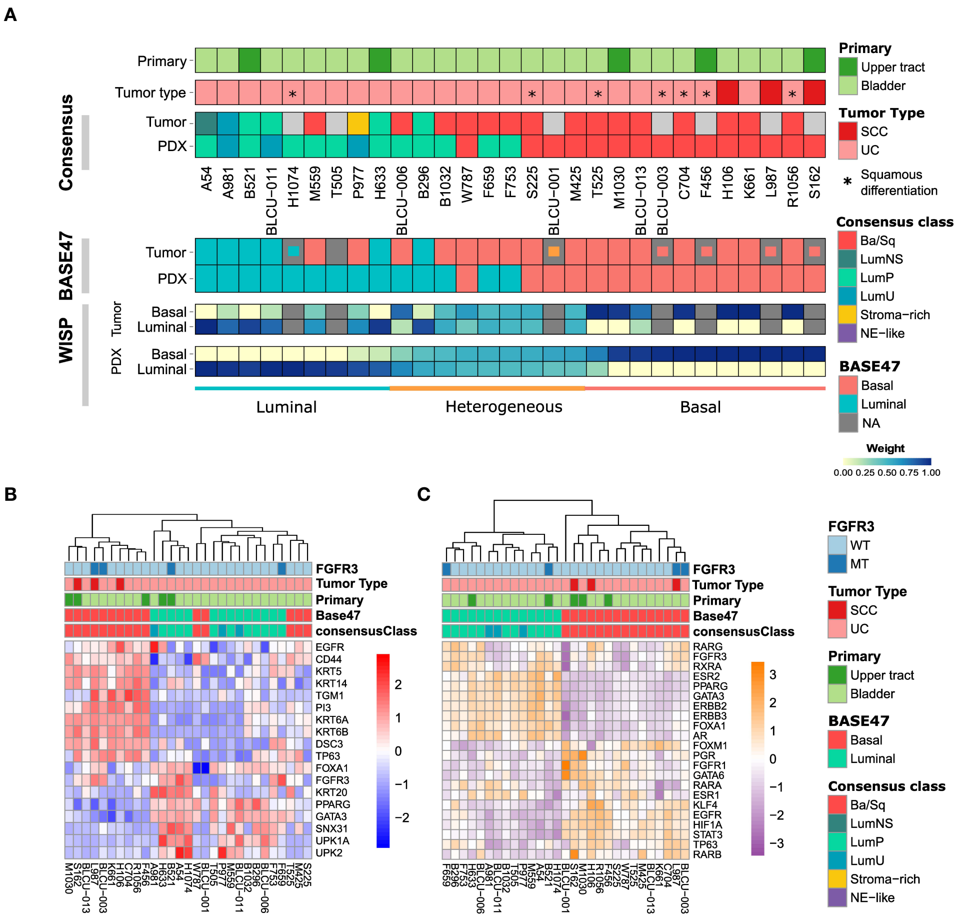

FIGURE 2
Transcriptomic analysis of patient tumors and paired PDXs. **(A)** Tumors and PDXs were classified into six subtypes using transcriptomic Affymetrix U133plus2 array data according to the molecular consensus classifier developed for MIBC, the corresponding box colors indicated in the legend on the right. A total of 22 patient tumor–PDX pairs and 7 individual PDXs were analyzed, where tumors without transcriptomic data are indicated in gray. Urothelial carcinomas with divergent squamous differentiation are highlighted with *. **(B)** Upper panels: tumors and PDXs were classified using transcriptomic data as luminal and basal subtypes according to the BASE47 classifier (27). In patient tumors with missing transcriptomic data, we assessed the luminal (blue), basal (red), or heterogeneous (orange) subtype by immunohistochemistry (IHC; inset small boxes), as defined in methods. Lower panels: the intra-tumoral heterogeneity and proportion of luminal and basal subtype admixture as evaluated from transcriptomic profiles using the WISP (Weighted *In Silico* Pathology) algorithm. Based on the PDX WISP results, samples were molecularly classified as luminal, basal, or heterogeneous. **(B)** Heatmap of PDX samples based on the gene expression of selected luminal or basal markers. **(C)** Heatmap of PDX samples based on the regulon activity of the main regulators previously identified within the different molecular subtypes of MIBC (9, 10).

(KRT5/6) in a subset of patient tumors and PDXs. We confirmed the presence of a subtype marker expression admixture *in situ*, with either spatially distinct areas showing different IHC profiles (defined hereafter as intratumoral heterogeneity) or a single-cell coexpression of the two markers, or a combination of both patterns of admixture. By comparing the results between tumors/PDXs classified as basal, luminal, or heterogenous based on the WISP analysis (Figures 2A, 3), we observed that tumors/PDXs classified as pure luminal or Ba/Sq based on transcriptomic data displayed higher GATA3 or KRT5/6 staining levels, respectively (Figure 3A). The WISP heterogeneous samples had more intermediate staining levels of both GATA3 and KRT5/6 (Figure 3A) and showed more intratumoral heterogeneity compared to pure Ba/Sq or luminal cases (10/15 vs. 4/29, p<0.01) (Figure 3B). Among samples with intratumoral heterogeneity, a GATA3-KRT5/6 coexpression at the single-cell level was also identified in 9/14 samples (Figures 3B, C).

Chemosensitivity of patient-derived xenografts

With cisplatin-based chemotherapy being the standard of care of MIBC and high-risk UTUC, we assessed the sensitivity of

10 PDXs representative of the different subtypes (six basal, four luminal) to cisplatin plus gemcitabine (Figure 4). We did not observe a significant difference between the proportion of basal (5/6, 83%) and luminal PDXs (2/4, 50%) with significant growth inhibition upon treatment (Fisher's exact test p=0.5). Due to the low number of recurrent genomic alterations and the number of models tested, it was not possible to statistically explore the association between genomic alterations and chemosensitivity.

EGFR-targeted therapy is effective in non-sarcomatoid basal/squamous patient-derived xenografts

In relation to the high EGFR activity in basal tumors, we have previously shown that EGFR is an effective therapeutic target in different *in vivo* basal preclinical models (15). The aggressive sarcomatoid variant of MIBC is suggested to occur through the progression of Ba/Sq tumors (38). We recently analyzed sarcomatoid tumor transcriptomes and identified a loss of EGFR regulon activity during the progression of Ba/Sq tumors to the sarcomatoid variant (Fontugne et al., unpublished results). In line with these findings, we identified a low EGFR regulon activity in a PDX (BLCU-001) compared to the other Ba/Sq PDXs, which was classified as a Ba/Sq sarcomatoid tumor (Figure 2C and Supplementary Table 1). To assess whether the loss of EGFR activity could impact the sensitivity to EGFR inhibition, we compared the effect of anti-EGFR treatment (erlotinib) in two Ba/Sq models presenting high EGFR-regulon activity (L987 and H106, Figure 2C) and BLCU-001 (Figure 5A). As expected, the two SCC Ba/Sq models were sensitive to erlotinib whereas the Ba/Sq model with sarcomatoid differentiation was resistant (Figure 5A). Of note, two other Ba/Sq PDXs (C704 and R1056)

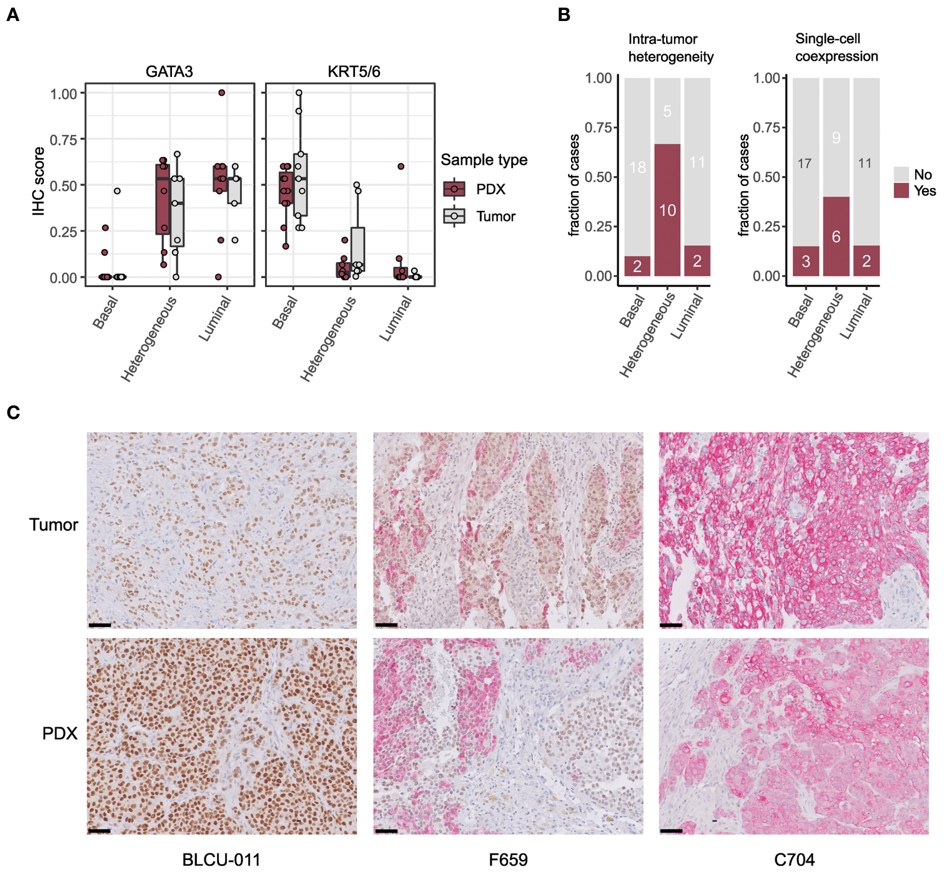

FIGURE 3
Intratumor heterogeneity in tumors and PDXs at the protein level by IHC. **(A)** GATA3 and KRT5/6 expression levels (normalized quick scores), grouped according to the PDX WISP molecular classification (luminal, heterogeneous, and Ba/Sq, Figure 2A). **(B)** Proportion of tumors with intratumoral heterogeneity (left) and GATA3 + KRT5/6 coexpression at the single-cell level (right), grouped according to the PDX WISP molecular classification (luminal, heterogeneous, and Ba/Sq, Figure 2A). **(C)** Patterns of dual IHC staining for GATA3 (brown, nuclear) and KRT5/6 (red, cytoplasmic) in the paired tumor/PDX of a luminal (BLCU-011), a heterogeneous (F659), and a Ba/Sq (C704) example.

were sensitive even when we used a lower dose of erdafitinib in a second experiment (Figure 5B).

Combined inhibition of FGFR and EGFR improves response of *FGFR3*-mutated patient-derived xenograft compared to FGFR inhibition alone

FGFR inhibitors have already demonstrated clinical efficacy in FGFR3-altered tumors (4). However, resistance to treatment is systematically observed over time. Consistently, the treatment of two *FGFR3*-mutated PDXs, one Ba/Sq and one LumP, both presenting high expression levels of FGFR3 protein compared to other non-mutated PDXs, with a pan-FGFR-inhibitor (BGJ398) (Supplementary Figure 3A) only reduced tumor growth (Supplementary Figure 3B). Different preclinical studies using bladder-derived cell lines identified EGFR activation as a mechanism of resistance to FGFR inhibition (39–41). Using reverse transcription–quantitative PCR (RT-qPCR), we confirmed that this mechanism could be relevant in our PDX models since anti-FGFR treatment not only induced the overexpression of EGFR but also ERBB2 and ERBB3 in our *FGFR3*-mutated L987 model (Supplementary Figure 3C).

Therefore, we then tested if a combination of FGFR3 and EGFR/ERBB2 inhibition could overcome the compensatory upregulation of EGFR signaling and increase the sensitivity of FGFR3-mutated PDXs to FGFR inhibition, as previously observed for RT112 xenografts harboring FGFR3-TACC3 fusion (39). We treated five PDXs (three *FGFR3*-mutated: L987, B521, F659; two Ba/Sq *FGFR3*-WT: R1056, C704) with a pan-FGFR inhibitor (erdafitinib) that recently obtained FDA approval for locally advanced or metastatic MIBC with *FGFR3* genomic alterations and an EGFR inhibitor [erlotinib, which has been described to have an ERBB2 inhibitory effect (42)] alone and in combination (Figure 5B). To limit toxicity, we used suboptimal doses for each inhibitor when administered in combination. In these conditions, monotherapies presented limited effects, with significant growth inhibition in two *FGFR3*-mutated and in two basal PDXs upon erdafitinib and erlotinib treatment, respectively. The combination of erlotinib plus erdafitinib led to an improved response in all *FGFR3*-mutated PDXs compared to each of the monotherapies, while no additional benefit was observed for the combination in the Ba/Sq *FGFR3*-WT PDXs (Figure 5B).

Discussion

The development of relevant preclinical models closely mimicking patient tumors is key in the identification of new potential therapies for precision medicine, and PDXs are widely used in this regard in oncology (24, 43).

We report here, like others (22–25), that PDXs derived from bladder and ureteral cancers preserved the histological and genomic properties of patient tumors. However, their transcriptomic profiles were less stable. Namely, we identified basal patient tumors giving rise to luminal PDXs. For these cases, both tumors and PDXs revealed high heterogeneity, suggesting intrinsic cell plasticity. Such heterogeneity and cell lineage plasticity were recently demonstrated by Sfakianos et al. in the basal N-butyl-N-(4-hydroxybutyl)-nitrosamine (BBN) chemically induced mouse bladder tumors using both single-cell transcriptomic analysis and Fluorescence-Activated Cell Sorting (FACS) analysis after the *in vivo* transplantation of FACS presorted and cultured tumor cells (44). Basal tumors present a more abundant stroma compared to luminal tumors including high infiltration by immune cells (9). Our results also suggest that, because the stroma in immune-deficient mice differs from human tumor stroma, the crosstalk between the tumor and stroma may impact the tumor cell phenotype. Such crosstalk has been reported in three-dimensional *ex vivo* models, where the absence of cancer-associated fibroblasts induced a shift from luminal tumors to basal organoids (45, 46) whereas basal organoids engrafted in mice then developed a luminal phenotype (45). Interestingly, the molecular heterogeneity of luminal/basal markers observed in tumor and PDX pairs also reinforces the relevance of our models in drug efficacy evaluation, given that tumor heterogeneity is a known cause of resistance to treatment (47).

We described potential actionable genomic alterations in our PDXs, such as *PIK3CA* mutation, *ERBB2* mutation/amplification, or *MDM2*-amplification (48, 49), whose frequencies are comparable with TCGA (10). Epigenetic drugs could also represent a promising therapeutic approach in monotherapy or in combination when considering the high proportions of PDXs harboring at least one mutation in epigenetic genes (50). Our models could thus be useful to evaluate such new potential therapies.

Previously, we proposed EGFR as a therapeutic target in basal MIBC based on findings from different *in vitro* and *in vivo* preclinical models (15). Here, we further validated the EGFR dependency of Ba/Sq tumors using PDX models. However, anti-EGFR treatments have shown disappointing results in the clinic, although some pathological responses have been observed in the neoadjuvant setting (51). This discrepancy between preclinical and clinical settings warrants further investigation. We hypothesize that the rich stroma of basal tumors contributes to anti-EGFR resistance, as recently demonstrated with cancer-associated fibroblasts in lung cancer (52). Indeed, rich stroma is absent in our preclinical models, with the exception of the BBN model, which presented only a moderate sensitivity to anti-EGFR treatment (15). Our results also suggest that sarcomatoid differentiation could be another mechanism of resistance to anti-

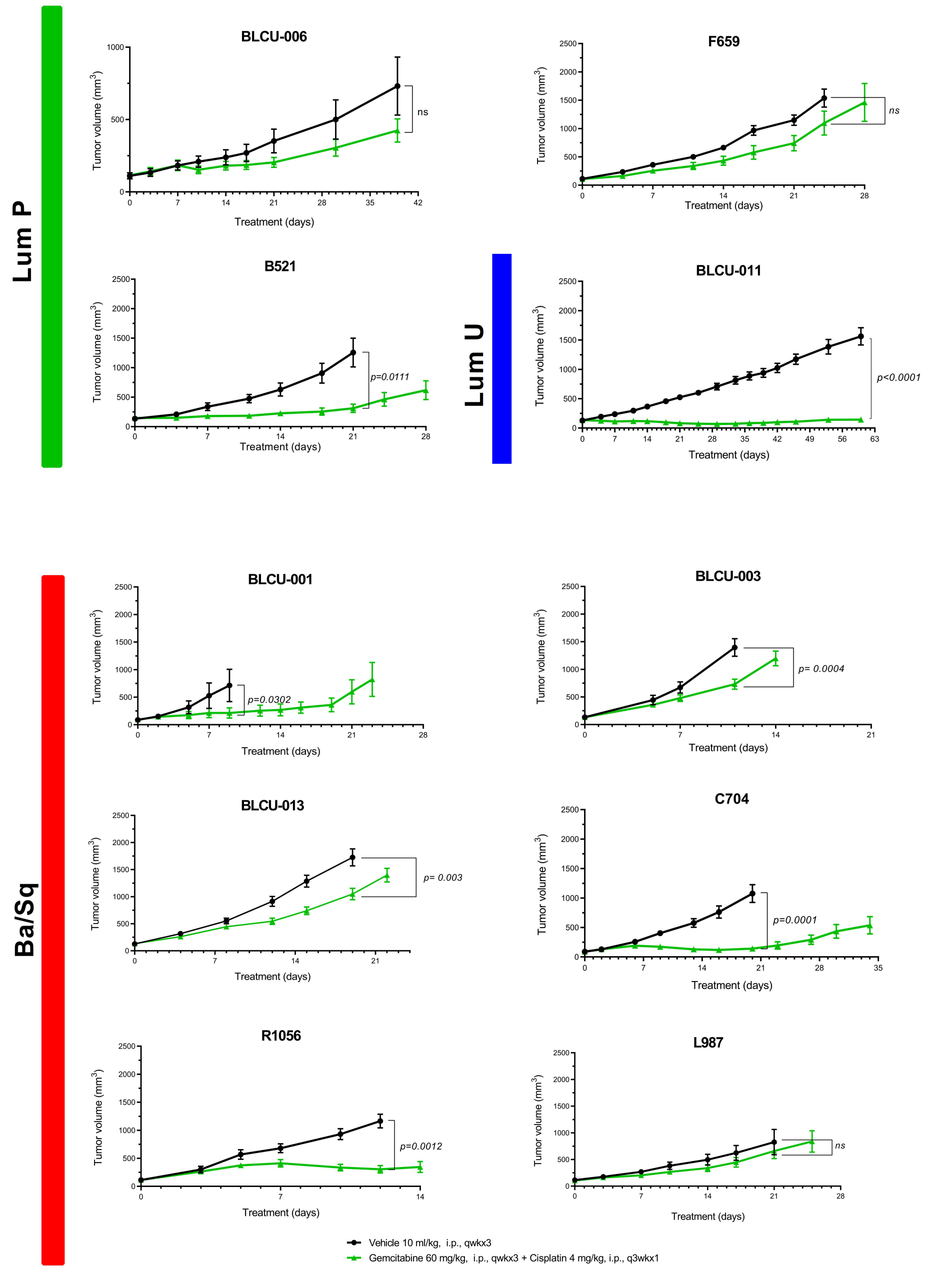

FIGURE 4
Chemosensitivity of representative basal and luminal PDX models. Mice with established PDXs (67–270 mm^3) were treated with cisplatin plus gemcitabine (green) as indicated, and control mice were treated with vehicle alone (black) (n = 7–10 animals per group). Tumor size was measured at the indicated time points. Data are presented as mean ± SEM. Results were compared using the Mann–Whitney test. n.s, non-significant.

EGFR treatment. In agreement, sarcomatoid differentiation is linked to EMT, which was previously shown to impair anti-EGFR sensitivity in lung cancer (53).

In agreement with previous studies (54, 55), we found that upper urinary tract and bladder urothelial carcinomas harbored similar genomic alterations but at different frequencies, except for the presence of MSI-H in one UTUC (54, 55). The diversity of our bank—including both MIBC [urothelial (UC) and squamous (SCC)] and UTUC—allowed us to observe that urothelial carcinoma PDXs originating from the upper urinary tract or bladder were also highly similar at the transcriptomic level. Additionally, we found that SCC samples did not classify into a

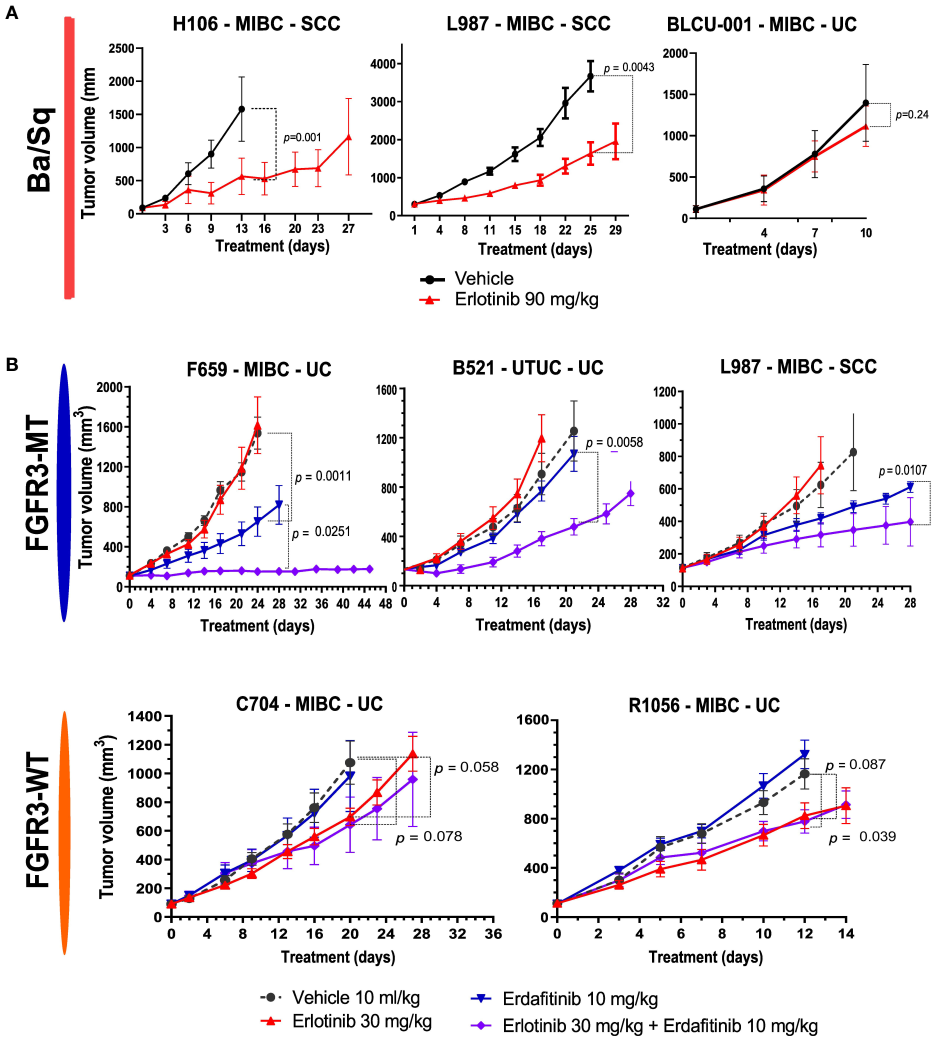

FIGURE 5
Sensitivity to anti-EGFR or the combination of EGFR and FGFR inhibitors in Ba/Sq and *FGFR3*-mutated PDXs. **(A)** Mice with established basal/squamous PDXs (67–270 mm^3) were treated with anti-EGFR (erlotinib 90 mg/kg, red) or control vehicle alone (black). **(B)** Mice with established *FGFR3*-mutated tumors and controls were treated with control vehicle (black), low-dose anti-EGFR (erlotinib 30 mg/kg, red), a pan-FGFR inhibitor (erdafitinib 10 mg/kg, blue), or the combination (purple), as indicated (n = 7–10 animals per group). Tumor size was measured at the indicated time points. Data are presented as mean ± SEM. Results were compared using the Mann–Whitney test.

molecularly distinct group of tumors, instead grouping with urothelial Ba/Sq carcinomas. Whereas up to now, SCC, UC, and UTUC were considered as highly different entities in terms of response to treatment, we found that the same molecular classifications/genetic alterations can predict the same therapeutic response for the three entities. Indeed, independently of the cell of origin, basal PDXs were sensitive to anti-EGFR therapies, except for sarcomatoid tumors, which are characterized by low EGFR activity. Furthermore, most FGFR3-mutated PDXs were sensitive to FGFR inhibition independently of their cell of origin or their luminal/basal phenotype.

Finally, it has been shown in RT112 xenografts (BCa cell line presenting an FGFR3-TACC3 fusion observed in 3% of MIBC) that a combination of anti-EGFR/anti-FGFR was more potent than anti-FGFR alone (39). We validated here these results using our more clinically relevant PDX models with *FGFR3* mutations (observed in 15% of MIBC) (three different models derived from UTUC, MIBC-UC, and MIBC-SCC) reinforcing the interest to further test this combination treatment in the clinics. For treatment optimization and to limit side effects and toxicity, it will be of interest to explore if this effect is more specifically associated with EGFR or HER2 inhibition.

Conclusion

Muscle-invasive bladder and upper urinary tract cancers are heterogeneous and aggressive diseases with no satisfactory treatment. We have developed and characterized highly relevant preclinical models for bladder and upper tract carcinoma, recapitulating the molecular heterogeneity and drug responses observed in the clinic. Our work supports a benefit of combined FGFR and EGFR inhibition in FGFR3-mutated tumors. Overall, our models represent an essential tool for the development of new efficient therapies against these aggressive cancer types.

Data availability statement

The datasets presented in this study can be found in online repositories. The names of the repository/repositories and accession number(s) can be found below: https://www.ncbi.nlm.nih.gov/geo/, GSE181962.

Ethics statement

This study was reviewed and approved by Comité de Protection des Personnes Sud-Ouest et Outre-mer, DC 2019-3565]. Written informed consent was obtained from all participants for their participation in this study. The animal study was reviewed and approved by CEEA-122.

Author contributions

IB-P had full access to all the data in the study and takes responsibility for the integrity of the data and the accuracy of the data analysis. HL, CB, ML and LC designed, performed experiments or bioinformatics analyses, analyzed and interpreted the data. HL, CB and ML developed the PDXs models. HL, XG, PR provided samples and helped with clinical data analysis. CB and ML performed the pharmacological characterization of the PDXs. CB, CK and JF prepared DNA and RNA for genomics analysis. CB performed STR analysis under TM supervision. CK performed and analyzed sanger sequencing. CK and VD performed immunohistochemical experiments under YA supervision. JF performed histo- and immunohistopathological analysis and designed pharmacological studies for sarcomatoid tumors under YA supervision. FD performed Western blot and RT-qPCR analysis. LC performed most of the bioinformatics analyses together with help of CSG, XM and AK for tumor's/PDXs' classification and for regulon analysis. ADR supervised AK and CG. EC normalized and annotated Affymetrix array data and centralized the data for bioinformatics analyses. JM-P and RB performed and analyzed targeted NGS under the supervision of IB. VL performed and supervised histopathological analysis of tumors and PDXs. YM and PL designed the study and supervised establishment of part of the PDXs and pharmacological characterization of PDXs. FR supervised the genomic analyses. TM and HL designed and supervised the establishment of part of the PDXs. IB-P and TM designed and supervised the research, analyzed and interpreted the data. LC, CB, JF, TM and IB-P wrote the paper. All authors contributed to the article and approved the submitted version.

Funding

This work was supported by a grant from Ligue Nationale Contre le Cancer (LC, FD, JF, CK, CG, XM, YA, FR, IB-P) as an associated team (Equipe labellisee'), the "Carte d'Identité des Tumeurs" program initiated, developed, and funded by Ligue Nationale Contre le Cancer. This work was supported by the Institut National du Cancer: PRTK project "BoBCaT". LC was supported by FRM (Fondation Recherche Médicale) and JF by the Fondation ARC pour la recherche sur le cancer. XM was supported by a fellowship from ITMO Cancer AVIESAN, within the framework of Cancer Plan. We also thank BPI France, the Region Alsace, the European Funds for Regional Development, the Strasbourg Urban Community, INSERM, and the University of Strasbourg for financial support (recipients TM and HL for the innovative Urolead SAS company that was acquired by Urosphere in 2017 and Urosphere supported by the European Funds for Regional Development).

Acknowledgments

We thank David Gentien from the genomics platform of Institut Curie. We also thank the Alsace incubator SEMIA, Strasbourg, France, for advices and financial support (recipients TM and HL for Urolead SAS). We also thank the competitivity pole Alsace Biovalley, Illkirch-Graffenstaden, France for advices and labelization (TM and HL, for Urolead SAS). Finally, we also thank Alsace Satt Conectus, Illkirch-Graffenstaden, France, for technology transfer and advices (TM and HL, for Urolead SAS).

Conflict of interest

Author's CB, ML, YM and PL were employed by Urosphere and author FD was employed by Inovarion, Institut Curie, Strasbourg University and Urosphere have a collaboration contract for the transcriptomic, genomic, and pharmacological characterization of the PDX.

The remaining authors declare that the research was conducted in the absence of any commercial or financial relationships that could be construed as a potential conflict of interest.

Publisher's note

Supplementary material

The Supplementary Material for this article can be found online at: https://www.frontiersin.org/articles/10.3389/fonc.2022.930731/full#supplementary-material

SUPPLEMENTARY FIGURE 1
Unsupervised hierarchical clustering and heatmap of PDX samples based on genes with the most variant expression (n=200). PDX identifiers indicated at the bottom. Classifications indicated according to legend on the right (as in Figure 2).

SUPPLEMENTARY FIGURE 2
Expression of NECTIN4 and TROP2 (*TACSTD2*) in PDXs. **(A)** Heatmap of PDX samples based on *NECTIN4* and *TACSTD2* gene expression. **(B)** *NECTIN4* and *TROP2* (TACSTD2) expression levels grouped according to the Base47 molecular classification (Wilcoxon test). **(C)** Correlation of the *NECTIN4* and *TACSTD2* gene expression (Pearson test).

SUPPLEMENTARY FIGURE 3
FGFR3 expression in PDXs and sensitivity to anti-FGFR of FGFR3 mutated PDXs. **(A)** FGFR3 protein levels (Western blot) of the different PDX models. The urinary BCa cell line, RT112, was used as control for WT FGFR3 (black arrow) and FGFR3-TACC3 (white arrow) protein expression. Beta-actin was used as loading control. Asterisk indicates non-specific band. **(B)** Mice with established *FGFR3*-mutated (FGFR3-MT) PDXs (67-270 mm3) were treated with a pan-FGFR inhibitor (BGJ398). Control mice were treated with vehicle alone (n = 7 to 10 animals per group). Tumor size was measured at the indicated time points. Data are presented as mean ± SEM. Results were compared using Mann-Whitney test. **(C)** EGFR, ERBB2 and ERBB3 expression (RT-qPCR analysis) in L987 model at the end of treatment in mice treated with vehicle or with the pan-FGFR inhibitor BGJ398.

SUPPLEMENTARY TABLE 1
Clinical and histological characteristics of patient tumors and matched PDXs.

SUPPLEMENTARY TABLE 2
Short Tandem repeat (STR) profiling of patient tumors and matched PDX(s).

SUPPLEMENTARY TABLE 3
List of the sequenced genes in the next-generation targeted sequencing panel.

SUPPLEMENTARY TABLE 4
Next-generation sequencing results (mutations, copy number alterations, microsatellite status and tumor mutational burden).

References

1. Sung H, Ferlay J, Siegel RL, Laversanne M, Soerjomataram I, Jemal A, et al. Global cancer statistics 2020: GLOBOCAN estimates of incidence and mortality worldwide for 36 cancers in 185 countries. *CA Cancer J Clin* (2021) 71(3):209–49. doi: 10.3322/caac.21660

2. Flaig TW, Spiess PE, Agarwal N, Bangs R, Boorjian SA, Buyyounouski MK, et al. Bladder cancer, version 3.2020, NCCN clinical practice guidelines in oncology. *J Natl Compr Cancer Netw JNCCN* (2020) 18(3):329–54.

3. Leow JJ, Chong YL, Chang SL, Valderrama BP, Powles T, Bellmunt J. Neoadjuvant and adjuvant chemotherapy for upper tract urothelial carcinoma: A 2020 systematic review and meta-analysis, and future perspectives on systemic therapy. *Eur Urol* (2021) 79(5):635–54. doi: 10.1016/j.eururo.2020.07.003

4. Loriot Y, Necchi A, Park SH, Garcia-Donas J, Huddart R, Burgess E, et al. Erdafitinib in locally advanced or metastatic urothelial carcinoma. *N Engl J Med* (2019) 381(4):338–48. doi: 10.1056/NEJMoa1817323

5. Tagawa ST, Balar AV, Petrylak DP, Kalebasty AR, Loriot Y, Fléchon A, et al. TROPHY-U-01: A phase II open-label study of sacituzumab govitecan in patients with metastatic urothelial carcinoma progressing after platinum-based chemotherapy and checkpoint inhibitors. *J Clin Oncol Off J Am Soc Clin Oncol* (2021) 39(22):2474–85. doi: 10.1200/JCO.20.03489

6. Powles T, Rosenberg JE, Sonpavde GP, Loriot Y, Durán I, Lee JL, et al. Enfortumab vedotin in previously treated advanced urothelial carcinoma. *N Engl J Med* (2021) 384(12):1125–35. doi: 10.1056/NEJMoa2035807

7. Chu CE, Sjöström M, Egusa EA, Gibb EA, Badura ML, Zhu J, et al. Heterogeneity in NECTIN4 expression across molecular subtypes of urothelial cancer mediates sensitivity to enfortumab vedotin. *Clin Cancer Res* (2021) 27 (18):5123–30. doi: 10.1158/1078-0432.CCR-20-4175

8. Chou J, Trepka K, Sjöström M, Egusa EA, Chu CE, Zhu J, et al. Expression across molecular subtypes of urothelial carcinoma and enfortumab vedotin-resistant cells. *Eur Urol Oncol* (2022) S2588-9311(21):00215–7. doi: 10.1007/978-3-030-89891-5_11

9. Kamoun A, de Reyniès A, Allory Y, Sjödahl G, Robertson AG, Seiler R, et al. A consensus molecular classification of muscle-invasive bladder cancer. *Eur Urol* (2020) 77(4):420–33. doi: 10.1016/j.eururo.2019.09.006

10. Robertson AG, Kim J, Al-Ahmadie H, Bellmunt J, Guo G, Cherniack AD, et al. Comprehensive molecular characterization of muscle-invasive bladder cancer. *Cell* (2017) 171(3):540–56.e25. doi: 10.1016/j.cell.2017.09.007

11. Taber A, Christensen E, Lamy P, Nordentoft I, Prip F, Lindskrog SV, et al. Molecular correlates of cisplatin-based chemotherapy response in muscle invasive bladder cancer by integrated multi-omics analysis. *Nat Commun* (2020) 11 (1):4858. doi: 10.1038/s41467-020-18640-0

12. Seiler R, Ashab HAD, Erho N, van Rhijn BWG, Winters B, Douglas J, et al. Impact of molecular subtypes in muscle-invasive bladder cancer on predicting response and survival after neoadjuvant chemotherapy. *Eur Urol* (2017) 72(4):544–54. doi: 10.1016/j.eururo.2017.03.030

13. Seiler R, Gibb EA, Wang NQ, Oo HZ, Lam HM, van Kessel KE, et al. Divergent biological response to neoadjuvant chemotherapy in muscle-invasive bladder cancer. *Clin Cancer Res* (2019) 25(16):5082–93. doi: 10.1158/1078-0432.CCR-18-1106

14. Sjödahl G, Abrahamsson J, Holmsten K, Bernardo C, Chebil G, Eriksson P, et al. Different responses to neoadjuvant chemotherapy in urothelial carcinoma molecular subtypes. *Eur Urol* (2021) S0302-2838(21):02138–2. doi: 10.1016/j.eururo.2021.10.035

15. Rebouissou S, Bernard-Pierrot I, de Reyniès A, Lepage ML, Krucker C, Chapeaublanc E, et al. EGFR as a potential therapeutic target for a subset of muscle-invasive bladder cancers presenting a basal-like phenotype. *Sci Transl Med* (2014) 6 (244):244ra91. doi: 10.1126/scitranslmed.3008970

16. Choi W, Czerniak B, Ochoa A, Su X, Siefker-Radtke A, Dinney C, et al. Intrinsic basal and luminal subtypes of muscle-invasive bladder cancer. *Nat Rev Urol* (2014) 11(7):400–10. doi: 10.1038/nrurol.2014.129

17. Seiler R, Ashab HAD, Erho N, van Rhijn BWG, Winters B, Douglas J, et al. Impact of molecular subtypes in muscle-invasive bladder cancer on predicting response and survival after neoadjuvant chemotherapy. *Eur Urol* (2017) 72(4):544–54. doi: 10.1016/j.eururo.2017.03.030

18. Rose M, Maurer A, Wirtz J, Bleilevens A, Waldmann T, Wenz M, et al. EGFR activity addiction facilitates anti-ERBB based combination treatment of

squamous bladder cancer. *Oncogene* (2020) 39(44):6856–70. doi: 10.1038/s41388-020-01465-y

19. Hassler MR, Bray F, Catto JWF, Grollman AP, Hartmann A, Margulis V, et al. Molecular characterization of upper tract urothelial carcinoma in the era of next-generation sequencing: A systematic review of the current literature. *Eur Urol* (2020) 78(2):209–20. doi: 10.1016/j.eururo.2020.05.039

20. Hidalgo M, Amant F, Biankin AV, Budinská E, Byrne AT, Caldas C, et al. Patient-derived xenograft models: an emerging platform for translational cancer research. *Cancer Discov* (2014) 4(9):998–1013. doi: 10.1158/2159-8290.CD-14-0001

21. Yoshida GJ. Applications of patient-derived tumor xenograft models and tumor organoids. *J Hematol OncolJ Hematol Oncol* (2020) 13(1):4. doi: 10.1186/s13045-019-0829-z

22. Pan CX, Zhang H, Tepper CG, yin LT, Davis RR, Keck J, et al. Development and characterization of bladder cancer patient-derived xenografts for molecularly guided targeted therapy. *PLoS One* (2015) 10(8):e0134346. doi: 10.1371/journal.pone.0134346

23. Jäger W, Xue H, Hayashi T, Janssen C, Awrey S, Wyatt AW, et al. Patient-derived bladder cancer xenografts in the preclinical development of novel targeted therapies. *Oncotarget* (2015) 6(25):21522–32. doi: 10.18632/oncotarget.3974

24. Tracey AT, Murray KS, Coleman JA, Kim K. Patient-derived xenograft models in urological malignancies: Urothelial cell carcinoma and renal cell carcinoma. *Cancers* (2020) 12(2):439. doi: 10.3390/cancers12020439

25. Kim K, Hu W, Audenet F, Almassi N, Hanrahan AJ, Murray K, et al. Modeling biological and genetic diversity in upper tract urothelial carcinoma with patient derived xenografts. *Nat Commun* (2020) 11(1):1975. doi: 10.1038/s41467-020-15885-7

26. Rochel N, Krucker C, Coutos-Thévenot L, Osz J, Zhang R, Guyon E, et al. Recurrent activating mutations of PPARγ associated with luminal bladder tumors. *Nat Commun* (2019) 10(1):253. doi: 10.1038/s41467-018-08157-y

27. Damrauer JS, Hoadley KA, Chism DD, Fan C, Tiganelli CJ, Wobker SE, et al. Intrinsic subtypes of high-grade bladder cancer reflect the hallmarks of breast cancer biology. *Proc Natl Acad Sci USA* (2014) 111(8):3110–5. doi: 10.1073/pnas.1318376111

28. Irizarry RA, Hobbs B, Collin F, Beazer-Barclay YD, Antonellis KJ, Scherf U, et al. Exploration, normalization, and summaries of high density oligonucleotide array probe level data. *Biostat Oxf Engl* (2003) 4(2):249–64. doi: 10.1093/biostatistics/4.2.249

29. Dai M, Wang P, Boyd AD, Kostov G, Athey B, Jones EG, et al. Evolving gene/transcript definitions significantly alter the interpretation of GeneChip data. *Nucleic Acids Res* (2005) 33(20):e175. doi: 10.1093/nar/gni179

30. Lachmann A, Giorgi FM, Lopez G, Califano A. ARACNe-AP: gene network reverse engineering through adaptive partitioning inference of mutual information. *Bioinformatics* (2016) 32(14):2233–5. doi: 10.1093/bioinformatics/btw216

31. Love MI, Huber W, Anders S. Moderated estimation of fold change and dispersion for RNA-seq data with DESeq2. *Genome Biol* (2014) 15(12):550. doi: 10.1186/s13059-014-0550-8

32. Alvarez MJ, Shen Y, Giorgi FM, Lachmann A, Ding BB, Ye BH, et al. Functional characterization of somatic mutations in cancer using network-based inference of protein activity. *Nat Genet* (2016) 48(8):838–47. doi: 10.1038/ng.3593

33. Sirab N, Drubay D, Maillé P, Popova T, Ngo C, Gentien D, et al. Multilayer spectrum of intratumoral heterogeneity in basal bladder cancer. *J Pathol* (2022) 256(1):108–18. doi: 10.1002/path.5813

34. Humphrey PA, Moch H, Cubilla AL, Ulbright TM, Reuter VE. The 2016 WHO classification of tumours of the urinary system and Male genital organs-part b: Prostate and bladder tumours. *Eur Urol* (2016) 70(1):106–19. doi: 10.1016/j.eururo.2016.02.028

35. Biton A, Bernard-Pierrot I, Lou Y, Krucker C, Chapeaublanc E, Rubio-Pérez C, et al. Independent component analysis uncovers the landscape of the bladder tumor transcriptome and reveals insights into luminal and basal subtypes. *Cell Rep* (2014) 9(4):1235–45. doi: 10.1016/j.celrep.2014.10.035

36. Halstead AM, Kapadia CD, Bolzenius J, Chu CE, Schriefer A, Wartman LD, et al. Bladder-cancer-associated mutations in RXRA activate peroxisome proliferator-activated receptors to drive urothelial proliferation. *eLife* (2017) 16(6):e30862. doi: 10.7554/eLife.30862

37. Korpal M, Puyang X, Jeremy Wu Z, Seiler R, Furman C, Oo HZ, et al. Evasion of immunosurveillance by genomic alterations of PPARγ/RXRα in bladder cancer. *Nat Commun* (2017) 8(1):103. doi: 10.1038/s41467-017-00147-w

38. Guo CC, Majewski T, Zhang L, Yao H, Bondaruk J, Wang Y, et al. Dysregulation of EMT drives the progression to clinically aggressive sarcomatoid bladder cancer. *Cell Rep* (2019) 27(6):1781–93.e4. doi: 10.1016/j.celrep.2019.04.048

39. Herrera-Abreu MT, Pearson A, Campbell J, Shnyder SD, Knowles MA, Ashworth A, et al. Parallel RNA interference screens identify EGFR activation as an escape mechanism in FGFR3-mutant cancer. *Cancer Discov* (2013) 3(9):1058–71. doi: 10.1158/2159-8290.CD-12-0569

40. Wang L, Šuštić T, Leite de Oliveira R, Lieftink C, Halonen P, van de Ven M, et al. A functional genetic screen identifies the phosphoinositide 3-kinase pathway as a determinant of resistance to fibroblast growth factor receptor inhibitors in FGFR mutant urothelial cell carcinoma. *Eur Urol* (2017) 71(6):858–62. doi: 10.1016/j.eururo.2017.01.021

41. Datta J, Damodaran S, Parks H, Ocrainiciuc C, Miya J, Yu L, et al. Activation mediates acquired resistance to fibroblast growth factor receptor inhibitor BGJ398. *Mol Cancer Ther* (2017) 16(4):614–24. doi: 10.1158/1535-7163.MCT-15-1010

42. Schaefer G, Shao L, Totpal K, Akita RW. Erlotinib directly inhibits HER2 kinase activation and downstream signaling events in intact cells lacking epidermal growth factor receptor expression. *Cancer Res* (2007) 67(3):1228–38. doi: 10.1158/0008-5472.CAN-06-3493

43. Bhimani J, Ball K, Stebbing J. Patient-derived xenograft models–the future of personalised cancer treatment. *Br J Cancer* (2020) 122(5):601–2. doi: 10.1038/s41416-019-0678-0

44. Sfakianos JP, Daza J, Hu Y, Anastos H, Bryant G, Bareja R, et al. Epithelial plasticity can generate multi-lineage phenotypes in human and murine bladder cancers. *Nat Commun* (2020) 11:2540. doi: 10.1038/s41467-020-16162-3

45. Lee SH, Hu W, Matulay JT, Silva MV, Owczarek TB, Kim K, et al. Tumor evolution and drug response in patient-derived organoid models of bladder cancer. *Cell* (2018) 173(2):515–28.e17. doi: 10.1016/j.cell.2018.03.017

46. Kim E, Choi S, Kang B, Kong J, Kim Y, Yoon WH, et al. Creation of bladder assembloids mimicking tissue regeneration and cancer. *Nature* (2020) 588(7839):664–9. doi: 10.1038/s41586-020-3034-x

47. Dagogo-Jack I, Shaw AT. Tumour heterogeneity and resistance to cancer therapies. *Nat Rev Clin Oncol* (2018) 15(2):81–94. doi: 10.1038/nrclinonc.2017.166

48. Koshkin VS, O'Donnell P, Yu EY, Grivas P. Systematic review: Targeting HER2 in bladder cancer. *Bladder Cancer* (2019) 5(1):1–12. doi: 10.3233/BLC-180196

49. Sathe A, Nawroth R. Targeting the PI3K/AKT/mTOR pathway in bladder cancer. *Methods Mol Biol Clifton NJ* (2018) 1655:335–50. doi: 10.1007/978-1-4939-7234-0_23

50. Morel D, Jeffery D, Aspeslagh S, Almouzni G, Postel-Vinay S. Combining epigenetic drugs with other therapies for solid tumours — past lessons and future promise. *Nat Rev Clin Oncol* (2020) 17(2):91–107. doi: 10.1038/s41571-019-0267-4

51. Pruthi RS, Nielsen M, Heathcote S, Wallen EM, Rathmell WK, Godley P, et al. A phase II trial of neoadjuvant erlotinib in patients with muscle-invasive bladder cancer undergoing radical cystectomy: clinical and pathological results. *BJU Int* (2010) 106(3):349–54. doi: 10.1111/j.1464-410X.2009.09101.x

52. Hu H, Piotrowska Z, Hare PJ, Chen H, Mulvey HE, Mayfield A, et al. Three subtypes of lung cancer fibroblasts define distinct therapeutic paradigms. *Cancer Cell* (2021) 39(11):1531–47.e10. doi: 10.1016/j.ccell.2021.09.003

53. Tulchinsky E, Demidov O, Kriajevska M, Barlev NA, Imyanitov E. EMT: A mechanism for escape from EGFR-targeted therapy in lung cancer. *Biochim Biophys Acta BBA - Rev Cancer* (2019) 1871(1):29–39. doi: 10.1016/j.bbcan.2018.10.003

54. Necchi A, Madison R, Pal SK, Ross JS, Agarwal N, Sonpavde G, et al. Comprehensive genomic profiling of upper-tract and bladder urothelial carcinoma. *Eur Urol Focus* (2021). 7(6):1339–46. doi: 10.1016/j.euf.2020.08.001

55. Sfakianos JP, Cha EK, Iyer G, Scott SN, Zabor EC, Shah RH, et al. Genomic characterization of upper tract urothelial carcinoma. *Eur Urol* (2015) 68(6):970–7. doi: 10.1016/j.eururo.2015.07.039

9.3 Discussion et perspectives

Nous avons donc montré ici qu'une combinaison par anti-FGFR et anti-EGFR était efficace in vivo dans les tumeurs *FGFR3*-mutées, et que les tumeurs basales sarcomatoïdes semblaient résistantes aux anti-EGFR *in-vivo*.

Cette combinaison par anti-FGFR et anti-EGFR pourrait donc être testée en clinique. Néanmoins, l'erdafinitib présente en monothérapie une toxicité non négligeable [20], et la combinaison de 2 inhibiteurs de tyrosines kinases est souvent trop toxique en clinique. Une combinaison avec doses diminuées pourrait être envisagée, ou une alternative mais qui serait à confirmer *in vivo* serait de remplacer l'erlotinib par un anticorps monoclonal type cetuximab/panitumumab.

Les anti-EGFR n'ont pas montré une grande efficacité en pratique clinique dans les TVIM métastatiques alors qu'ils ont montré une efficacité dans les tumeurs basales *in vitro* et dans une moindre mesure *in vivo*, confirmée ici dans 2 modèles PDXs [22]. Le rôle du stroma dans cette résistance va être étudié via des modèles organoïdes, comme démontré dans le cancer du poumon avec les fibroblastes associés à la tumeur qui peuvent entrainer une résistance aux anti-EGFR [152].

L'hétérogénéité intra-tumorale est un point crucial dans le développement des cancers et dans la résistance aux traitements, dont le rôle pronostique/prédictif dans le cancer de vessie est encore peu clair. Une étude du laboratoire réalisée en collaboration avec des équipes des hôpitaux Charles Nicolle à Rouen et de l'hôpital Saint-Louis et présentée à l'ESMO2022 de la cohorte VESPER (patients traités pour un TVIM non métastatique par chimiothérapie néoadjuvante[82]), a montré que les tumeurs basales présentaient un risque de rechute tumorale supérieur aux tumeurs luminales. De manière intéressante, en cas de tumeurs hétérogènes au niveau histologique et/ou phénotypique sur le plan luminal/basale, la réalisation d'une classification moléculaire sur ces différentes parties hétérogènes permettait de retrouver dans environ 50% des cas plusieurs sous-types moléculaires chez le même patient. La présence du phénotype basal conférait un mauvais pronostic, quel que soit l'autre contingent associé. Nos données sur les couples PDX/tumeurs d'origine et les données rapportées dans l'étude VESPER ainsi que dans la littérature [80] montrent donc que la classification consensus de 6 sous types est en fait trop restrictive dans 10-30% des tumeurs, qui selon la zone testée peuvent présenter un sous type moléculaire différent. Cela complexifie l'utilisation de cette classification comme biomarqueur en pratique clinique, et nécessite de mieux comprendre cette hétérogénéité, l'évolution de ces contingents ainsi que la plasticité qui peut exister au sein d'une tumeur. Des analyses par transcriptomique spatiale et des analyses de cellules/noyaux uniques vont probablement permettre de mieux comprendre cette hétérogénéité et sa plasticité.

La caractérisation de cette cohorte de PDX va également permettre de tester de nouvelles drogues/combinaisons, dans des situations ou un biomarqueur est potentiellement défini. Par exemple, une validation des résultats observées dans l'**Article 3** avec le birinapant (efficace dans une lignée amplifiée *BIRC2*) est en cours sur des PDXs présentant une altération génomique d'intérêt, et d'autres traitements pourraient être testés, comme un inhibiteur PIK3 en cas de mutation de *PIK3CA,* inhibiteur de MDM2/MDMX dans les PDXs présentant une amplification de *MDM2,* anticorps conjugué ciblant HER2 dans les PDXs mutées ou amplifiées pour *ERBB2*, traitement ciblant l'épigénétique…*).*

10 Biomarqueurs de réponses aux inhibiteurs de points de contrôle immunitaires

10.1 Article 2 : Tertiary lymphoid structures marker CXCL13 is associated with better survival for patients with advanced-stage bladder cancer treated with immunotherapy

10.1.1 Introduction

Suite à la publication d'articles ayant étudié la présence de STL comme biomarqueurs de réponse à l'immunothérapie dans les cancers non urothéliaux [88,153], nous avons décidé d'explorer ce biomarqueur dans la réponse aux IPI dans les cancers urothéliaux dans l'article présenté ci-dessous.

Nous ne disposons pas de cohorte propre à notre équipe et avons décidé d'utiliser les données déjà publiées dans la littérature, soit de patients traités pour un cancer urothélial sans IPI -TCGA et Seiler *et al* [27,101] ou par IPI (atezolizumab) dans l'essai clinique IMVIGOR210 [13].

Du fait de l'absence de données histologiques dans la cohorte de Seiler *et al* et dans l'essai IMVIGOR, nous avons étudié si l'expression de *CXCL13*, cytokine induisant la formation de STL[153], était :

1) Associée à un meilleur pronostic chez les patients traités par atezolizumab.
2) Prédictive de réponse aux IPI et non facteur pronostic en général, en étudiant l'effet pronostic de l'expression de *CXCL13* chez des patients non traités par IPI dans différentes cohortes (TCGA et Seiler *et al*).
3) Associée à la présence de STL en corrélant la présence de STL sur les photographies de lames histologiques du TCGA (cohorte vessie) et l'expression de *CXCL13*.

Ces 3 hypothèses ont bien été vérifiées en analysant les données, et nous avons donc pu montrer que l'expression de *CXCL13*, et donc les STL, sont un biomarqueurs de réponse aux IPI dans les cancers urotheliaux avancés, ce qui a été confirmé dans un article publié la même année [122].

10.1.2 Article

European Journal of Cancer 148 (2021) 181–189

Available online at www.sciencedirect.com

ScienceDirect

journal homepage: www.ejcancer.com

Original Research

Tertiary lymphoid structures marker *CXCL13* is associated with better survival for patients with advanced-stage bladder cancer treated with immunotherapy

Clarice S. Groeneveld [a,b,1], Jacqueline Fontugne [b,c,1], Luc Cabel [b], Isabelle Bernard-Pierrot [b], François Radvanyi [b], Yves Allory [b,c,2], Aurélien de Reyniès [a,*,2]

[a] *Cartes d'Identité des Tumeurs (CIT) Program, Ligue Nationale Contre le Cancer, Paris, France*
[b] *Molecular Oncology, PSL Research University, CNRS, UMR 144, Institut Curie, Equipe Labellisée Ligue Nationale Contre le Cancer, Paris, France*
[c] *Department of Pathology, Institut Curie, Saint-Cloud, France*

Received 23 October 2020; received in revised form 22 December 2020; accepted 29 January 2021
Available online 18 March 2021

KEYWORDS
Bladder cancer;
Immunotherapy;
CXCL13;
Tertiary lymphoid structures;
Response to immunotherapy

Abstract ***Introduction:*** Immune checkpoint inhibitors (ICIs) have proved to be an effective treatment for up to 40% of muscle-invasive bladder cancer (MIBC), but there is still a need for better performing biomarkers allowing to improve prediction of response to ICI. Response to immunotherapy in soft-tissue sarcoma, melanoma and renal cell carcinoma have been recently linked to the presence of tertiary lymphoid structures (TLS) in the tumour. TLS are organised aggregates of T, B and dendritic cells, participating in adaptive antitumor immune response. The chemokine *CXCL13* is involved in the formation of TLS, and is reported as a reliable transcriptomic marker of TLS.

Objectives: In this study, we sought to assess whether *CXCL13* transcript expression can be a prognostic biomarker for ICI-treated MIBC patients and also investigated whether it can serve a biomarker of TLS in MIBC.

Methods: We analysed transcriptomic data from three publicly available MIBC cohorts and evaluated pathological slides from the TCGA-BLCA cohort for TLS presence and stage of maturation.

Results: We showed that *CXCL13* was independently associated with both prolonged survival (HR = 0.8, 95% CI [0.68–0.94]) and objective response ($p < 0.0001$) in patients treated with

---

* *Corresponding author*: Ligue Nationale Contre le Cancer, 14 rue Corvisart, 75013, Paris, France.
E-mail address: aurelien.dereynies@ligue-cancer.net (A. de Reyniès).

[1] These authors contributed equally to this work. [2] These authors contributed equally to this work.

https://doi.org/10.1016/j.ejca.2021.01.036

ICI, at the difference of others immunological signatures. However, it was not a predictor for non−ICI-treated MIBC, suggesting a predictive effect of ICI efficacy. Finally, we validated that *CXCL13* expression was correlated with tumour TLS in TCGA data set ($p < 0.001$), and can serve as a marker of TLS in bladder cancer.

Conclusion: These results support that *CXCL13* expression, as a surrogate for tumour TLS, is a relevant candidate predictive biomarker of response to ICI for patients with advanced-stage bladder cancer.

1. Introduction

Immune checkpoint inhibitors (ICIs) have recently demonstrated efficacy in localized and metastatic muscle-invasive bladder cancer (MIBC). Although promising results have been achieved using ICI, 60−85% of patients do not respond. Currently, PD-L1 expression is the main predictive biomarker identified for ICI. The investigators of the IMvigor210 trial [1] carried out an extensive search for predictive biomarkers of ICI in bladder cancer, and proposed TGF-β and Tumor Mutational Burden (TMB) in the metastatic setting. Recently, immune infiltration and interferon signatures were suggested as predictive biomarkers of response to ICI in the neoadjuvant setting [2]. However, identification of new biomarkers that improve prediction of response to ICI in MIBC is still needed.

Organized lymphocyte aggregates known as tertiary lymphoid structures (TLS) can form in various tissues in response to chronic inflammation, including in cancer. *CXCL13,* a B cell chemoattractant*,* is one of the major chemokines involved in TLS formation [3]. The presence of TLS in tumours is associated with favourable prognosis in many tumour types, and has recently been shown to promote immunotherapy response in melanoma, soft-tissue sarcoma and renal cell carcinoma [4−6]. In bladder cancer, TLS have been reported to be more common in MIBCs than in early-stage tumours [7].

As *CXCL13* is a predictive marker in other ICI-responsive tumour types, our main aim was to assess whether *CXCL13* expression would also be predictive of ICI response in bladder cancer after controlling for known predictive factors through multivariate modelling. We tested this hypothesis in the IMvigor210 cohort of advanced-stage urothelial carcinoma patients treated with atezolizumab, an anti−PD-L1 monoclonal antibody (n = 348) [1]. We also tested the prognostic value of CXCL13 expression in two ICI-naïve cohorts, TCGA-BLCA (non-metastatic all MIBC, n = 408) [8] and the Seiler neoadjuvant chemotherapy-treated cohort (non-metastatic all MIBC, n = 305) [9]. We then validated the correlation of *CXCL13* expression with the presence of TLS in tumours, through TLS histological assessment in the TCGA-BLCA MIBC cohort.

2. Material and methods

2.1. Cohort gene expression and clinical data

We used the RNA-seq gene expression and clinical data for IMvigor210, available from the IMvigor210CoreBiologies R package (v. 1.0.0), available at http://research-pub.gene.com/IMvigor210CoreBiologies/.de We used the provided normalized counts.

We downloaded TCGA RNA-seq data and updated clinical annotation, from the Genomic Data Commons using the R package TCGAbiolinks (v. 2.14.1) as HTSeq—counts for all primary solid tumours. We then upper-quartile normalized the counts and applied a $\log_2$-transformation.

Finally, we obtained microarray gene expression data (Affymetrix Human Exon 1.0 ST Array) from formalin-fixed, paraffin-embedded (FFPE) samples for the Seiler cohort from Gene Expression Omnibus (GSE87304) using the GEOquery R package (v. 2.54.1), re-processed the CEL files using the frma R package (v. 1.40.0), annotated using R package ensembldb (v. 2.12.1, Ensembl 99) and applied a $\log_2$-transformation.

2.2. Classification and signature scores

In each data set, we then classified the samples in the consensus, UNC and Lund subtypes using R packages consensusMIBC (v. 1.1.0, https://github.com/cit-bioinfo/consensusMIBC) and BLCAsubtyping (v. 2.1.1, https://github.com/cit-bioinfo/BLCAsubtyping). We then applied MCPcounter (v. 1.1.0, https://github.com/ebecht/MCPcounter) to estimate infiltration by different immune populations. We calculated scores for immune and bladder-related signatures (Supplementary Table 3) by centring the mean gene expression of signature genes.

2.3. Association of *CXCL13* expression with other variables

We performed Wilcoxon or Kruskal–Wallis tests to associate *CXCL13* expression with categorical variables (2 or more than 2, respectively), and reported Spearman correlation coefficients (rho) for any comparison of two continuous variables. All analyses were conducted using R version 3.6.3.

2.4. Survival models

For the Kaplan–Meier survival curves, we discretized the expression values of *CXCL13* using the arules R package (v. 1.6–5) and plot the curves using R package survminer (v. 0.4.6).

We assessed prognostic clinical variables available in the cohort data, transcriptomic signatures that have been previously established as prognostic, and other transcriptomic signatures of immune populations or immune signalling as well as *CXCL13* expression in univariate models. All used signatures are reported in Supplementary Table 4.

To find the reported multivariate model, we selected all investigated features that were significant to $p < 0.05$ in the univariate models (13 variables) and fit a multivariate Cox model. Then, we performed model selection using the stepwise akaike information criterion (AIC) model implemented in the MASS R package (v. 7.3–51.3) using default parameters to obtain the final reported multivariate Cox model.

We implemented a similar procedure for building the multivariate Cox model for the TCGA cohort, but kept only one when two high collinear variables were significant for the entry to the stepwise AIC.

2.5. Histological evaluation of TLS and lymphocytic tumour infiltration in TCGA H&E slides

TCGA H&E-stained slides were reviewed by a genitourinary pathologist using the Cancer Digital Slide Archive platform. Slides from both frozen and FFPE material were assessed when available.

Koti *et al.* previously confirmed that TLS in bladder cancer comprised all stages of maturation. We thus used a published scale to count all forms of TLS as follows: 1) lymphocyte aggregates (Agg), defined by ill-defined clusters of lymphocytes, 2) primary follicles (FL1), well defined round- or oval-shaped clusters of lymphocytes or plasma cells without a germinal centre and 3) secondary follicles (FL2), with a formed germinal centre [11]. The absolute number of TLS was determined within the tumour borders and at its immediate periphery.

To ensure we included samples with FL2 and a wide-range of *CXCL13* expression, we selected 100 samples from TCGA, consisting of 25 samples with the highest *CXCL13* expression; 25 samples with the lowest *CXCL13* expression; and 50 other random samples (quartile balanced, i.e. 12 samples from the highest and lowest quartile, having excluded the 50 highest and lowest, and 13 samples from the two middle quartiles).

Non-invasive tumour components, areas of necrosis, coagulation artifacts or tumour resection sites with giant cell reaction were excluded from the histological analysis.

3. Results

3.1. Association between CXCL13 and patient characteristics in IMvigor210 (atezolizumab in advanced MIBC)

We first evaluated how CXCL13 expression was related to other available clinical variables in IMvigor210 (Table 1). We found that CXCL13 expression did not differ with sex, race or tobacco use history, but was higher in patients with lymph node infiltration alone when compared to visceral and liver metastases

Table 1
Association between CXCL13 expression and clinico-biological characteristics.

Variable	n	CXCL13 expression (centred) median	P-value
Sex			
Female	76	−0.006	0.56
Male	272	0.14	
Tobacco use history			
Never	116	0.049	0.69
Previous	197	0.14	
Current	35	0.16	
Metastatic disease			
Lymph nodes only	60	0.700	<0.0001
Visceral (without liver)	158	−0.092	
Liver	98	0.10	
Baseline ECOG score			
0	134	0.18	0.71
1	196	0.10	
2	18	0.29	
PD-L1 IC Level			
IC0	97	−0.68	<0.0001
IC1	132	0.064	
IC2+	118	0.65	
PD-L1 TC Level			
TC0	275	−0.014	<0.0001
TC1	22	0.39	
TC2+	50	0.60	
Tissue			
Bladder	195	0.107	0.0003
Kidney	67	0.046	
Ureter	26	0.048	
Lymph node	26	0.954	
Lung	10	−0.305	
Liver	5	−1.126	
Other	11	0.141	

ECOG, Eastern Cooperative Oncology Group; IC, tumour-infiltrating immune cells; TC, tumour cells.

($p < 0.001$). Unsurprisingly, *CXCL13* expression was higher in metastases taken from lymph nodes and lower in samples taken from liver metastases than in other tumours in the cohort ($p < 0.001$).

3.2. CXCL13 is predictive of survival and differs between responders and non-responders to ICI treatment

Higher *CXCL13* expression was associated with better prognosis in IMvigor210 series (log-rank $p = 0.0018$; Fig. 1A), independently from *CD8A, PD-L1,* but better with higher expression of B-cell marker *CD19* expression (Supplementary Fig. 1A–C). It continued to be highly associated with survival even after removing samples that metastasised to the lymph node (log-rank $p < 0.001$, Supplementary Fig. 1D). For a more complete model of survival in IMvigor210, we first fit univariate Cox models for all commonly used biomarkers of ICI response, those reported by Mariathasan *et al.* [1] (Supplementary Table 1) as well as common MIBC mutations including *ARID1A*, which has been reported in conjunction with *CXCL13* to be predictive [10]. We then selected all factors that were significantly predictive of survival in the univariate setting to build a multivariate Cox model using a stepwise AIC feature selection procedure. *CXCL13* expression remained in the model (hazard ratio [HR] = 0.8, 95% confidence interval [CI; 0.68–0.94])—together with baseline Eastern Cooperative Oncology Group score, TMB and metastatic disease status and TGF-β— while features such as INF-ɣ signature and *CD8* and *PD-L1* expressing tumour-infiltrating immune/tumour cells (IC/TC) and *ARID1A* mutation were dropped (Fig. 1B). This evidence shows that *CXCL13* was a stronger predictor of survival in this cohort than many previously reported markers.

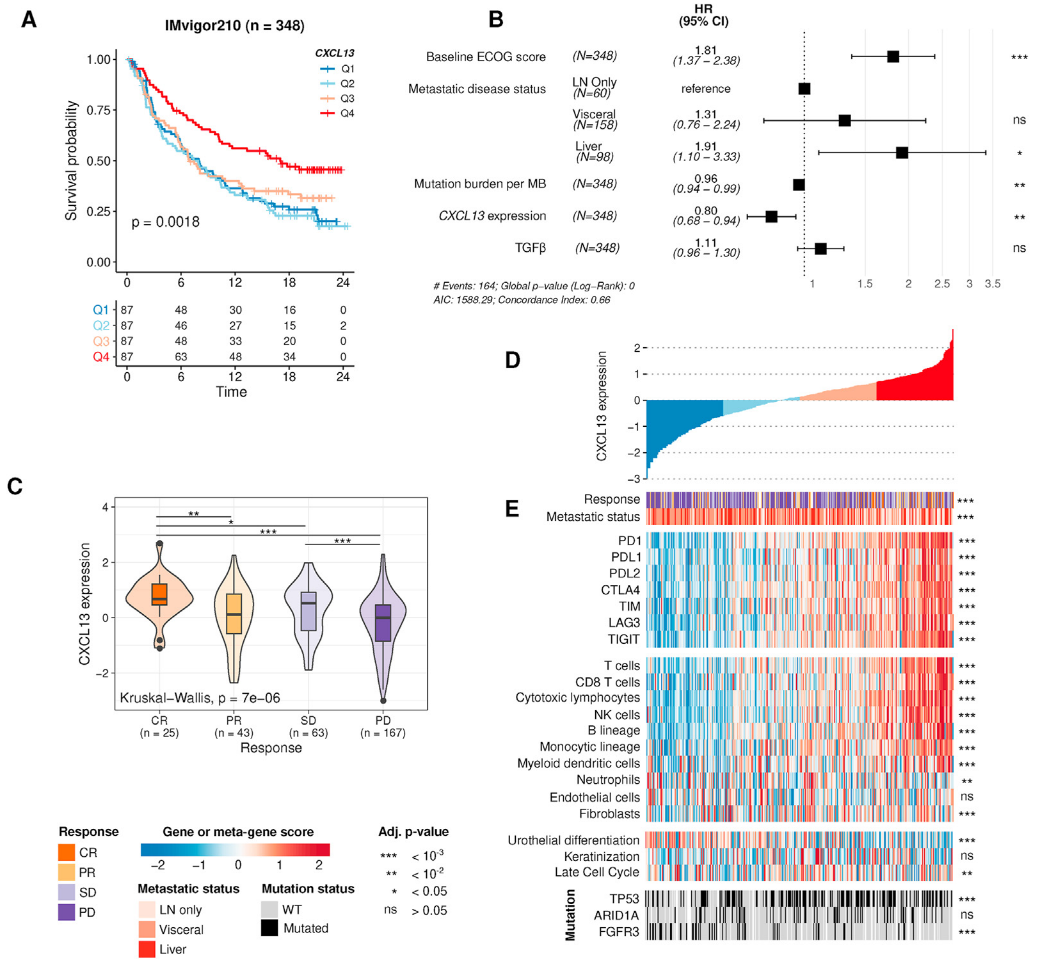

Fig. 1. Assessment of *CXCL13* expression in IMvigor210. (A) Kaplan–Meier curve for overall survival (OS) of *CXCL13* quartiles, showing better survival for patients with high levels of *CXCL13*. (B) Forest plot of a multivariate Cox model for OS considering the main predictors found in the univariate Cox analyses selected algorithmically using a stepwise AIC feature selection procedure. (C) Association of *CXCL13* expression with atezolizumab response, showing higher expression of CXCL13 in complete responders. (D) Distribution of *CXCL13* expression, ordering the cohort. (E) Expression of checkpoint inhibitors, quantification of immune populations, bladder cancer signature scores and the mutations of *TP53, ARID1A* and *FGFR3*, ordered by increasing *CXCL13* expression. ECOG, Eastern Cooperative Oncology Group.

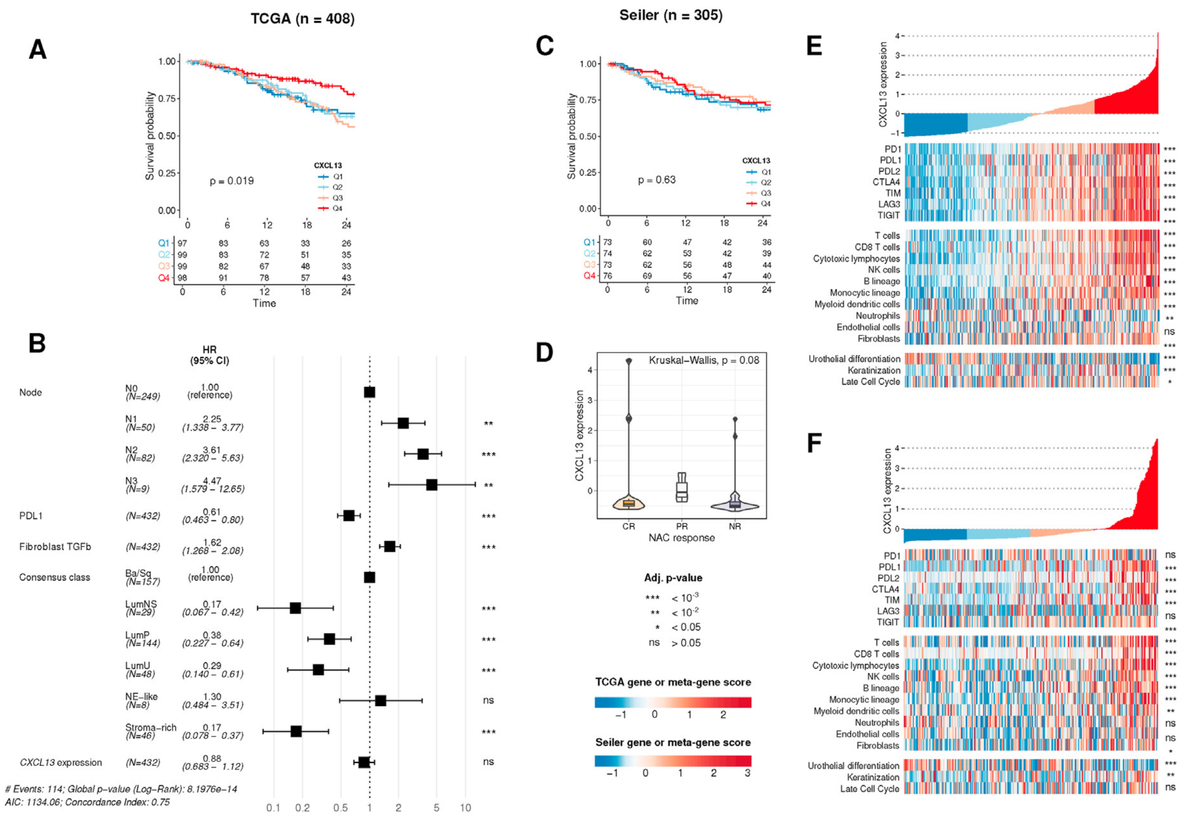

Fig. 2. Assessment of survival using CXCL13 expression in TCGA and Seiler cohorts. (A) Kaplan–Meier curve for specific OS stratified by *CXCL13* expression in TCGA-BLCA. (B) Forest plot of Cox multivariate model for specific OS in TCGA-BLCA, showing that CXCL13 is not significant when considering other markers in this cohort. (C) Kaplan–Meier curve for OS stratified by *CXCL13* expression in the Seiler cohort. (D) Association of neoadjuvant chemotherapy response and *CXCL13* expression in the Seiler cohort. Association of *CXCL13* expression with checkpoint inhibitor, immune population signatures and bladder cancer signature scores in (E) TCGA-BLCA and (F) Seiler cohorts.

After establishing an association between *CXCL13* expression and survival after ICI, we sought to determine whether it was also associated with response. *CXCL13* expression was significantly higher in atezolizumab responders than non-responders ($p < 0.001$), and was highest for complete responders (Fig. 1C, $p < 0.05$ in all tests). *CXCL13* expression was significantly correlated with the expression of all immune checkpoint genes and with the presence of all estimated immune and stromal cell populations, except for endothelial cells, and was negatively correlated with urothelial differentiation (Fig. 1D and E).

3.3. *CXCL13 expression is not a strong predictor of survival for patients not treated with ICI*

To determine whether the association of *CXCL13* expression with better prognosis was specific to ICI-treated patients, we then tested the association of *CXCL13* expression with survival in the ICI-naïve TCGA-BLCA cohort and the neoadjuvant chemotherapy-treated Seiler cohort. Higher *CXCL13* expression was associated with better survival in the TCGA-BLCA cohort in the Kaplan–Meier curve and univariate Cox model, but not in a multivariate model considering established prognostic factors (HR = 0.88, 95% CI [0.68–1.12]) (Fig. 2A and B). In the Seiler cohort, there was no association between *CXCL13* expression and survival ($p = 0.63$; Fig. 2C), and there was no difference in *CXCL13* expression between responders and non-responders to neoadjuvant chemotherapy ($p = 0.08$; Supplementary Fig. 2D). Overall, we observed that *CXCL13* expression was similarly correlated to expression of immune checkpoint genes and immune population signatures in both TCGA and Seiler cohorts (Fig. 2E and F).

3.4. *CXCL13 expression serves as a transcriptomic biomarker of tumour TLS*

We investigated whether the gene expression of *CXCL13* could serve as a transcriptomic surrogate of histologically identified TLS in bladder cancer, as previously described in other cancers [3]. We selected

100 samples from the TCGA cohort with varying *CXCL13* expression for histological evaluation of TLS (Supplementary Table 2, Methods). We counted TLS at all stages of maturation: lymphocyte aggregates (Agg), primary follicles (FL1) and secondary follicles (FL2) (Fig. 3A–C; Supplementary Table 2). TLS histological evaluation was performed in frozen sections, from which gene expression was acquired, blind to *CXCL13* expression level. We classified the samples as TLS+ when they contained at least 1 count of Agg, FL1 or FL2, and TLS− otherwise, as proposed by Calderaro *et al.* [11]. We found a positive correlation ($\rho = 0.4$, $p < 0.001$) between *CXCL13* expression and TLS (Fig. 3D). The presence of TLS at any stage of maturation was associated with higher *CXCL13* expression, supporting the use of *CXCL13* as a surrogate marker of TLS formation in bladder cancer (Fig. 3G and H; Area Under the ROC (Receiver Operating Charateristic) Curve (*AUC*) = 0.9 for FL2+, and 0.75 for TLS+).

3.5. *CXCL13 expression correlates with other signatures of TLS*

Starting from the initial survival analysis, we also evaluated three other TLS signatures [3]. Although the $T_{(FH)}$ cell signature was also predictive of survival in univariate models, *CXCL13* expression alone was a better predictor. All three signatures were strongly correlated with *CXCL13* (Fig. 4A), as well as also to immune population signatures (Fig. 4B). Considering TLS identified in our pathological analysis, all TLS signatures were similarly correlated with TLS presence (Fig. 4C), and all signature scores were higher for TLS+ and specifically FL2+ patients (Fig. 4D–F).

3.6. *CXCL13 expression and tumour TLS are associated with molecular subtypes of bladder cancer*

As molecular subtypes have previously been studied as features to predict immunotherapy [1], we investigated

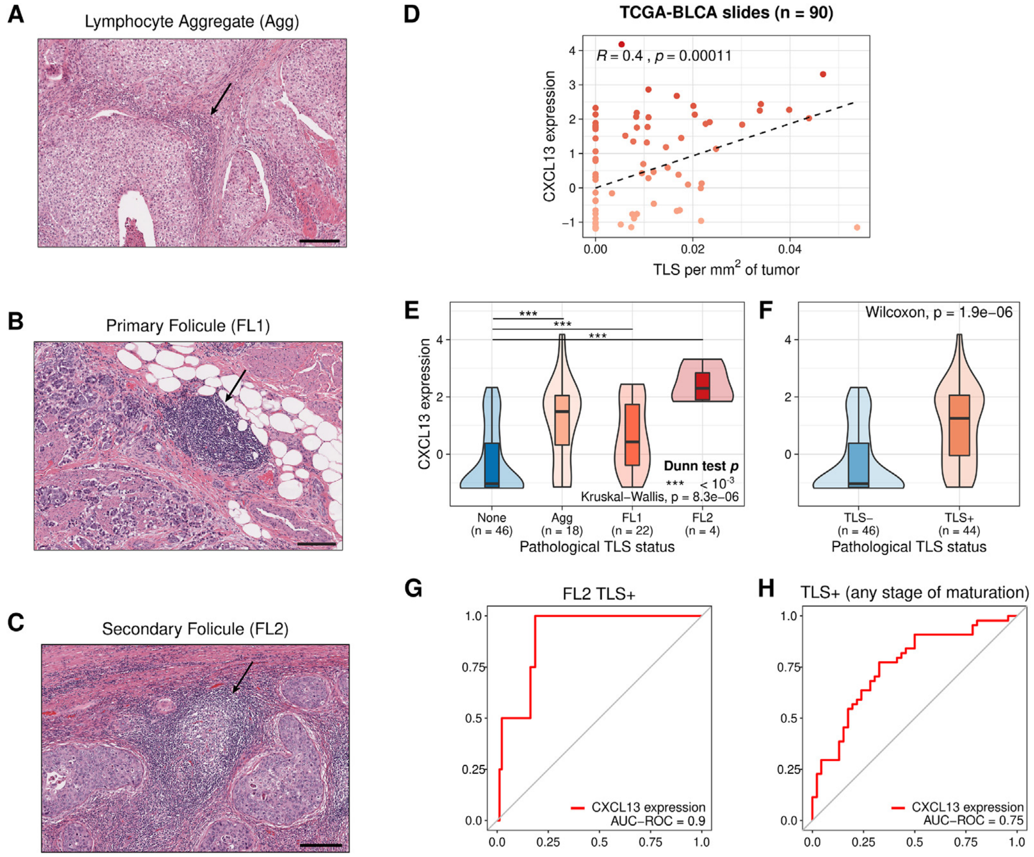

Fig. 3. Histological evaluation of TLS in the TCGA-BLCA cohort. Representative images of TLS in H&E-stained corresponding formalin-fixed, paraffin-embedded (FFPE) slides of the TCGA cohort, presenting as a (A) lymphocyte aggregate (Agg) (B) primary follicle (FL1) and (C) secondary follicle with germinal centre (FL2); scale bars: 200 μm, arrows point to TLS. (D) Correlation between *CXCL13* expression and TLS density (measured as TLS count per mm^2 of tumour), showing that higher TLS density correlates with higher CXCL13 expression. (E) Association of *CXCL13* expression with pathological TLS at each stage of maturation or (F) TLS presence or absence. Tumours with mature TLS (FL2) have higher overall levels of *CXCL13*. ROC curves for predicting TLS in slides from *CXCL13* expression for (G) FL2+ and (H) TLS+ at any stage of maturation. *CXCL13* expression can predict presence TLS, but especially FL2 TLS (AUC-ROC = 0.9). CI, confidence interval; HR, hazard ratio; TLS, tertiary lymphoid structures.

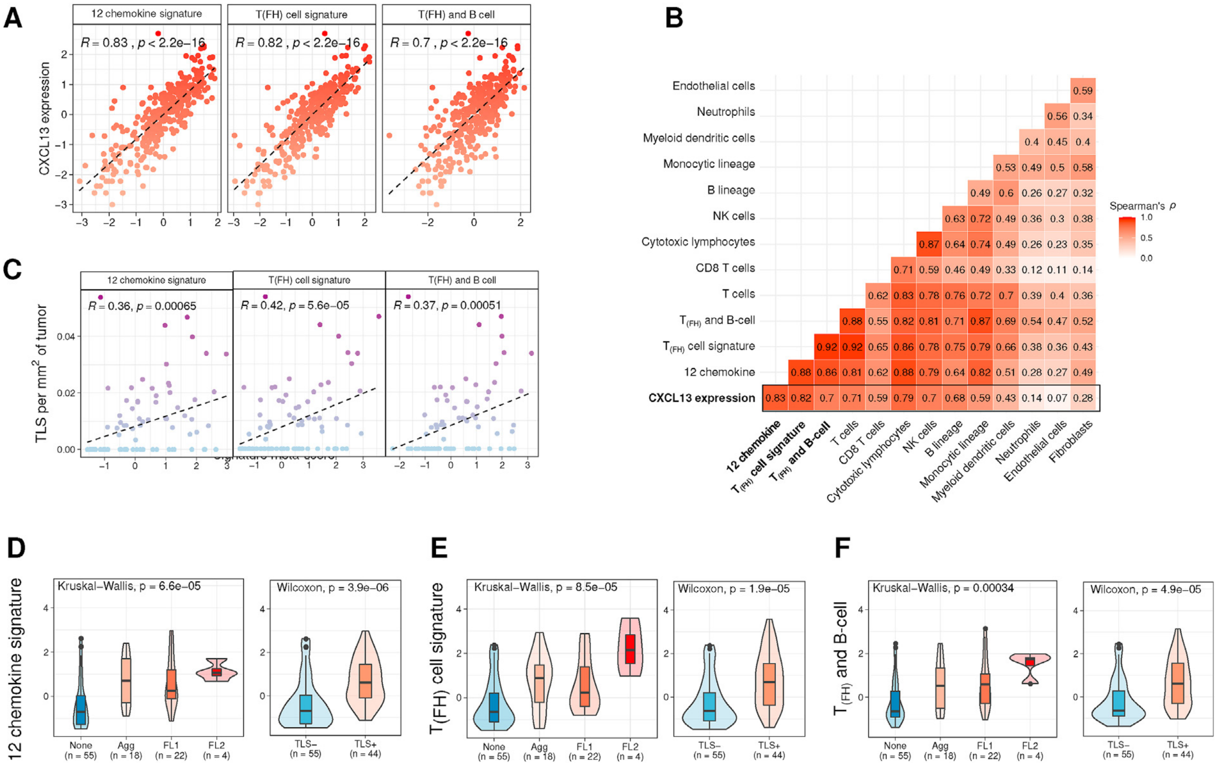

Fig. 4. Signatures of tertiary lymphoid structures. (A) Three other TLS signatures are highly correlated with CXCL13 expression. (B) Correlation matrix of TLS signatures to immune population signatures from MCPcounter. (C) All TLS signatures are significantly correlated with identified TLS per area in the TCGA cohort H&E slides. (D) TLS+ patients have higher signature scores for all TLS signatures.

CXCL13 expression and TLS in relation to molecular subtypes using the consensus [12] classification scheme. As expected, *CXCL13* expression differed between subtypes in all three cohorts (Supplementary Fig. 2A). TLS counts determined in the TCGA cohort were also significantly different between consensus subtypes (Fisher's exact test; $p = 0.01$), where there were more TLS+ samples in stroma-rich, Ba/Sq and LumNS subtypes. Notably, FL2 were only identified in slides from stroma-rich and Ba/Sq tumours (Supplementary Fig. 2B).

4. Discussion

Treatment for bladder cancer patients with advanced-stage disease, especially those who were non-responders to cisplatin-based chemotherapy, had remained stagnant for decades before the advent of immunotherapies. Response rates to ICI for these patients, although encouraging, can still be maximized by the identification and application of context-dependent specific biomarkers [13].

We believe that our results, however preliminary, indicate that *CXCL13* expression is a prognostic biomarker in the advanced-stage setting for ICI-treated MIBC patients. We found that it outperformed commonly used ICI response markers such as PD-L1 expression [1], INF-ɣ [2] and tGE8 [13] even in unsupervised multivariate survival models for the IMvigor210 cohort. Importantly, even if *CXCL13* expression was associated with loco-regional lymph-node infiltration (*LN* only), it was still prognostic when controlling for this clinical variable. *CXCL13* in combination with *ARID1A* mutation has been recently identified as a prognostic marker for ICI response by Goswami *et al.* [10]. To account for these results, we added *ARID1A* mutation to our list of possible biomarkers. Although we found that *ARID1A* mutation was predictive of survival on its own, it was not significant in the multivariate model when accounting for other covariates. These results do not discard the use of combined *ARID1A* mutation and *CXCL13* expression as indicative of better prognosis, but point towards *CXCL13* expression alone being more robust.

CXCL13 is secreted by lymphocytes and stromal cells to recruit lymphoid tissue inducer cells, and has been directly implicated in the formation of TLS at the inflammation site [14]. It is also an important chemokine controlling B-cell trafficking in secondary lymphoid organs, which traditionally have been described as the sites where adaptive immune anti-tumour responses occur [3]. Indeed, PD-L1 inhibition in tumour draining lymph nodes can lead to anti-tumour response by seeding the tumour with activated T-cells [15]. TLS can play a similar role at the tumour site—be a proximal environment where dendritic cells can present tumour antigens to activate T and B cells, resulting in generation of T_h, cytotoxic T, memory B and even antibody-producing plasma cells [3,16,17].

Although we also tested more complex signatures of TLS that have been used in other contexts [3,18–20], we found that expression of this single gene marker was the best prognostic marker, and performed better or almost identically to the multi-gene signatures as a surrogate for TLS in bladder. In addition, there is a significant advantage to using a single gene marker over a transcriptomic signature, as it can also be more easily quantified by techniques such as RT-PCR and immunohistochemistry, which need to be evaluated in this context. As biomarkers of ICI response can be specific to a setting, such as INF-ɣ being predictive in the neoadjuvant PURE-01 trial but not in IMvigor210 in our analysis, the utility of *CXCL13* as a biomarker in the neoadjuvant setting should also be evaluated.

We then determined that *CXCL13* expression was correlated with the presence of TLS in the tumour, as evaluated on haematoxylin and eosin (H&E) stains. We acknowledge here that the lack of *in situ* techniques to identify typical markers of TLS, is a limitation of our study. However, although *in situ* techniques may be crucial to confirm that some less mature lymphocytic aggregates are true TLS, the identification of a lymphoid aggregate with a germinal centre (FL2) undoubtedly corresponds to a true TLS and is readily identifiable on an H&E stain alone. In addition, previous studies have reported a strong correlation between lymphoid aggregates identified on H&E alone and the corresponding validation using typical immunohistochemical markers of TLS [7,21]. However, others suggest that the true number of TLS is underestimated on morphological H&E assessment alone [22]. Finally, exploring the role of histological evaluation of TLS—including with *in situ* techniques and estimating factors such as number, type, localization—as a prognostic or predictive biomarker for ICI-treated bladder cancer patients will require further studies.

Recently, Gao *et al.* found that histological evaluation of TLS was a biomarker of response to combination therapy with PD-L1 and CTLA-4 inhibitors in patients with localized MIBC [23], supporting TLS assessment as a biomarker in the neoadjuvant setting. The NABUCCO trial [24], using a combination of PD-1 and CTLA-4 inhibitors, had contradictory findings regarding TLS. Baseline TLS presence was not associated with response, but immature TLS were in fact associated with non-complete response. Conversely, complete responders had an enrichment in TLS on-treatment. This indicates that the formation of TLS during treatment itself can be beneficial. Also, it could mean that lymphoid aggregates, that is immature TLS, could release inhibitory/immunosuppressive molecules such as TGFb, as previously reported in hepatocellular carcinoma [25]. On the contrary, FL2 TLS are expected to provide the best anti-tumour response, and we have found that tumours presenting FL2 TLS have the highest expression of *CXCL13*.

We propose that the bladder cancer community considers the inclusion of *CXCL13* expression and histological evaluation of TLS as features to be assessed for future and ongoing immunotherapy clinical trials.

Author statement

Clarice S. Groeneveld had full access to all the data in the study and takes responsibility for the integrity of the data and the accuracy of the data analysis.

Clarice S. Groeneveld: Conceptualization, Data curation, Formal analysis, Methodology, Visualization, Writing original draft, Writing review & editing; **Jacqueline Fontugne:** Conceptualization, Data Curation, Formal analysis, Methodology, Visualization, Writing original draft, Writing review & editing; **Luc Cabel:** Conceptualization, Methodology, Writing review & editing; **Isabelle Bernard-Pierrot:** Conceptualization, Supervision, Writing review & editing; **François Radvanyi:** Conceptualization, Supervision, Writing review & editing; **Yves Allory:** Conceptualization, Methodology, Supervision, Writing review & editing; **Aurélien de Reyniès:** Conceptualization, Methodology, Supervision, Writing review & editing.

Data availability

IMvigor210—http://research-pub.gene.com/IMvigor210CoreBiologies/

TCGA-BLCA—GDC via TCGAbiolinks R package or from Xena Browser (https://gdc.xenahubs.net/download/TCGA-BLCA.htseq_counts.tsv.gz).

Seiler—GEO Accession GSE87304.

TCGA-BLCA H&E slides—https://cancer.digitalslidearchive.org/

Conflict of interest statement

The authors declare that they have no known competing financial interests or personal relationships that could have appeared to influence the work reported in this paper.

Acknowledgements

This work was supported by a grant from *Ligue Nationale Contre le Cancer* (JF, LC, YA, FR, IBP) as an associated team (*Equipe labellisée*), the "*Carte d'Identité des Tumeurs*" program initiated, developed and funded by *Ligue Nationale Contre le Cancer*. In addition, CSG was supported by the PRT-K BoBCaT grant from the

Institut National du Cancer, JF was supported by the *Fondation ARC pour la recherche sur le cancer* and LC was supported by the *Fondation pour la Recherche Médicale.*

Appendix A. Supplementary data

Supplementary data to this article can be found online at https://doi.org/10.1016/j.ejca.2021.01.036.

References

[1] Mariathasan S, Turley SJ, Nickles D, et al. TGFβ attenuates tumour response to PD-L1 blockade by contributing to exclusion of T cells. Nature 2018;554(7693):544–8. https://doi.org/10.1038/nature25501.

[2] Necchi A, Raggi D, Gallina A, et al. Impact of molecular subtyping and immune infiltration on pathological response and outcome following neoadjuvant pembrolizumab in muscle-invasive bladder cancer. Eur Urol 2020:1–10. https://doi.org/10.1016/j.eururo.2020.02.028.

[3] Sautès-Fridman C, Petitprez F, Calderaro J, Fridman WH. Tertiary lymphoid structures in the era of cancer immunotherapy. Nat Rev Canc 2019;19(6):307–25. https://doi.org/10.1038/s41568-019-0144-6.

[4] Cabrita R, Lauss M, Sanna A, et al. Tertiary lymphoid structures improve immunotherapy and survival in melanoma. Nature 2020; 577(February 2019). https://doi.org/10.1038/s41586-019-1914-8.

[5] Petitprez F, de Reynies A, Keung EZ, et al. B cells are associated with survival and immunotherapy response in sarcoma. Nature 2020;577(January):556–60. https://doi.org/10.1038/s41586-019-1906-8.

[6] Helmink BA, Reddy SM, Gao J, et al. B cells and tertiary lymphoid structures promote immunotherapy response. Nature 2020;577(7791):549–55. https://doi.org/10.1038/s41586-019-1922-8.

[7] Koti M, Xu AS, Ren KYM, et al. Tertiary lymphoid structures associate with tumour stage in urothelial bladder cancer. Bladder Cancer 2017;3(4):259–67. https://doi.org/10.3233/BLC-170120.

[8] Robertson AG, Kim J, Al-Ahmadie H, et al. Comprehensive molecular characterization of muscle-invasive bladder cancer. Cell 2017;171(3):540–56. https://doi.org/10.1016/J.CELL.2017.09.007. e25.

[9] Seiler R, Ashab HAD, Erho N, et al. Impact of molecular subtypes in muscle-invasive bladder cancer on predicting response and survival after neoadjuvant chemotherapy. Eur Urol 2017; 72(4):544–54. https://doi.org/10.1016/j.eururo.2017.03.030.

[10] Goswami S, Chen Y, Anandhan S, et al. *ARID1A* mutation plus *CXCL13* expression act as combinatorial biomarkers to predict responses to immune checkpoint therapy in mUCC. Sci Transl Med 2020;12(548). https://doi.org/10.1126/scitranslmed.abc4220.

[11] Calderaro J, Petitprez F, Becht E, et al. Intra-tumoral tertiary lymphoid structures are associated with a low risk of early recurrence of hepatocellular carcinoma. J Hepatol 2019;70(1): 58–65. https://doi.org/10.1016/j.jhep.2018.09.003.

[12] Kamoun A, Reyniès A de, Allory Y, et al. A consensus molecular classification of muscle-invasive bladder cancer. Eur Urol 2020; 77(4). https://doi.org/10.1016/j.eururo.2019.09.006.

[13] Powles T, Kockx M, Rodriguez-Vida A, et al. Clinical efficacy and biomarker analysis of neoadjuvant atezolizumab in operable urothelial carcinoma in the ABACUS trial. Nat Med 2019;25(11): 1706–14. https://doi.org/10.1038/s41591-019-0628-7.

[14] Meier D, Bornmann C, Chappaz S, et al. Ectopic lymphoid-organ development occurs through interleukin 7-mediated enhanced survival of lymphoid-tissue-inducer cells. Immunity 2007;26(5): 643–54. https://doi.org/10.1016/j.immuni.2007.04.009.

[15] Dammeijer F, van Gulijk M, Mulder EE, et al. The PD-1/PD-L1-checkpoint restrains T cell immunity in tumor-draining lymph nodes. Canc Cell 2020;38(5):685–700. https://doi.org/10.1016/j.ccell.2020.09.001. e8.

[16] Goc J, Germain C, Vo-Bourgais TKD, et al. Dendritic cells in tumor-associated tertiary lymphoid structures signal a Th1 cytotoxic immune contexture and license the positive prognostic value of infiltrating CD8+T cells. Canc Res 2014;74:705–15. https://doi.org/10.1158/0008-5472.CAN-13-1342.

[17] Kroeger DR, Milne K, Nelson BH. Tumor-infiltrating plasma cells are associated with tertiary lymphoid structures, cytolytic T-cell responses, and superior prognosis in ovarian cancer. Clin Canc Res 2016;22:3005–15. https://doi.org/10.1158/1078-0432.CCR-15-2762.

[18] Coppola D, Nebozhyn M, Khalil F, et al. Unique ectopic lymph node-like structures present in human primary colorectal carcinoma are identified by immune gene array profiling. Am J Pathol 2011;179(1):37–45. https://doi.org/10.1016/j.ajpath.2011.03.007.

[19] Messina JL, Fenstermacher DA, Eschrich S, et al. 12-chemokine gene signature identifies lymph node-like structures in melanoma: potential for patient selection for immunotherapy? Sci Rep 2012;2(1):1–6. https://doi.org/10.1038/srep00765.

[20] Hennequin A, Derangère V, Boidot R, et al. Tumor infiltration by Tbet+ effector T cells and CD20+ B cells is associated with survival in gastric cancer patients. OncoImmunology 2016;5:2. https://doi.org/10.1080/2162402X.2015.1054598.

[21] He W, Zhang D, Liu H, et al. The high level of tertiary lymphoid structure is correlated with superior survival in patients with advanced gastric cancer. Front Oncol 2020;10:980. https://doi.org/10.3389/fonc.2020.00980.

[22] Buisseret L, Desmedt C, Garaud S, et al. Reliability of tumor-infiltrating lymphocyte and tertiary lymphoid structure assessment in human breast cancer. Mod Pathol 2017;30(9):1204–12. https://doi.org/10.1038/modpathol.2017.43.

[23] Gao J, Navai N, Alhalabi O, et al. Neoadjuvant PD-L1 plus CTLA-4 blockade in patients with cisplatin-ineligible operable high-risk urothelial carcinoma. Nat Med 2020;26(12). https://doi.org/10.1038/s41591-020-1086-y.

[24] van Dijk N, Gil-Jimenez A, Silina K, et al. Preoperative ipilimumab plus nivolumab in locoregionally advanced urothelial cancer: the NABUCCO trial. Nat Med 2020. https://doi.org/10.1038/s41591-020-1085-z.

[25] Meylan M, Petitprez F, Lacroix L, et al. Early hepatic lesions display immature tertiary lymphoid structures and show elevated expression of immune inhibitory and immunosuppressive molecules. Clin Canc Res 2020;26(16). https://doi.org/10.1158/1078-0432.ccr-19-2929. clincanres.2929.2019.

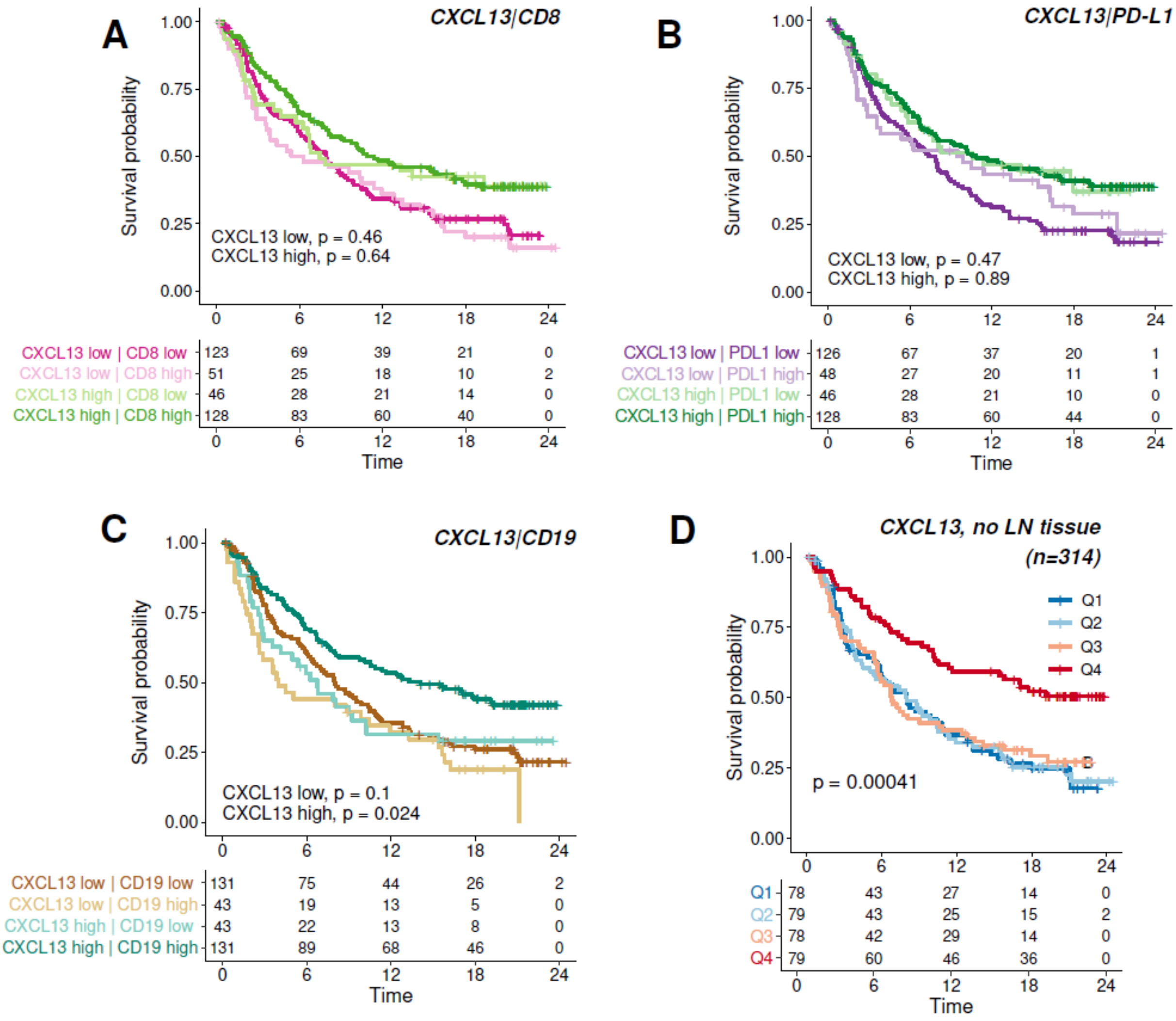

Supplementary Fig. 1. Assessment of *CXCL13* expression in combination with other immune markers in IMvigor210 cohort. Kaplan–Meier curve for OS in the IMvigor210 cohort stratified by high- and low-expression of (A) CXCL13 and CD8A, (B) CXCL13 and PD-L1, and (C) CXCL13 and CD19. For patients with high CXCL13 expression, we verified whether patients also with high expression of the second immune marker had better prognosis than those with high CXCL13 but low marker expression. We did the same for patients with low CXCL13 expression. We only found significant differences for CD19, where high expression of CD19 concomitant with high expression of CXCL13 leads to better outcomes than high CXCL13 with low CD19. (D) Evaluation of IMvigor210 cohort CXCL13 survival without samples from lymph node metastasis. As CXCL13 expression is significantly higher for these samples, we investigated whether they could bias survival and found a strong association even when they were removed.

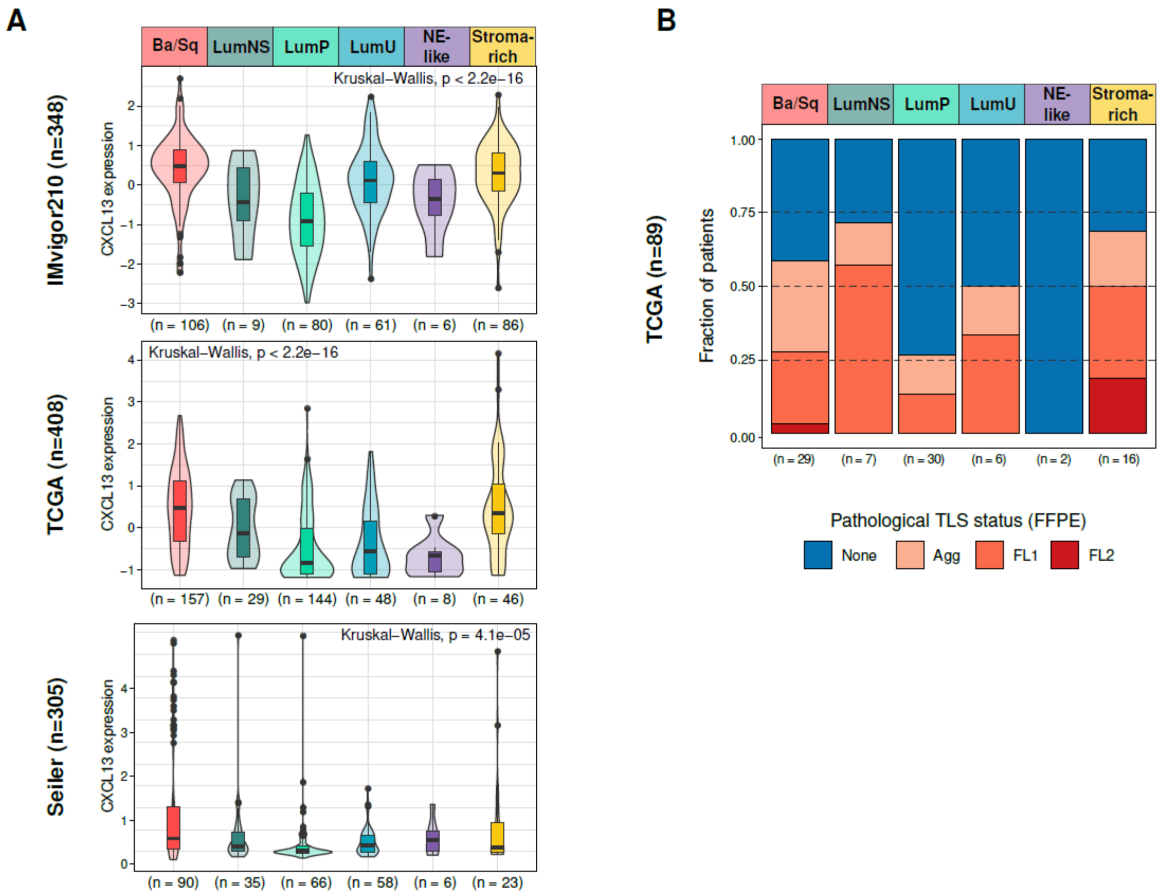

Supplementary Fig. 2. *CXCL13* expression and histological TLS in molecular subtypes. (A) CXCL13 expression varies significantly between subtypes in all three evaluated cohorts. (B) Proportion of samples with Agg, FL1, FL2 or no TLS identified in each class of consensus and Lund subtypes. There was a significant difference between TLS+ tumours in the consensus classification (FET = 0.01).

10.1.3 Discussion et Perspectives

Nous avons pu donc montrer que l'expression de *CXCL13* (et donc la présence de STL) est un biomarqueur de réponse aux IPI dans les cancers urothéliaux avancés.

Pour utiliser l'expression de *CXCL13* comme biomarqueur, il faudra déterminer sa sensibilité et spécificité dans le contexte, et ainsi déterminer un seuil d'expression utilisable en clinique, en analysant l'expression de *CXCL13* selon une technique précise, validée sur plusieurs cohortes.

Il reste de nombreux axes à explorer sur cette thématique. En effet, ici nous avons résumé les STL à l'expression de *CXCL13*, mais il est nécessaire de mieux étudier la présence des STL eux-mêmes comme biomarqueur de réponse aux IPI au niveau histologique. Un projet du laboratoire est donc prévu pour étudier le lien entre la réponse aux IPI et le nombre de STL ainsi que leurs types (agrégats, follicules..). Ceci permettrait de proposer un biomarqueur utilisable sur une lame histologique disponible en pratique courante plutôt que sur la réalisation d'analyse génomique d'expression.

A un niveau biologique, il sera intéressant, dans les cancers de vessie, de mieux comprendre la localisation de ces STL par rapport à la tumeur (proche ou à distance), et les facteurs biologiques expliquant la présence ou non de STL pour permettre une modulation thérapeutique éventuelle. L'équipe du Dr Loriot a ainsi très récemment retrouvé que des lymphocytes T CD4 « helper » spécifiques d'*Escherichia Coli* sécrétaient CXCL13 et étaient associés à une meilleure réponse aux IPI [154]. Des données de transcriptomique spatiale et de transcriptomique sur noyaux uniques sur des lames histologiques de cancer de vessie comportant des STL pourraient permettre de mieux comprendre les phénomènes biologiques en jeu.

10.2 Analyse d'une large cohorte de cancer de vessie par analyse par séquencage d'ARN à noyau unique et caractérisation de biomarqueurs de réponse aux anti PD-1/L-1

10.2.1 Introduction

Dans le cadre d'une collaboration avec l'institut Gustave-Roussy et le Dr Loriot ainsi que la start-up Celsius, j'ai pu commencer l'analyse d'une cohorte de patients ayant un cancer de vessie, 1) métastatique traités par IPI (cohorte MATCH-R décrite ci-dessous) et 2) ayant eu une cystectomie pour un cancer non métastatique (**Figure 1**). Ce travail est en cours et encore à un stade préliminaire, je ne décrirai ici que les principaux résultats obtenus pour le moment. Ce projet a eu 1 an de retard suite à des problématiques légales sur le contrat tripartite de collaboration (dont un centre aux Etats-Unis).

L'étude MATCH-R (NCT02517892) a pour objectif d'étudier prospectivement les mécanismes de sensibilité ou de résistance aux traitements systémiques, dans plusieurs cancers traités par différentes thérapeutiques. Ici n'est étudiée que la cohorte de vessie métastatique traitée par anticorps anti-PD-1/PD-L1. Cette cohorte a permis la réalisation d'une biopsie avant, pendant (~8 semaines) et au moment de la progression tumorale.

Les objectifs de ce travail sont multiples, principalement basés sur des analyses par cellules uniques, et résumés ici en 2 parties :

- Partie 1 : Décrire le microenvironnement des cancers de vessie métastatiques et non-métastatiques, globalement et selon le sous-type moléculaire.
- Partie 2 : Déterminer des biomarqueurs de réponse/résistance avant traitement ou en cours de traitement par IPI (anti-PD-1/L1).

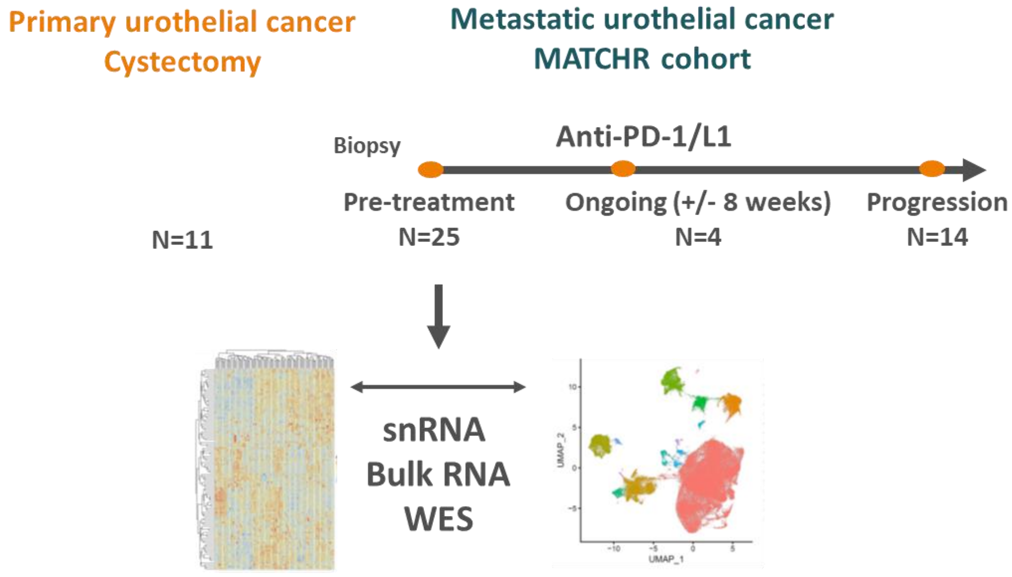

Figure 1 : Description de la cohorte étudiée, avec en majorité des échantillons de la cohorte MATCH-R (métastatique, avec des échantillons avant traitement (= baseline), en cours d'anti PD-1/PD-L1 ou à la progression) et des pièces de cystectomies.

snRNA : single-nuclei RNA, WES: whole-exome sequencing

Les échantillons tumoraux ont été collectés à l'Institut Gustave Roussy, soit lors d'une biopsie dans le cadre de la cohorte MATCH-R ou par cystectomie.

Les échantillons congelés ont été transférés à Celsius qui a procédé au séquençage d'ARN de noyau unique (snRNA, 10x genomics Chromium Single Cell 5') la méthode est décrite dans la partie méthode.

10.2.2 Méthode (résumé)

Séquençage / alignement / contrôle qualité

- Après séquençage (10x Chromium 5 '), un alignement des « reads » sur le génome a été effectué en utilisant Kallisto Bustools.
- Les doublets potentiels ont été enlevés en utilisant 2 packages (DoubletFinder et scds), les noyaux de mauvaise qualité ont été filtrés (<200 genes/noyau, <1000 counts/noyau).
- Seuls les gènes retrouvés dans au moins 5 noyaux ont été gardés pour les analyses.

Normalisation / Clustering

- Le package Seurat a été utilisé pour les analyses suivantes [155].
- Chaque échantillon a été normalisé individuellement (méthode SCT Seurat) puis l'ensemble des noyaux des différents échantillons a été regroupé. J'ai ensuite réalisé un clustering des snRNA basé sur la PCA (33 dimensions) selon la méthode de Louvain (résolution 0.5).

Annotation

- Une annotation de chacun des clusters a été effectuée selon les gènes surexprimés dans un cluster par rapport aux autres.
- Les gènes principaux utilisés pour l'annotation étaient : tumoraux (*EPCAM/KRT19*) après exclusion d'autres contingents épithéliaux dont pulmonaire (*SFTPB/SLC34A2*) et hépatiques (*APOB/HP*), fibroblastes/péricytes (*COL1A1*, *DCN*+), endothéliales (*PECAM1*+), lymphocytes B (*MS4A1*+), lymphocytes T (*CD2/CD3E/CD3D*+), myéloïdes (LYZ+), myocytes (TTN+), adipocytes (LPL+), ostéoclastes (TNFSRF11A+).

Intégration

- Du fait que les clusters se séparent sans intégration selon leur type cellulaire et non selon l'échantillon dans l'ensemble du set, aucune intégration n'a été effectué pour l'annotation des grands types cellulaires, pour ne pas perdre d'information biologique. Une intégration sur ce set en utilisant Harmony (une méthode d'intégration, data non montrée, en utilisant chaque échantillon) ne permet plus par exemple de retrouver les cellules pulmonaires ou hépatiques qui se confondent avec les cellules épithéliales tumorales.
- Pour la partie étudiant les sous types des cellules immunitaires, une intégration en utilisant le package Harmony a été effectuée devant la présence d'un effet batch [156].

10.2.3 Résultats

Les principales caractéristiques cliniques de cette cohorte sont présentées **Table 1 et Table 2**. La majorité de cette cohorte est donc constituée de patients de la cohorte MATCH-R, dont les sites de biopsies sont variables (hépatiques, pulmonaires, ganglionnaires..).

	Primaire	**MATCH-R**			
	(N=11)	Baseline (N=25)	En cours (N=4)	Progression (N=14)	Total (N=54)
consensusClass					
Ba/Sq	2 (18.2%)	5 (20.0%)	0 (0%)	1 (7.1%)	8 (14.8%)
LumP	6 (54.5%)	13 (52.0%)	1 (25.0%)	3 (21.4%)	23 (42.6%)
LumU	2 (18.2%)	4 (16.0%)	0 (0%)	3 (21.4%)	9 (16.7%)
Stroma-rich	1 (9.1%)	1 (4.0%)	3 (75.0%)	3 (21.4%)	8 (14.8%)
LumNS	0 (0%)	2 (8.0%)	0 (0%)	3 (21.4%)	5 (9.3%)
NE-like	0 (0%)	0 (0%)	0 (0%)	1 (7.1%)	1 (1.9%)

Table 1 : Classification consensus moléculaire de la cohorte basée sur du « pseudo-bulk » des échantillons avec application du package consensusMIBC. Le pseudo-bulk consiste à considérer l'ensemble de l'expression des noyaux d'un échantillon comme équivalent au transcriptome global de cet échantillon

Dans la cohorte MATCH-R, la majorité des échantillons correspond au prélèvement pré traitement (N=25), avec peu d'échantillons en cours de traitement disponibles (N=4). Ceci correspond au fait que 1) la majorité des patients (~75%) sont en progression d'emblée, et que le 1er prélèvement à 8 semaines correspond en fait au prélèvement à progression, 2) tous les patients ne réalisent pas de biopsie par la suite 3) 1 patient est en réponse complète et ne pouvait donc pas être biopsié.

Sur les 46 échantillons de la cohorte MATCH-R et les 15 pièces de cystectomies, j'ai retenu respectivement 43 et 11 échantillons de scRNA qui disposaient d'au moins 500 noyaux/échantillon, pour un total de 54. 169651 noyaux ont été utilisés pour les analyses.

10.2.3.1 Partie 1 description du microenvironnement des cancers de vessie

La grande majorité des noyaux analysés correspondent à des noyaux de cellules tumorales (70%) avec ensuite par fréquence décroissante les fibroblastes/péricytes (~9%), cellules endothéliales(~5%), lymphocytes T (~5%), myéloïdes(~4%) puis lymphocytes B (~3%) **(Figure 2-3)**.

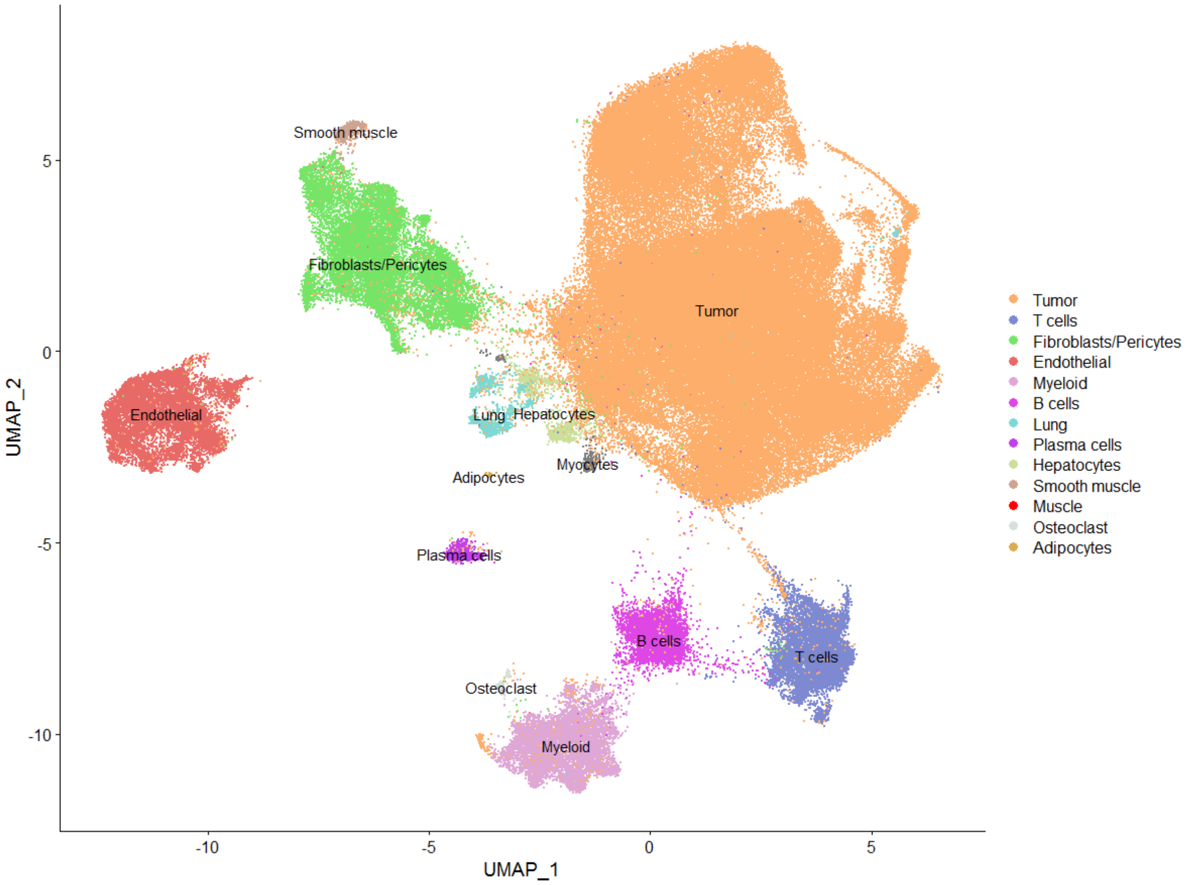

Figure 2 : Coordonnées UMAP des snRNA avec annotations des principaux types cellulaires observés

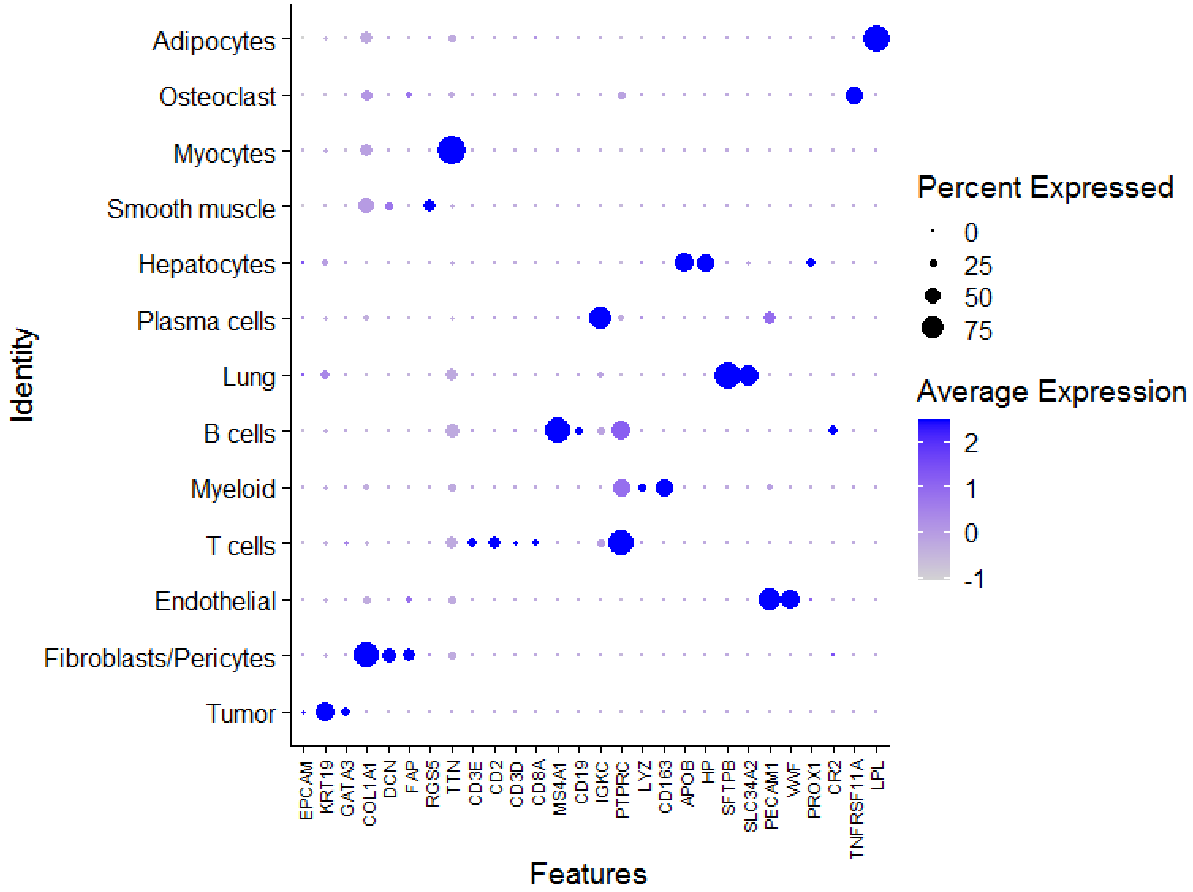

Figure 3 : Expression des principaux gènes selon le type cellulaire

En utilisant du « pseudo-bulk », j'ai classifié chaque échantillon selon son sous type moléculaire en utilisant le package consensusMIBC (**Table 1**). La **Figure 4** présente la répartition de chaque type cellulaire par échantillon classée selon le sous type moléculaire et la **Figure 5** leur distribution de répartition selon le sous type moléculaire.

On peut observer que la proportion de cellules immunitaires et du stroma (fibroblastes et cellules immunitaires) est supérieure dans les stroma-rich, Ba/Sq et LumNS comparés aux LumP/LumU. Les phénotypes stroma-rich sont très pauvres en cellules tumorales. La limite de cette analyse est que la méthode utilisée prend déjà partiellement en compte l'existence de stroma, mais les principaux gènes caractéristiques de la classe luminal (*PPARG/GATA3/FOXA1*) ou Ba/Sq (*KRT5/6A/14*) sont bien exprimés dans les sous type correspondants (**Figure 6**).

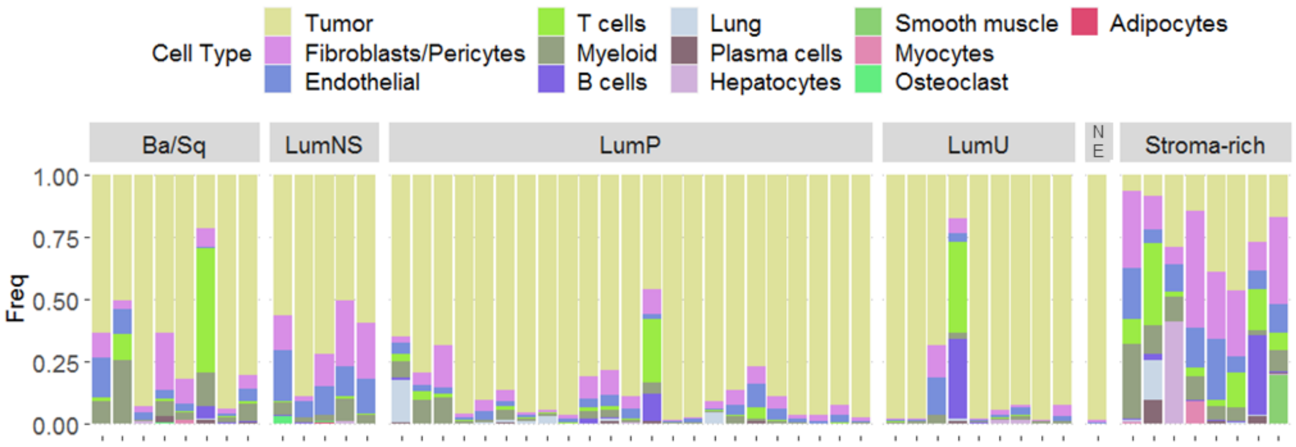

Figure 4 : Répartition des types cellulaires par échantillon selon les sous types moléculaires. NE : NE-like

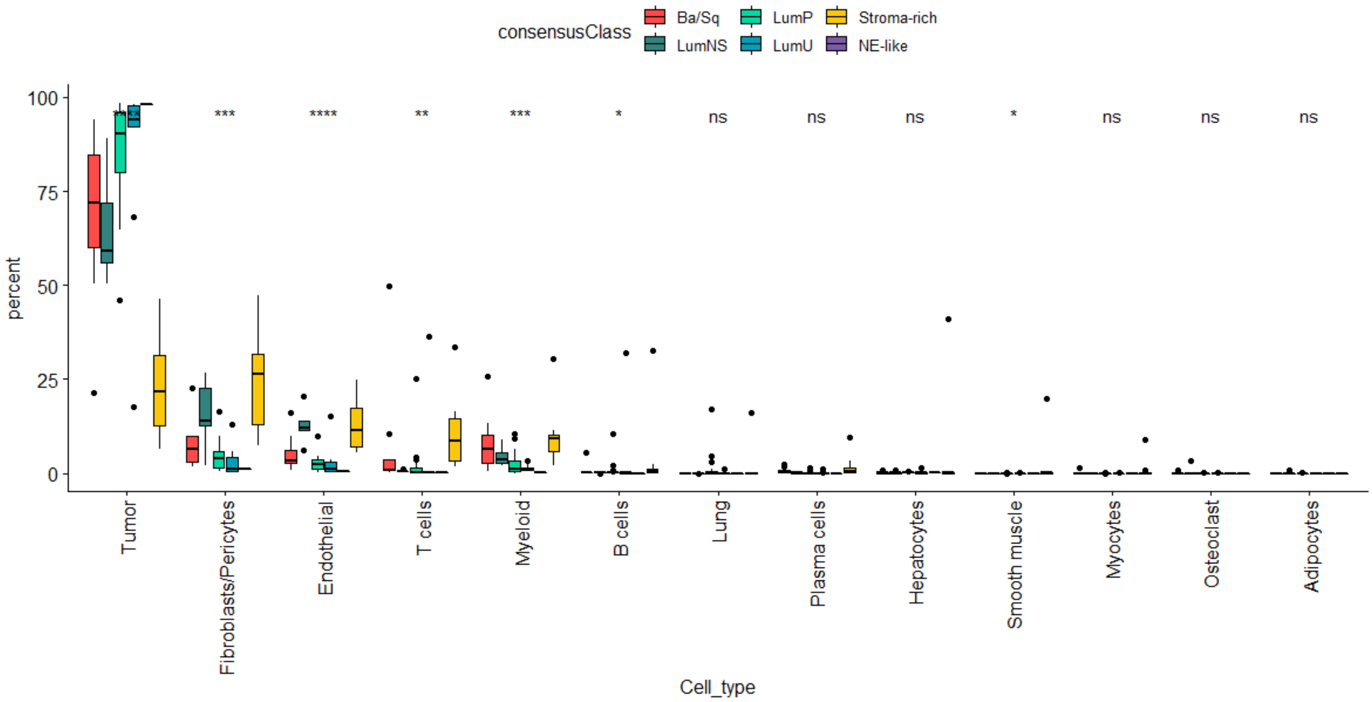

Figure 5 : Distribution de chaque type cellulaire selon le sous-type moléculaire. Ns : non-significatif

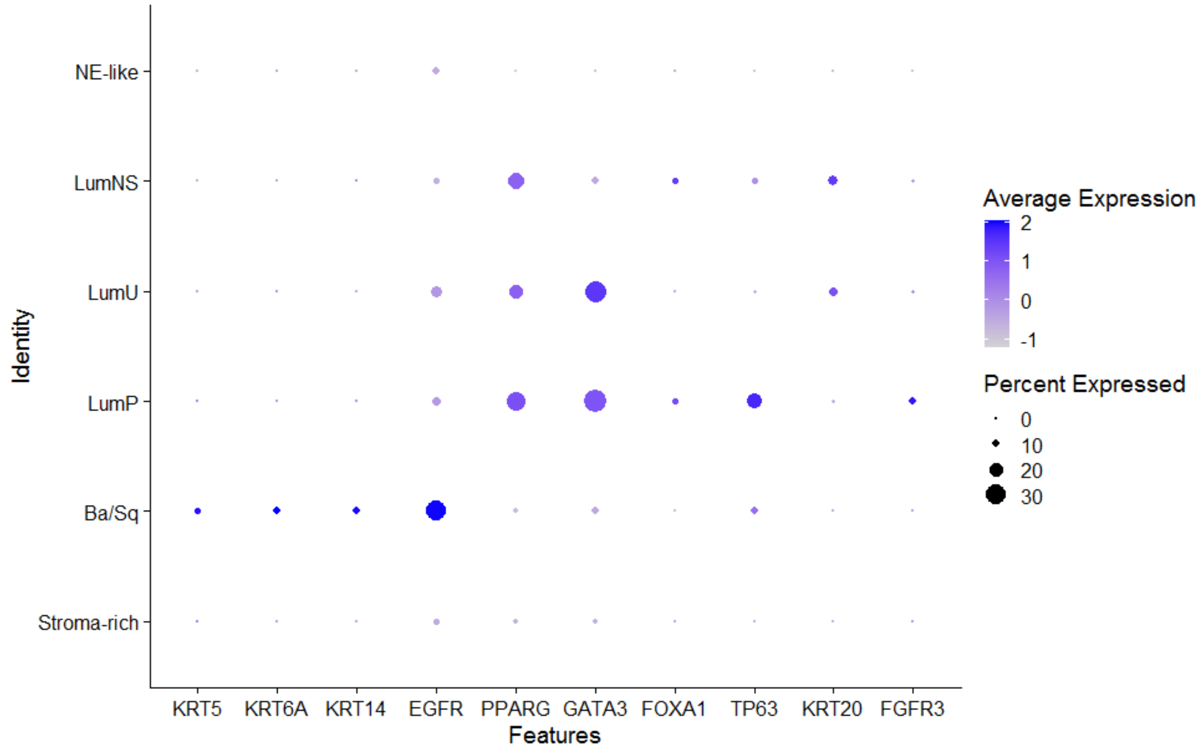

Figure 6 : Expression des principaux marqueurs caractéristiques luminaux (PPARG/GATA3/FOXA1, FGFR3, KRT20) ou Ba/Sq (KRT5-6A-14/EGFR) selon le sous type moléculaire

A noter que je n'ai pas observé de différence significative selon la cohorte (métastatique versus primaire, **Figure 7**), même s'il existe une tendance à ce que le stroma soit plus présent dans la cohorte MATCH-R que primaire, probablement lié au fait qu'ici la majorité des tumeurs primaires étaient LumP (plus faiblement infiltrées).

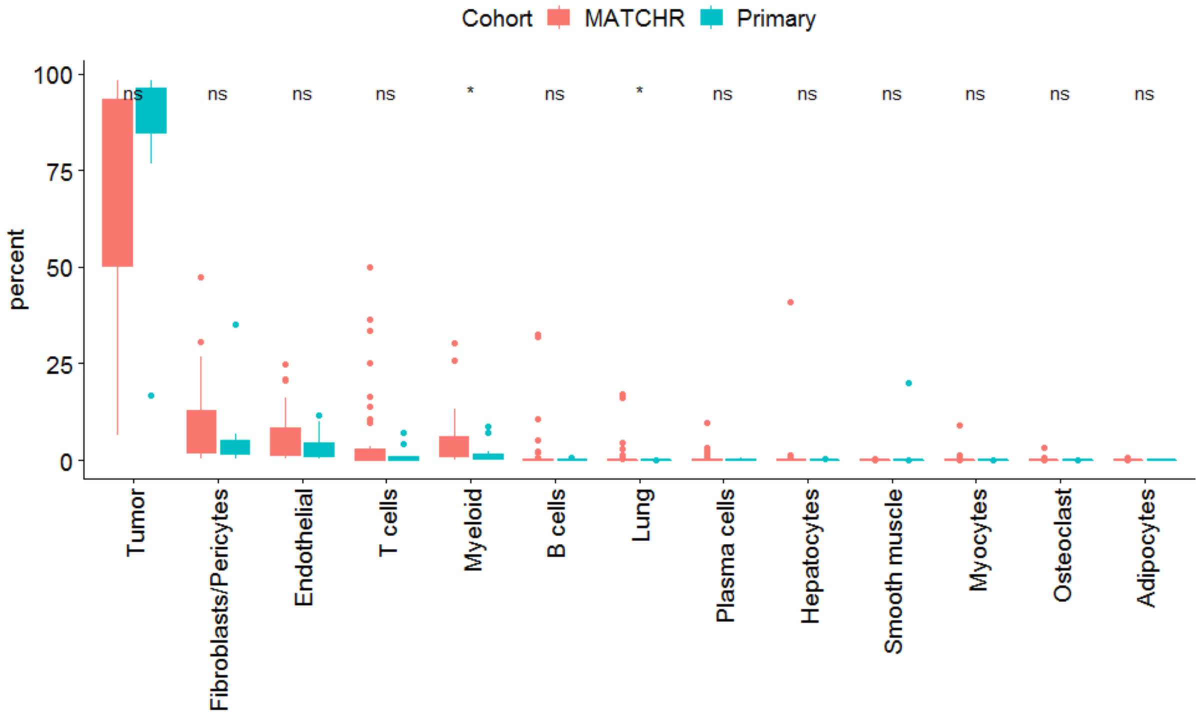

Figure 7 : Distribution de la répartition des types cellulaires selon la cohorte MATCH-R (échantillons métastatiques) ou cancer primaire (cystectomies) .

Une autre observation attendue est que le site de prélèvement influence la répartition des types cellulaires observés (**Figure 8**), en particulier un pourcentage supérieur de lymphocytes B dans les prélèvements tumoraux ganglionnaires.

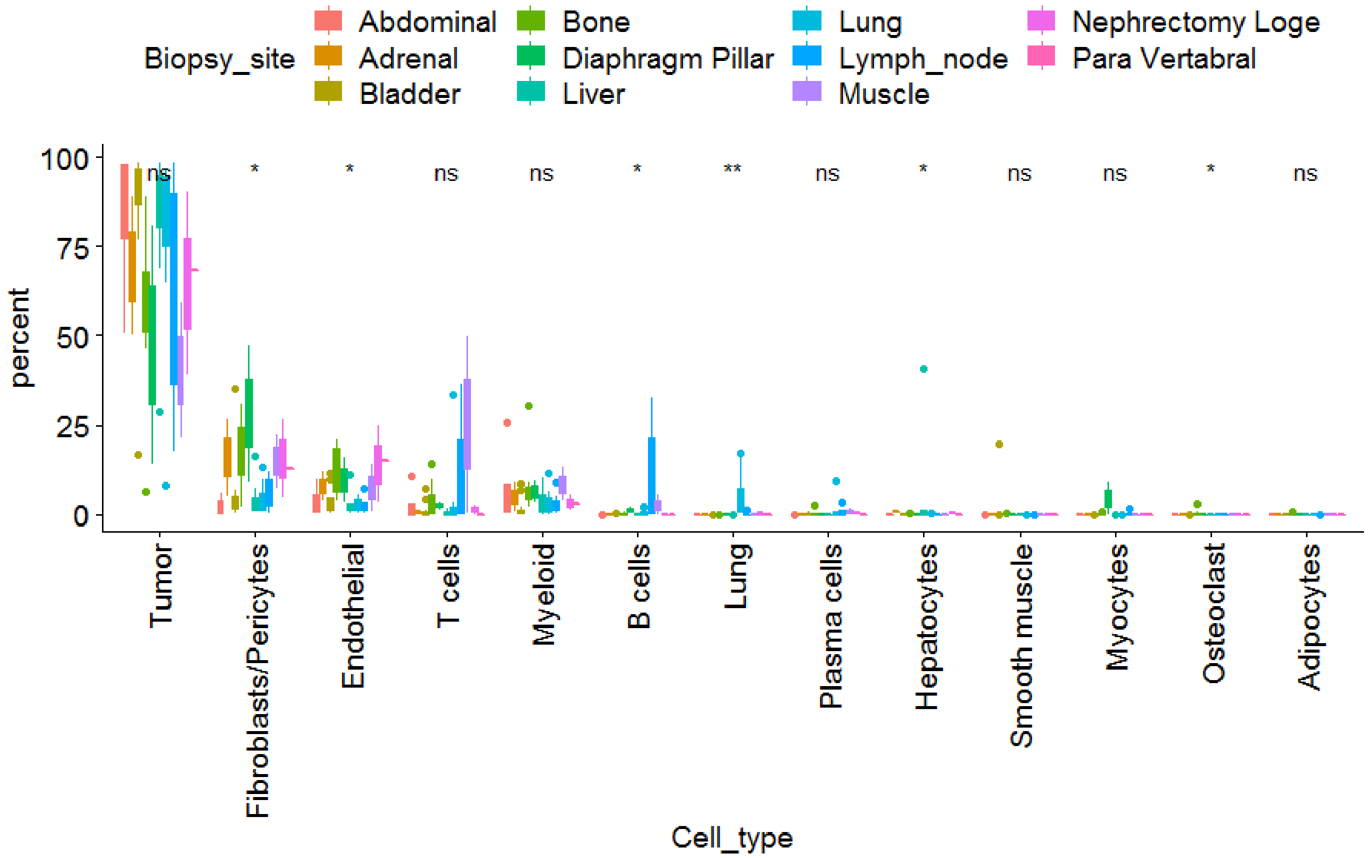

Figure 8 : Distribution de la répartition des types cellulaires selon le site de prélèvement

En étudiant la corrélation entre la distribution de ces types cellulaires (**Figure 9**), on peut observer que les lymphocytes T/B et les cellules plasmatiques sont généralement co-présentes, alors que d'un autre coté il y a une coprésence des cellules endothéliales/ fibroblastes et cellules myéloïdes.

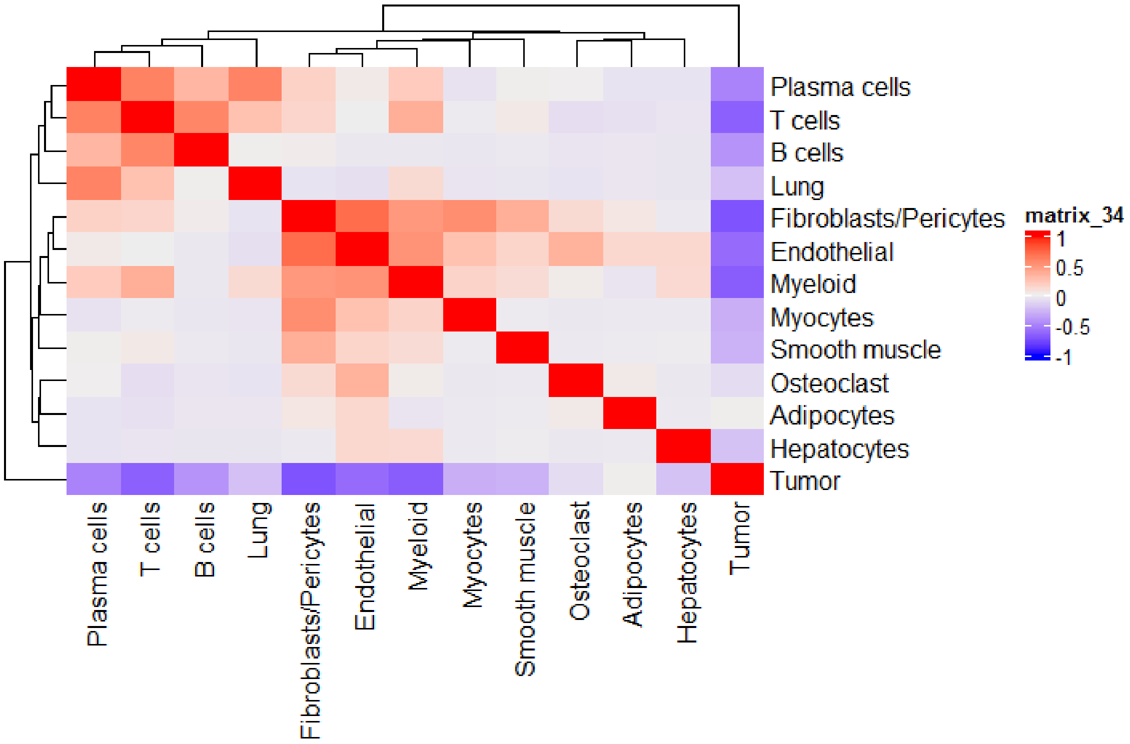

Figure 9 : Heatmap de la corrélation de la distribution des différents types cellulaires (Pearson)

En conclusion de cette partie, ces analyses préliminaires suggèrent que :

1) Les sous-types moléculaires Ba/Sq, LumNS et Stroma-Rich sont plus infiltrés en stroma que les LumP/LumU, confirmant les analyses de déconvolution réalisés sur des données transcriptomiques. Le phénotype stroma-rich est très pauvre en cellules tumorales.
2) Le site de biopsie influence les types cellulaires observés, ce qui n'a que très peu été décrit par analyse en cellule unique dans la littérature, les données de biopsies métastatiques étant rares.
3) Il y a une coprésence de certains types cellulaires.

10.2.3.2 Partie 2 biomarqueurs de réponse aux anti-PD-1/L1

Pour cette partie, il ne sera étudié que la cohorte MATCH-R (147927 noyaux, 43 échantillons), et ne sera présenté que les analyses quantitatives de la distribution des types et sous-types cellulaires.

Pour mieux caractériser les cellules immunitaires (donc en excluant les fibroblastes/péricytes et les cellules endothéliales), j'ai réalisé un nouveau « clustering » en ne gardant que les noyaux annotés de lymphocytes T/B, cellules plasmatiques et cellules myéloïdes. Du fait de la présence d'un effet « batch » à l'intérieur de chacun de ces types cellulaires, j'ai réalisé une intégration en utilisant le package Harmony.

J'ai pu alors annoter les sous types cellulaires selon les gènes exprimés dans chaque cluster (**Figure 10-11**). On observe que la majorité des cellules myéloïdes sont des TAM M2 ainsi que quelques monocytes, alors que les cellules dendritiques sont très rarement détectées.

Pour les lymphocytes T, on retrouve la présence de Lymphocytes T naïf/CD4, de Treg ainsi que de NK/T, T CD8 effecteur et T exhausted. A noter que du fait de la présence d'ARN ambiant dépendant de chaque échantillon, j'ai considéré certains noyaux comme « Ambient RNA », car co-exprimant des marqueurs de différents types cellulaires (gardés pour le moment pour identifier des biais potentiels).

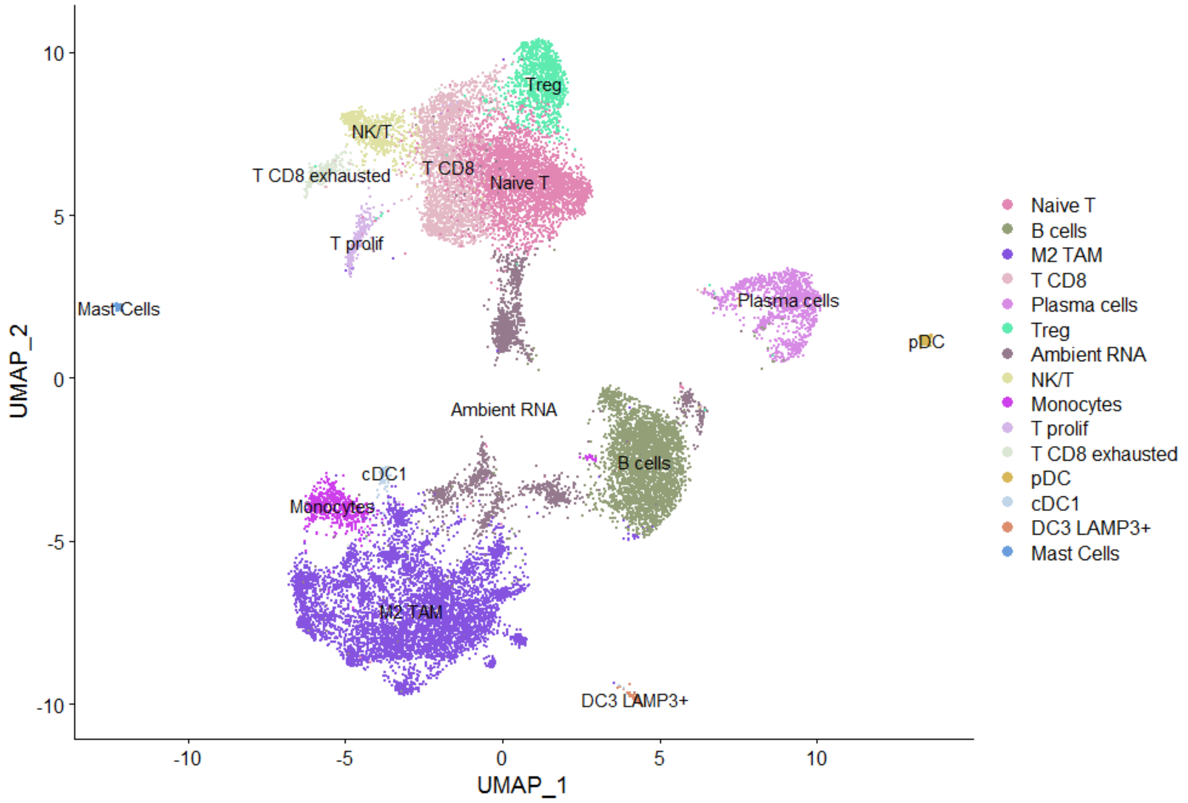

Figure 10 : Coordonnées UMAP des cellules immunitaires après intégration

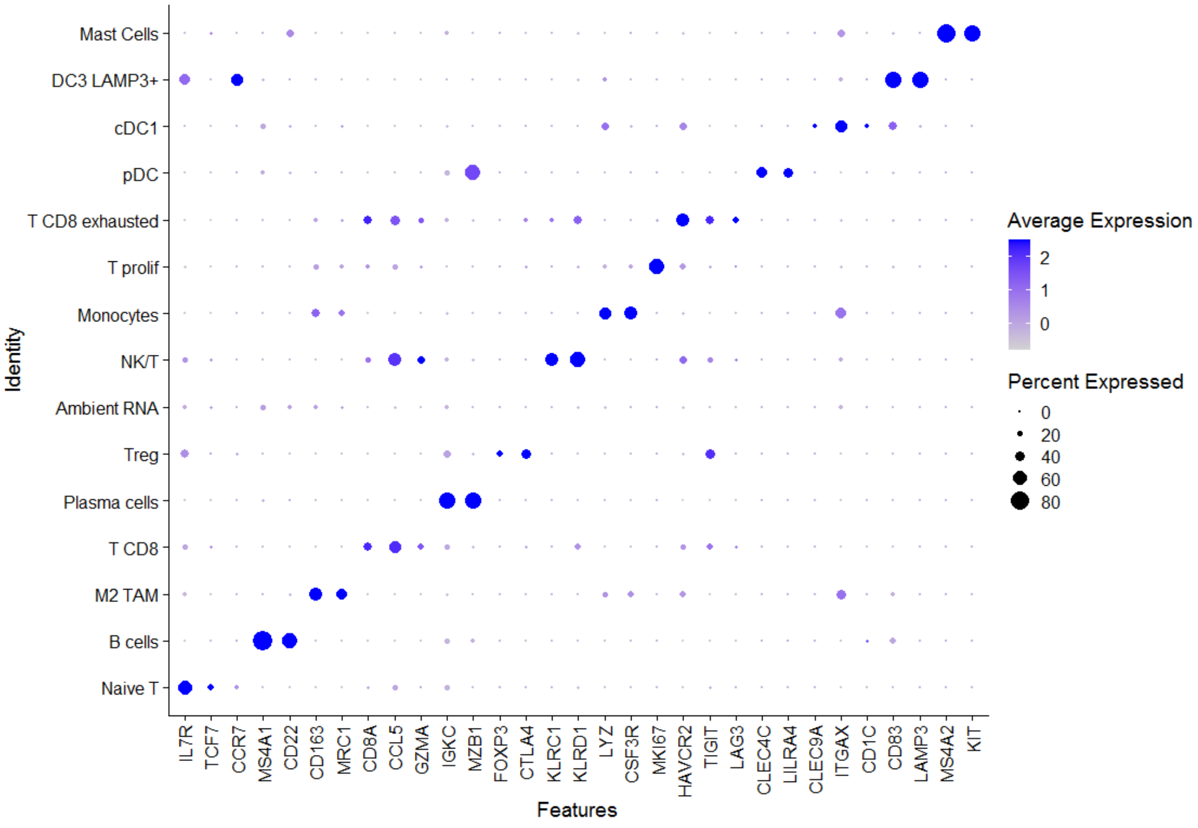

Figure 11 : Expression des principaux gènes de chaque sous type cellulaire

On retrouve la coprésence de certains sous-types de cellules immunitaires, comme les Treg et les T CD8 (**Figure 12**).

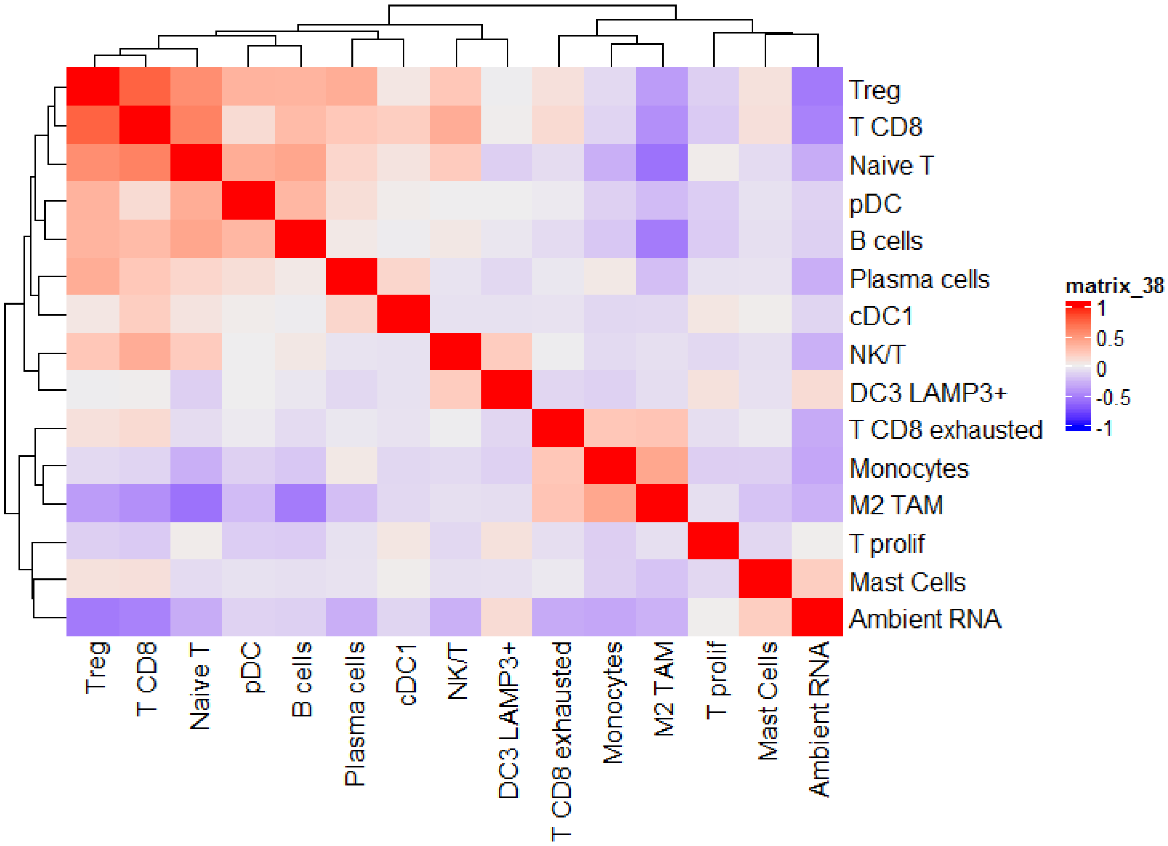

Figure 12 : Heatmap de la corrélation de la distribution des différents types cellulaires (Pearson)

En comparant la répartition des sous-types immunitaires entre les répondeurs et les non-répondeurs, on observe que les patients répondeurs présentaient plus de cellules plasmatiques que les non-répondeurs ($p<0.01$, qu'importe le moment de la biopsie) (**Figure 13**).

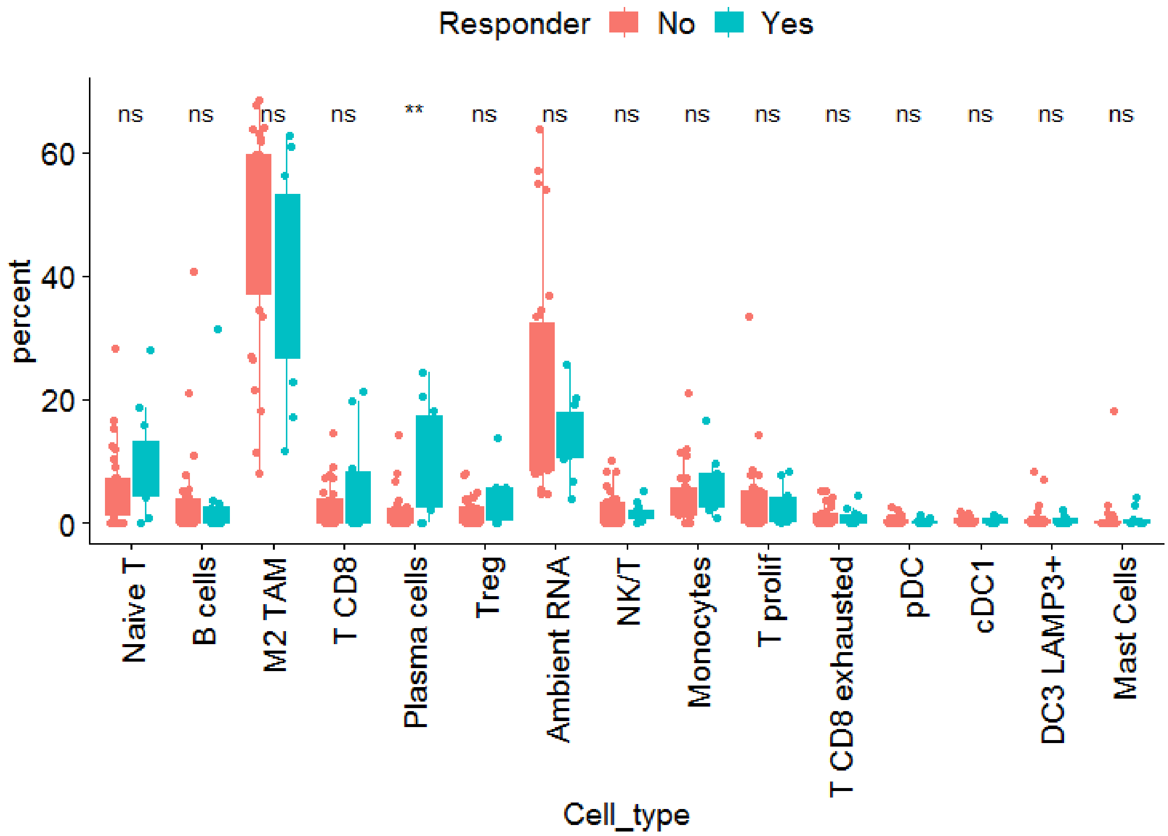

Figure 13 : Distribution de la répartition des types cellulaires selon la réponse ou non aux anti-PD1/L1. Ns : non-significatif

Lorsqu'on analyse la répartition des sous-types immunitaires selon le timing de la biopsie, on observe sur la biopsie en cours de traitement un pourcentage supérieur de lymphocytes T CD8, Treg et de cellules plasmatiques, avec une tendance à un taux inférieur de TAM M2 (**Figure 14**).

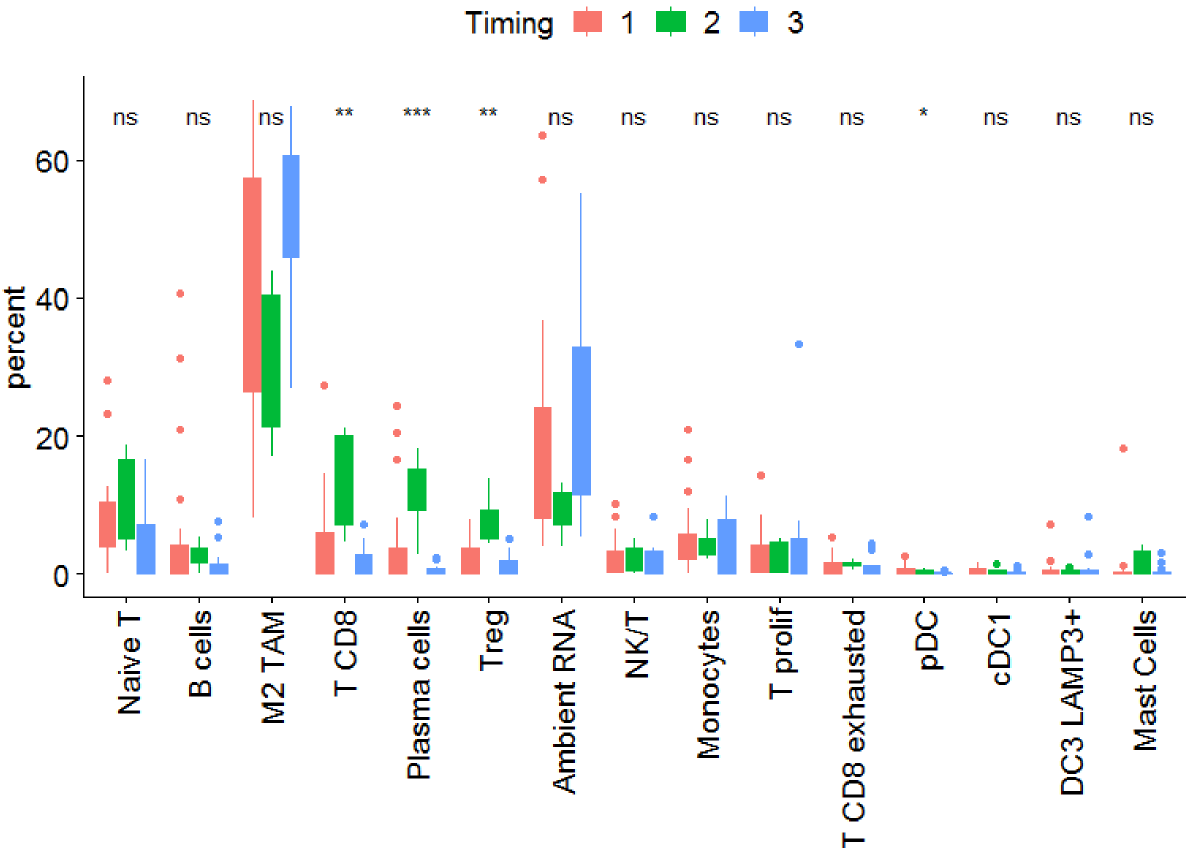

Figure 14 : Distribution de la répartition des types cellulaires selon le timing de la biopsie. 1=Baseline, 2= en cours de traitement ~8 semaines, 3= à progression

En analysant les patients individuellement (**Figure 15**), on constate chez les 3 patients ayant eu une réponse et avec un prélèvement avant et en cours de traitement que la modification de microenvironnement immunitaire n’est pas identique.

En effet, on peut constater une augmentation de lymphocytes T CD8 et Treg chez les 3 patients, mais une augmentation des cellules plasmatiques seulement chez MR464 et une baisse des TAM M2 chez 2 patients (MR464/MR498).

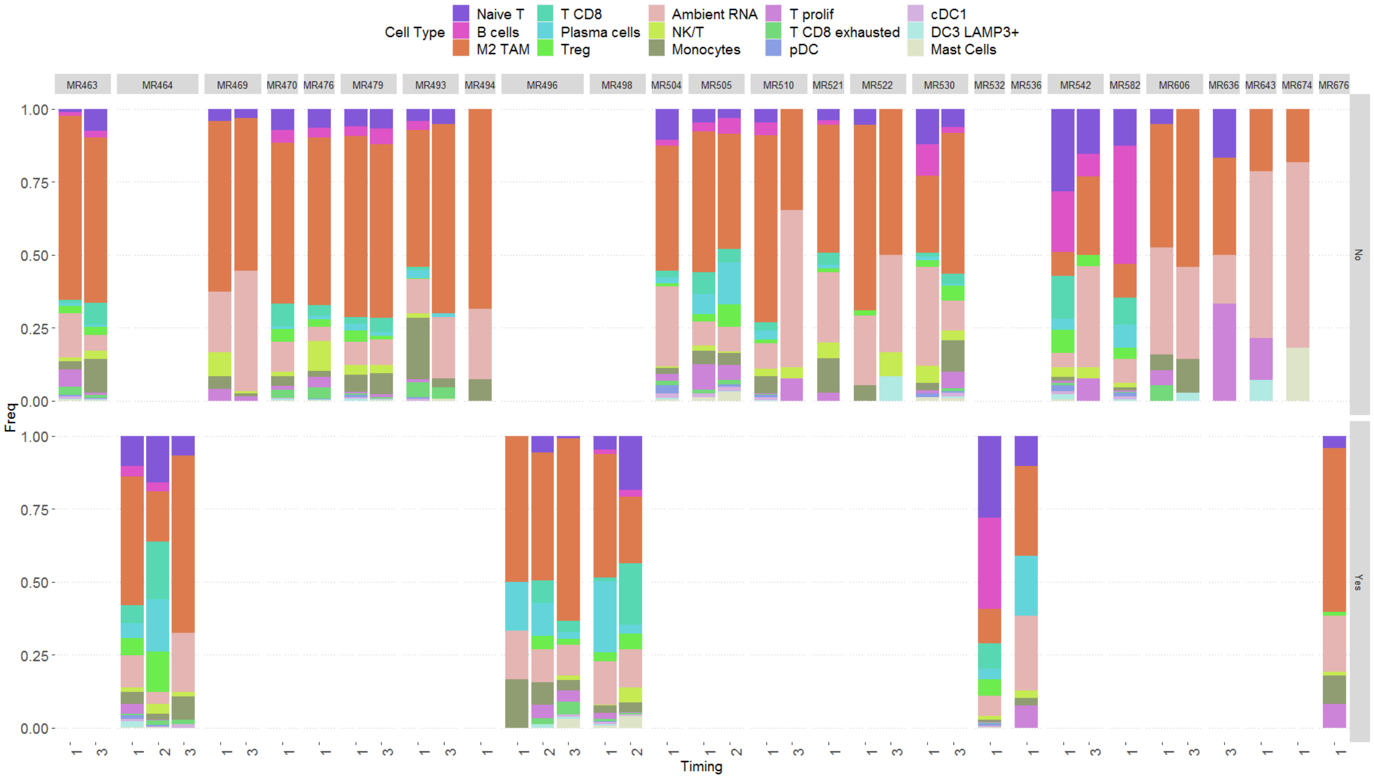

Figure 15 : Répartition des types cellulaires par échantillon, patient et selon le timing de la biopsie et la réponse ou non aux anti-PD1/L1 (haut = non répondeur, bas = répondeur)

En conclusion de cette partie, ces données préliminaires suggèrent que :

1) La présence de cellules plasmatiques est un biomarqueur de réponse aux anti-PD-1/L1 dans les cancers de vessie.
2) On peut observer une augmentation des T CD8, Treg et cellules plasmatiques sous anti-PD-1/L1, avec une baisse des TAM M2.
3) La variation quantitative des sous types immunitaires est différente selon les patients en cas de réponse tumorale aux anti-PD-1/L1.

10.2.4 Discussion

Ce travail est encore à un stade préliminaire. Les analyses par séquençage d'exome entier d'une partie des tumeurs de la cohorte MATCH-R ainsi que les analyses des transcriptomes permettront respectivement de mieux caractériser les tumeurs et de valider/confirmer certains résultats observés sur les données de snRNA, en particulier le sous type moléculaire. La collecte des blocs tumoraux pour analyses pathologiques des tumeurs et de leur microenvironnement, permettra également de confirmer/valider certains résultats.

L'absence d'enrichissement en cellules immunitaires ou stromales lors du séquençage limite la possibilité d'étudier de manière très précise certains sous type rares (ex cellules dendritiques), car la majorité des noyaux séquencés sont tumoraux.

Sur ces analyses préliminaires, il est confirmé certains résultats observés sur des données de transcriptome globales, comme la différence d'infiltrat immunitaire/stromale selon le sous-type moléculaire, avec les LumP comme le sous type le moins infiltré.

Concernant les biomarqueurs, il a été montré dans d'autres cancers que la présence intra tumoral de cellules plasmatiques, en particulier dans le cadre de STL était un biomarqueur de réponse aux IPI [157], et dans l'**Article 2** nous avons pu montrer sur des données de transcriptomes bulk que les STL (via l'expression de *CXCL13*) étaient un biomarqueur de réponse dans les cancers de vessie. Ici, la coprésence de cellules plasmatiques, T et B dans cette cohorte semble être en faveur de la présence de STL, non visibles sur les analyses par snRNA, mais dont la présence pourrait être confirmée sur les coupes histologiques des échantillons correspondants.

De nombreuses analyses sont nécessaires dans le cadre de ce travail, et de manière non exhaustive :

- Etude de l'interaction cellules épithéliales et cellules stromales (ligand-récepteur).
- Etude des variations d'expression en cours de traitement par anti-PD-1/L1 selon le sous type cellulaire, avec le problème du bruit de fond retrouvé dans certains échantillons, secondaires à la technologie utilisée (séquençage de noyaux uniques).
- Inférence des réseaux de régulation de gènes des cellules tumorales ou immunitaires selon le sous-type moléculaire ou, une fois connue, selon la présence de certaines altérations génomiques (ex mutation de *FGFR3*).

11 Identifications de nouvelles pistes thérapeutiques

11.1 Article 3 : DepMap

11.1.1 Introduction

La base de données fonctionnelles DepMap est extrêmement riche, et permet d'accéder à des données fonctionnelles à large échelle, impossible à générer par un seul laboratoire à l'heure actuelle.

La partie Achilles, avec l'inhibition par CRISPR-CAS9 de plus de 17000 gènes dans plus de 1000 lignées cellulaires cancéreuses est un travail gigantesque, pouvant servir à la découverte de nombreuses cibles potentiellement thérapeutiques ou mécanismes biologiques importants de la viabilité cellulaire tumorale.

31 lignées urinaires cancéreuses ont ainsi été incluses dans la base Achilles (31 dans la version 22Q4 utilisée dans l'article ci-dessous). La plupart des études a été réalisée sur un versant pan-cancer[136,158], même si récemment des articles ont commencé à étudier les gènes impactant la viabilité pour un cancer donné, comme le mélanome [159].

Mon travail ici (**Article 3**, en préparation) était donc d'explorer la base Achilles pour les lignées urinaires cancéreuses afin de rechercher de nouvelles cibles thérapeutiques potentielles. Plusieurs options ont été explorées, en particulier de déterminer les gènes impactant la viabilité dans les lignées urinaires en tenant ou sans tenir compte des autres lignées non urinaires.

J'ai privilégié l'option de l'étude comparative des lignées urinaires et non urinaires, afin de déterminer des gènes plus spécifiques du lignage urinaire. L'inconvénient de cette méthode est de ne pas révéler des gènes impactant la viabilité des lignées urinaires mais également de manière pan cancer, qui pourraient également être intéressant à inhiber au niveau thérapeutique.

Avec cette méthode comparative, j'ai ainsi pu mettre en évidence de nombreux gènes impactant de manière plus spécifique la viabilité des lignées cancéreuses urinaires. Certains étaient connus pour être impliqués dans la biologie tumorale des cancers urotheliaux, comme *PPARG* et *RXRA*, mais j'ai pu découvrir d'autres gènes comme par exemple *RARG, BIRC2, ARHGEF7* ayant un rôle oncogénique dans une partie des lignées urinaires. En particulier, le rôle de *RARG* comme partenaire de *RXRA* n'était pas connu même si une activité régulon de RARγ élevée dans les tumeurs LumP était évoquée dans l'article sur la classification consensus des TVIM[28]. Nous avons pu montrer que les tumeurs LumP présentaient un régulon élevé pour PPARγ/RXRα/RARΓ, alors que les Ba/Sq présentaient un régulon élevé seulement pour RXRα/RARγ et les LumP pour RXRα/PPARγ.

La découverte du rôle sur la viabilité cellulaire de BIRC2 (=cIAP1)/RNF31 m'a permis de déterminer que les Smac-mimétiques (inhibiteurs de cIAP1/2-XIAP) étaient efficaces *in vitro* et *in vivo* dans une partie des lignées tumorales urinaires, et que l'expression de *RIPK1* et/ou l'amplification de *BIRC2* pouvaient être un biomarqueur de sensibilité. Ces hypothèses sont en train d'être testées dans la cohorte de PDX caractérisé à l'**Article 1**, ou 2 PDXs présentent une amplification de *BIRC2*, et certaines une expression importante de *RIPK1*.

Cette base permet également d'explorer les gènes ayant un effet suppresseur de la prolifération, et en associant ces 2 critères (gènes impactant la viabilité et gènes suppresseurs de la prolifération), il est possible de trouver des gènes ayant un rôle dual, oncogéniques dans certaines lignées et suppresseurs de la prolifération dans d'autres.

Ainsi, j'ai montré qu'AHR/ARNT avait bien un rôle suppresseur de la prolifération dans une lignée cancéreuse urinaire (UMUC6), alors qu'il avait été montré un rôle oncogénique d'AHR dans les lignées urothéliales de phénotype luminal [73].

11.1.2 Article 3 : En préparation

Analysis of CRISPR screen and functional validation identifies new pro-tumoral and tumor suppressive genes associated with sensitivity to targeted therapies in urinary cancer cells.

Luc Cabel[1,2], Clément Hua[1,2], Jacqueline Fontugne[1,3,4], Clarice S. Groeneveld[1,2,5], Natacha Rochel[6-9], François Radvanyi[1,2], Isabelle Bernard-Pierrot[1,2,10]

[1] Institut Curie, CNRS, UMR144, Molecular Oncology team, PSL Research University, Paris, France
[2] Sorbonne Universités, UPMC Univ Paris 06, Paris, France
[3] Department of Pathology, Institut Curie, Saint-Cloud, France
[4] UVSQ, Paris-Saclay University, France
[5] La ligue contre le cancer, Paris, France
[6] Institut de Génétique et de Biologie Moléculaire et Cellulaire (IGBMC),
[7] Institut National de La Santé et de La Recherche Médicale (INSERM)
[8] U1258/Centre National de Recherche Scientifique (CNRS)
[9] UMR7104/Université de Strasbourg, Illkirch, France
[10] To whom correspondence should be addressed

Dr Isabelle Bernard-Pierrot, Institut Curie, 26 rue d'Ulm, 75005 Paris

E-mail: Isabelle.Bernard-Pierrot@curie.fr

Tel: +33 1 42 34 63 40, Fax: +33 1 42 34 63 49

Keyword: bladder, urothelial, urinary, CRISPR screen, oncogene, tumor suppressor gene, dual gene, DepMap, RARG, BIRC2, cIAP1, birinapant, biomarker

Abstract

Background

Muscle-invasive bladder cancers (MIBC) are still of poor outcome despite recent new treatments. In this study, we aimed to identify new potential tumor suppressors or essential genes in bladder cancer via the analysis of the cancer dependency Map (DepMap).

Method:

We analyzed CRISPR screen results from DepMap Database (22Q2) to find new essential genes (dependency probability >50%) or proliferation suppressive genes (Chronos score >0.4) in urinary cancer cell lines (UCC, n=31).

We evaluated the *in vitro* effect of RARG inhibition (pan-RAR drug - AGN-194310), AHR activation (agonist, FICZ) and cIAP inhibition (birinapant) on urinary cancer cell line viability. Effect of birinapant was further evaluated *in vitro* in UMUC14 and SCaBER xenografts.

Results

Through CRISPR screen analysis, we identified new putative tumor suppressors or genes with dual tumor suppressor/oncogene role, including AHR/ARNT complex. Decrease in viability upon treatment with an AHR agonist in a subset of UCC, FICZ, further supported the dual role of AHR. We then identified 43 genes with more frequent essentiality in UCC cells compared to other epithelial cancer cell lines, including *ARHGEF7,* essential in 77% of UCC. The *ARHGEF7* dependency was associated with a low expression of its paralog, *ARHGEF6*. As expected in Luminal UC, we identified a RXRα-PPARγ co-dependency, whereas an RXRα-RARγ co-dependency was found in a subset of Basal/squamous UCC, further supported by a high RARG and RXRα protein activity inference in Basal/Squamous tumors from TCGA. Finally, we identified that 30% of UCC were BIRC2(cIAP1)/RNF31 dependent. We validated that birinapant (cIAP1/2-XIAP inhibitor) was effective in a subset of UCC, both *in vitro* and *in vivo* using xenografts, and identified *BIRC2* amplifications or *RIPK1* expression as potential biomarkers of efficacy.

Conclusion

Our analysis of DepMap database allowed the identification of new pro-proliferative genes in BCa, such as the RXRα-RARγ complex in basal tumors or BIRC2, and the new dual or tumor suppressive genes, such as AHR. Existence of agonists of TSG or antagonists of pro-tumoral genes offers new potential therapeutic options for MIBC.

Introduction

Bladder cancer (BCa) is the 9th most common cancer type worldwide with an estimated 550,000 new cases in 2018[1]. Histologically, 90 to 95% of BCa are urothelial carcinomas (UC) and 5% are squamous cell carcinomas (SCC) [2]. Patients with muscle-invasive BCa (MIBC) have a very poor outcome, with an overall 5-year survival of 50-60% and less than 10% for patients with locally advanced disease or distant metastasis, respectively. In the advanced setting, chemotherapy, immune checkpoint or FGFR inhibitors (for tumors presenting *FGFR2/3* genetic alterations) may be administered [2,3]. However, despite these treatments, outcome remains poor, and identification of new therapies is still needed.

With the aim to improve prediction of clinical outcome and treatment response, an international consortium has recently established a consensus molecular classification for MIBC, based on transcriptomic data including 6 subtypes, facilitating inter-study comparisons [4]. These subtypes can be divided into the broad luminal (differentiated) and basal/squamous (Ba/Sq) groups. PPARγ pathway activation, through *PPARG* amplifications or *RXRA* and *PPARG* activating mutations, is a known key feature of luminal tumors and a potential therapeutic target [5–10]. On the other hand, the Ba/Sq subtype and bladder SCC are associated with EGFR activation and sensitivity to anti-EGFR treatments in preclinical models [4,6,11].

Biological technology development has enabled large-scale functional screening in human cancer cell lines [12,13]. Several consortium efforts have enabled the study of gene inhibition effect on cell proliferation, using siRNA (Demeter2)[14], CRISPR-Cas9 (DepMap) [15,16], or drugs (PRISM[17], CTRP[18]). In parallel, the cell lines in these studies have been molecularly characterized, with available genomic, transcriptomic, methylation and protein data[19]. Integration of these data allows the discovery of gene essentiality or proliferation-suppressive genes and synthetic lethality across cancer cell lines, with potential associated biomarkers[16,17,20,21]. However, these datasets have been generally exploited from a pan-cancer perspective, while there are likely cancer type specificities.

In this study, we analyzed the cancer dependency Map in urothelial cancer cells (UCC) specifically to gain insight into BCa biology and identify new potential therapeutic targets or efficient drugs.

Results

CRISPR screen identifies new putative tumor suppressor and dual genes including AHR/ARNT complex in urinary cancer cell lines (UCC)

To search for gene dependencies or proliferation suppressive genes in UCC, we analyzed DepMap 22Q2 (Cancer dependency Map) from the Project Achilles (Broad Institute), which is the largest database of CRISPR-CAS9 screening data (**Figure 1A**). This database includes a total of 1086 cell lines, including 31 UCC. We excluded 256 non-epithelial cell lines, i.e. hematological, from peripheral nervous system, bone or soft tissue, from our analysis.

In DepMap, genes with a positive Chronos value were demonstrated to suppress proliferation[20]. To identify proliferation suppressive genes in UCC, we selected genes presenting a Chronos score >0.4 in at least 2 cell lines (**Figure 1B**). We noticed that among the 29 proliferation suppressive genes, several presented a dual effect in UCC (pro-proliferative - Chronos score < -0.4 - or proliferation-suppressive effect) depending on the cell line, including *ARNT, CREBBP, TSC2, KEEP1, AMBRA1, EP300.* Eleven out of 29 genes were known to be tumor suppressor genes (TSGs) or dual TSG-oncogenes in COSMIC database (Cancer Gene Census - *NF2, PTEN, TSC1/2, CDKN1A, TP53, ARNT*) **(Figure 1B)**. We thus identified 18 new putative dual or TSGs, including *ZNF611, USP28, GNGT2, SOX13, PRAG1 or TNFRSF10B*. We further searched for genetic alterations that could support the tumor suppressor role of these 18 genes, in human MIBC from TCGA cohort (N=408)[22]. Deep-deletions and truncating mutations were observed in well-known TSGs *TP53* and *PTEN*, as expected (**Figure 1C**). We also observed deep deletions in PRAG1 (10%) and TNFRSF10B (9%), reinforcing the interest of further elucidating the tumor suppressor role of these two genes in UCC.

We also identified a potential dual role for ARNT depending on the cell line (**Figure 1B**). We recently described that AHR, its partner, was oncogenic in luminal urothelial cancer, and that APOBEC led to *AHR* Q383H activating mutation[23]. We therefore investigated if the complex and therefore AHR also displayed a dual role in UCC. The knock-out of either gene induced hyper-proliferation in several cell lines, enriched in basal subtype – with the strongest effect observed in UMUC6 – and cell death in others, the strongest effects being observed in TCCsup and UMUC9 (**Figure**

1D). Treatment of UMUC6 cells with FICZ, a specific and potent agonist of AHR, induced a dose-dependent decrease in cell viability after 72H, confirming the proliferation suppressive role of AHR in UMUC6. The cell-specificity of this role was further demonstrated by the absence of effect of FICZ treatment on UMUC9 cell viability (**Figure 1E**).

To further explore the molecular mechanism of the cell-specific proliferation suppressive effect of ARNT and AHR, we performed gene set enrichment analysis (GSEA) using the differentially expressed genes after 6h-treatment of FICZ 100nM in both cell lines (UMUC6 and UMUC9). We observed that DNA replication/repair and cell cycle checkpoints were inhibited in UMUC6 but not in UMUC9, while activated pathways were similar (**Figure 1F and supplementary Table 1 and Figure 1**).

DepMap analysis reveals essential genes operating more frequently in UCC than in other cancer cell lines

We then focused on genes whose knockout induced cell death or inhibition of cell proliferation in UCC cells and compared the frequency of their essentiality in UCC to other cell lines. Beside statistically significant difference ($p < 0.01$), we also filtered genes to be essential in at least 3 UCC. With this analysis, we found 43 genes that were more frequently essential in UCC compared to other cancer cell lines (**Figure 2A**). As expected, we found some genes known to be important in the biology of bladder cancer such as *PPARG/RXRA*[9,24] *or FGFR3*[25]*,* but also some new potential drivers. ARHGEF7 (Rho Guanine Nucleotide Exchange Factor 7) was the most frequently essential, in 77% of UCC versus 35% for others ($p<0.0001$) (**Figure 2A**). Interestingly, searching for biomarkers of ARHGEF7 dependency, we observed that ARHGEF7 dependency was the most correlated with *ARHGEF6* expression (an ARHGEF7 paralog) (Figure 2B, left panel). All the ARHGEF7-dependant UCC had a low expression of *ARHGEF6* (**Figure 2B, right panel**) supporting the idea of a synthetic lethality between this pair of paralogs in the context of UCC[26]. We then tried to identify potential efficient drug in ARHGEF7-dependent UCC, using the PRISM database. Dasatinib, a multi-target tyrosine kinase inhibitor (i.e Src, Bcr/Abl) was the most correlated drug with ARHGEF7 dependency in terms of AUC, offering a potential therapeutic strategy for ARHGEF7 high/ ARHGEF6 low MIBC (**Figure 2C**).

Aiming to identify complexes between these 43 essential genes, we then searched for their protein-protein interaction (PPI) using the STRING-db database (**Figure 2D**). We observed several protein complexes such as PPARG/RXR/RARG, BIRC2/RNF31, COMMD3/COMMD8 and B3GALT6/B3GAT3. We then decided to explore more deeply the RARG/RXRA/PPARG and BIRC2/RNF31 dependency.

DepMap reveals a pro-tumoral role of the RXRα/RARγ complex in Ba/Sq MIBC

PPARγ pathway activation in luminal tumors through *PPARG* amplification or activating mutations of either *PPARG* or its heterodimeric partner *RXRA* has been demonstrated to induce both cell and non-cell autonomous pro-tumoral activities[4,7,9,22,24,27]

We then further analyzed UCC co-dependency to PPARG, RXRA and RARG. We discovered that beyond its key role in *PPARG* dependency in luminal UCC, *RXRA* could also drive a *RARG* dependency in a cluster of UCC enriched in basal/squamous subtype (UMUC6, KU1919, RT112/ and CAL29) (**Figure 3A**). A significant correlation of dependency in UCC was observed between *RXRA* and *PPARG* but also between *RXRA* and *RARG.* In contrast, the dependency correlation between *PPARG* and *RARG* was low, supporting that the two do not form a functional complex (**Figure 3B**). We then assessed the relevance of both RXRα/RARγ and RXRα/PPARγ complexes in MIBC. We inferred RXRα, PPARγ and RARγ protein activity using VIPER algorithm and the respective signature, or “regulon”, proposed in bladder TCGA cohort [22]. We observed 3 subgroups of MIBCs among tumors with high RXRα regulon activity (high≥ median): PPARγ$^{\mathbf{high}}$/RARγ$^{\text{low}}$ observed in LumU MIBC, PPARγ$^{\mathbf{high}}$/RARγ$^{\mathbf{high}}$ observed in LumP and PPARγ$^{\text{low}}$/RARγ$^{\mathbf{high}}$ observed in Ba/Sq MIBC (**Figure 3C**). Given the protumoral role of RXRA/RARG (**Figure 3A**), the PPARγ-independent but RARγ-dependent activation of RXRα in Ba/Sq tumors and some LumU suggested a therapeutic benefit for RARγ inhibitors. We treated UCCs with a pan-RAR inhibitor, AGN-194310. *RARG*-dependent cells (KU1919/UMUC6) showed a moderate decrease in cell viability after 72h of treatment, unlike the two *RARG*-independent cell lines (VMCUB1/UMUC9) (**Figure 3D**).

BIRC2 dependency and Smac-mimetics efficacy in UCC *in vitro* and *in vivo*

We finally focused on a second complex involving two essential genes, *BIRC2* (=cIAP1) and *RNF31* (E3 ubiquitin-protein ligase involved in the LUBAC complex) (Figure 3D). This complex was of particular interest given its involvement in the inhibition of apoptosis/necroptosis (via inhibition of caspases) and activation of NFKB pathway, after activation of receptor such as TNF-receptor[28–31.]

Supporting that the two proteins form a complex, we observed a co-dependency for both genes in UCC (Pearson correlation R=0.48, p=0.0079), (**Figure 4A).** Furthermore, we observed that one line cell, SCaBER, was amplified for *BIRC2* (**Figure 4A**). Interestingly *BIRC2* amplifications were also observed in ~5% of MIBCs (TCGA cohort, n=408) and were associated with a higher expression of *BIRC2* (**Figure 4B**).

cIAP1-2/XIAP can be inhibited using Smac mimetics. We wondered whether BIRC2-dependent UCC could be sensitive to these inhibitors. We first explored publicly available data from Prism drug screen testing 3 Smac mimetics (birinapant, LCL161 and GDC-0152) in UCC. *BIRC2*-amplified cell line - SCaBER - was sensitive (**Figure 4C)**. We searched for other biomarkers of efficacy of the 3 inhibitors at the expression level and observed that *RIPK1* expression was the most anti-correlated gene between inhibitors AUC and expression level (**Figure 4D**). Interestingly, *RIPK1* was already shown to be a biomarker of smac mimetic sensitivity in other studies [32]. We then sought to validate the efficacy of one of the smac mimetics, birinapant, in the *BIRC2*-amplified cell line (SCaBER), a cell-line with a high *RIPK1* expression (UMUC14, also BIRC2-dependent according to DepMap, **Figure 4A),** and two BIRC2-independent control cell lines (KU1919/TCCSUP). We observed that birinapant was efficient especially in the SCaBER cell line and UMUC14, and ineffective in TCCSUP/KU1919 (**Figure 4E**). We observed an increase in caspase 3/7 activity at 24h after birinapant treatment in UMUC14 and SCaBER, demonstrating that apoptosis induction was one mechanism of action of the drug (**Figure 4F**).

We finally confirmed *in vivo* the efficacy of birinapant treatment in xenografts of SCaBER (**Figure 4G**) or UMUC14 cells (**Figure 4H).** Of note, the effect observed for UMUC14 was significant when tumor size was measured after dissection, avoiding size variability associated with the presence of an important hematoma (**Figure 4H**, right panel).

Our results showed that Smac mimetics were efficient in a significant proportion of UCC and suggested that *BIRC2* amplification or *RIPK1* expression might be potential biomarkers of efficacy in urothelial cancer.

Discussion

In this study, we explored the CRISPR screen data gathered in DepMap database to identify new pro-tumoral genes or genes with proliferation-suppressive effects in UCC.

We identified genes with a proliferation-suppressive effect, such as *PRAG1* or *TNFRSF10B,* and genes with dual pro-tumoral and tumor suppressive effect, such as *ARNT* and its binding partner *AHR.* This dual effect, associated with molecular subtypes, could impact clinical practice as AHR inhibitors are currently being investigated in clinical trials (e.g., NCT05472506).

Within the nuclear receptor family, the role of PPARγ/RXRα complex in urothelial cancer has been described in recent years [33]. PPARγ has been shown to be protumorigenic in luminal tumors, and a tumor suppressor in basal tumors[9,34]. Here, we identified a pro-tumorigenic PPARG-independent but RARG-dependent role of RXRA mostly identified in basal tumors. Recently, mutations in *RARG* have been described, although their functional impact is unknown [35]. In LumP tumors, we observed a high activity for the three nuclear receptors, the regulation of the complexes in this context remains to be explored. Indeed, we can hypothesize that a competitive binding with RXRα can modulate RARy or PPARγ activity.

Smac mimetics have been developed for several years to treat different cancer types[36]. In preclinical models, Smac mimetic efficacy has been observed in breast[32,37–39], ovarian[40,40,41], gastric[42], colorectal[43] and other cancer models. Some studies have reported the existence of a *BIRC2* amplification, shown to be oncogenic [44], and a potential biomarker of Smac mimetic sensitivity in head and neck cancer [45–47]. *In vitro,* a study found only 1/6 urinary cell lines to be sensitive to birinapant (J82)[28], another described RT112 as moderately sensitive[48] and recently a novel Smac-mimetic Tolinapant was reported inefficient in RT4 and 5637[49]. Smac-mimetics have been shown to act through induction of apoptosis[39,50], to increase TNF-a expression and NFKB pathway. Here, the sensitivity to birinapant treatment we observed for two UCCs was associated with an increase in caspase3/7 activity, in agreement with the described pro-apoptotic role of birinapant. Birinapant sensitivity was associated with *BIRC2* amplification, found in 5% of MIBCs, or *RIPK1* overexpression. Gemcitabine or carboplatin, used in the clinical management of MIBC, have been shown to be synergistic with birinapant in other tumor models[39,40,40,41.] . This observation suggests that treatment combinations, such as Gemcitabine-birinapant could be tested in clinical practice, in particular for cisplatin-ineligible patients.

Conclusion

Analysis of CRISPR screen from DepMap database identified a dual role for AHR/ARNT complex with pro-tumoral properties in luminal tumors and tumor suppressive properties in basal tumors, and pro-tumoral properties for ARHGEF7 and BIRC2. It also reveals a PPARγ -independent but RARγ dependent pro-tumoral role for RXRα in basal tumors. The identification of these new driver genes allowed us to propose new potential therapies including birinapant in urinary cancer cells.

Figure Legends

Figure 1: Identification of new proliferation suppressive or dual genes in UCC through CRISPR screen analysis in DepMap

A Design of the analysis of DepMap CRISPR-Cas9 knockout screen Database

B Distribution of Chronos score for each gene with a proliferation-suppressive effect in UCC. Genes are colored according to their role in COSMIC Cancer Gene Census database.

C OncoPrint showing the distribution of genomic alterations of 18 new potential dual or tumor suppressor genes in 408 MIBC from TCGA. TP53 and PTEN TSG were used as control.

D Heatmap of UCC based on AHR and ARNT DepMap Chronos score.

E Effect on cell viability measured by cell titer-Glo of FICZ (100nm) after 72h of treatment in UMUC6 or UMUC9. Data are presented as mean ± SD of 3 independent experiment.

F Gene set enrichment analysis (GSEA) of differentially expressed genes (DEG) after FICZ (6h, 100nM) in UMUC6 or UMUC9.

Figure 2: Identification of essential genes operating more frequently in UCC than in other cancer cells.

A Volcano plot based on the percentage difference of genes predicted as essential in UCC versus others (In red genes with $p<0.01$ and essentials in at least 3 UCC).

B List of genes whose expression is significantly correlated with ARHGEF7 dependency in UCC (left) and scatterplot of ARHGEF7 dependency and ARHGEF6 expression in UCC (right)

C Correlation between ARHGEF7 dependency in DepMap and drug efficacy in the PRISM database (left) and scatter plot of dasatinib AUC versus ARHGEF7 dependency in UCC (right)

D Protein–protein interactions from the STRING database between genes predicted as essential in urinary cell lines (High confidence >0.7)

Figure 3: Pro-tumoral role of RXRA/RARG in basal MIBC

A Heatmap of UCC based on *PPARG*, *RXRA* and *RARG* dependency probability (DepMap) according to molecular subtype and *PPARG/RXRA* genomic alterations

B Correlation between *PPARG*, *RXRA* and *RARG* Chronos score in UCC

C Protein activity of PPARy and RARy according to the molecular consensus class in MIBC bladder cancer (TGCA) with a high-RXRα protein activity (defined by protein activity ≥ median).

D In vitro efficacy of AGN194310 (pan-RAR inhibitor) after 72h of treatment in 4 UCC. Data are presented as mean ± SD of 3 independent experiments conducted in triplicate. Statistical differences were evaluated using Student t-test.

Figure 4: BIRC2 dependency and Smac mimetics efficacy in UCC

A Correlation between *BIRC2* and *RNF31* Chronos score in UCC

B Correlation between *BIRC2* copy number alterations and RNA expression in MIBC from TCGA cohort(n=408)

C Smac mimetics efficacy in Prism (AUC) in UCC, with SCaBER as unique UCC presenting a *BIRC2*-amplification

D Correlation between *in vitro* birinapant efficacy and RNA expression in UCC. AUC for each drug was determined in Prism

E *In vitro* evaluation of effect of birinapant on cell viability measured by cellTiterGlo after 72h of treatment in a panel of UCC. Data are presented as mean ± SD of three independent experiments conducted in triplicate. AUC was computed from the experiment. *RIPK1* expression and *BIRC2* amplification status come from CCLE database

F *In vitro* Caspase 3/7 activity after 24h of birinapant in UMUC14 (left) and SCaBER (right)

G-H In vivo efficacy of birinapant in mice xenografts of SCaBER (left) and UMUC14 (right). Mice with established SCaBER **(G)** or UMUC14 **(H)** xenografts were treated with birinapant (intraperitoneal, 30mg/kg, red) or control vehicle alone (blue) every 3 days (5 animals per group with 2 tumors/animal). Tumor size was measured at the indicated time points. Data are presented as mean ± sem. Results were compared using Mann-Whitney test. **H, right panel,** for UMUC14 due to the presence of hematoma, resected lesions were measured after tumor dissection.

Supplemental Figure 1: Most significant regulated pathways and genes after AHR agonist (FICZ) treatment

A Most enriched Reactome pathways score determined by GSEA of differentially expressed genes after FICZ treatment in UMUC6 or UMUC9 (top 20 pathways in each cell lines ranked by p-value after the following filters: NES > 1.8 and p-value < 0.01). The level of significance of the pathway enrichment is indicated for each cell lines (* p<0.05, ** p<0.01, *** p<0.001, ns: not significant).

B Gene-Concept network of the top ten enriched pathway after FICZ treatment in UMUC6.

Supplemental Table 1: Differentially expressed genes after FICZ (AHR agonist) treatment (6h) in UMUC6 or UMUC9 and Gene Set Enrichment Analysis

Methods

Cell-lines, DepMap and multi-omics data

Genome-wide CRISPR dependency data (DepMap Public 22Q2 Primary Files) were downloaded from Broad Institute DepMap web portal (https://DepMap.org/portal/download/).

We defined a gene as essential in a cell line if the Probability that knocking out the gene has a real depletion was ≥50% in the 22Q2CRISPR_gene_dependency file from DepMap portal.

We defined a gene with a proliferation-suppressive effect in cell line if the Chronos score was >0.4 (for example, PTEN a known tumor-suppressor had a median at ~0.2). Tumor suppressor, dual gene or oncogene status were retrieved from the COSMIC Cancer Gene Census (version v96).

Cancer cells information, including mutation, gene expression, gene-level relative copy number data were retrieved from the Cancer Cell Line Encyclopedia (CCLE) project (22Q2). These multi-omics data can be downloaded from Broad Institute DepMap web portal (https://DepMap.org/portal/download/).

Drug sensitivity Area under the ROC Curve (AUC) in PRISM repurposing screen 19Q4 release (PRISM) can be accessed from Broad Institute DepMap web portal (https://depmap.org/portal/download/). For each drug, we considered the results of the most recent screen (MTS010, MTS006, MTS005, HTS002 in that order). All values of AUC superior to 1 were discarded.

TCGA-BLCA MIBC RNA-seq data were downloaded from Xena Browser (https://gdc.xenahubs.net/download/TCGA-BLCA.htseq_counts.tsv.gz).

Protein activity - VIPER

The VIPER algorithm tests for protein/regulon enrichment based on gene expression signatures [51], using the signatures obtained from bladder TCGA[22], and we computed the enrichment of each protein/regulon on the gene expression signature using different implementations of the analytic Rank-based Enrichment Analysis algorithm (Dorothea Package R v1.2.2).

Cell culture

The human bladder cancer-derived cell lines UMUC9, UMUC14, VMCUB1, SCaBER, UMUC6, CAL29, KU1919, TCCSUP were obtained from DSMZ (Heidelberg, Germany). KMBC2 cells were purchased from JCRB cell bank (Japan). RT112 and KU1919 cells were cultured in RPMI medium and all the other cells were cultured in DMEM medium, at 37 °C in an atmosphere of 5% CO2 in. All cell media were supplemented with 10% fetal bovine serum (FBS). Cells were routinely tested for mycoplasma contamination.

Drug

AGN-194310, birinapant and FICZ (6-Formylindolo[3,2-b]carbazole) were purchased from MedChemExpress®.

Cell viability assay and caspase-3/7 activity measures

Cells were seeded in triplicate in 96-well plates and left to adhere overnight. Afterwards, cells were treated for 72 h with gradient concentrations of the tested drugs. Control cells were treated with DMSO.

Cell viability was assessed with the CellTiter-Glo assay (Promega®) after 72 h of treatment.

Caspase-3/7 activity were measured using Caspase-Glo® 3/7 assay system (Promega #G8091).

Xenograft models

Six-week-old female Swiss nu/nu mice (Charles River Laboratories, Saint-Germain-Nuelles, France) were raised in the animal facilities of Institut Curie, in specific pathogen-free conditions. They were housed and cared for in accordance with the institutional guidelines of the French National Ethics Committee (Ministère de l’Agriculture et de la Forêt, Direction de la Santé et de la Protection Animale, Paris, France), under the supervision of authorized investigators. Experimental procedures were specifically approved by the ethics committee of the Institut Curie CEEA-IC #118 (Authorization APAFiS#26671 2020072108262352-v2 given by National Authority) in compliance with the international guidelines. Mice received a subcutaneous injection, into each flank (dorsal region), of 5×10^6 UMUC14 or SCaBER bladder cancer cells.

Mice were randomly separated into groups of five mice when tumours reached a volume of 50 mm3 (±5). Mice were treated every 3 days, with an intraperitoneal injection of birinapant (30mg/kg, 10% captisol and 10% DMSO) or of vehicle (Captisol 10%/DMSO10%)), until ethical necessity to sacrifice mice in the control group.

Tumor size was measured with a calliper, and tumour volume in mm3 was calculated as follows: π/6 × (largest diameter) × (shortest diameter)2. For UMUC14 due to the presence of hematoma, tumor size was also measured after tumor dissection.

RNA extraction and sequencing

Cell lines 3'RNA-seq (Lexogen 3'Seq)

Cell lines RNA were extracted using Qiagen RNeasy kit coupled with DNAse treatment.

RNA sequencing libraries were prepared from 200ng of total RNA using the QuantSeq FWD 3'mRNA Seq LEXOGEN Standard (CliniSciences). Libraries were prepared according to the manufacturer's recommendations. The first step enables the synthesis of double strand cDNA, by revers transcription, using oligo dT priming. A qPCR optimization step was performed in order to estimate the most appropriate number of PCR cycles for library amplification. The resulting amplified and barcoded libraries were then equimolarly pooled and quantified using a qPCR method (KAPA library quantification kit, Roche). The sequencing was carried out using single-read mode (SR100) on an Illumina Novaseq 6000 instrument. The sequencing configuration was set to reach an average of 10 million reads per sample. RNA-seq analysis

RNA-seq were aligned on genome hg38 using STAR with default parameters. RNA-seq were integrated using Deseq2 default parameters and rlog normalization, then analyzed with Deseq2.

UCC molecular classification

The method for the molecular classification of UCC was described elsewhere[52]

Pathway enrichment

Gene-set enrichment analysis (GSEA) was used with shrunken log2 fold-change values resulting from the differential expression analysis between control and treated cell lines. Human pathways were sourced from Reactome as implemented in R package

ReactomePA (v 1.34.0) and Normalized enrichment scores, cnetplot and GSEA plot were then obtained using also ReactomePA.

Statistical and bioinformatics analysis

Wilcoxon's rank sum test, Fisher's exact test and Kruskal-Wallis tests were used for the comparisons. Pearson correlation coefficient was used for correlation analysis. A value of $P < 0.05$ in two-tailed tests was considered statistically significant. For the comparison of data between xenograft treatments, the non-parametric Wilcoxon test was used, with the vehicle group as the reference group.

AUC (Area Under the drug response Curve) was computed with the function computeAUC from the R package PharmacoGx (v2.6.0).

R version 4.0.2.4 or ggplot2 3.3.5 were used for analyses and for the associated visualizations.

Acknowledgement

This work was supported by the Fondation pour la Recherche Médicale, grant number FDM201906008607, to LC

Bibliography

1. Sung, H., Ferlay, J., Siegel, R.L., Laversanne, M., Soerjomataram, I., Jemal, A., and Bray, F. (2021). Global Cancer Statistics 2020: GLOBOCAN Estimates of Incidence and Mortality Worldwide for 36 Cancers in 185 Countries. CA. Cancer J. Clin. *71*, 209–249. 10.3322/caac.21660.

2. Flaig, T.W., Spiess, P.E., Agarwal, N., Bangs, R., Boorjian, S.A., Buyyounouski, M.K., Chang, S., Downs, T.M., Efstathiou, J.A., Friedlander, T., et al. (2020). Bladder Cancer, Version 3.2020, NCCN Clinical Practice Guidelines in Oncology. J. Natl. Compr. Cancer Netw. JNCCN *18*, 329–354. 10.6004/jnccn.2020.0011.

3. Loriot, Y., Necchi, A., Park, S.H., Garcia-Donas, J., Huddart, R., Burgess, E., Fleming, M., Rezazadeh, A., Mellado, B., Varlamov, S., et al. (2019). Erdafitinib in Locally Advanced or Metastatic Urothelial Carcinoma. N. Engl. J. Med. *381*, 338–348. 10.1056/NEJMoa1817323.

4. Kamoun, A., de Reyniès, A., Allory, Y., Sjödahl, G., Robertson, A.G., Seiler, R., Hoadley, K.A., Groeneveld, C.S., Al-Ahmadie, H., Choi, W., et al. (2020). A Consensus Molecular Classification of Muscle-invasive Bladder Cancer. Eur. Urol. *77*, 420–433. 10.1016/j.eururo.2019.09.006.

5. Biton, A., Bernard-Pierrot, I., Lou, Y., Krucker, C., Chapeaublanc, E., Rubio-Pérez, C., López-Bigas, N., Kamoun, A., Neuzillet, Y., Gestraud, P., et al. (2014). Independent component analysis uncovers the landscape of the bladder tumor transcriptome and reveals insights into luminal and basal subtypes. Cell Rep. *9*, 1235–1245. 10.1016/j.celrep.2014.10.035.

6. Choi, W., Czerniak, B., Ochoa, A., Su, X., Siefker-Radtke, A., Dinney, C., and McConkey, D.J. (2014). Intrinsic basal and luminal subtypes of muscle-invasive bladder cancer. Nat. Rev. Urol. *11*, 400–410. 10.1038/nrurol.2014.129.

7. Halstead, A.M., Kapadia, C.D., Bolzenius, J., Chu, C.E., Schriefer, A., Wartman, L.D., Bowman, G.R., and Arora, V.K. (2017). Bladder-cancer-associated mutations in RXRA activate peroxisome proliferator-activated receptors to drive urothelial proliferation. eLife *6*. 10.7554/eLife.30862.

8. Korpal, M., Puyang, X., Jeremy Wu, Z., Seiler, R., Furman, C., Oo, H.Z., Seiler, M., Irwin, S., Subramanian, V., Julie Joshi, J., et al. (2017). Evasion of immunosurveillance by genomic alterations of PPARγ/RXRα in bladder cancer. Nat. Commun. *8*, 103. 10.1038/s41467-017-00147-w.

9. Rochel, N., Krucker, C., Coutos-Thévenot, L., Osz, J., Zhang, R., Guyon, E., Zita, W., Vanthong, S., Hernandez, O.A., Bourguet, M., et al. (2019). Recurrent activating mutations of PPARγ associated with luminal bladder tumors. Nat. Commun. *10*, 253. 10.1038/s41467-018-08157-y.

10. Warrick, J.I., Walter, V., Yamashita, H., Chung, E., Shuman, L., Amponsa, V.O., Zheng, Z., Chan, W., Whitcomb, T.L., Yue, F., et al. (2016). FOXA1, GATA3 and PPARɣ Cooperate to Drive Luminal Subtype in Bladder Cancer: A Molecular Analysis of Established Human Cell Lines. Sci. Rep. *6*, 38531. 10.1038/srep38531.

11. Rebouissou, S., Bernard-Pierrot, I., de Reyniès, A., Lepage, M.-L., Krucker, C., Chapeaublanc, E., Hérault, A., Kamoun, A., Caillault, A., Letouzé, E., et al. (2014). EGFR as a potential therapeutic target for a subset of muscle-invasive bladder cancers presenting a basal-like phenotype. Sci. Transl. Med. *6*, 244ra91. 10.1126/scitranslmed.3008970.

12. Choi, A., Jang, I., Han, H., Kim, M.-S., Choi, J., Lee, J., Cho, S.-Y., Jun, Y., Lee, C., Kim, J., et al. (2021). iCSDB: an integrated database of CRISPR screens. Nucleic Acids Res. *49*, D956–D961. 10.1093/nar/gkaa989.

13. Onishi, I., Yamamoto, K., Kinowaki, Y., Kitagawa, M., and Kurata, M. (2021). To Discover the Efficient and Novel Drug Targets in Human Cancers Using CRISPR/Cas Screening and Databases. Int. J. Mol. Sci. *22*, 12322. 10.3390/ijms222212322.

14. McFarland, J.M., Ho, Z.V., Kugener, G., Dempster, J.M., Montgomery, P.G., Bryan, J.G., Krill-Burger, J.M., Green, T.M., Vazquez, F., Boehm, J.S., et al. (2018). Improved estimation of cancer dependencies from

large-scale RNAi screens using model-based normalization and data integration. Nat. Commun. *9*, 4610. 10.1038/s41467-018-06916-5.

15. Meyers, R.M., Bryan, J.G., McFarland, J.M., Weir, B.A., Sizemore, A.E., Xu, H., Dharia, N.V., Montgomery, P.G., Cowley, G.S., Pantel, S., et al. (2017). Computational correction of copy number effect improves specificity of CRISPR-Cas9 essentiality screens in cancer cells. Nat. Genet. *49*, 1779–1784. 10.1038/ng.3984.

16. Tsherniak, A., Vazquez, F., Montgomery, P.G., Weir, B.A., Kryukov, G., Cowley, G.S., Gill, S., Harrington, W.F., Pantel, S., Krill-Burger, J.M., et al. (2017). Defining a Cancer Dependency Map. Cell *170*, 564-576.e16. 10.1016/j.cell.2017.06.010.

17. Yu, C., Mannan, A.M., Yvone, G.M., Ross, K.N., Zhang, Y.-L., Marton, M.A., Taylor, B.R., Crenshaw, A., Gould, J.Z., Tamayo, P., et al. (2016). High-throughput identification of genotype-specific cancer vulnerabilities in mixtures of barcoded tumor cell lines. Nat. Biotechnol. *34*, 419–423. 10.1038/nbt.3460.

18. Seashore-Ludlow, B., Rees, M.G., Cheah, J.H., Cokol, M., Price, E.V., Coletti, M.E., Jones, V., Bodycombe, N.E., Soule, C.K., Gould, J., et al. (2015). Harnessing Connectivity in a Large-Scale Small-Molecule Sensitivity Dataset. Cancer Discov. *5*, 1210–1223. 10.1158/2159-8290.CD-15-0235.

19. Ghandi, M., Huang, F.W., Jané-Valbuena, J., Kryukov, G.V., Lo, C.C., McDonald, E.R., Barretina, J., Gelfand, E.T., Bielski, C.M., Li, H., et al. (2019). Next-generation characterization of the Cancer Cell Line Encyclopedia. Nature *569*, 503–508. 10.1038/s41586-019-1186-3.

20. Lenoir, W.F., Morgado, M., DeWeirdt, P.C., McLaughlin, M., Griffith, A.L., Sangree, A.K., Feeley, M.N., Esmaeili Anvar, N., Kim, E., Bertolet, L.L., et al. (2021). Discovery of putative tumor suppressors from CRISPR screens reveals rewired lipid metabolism in acute myeloid leukemia cells. Nat. Commun. *12*, 6506. 10.1038/s41467-021-26867-8.

21. Christodoulou, E., Rashid, M., Pacini, C., Droop, A., Robertson, H., Groningen, T. van, Teunisse, A.F.A.S., Iorio, F., Jochemsen, A.G., Adams, D.J., et al. (2020). Analysis of CRISPR-Cas9 screens identifies genetic dependencies in melanoma. Pigment Cell Melanoma Res. 10.1111/pcmr.12919.

22. Robertson, A.G., Kim, J., Al-Ahmadie, H., Bellmunt, J., Guo, G., Cherniack, A.D., Hinoue, T., Laird, P.W., Hoadley, K.A., Akbani, R., et al. (2017). Comprehensive Molecular Characterization of Muscle-Invasive Bladder Cancer. Cell *171*, 540-556.e25. 10.1016/j.cell.2017.09.007.

23. Shi, M.-J., Meng, X.-Y., Fontugne, J., Chen, C.-L., Radvanyi, F., and Bernard-Pierrot, I. (2020). Identification of new driver and passenger mutations within APOBEC-induced hotspot mutations in bladder cancer. Genome Med. *12*, 85. 10.1186/s13073-020-00781-y.

24. Goldstein, J.T., Berger, A.C., Shih, J., Duke, F.F., Furst, L., Kwiatkowski, D.J., Cherniack, A.D., Meyerson, M., and Strathdee, C.A. (2017). Genomic Activation of PPARG Reveals a Candidate Therapeutic Axis in Bladder Cancer. Cancer Res. *77*, 6987–6998. 10.1158/0008-5472.CAN-17-1701.

25. Mahe, M., Dufour, F., Neyret-Kahn, H., Moreno-Vega, A., Beraud, C., Shi, M., Hamaidi, I., Sanchez-Quiles, V., Krucker, C., Dorland-Galliot, M., et al. (2018). An FGFR3/MYC positive feedback loop provides new opportunities for targeted therapies in bladder cancers. EMBO Mol. Med. *10*. 10.15252/emmm.201708163.

26. De Kegel, B., Quinn, N., Thompson, N.A., Adams, D.J., and Ryan, C.J. (2021). Comprehensive prediction of robust synthetic lethality between paralog pairs in cancer cell lines. Cell Syst. *12*, 1144-1159.e6. 10.1016/j.cels.2021.08.006.

27. Choi, W., Porten, S., Kim, S., Willis, D., Plimack, E.R., Hoffman-Censits, J., Roth, B., Cheng, T., Tran, M., Lee, I.-L., et al. (2014). Identification of distinct basal and luminal subtypes of muscle-invasive bladder cancer with different sensitivities to frontline chemotherapy. Cancer Cell *25*, 152–165. 10.1016/j.ccr.2014.01.009.

28. Benetatos, C.A., Mitsuuchi, Y., Burns, J.M., Neiman, E.M., Condon, S.M., Yu, G., Seipel, M.E., Kapoor, G.S., Laporte, M.G., Rippin, S.R., et al. (2014). Birinapant (TL32711), a bivalent SMAC mimetic, targets TRAF2-associated cIAPs, abrogates TNF-induced NF-κB activation, and is active in patient-derived xenograft models. Mol. Cancer Ther. *13*, 867–879. 10.1158/1535-7163.MCT-13-0798.

29. Borghi, A., Verstrepen, L., and Beyaert, R. (2016). TRAF2 multitasking in TNF receptor-induced signaling to NF-κB, MAP kinases and cell death. Biochem. Pharmacol. *116*, 1–10. 10.1016/j.bcp.2016.03.009.

30. Shen, R.R., Zhou, A.Y., Kim, E., O'Connell, J.T., Hagerstrand, D., Beroukhim, R., and Hahn, W.C. (2015). TRAF2 is an NF-κB activating oncogene in epithelial cancers. Oncogene *34*, 209–216. 10.1038/onc.2013.543.

31. Zhu, J., Zhuang, T., Yang, H., Li, X., Liu, H., and Wang, H. (2016). Atypical ubiquitin ligase RNF31: the nuclear factor modulator in breast cancer progression. BMC Cancer *16*, 538. 10.1186/s12885-016-2575-8.

32. Bardia, A., Parton, M., Kümmel, S., Estévez, L.G., Huang, C.-S., Cortés, J., Ruiz-Borrego, M., Telli, M.L., Martin-Martorell, P., López, R., et al. (2018). Paclitaxel With Inhibitor of Apoptosis Antagonist, LCL161, for Localized Triple-Negative Breast Cancer, Prospectively Stratified by Gene Signature in a Biomarker-Driven Neoadjuvant Trial. J. Clin. Oncol. Off. J. Am. Soc. Clin. Oncol., JCO2017748392. 10.1200/JCO.2017.74.8392.

33. Peng, T., Wang, G., Cheng, S., Xiong, Y., Cao, R., Qian, K., Ju, L., Wang, X., and Xiao, Y. (2020). The role and function of PPARγ in bladder cancer. J. Cancer *11*, 3965–3975. 10.7150/jca.42663.

34. Kamoun, A., de Reyniès, A., Allory, Y., Sjödahl, G., Robertson, A.G., Seiler, R., Hoadley, K.A., Groeneveld, C.S., Al-Ahmadie, H., Choi, W., et al. (2019). A Consensus Molecular Classification of Muscle-invasive Bladder Cancer. Eur. Urol. 10.1016/j.eururo.2019.09.006.

35. Nakauma-González, J.A., Rijnders, M., van Riet, J., van der Heijden, M.S., Voortman, J., Cuppen, E., Mehra, N., van Wilpe, S., Oosting, S.F., Rijstenberg, L.L., et al. (2022). Comprehensive Molecular Characterization Reveals Genomic and Transcriptomic Subtypes of Metastatic Urothelial Carcinoma. Eur. Urol. *81*, 331–336. 10.1016/j.eururo.2022.01.026.

36. Chang, Y.-C., and Cheung, C.H.A. (2021). An Updated Review of Smac Mimetics, LCL161, Birinapant, and GDC-0152 in Cancer Treatment. Appl. Sci. *11*, 335. 10.3390/app11010335.

37. Benetatos, C.A., Mitsuuchi, Y., Burns, J.M., Neiman, E.M., Condon, S.M., Yu, G., Seipel, M.E., Kapoor, G.S., Laporte, M.G., Rippin, S.R., et al. (2014). Birinapant (TL32711), a bivalent SMAC mimetic, targets TRAF2-associated cIAPs, abrogates TNF-induced NF-κB activation, and is active in patient-derived xenograft models. Mol. Cancer Ther. *13*, 867–879. 10.1158/1535-7163.MCT-13-0798.

38. Guillen, K.P., Fujita, M., Butterfield, A.J., Scherer, S.D., Bailey, M.H., Chu, Z., DeRose, Y.S., Zhao, L., Cortes-Sanchez, E., Yang, C.-H., et al. (2022). A human breast cancer-derived xenograft and organoid platform for drug discovery and precision oncology. Nat. Cancer *3*, 232–250. 10.1038/s43018-022-00337-6.

39. Xie, X., Lee, J., Liu, H., Pearson, T., Lu, A.Y., Tripathy, D., Devi, G.R., Bartholomeusz, C., and Ueno, N.T. (2021). Birinapant Enhances Gemcitabine's Antitumor Efficacy in Triple-Negative Breast Cancer by Inducing Intrinsic Pathway-Dependent Apoptosis. Mol. Cancer Ther. *20*, 296–306. 10.1158/1535-7163.MCT-19-1160.

40. Hernandez, L.F., Dull, A.B., Korrapati, S., and Annunziata, C.M. (2021). Smac-mimetic enhances antitumor effect of standard chemotherapy in ovarian cancer models via Caspase 8-independent mechanism. Cell Death Discov. *7*, 134. 10.1038/s41420-021-00511-2.

41. Singh, T., Neal, A., Dibernardo, G., Raheseparian, N., Moatamed, N.A., and Memarzadeh, S. (2022). Efficacy of birinapant in combination with carboplatin in targeting platinum-resistant epithelial ovarian cancers. Int. J. Oncol. *60*, 35. 10.3892/ijo.2022.5325.

42. Zhu, D.L., and Shuai, L.Y. (2021). Effects of Birinapant on Proliferation and Invasion of MGC-803 Gastric Cancer Cells and Mechanism Underlying These Effects. Bull. Exp. Biol. Med. *171*, 56–61. 10.1007/s10517-021-05172-w.

43. McCann, C., Matveeva, A., McAllister, K., Van Schaeybroeck, S., Sessler, T., Fichtner, M., Carberry, S., Rehm, M., Prehn, J.H.M., and Longley, D.B. (2021). Development of a protein signature to enable clinical positioning of IAP inhibitors in colorectal cancer. FEBS J. *288*, 5374–5388. 10.1111/febs.15801.

44. Choschzick, M., Tabibzada, A.M., Gieseking, F., Woelber, L., Jaenicke, F., Sauter, G., and Simon, R. (2012). BIRC2 amplification in squamous cell carcinomas of the uterine cervix. Virchows Arch. Int. J. Pathol. *461*, 123–128. 10.1007/s00428-012-1268-1.

45. Eytan, D.F., Snow, G.E., Carlson, S., Derakhshan, A., Saleh, A., Schiltz, S., Cheng, H., Mohan, S., Cornelius, S., Coupar, J., et al. (2016). SMAC Mimetic Birinapant plus Radiation Eradicates Human Head and Neck Cancers with Genomic Amplifications of Cell Death Genes FADD and BIRC2. Cancer Res. *76*, 5442–5454. 10.1158/0008-5472.CAN-15-3317.

46. Imoto, I., Yang, Z.Q., Pimkhaokham, A., Tsuda, H., Shimada, Y., Imamura, M., Ohki, M., and Inazawa, J. (2001). Identification of cIAP1 as a candidate target gene within an amplicon at 11q22 in esophageal squamous cell carcinomas. Cancer Res. *61*, 6629–6634.

47. Roohollahi, K., de Jong, Y., Pai, G., Zaini, M.A., de Lint, K., Sie, D., Rooimans, M.A., Rockx, D., Hoskins, E.E., Ameziane, N., et al. (2022). BIRC2-BIRC3 amplification: a potentially druggable feature of a subset of head and neck cancers in patients with Fanconi anemia. Sci. Rep. *12*, 45. 10.1038/s41598-021-04042-9.

48. Vallo, S., Stege, H., Berg, M., Michaelis, M., Winkelmann, R., Rothweiler, F., and Cinatl, J. (2020). Tumor necrosis factor-related apoptosis-inducing ligand as a therapeutic option in urothelial cancer cells with acquired resistance against first-line chemotherapy. Oncol. Rep. *43*, 1331–1337. 10.3892/or.2020.7487.

49. Wang, L., Hu, C., Zhao, Y., and Hu, X. (2022). Novel smac mimetic ASTX660 (Tolinapant) and TNF-α synergistically induce necroptosis in bladder cancer cells in vitro upon apoptosis inhibition. Biochem. Biophys. Res. Commun. *602*, 8–14. 10.1016/j.bbrc.2022.02.053.

50. Ma, O., Cai, W.-W., Zender, L., Dayaram, T., Shen, J., Herron, A.J., Lowe, S.W., Man, T.-K., Lau, C.C., and Donehower, L.A. (2009). MMP13, Birc2 (cIAP1), and Birc3 (cIAP2), amplified on chromosome 9, collaborate with p53 deficiency in mouse osteosarcoma progression. Cancer Res. *69*, 2559–2567. 10.1158/0008-5472.CAN-08-2929.

51. Alvarez, M.J., Shen, Y., Giorgi, F.M., Lachmann, A., Ding, B.B., Ye, B.H., and Califano, A. (2016). Functional characterization of somatic mutations in cancer using network-based inference of protein activity. Nat. Genet. *48*, 838–847. 10.1038/ng.3593.

52. Neyret-Kahn, H., Fontugne, J., Meng, X.Y., Groeneveld, C.S., Cabel, L., Ye, T., Guyon, E., Krucker, C., Dufour, F., Chapeaublanc, E., et al. (2022). Epigenomic mapping identifies a super-enhancer repertoire that regulates cell identity in bladder cancers through distinct transcription factor networks. 2022.01.11.475197. 10.1101/2022.01.11.475197.

FIG1

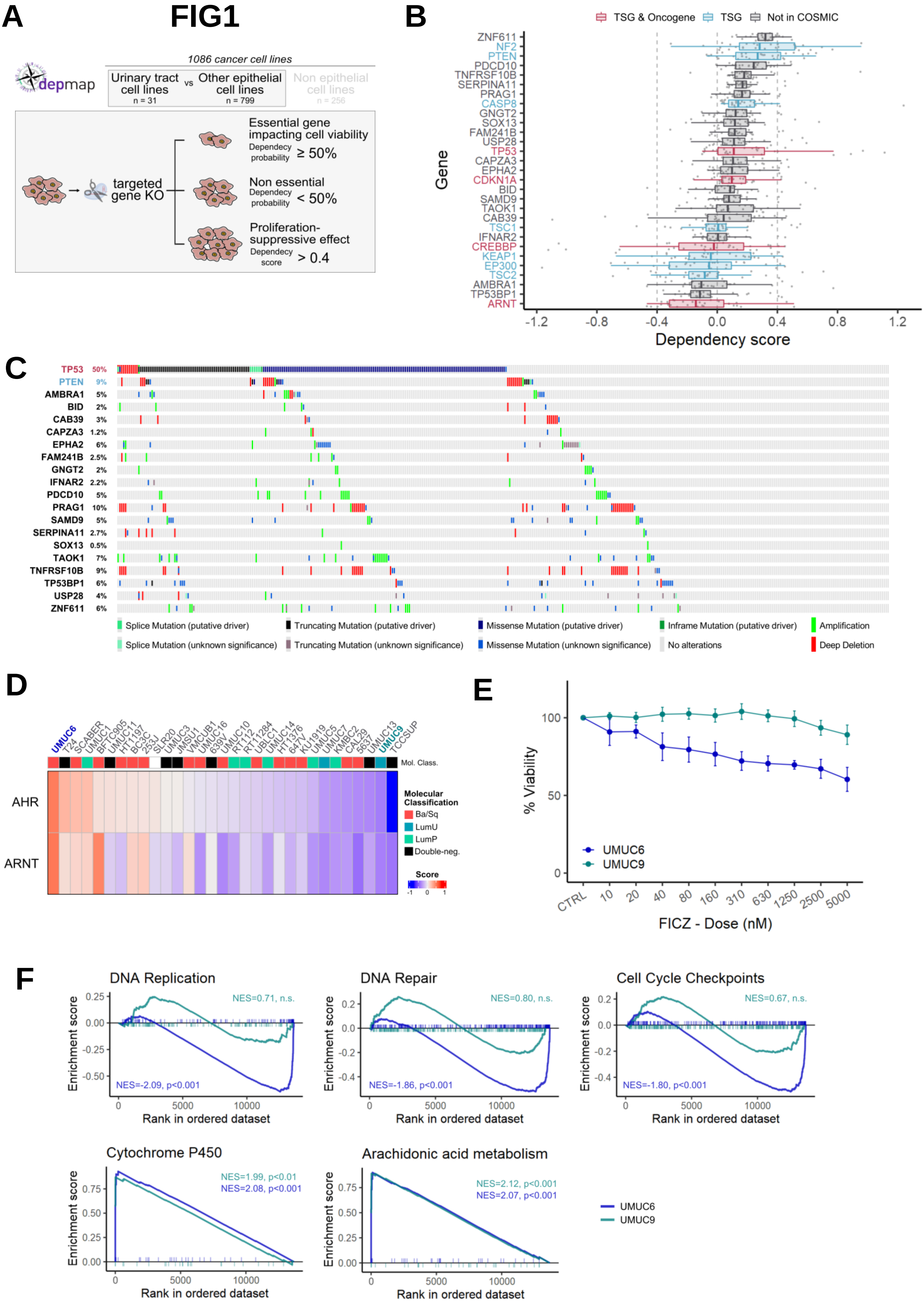
A
1086 cancer cell lines
depmap
Urinary tract cell lines n = 31
vs
Other epithelial cell lines n = 799
Non epithelial cell lines n = 256
targeted gene KO
Essential gene impacting cell viability
Dependecy probability ≥ 50%
Non essential
Dependecy probability < 50%
Proliferation-suppressive effect
Dependecy score > 0.4
B
TSG & Oncogene
TSG
Not in COSMIC
Gene
ZNF611
NF2
PTEN
PDCD10
TNFRSF10B
SERPINA11
PRAG1
CASP8
GNGT2
SOX13
FAM241B
USP28
TP53
CAPZA3
EPHA2
CDKN1A
BID
SAMD9
TAOK1
CAB39
TSC1
IFNAR2
CREBBP
KEAP1
EP300
TSC2
AMBRA1
TP53BP1
ARNT
-1.2
-0.8
-0.4
0.0
0.4
0.8
1.2
Dependency score
C
TP53 50%
PTEN 9%
AMBRA1 5%
BID 2%
CAB39 3%
CAPZA3 1.2%
EPHA2 6%
FAM241B 2.5%
GNGT2 2%
IFNAR2 2.2%
PDCD10 5%
PRAG1 10%
SAMD9 5%
SERPINA11 2.7%
SOX13 0.5%
TAOK1 7%
TNFRSF10B 9%
TP53BP1 6%
USP28 4%
ZNF611 6%
Splice Mutation (putative driver)
Truncating Mutation (putative driver)
Missense Mutation (putative driver)
Inframe Mutation (putative driver)
Amplification
Splice Mutation (unknown significance)
Truncating Mutation (unknown significance)
Missense Mutation (unknown significance)
No alterations
Deep Deletion
D
UMUC6
T24
SCABER
UMUC1
BFTC905
UMUC11
HT1197
BC3C
253J
SLR20
UMUC3
JMSU1
VMCUB1
UMUC16
639V
UMUC10
RT112
RT11284
UBLC1
UMUC14
HT1376
647V
KU1919
UMUC5
UMUC7
KMBC2
CAL29
5637
UMUC13
UMUC9
TCCSUP
Mol. Class.
AHR
ARNT
Molecular Classification
Ba/Sq
LumU
LumP
Double-neg.
Score
-1
0
1
E
% Viability
100
50
0
UMUC6
UMUC9
CTRL
10
20
40
80
160
310
630
1250
2500
5000
FICZ - Dose (nM)
F
DNA Replication
NES=0.71, n.s.
NES=-2.09, p<0.001
Enrichment score
0.25
0.00
-0.25
-0.50
0
5000
10000
Rank in ordered dataset
DNA Repair
NES=0.80, n.s.
NES=-1.86, p<0.001
Enrichment score
0.2
0.0
-0.2
-0.4
0
5000
10000
Rank in ordered dataset
Cell Cycle Checkpoints
NES=0.67, n.s.
NES=-1.80, p<0.001
Enrichment score
0.2
0.0
-0.2
-0.4
0
5000
10000
Rank in ordered dataset
Cytochrome P450
NES=1.99, p<0.01
NES=2.08, p<0.001
Enrichment score
0.75
0.50
0.25
0.00
0
5000
10000
Rank in ordered dataset
Arachidonic acid metabolism
NES=2.12, p<0.001
NES=2.07, p<0.001
Enrichment score
0.75
0.50
0.25
0.00
0
5000
10000
Rank in ordered dataset
UMUC6
UMUC9

FIG2

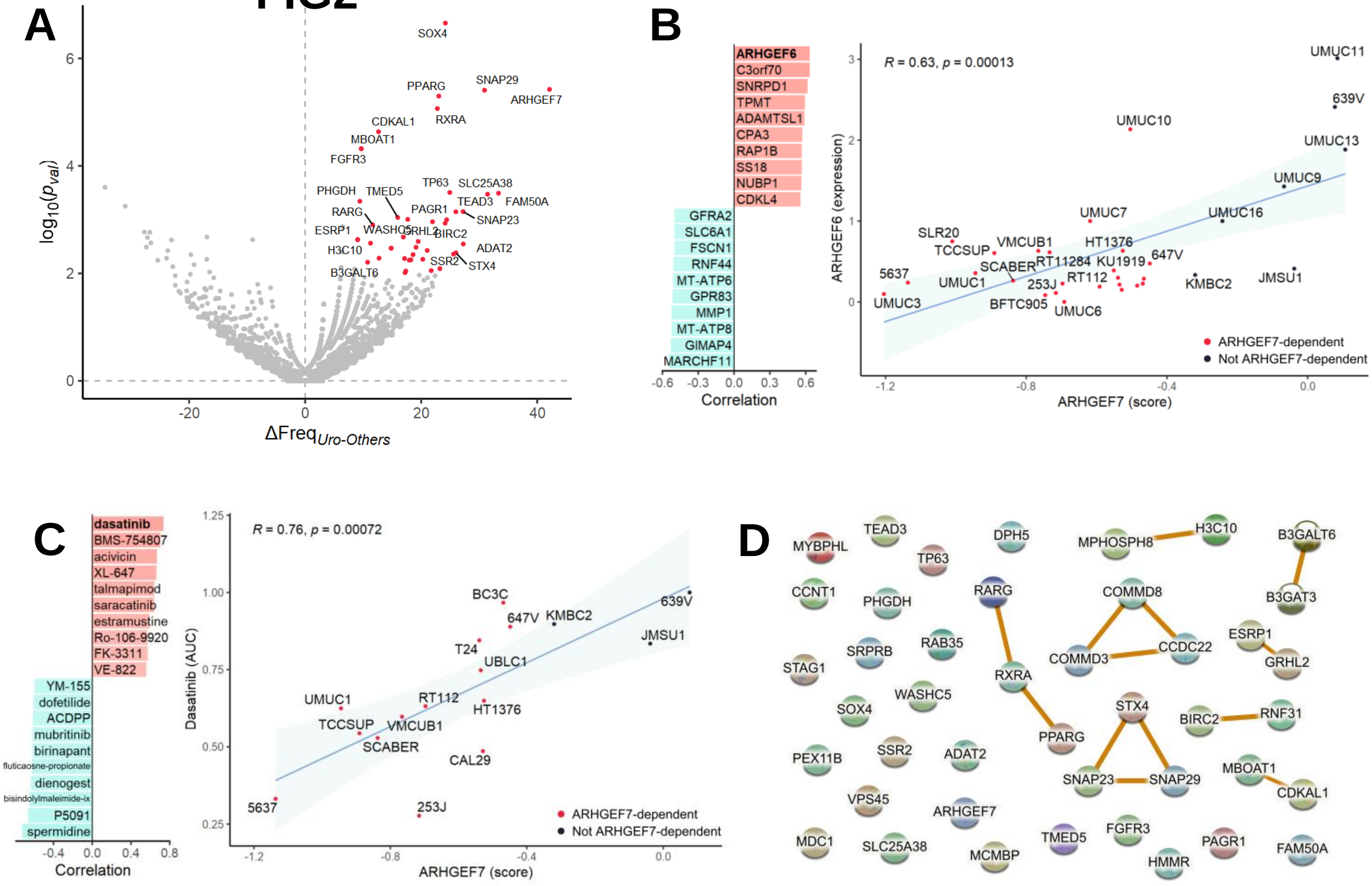
A
log10(pval)
ΔFreqUro-Others
SOX4
PPARG
SNAP29
ARHGEF7
RXRA
CDKAL1
MBOAT1
FGFR3
PHGDH
TMED5
TP63
SLC25A38
TEAD3
FAM50A
RARG
PAGR1
SNAP23
ESRP1
WASHC5
GRHL2
BIRC2
H3C10
ADAT2
SSR2
STX4
B3GALT6
B
ARHGEF6
C3orf70
SNRPD1
TPMT
ADAMTSL1
CPA3
RAP1B
SS18
NUBP1
CDKL4
GFRA2
SLC6A1
FSCN1
RNF44
MT-ATP6
GPR83
MMP1
MT-ATP8
GIMAP4
MARCHF11
Correlation
R = 0.63, p = 0.00013
ARHGEF6 (expression)
ARHGEF7 (score)
ARHGEF7-dependent
Not ARHGEF7-dependent
C
dasatinib
BMS-754807
acivicin
XL-647
talmapimod
saracatinib
estramustine
Ro-106-9920
FK-3311
VE-822
YM-155
dofetilide
ACDPP
mubritinib
birinapant
fluticaosne-propionate
dienogest
bisindolylmaleimide-ix
P5091
spermidine
Correlation
R = 0.76, p = 0.00072
Dasatinib (AUC)
ARHGEF7 (score)
ARHGEF7-dependent
Not ARHGEF7-dependent
D
MYBPHL
TEAD3
TP63
DPH5
MPHOSPH8
H3C10
B3GALT6
CCNT1
PHGDH
RARG
COMMD8
B3GAT3
SRPRB
RAB35
COMMD3
CCDC22
ESRP1
STAG1
RXRA
GRHL2
SOX4
WASHC5
STX4
BIRC2
RNF31
PEX11B
SSR2
ADAT2
PPARG
SNAP23
SNAP29
MBOAT1
CDKAL1
VPS45
ARHGEF7
MDC1
SLC25A38
MCMBP
TMED5
FGFR3
PAGR1
FAM50A
HMMR

FIG3

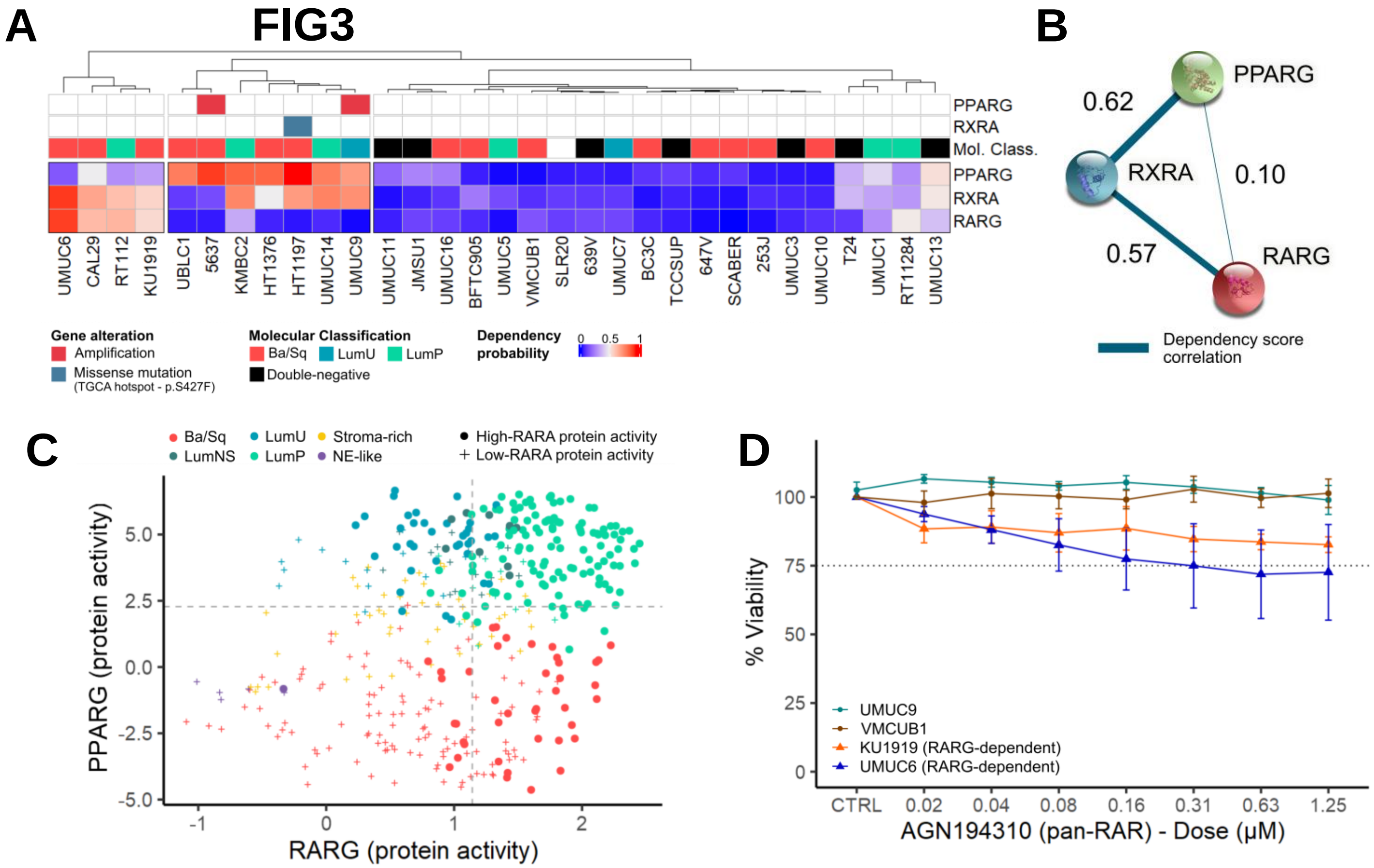
A
PPARG
RXRA
Mol. Class.
PPARG
RXRA
RARG
UMUC6
CAL29
RT112
KU1919
UBLC1
5637
KMBC2
HT1376
HT1197
UMUC14
UMUC9
UMUC11
JMSU1
UMUC16
BFTC905
UMUC5
VMCUB1
SLR20
639V
UMUC7
BC3C
TCCSUP
647V
SCABER
253J
UMUC3
UMUC10
T24
UMUC1
RT11284
UMUC13
Gene alteration
Amplification
Missense mutation
(TGCA hotspot - p.S427F)
Molecular Classification
Ba/Sq
LumU
LumP
Double-negative
Dependency probability
0
0.5
1
B
PPARG
0.62
RXRA
0.10
0.57
RARG
Dependency score correlation
C
Ba/Sq
LumU
Stroma-rich
LumNS
LumP
NE-like
High-RARA protein activity
Low-RARA protein activity
PPARG (protein activity)
5.0
2.5
0.0
-2.5
-5.0
-1
0
1
2
RARG (protein activity)
D
100
75
50
25
0
% Viability
UMUC9
VMCUB1
KU1919 (RARG-dependent)
UMUC6 (RARG-dependent)
CTRL
0.02
0.04
0.08
0.16
0.31
0.63
1.25
AGN194310 (pan-RAR) - Dose (μM)

FIG4

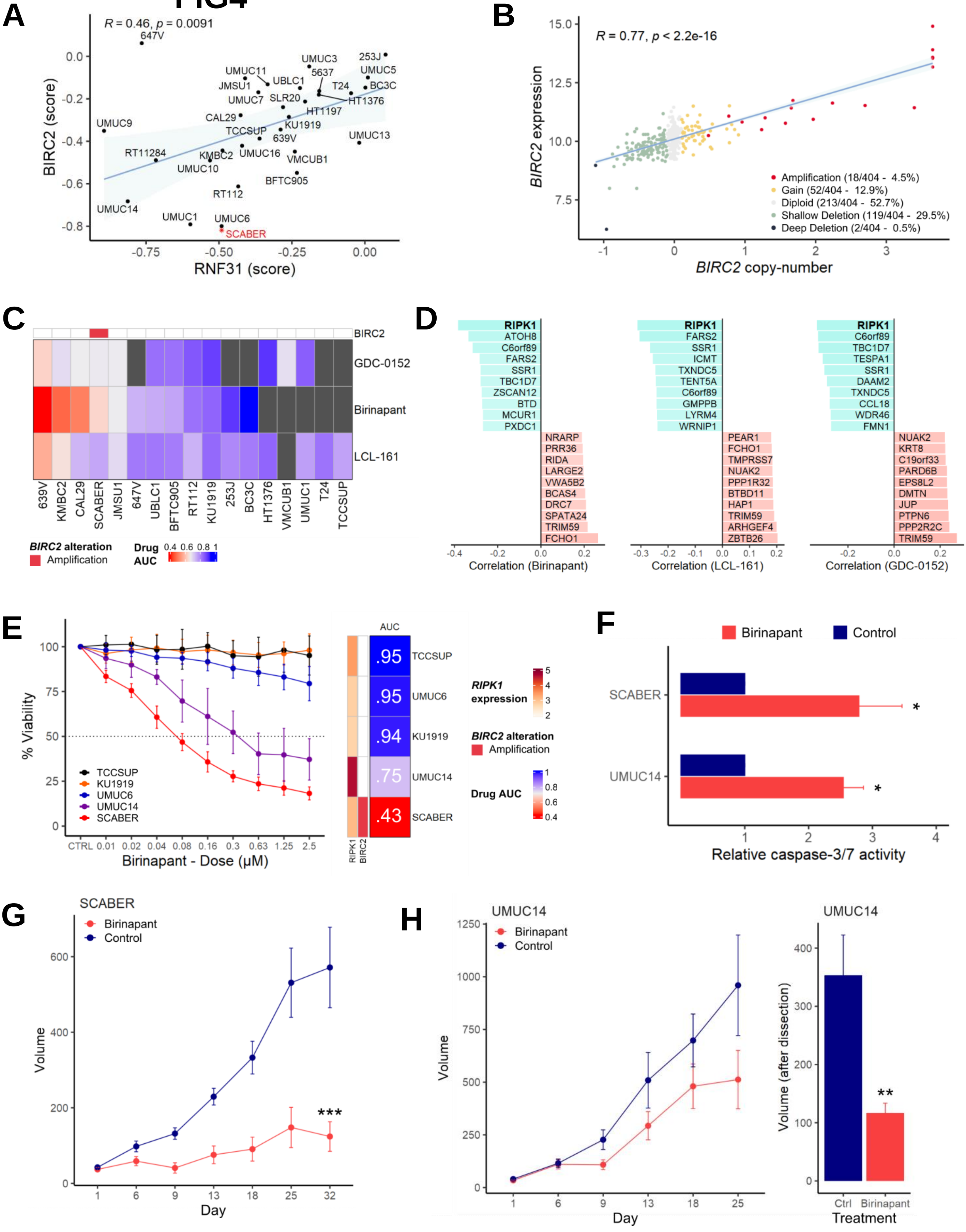
A
R = 0.46, p = 0.0091
647V
UMUC3
253J
UMUC11
5637
UMUC5
JMSU1
UBLC1
T24
BC3C
UMUC7
SLR20
HT1376
HT1197
CAL29
KU1919
UMUC9
TCCSUP
639V
UMUC13
RT11284
KMBC2
UMUC16
VMCUB1
UMUC10
BFTC905
RT112
UMUC14
UMUC1
UMUC6
SCABER
BIRC2 (score)
RNF31 (score)
0.0
-0.2
-0.4
-0.6
-0.8
-0.75
-0.50
-0.25
0.00
B
R = 0.77, p < 2.2e-16
BIRC2 expression
BIRC2 copy-number
15.0
12.5
10.0
7.5
-1
0
1
2
3
Amplification (18/404 - 4.5%)
Gain (52/404 - 12.9%)
Diploid (213/404 - 52.7%)
Shallow Deletion (119/404 - 29.5%)
Deep Deletion (2/404 - 0.5%)
C
BIRC2
GDC-0152
Birinapant
LCL-161
639V
KMBC2
CAL29
SCABER
JMSU1
647V
UBLC1
BFTC905
RT112
KU1919
253J
BC3C
HT1376
VMCUB1
UMUC1
T24
TCCSUP
BIRC2 alteration
Amplification
Drug AUC
0.4 0.6 0.8 1
D
RIPK1
ATOH8
C6orf89
FARS2
SSR1
TBC1D7
ZSCAN12
BTD
MCUR1
PXDC1
NRARP
PRR36
RIDA
LARGE2
VWA5B2
BCAS4
DRC7
SPATA24
TRIM59
FCHO1
-0.4
-0.2
0.0
0.2
Correlation (Birinapant)
RIPK1
FARS2
SSR1
ICMT
TXNDC5
TENT5A
C6orf89
GMPPB
LYRM4
WRNIP1
PEAR1
FCHO1
TMPRSS7
NUAK2
PPP1R32
BTBD11
HAP1
TRIM59
ARHGEF4
ZBTB26
-0.3
-0.2
-0.1
0.0
0.1
0.2
Correlation (LCL-161)
RIPK1
C6orf89
TBC1D7
TESPA1
SSR1
DAAM2
TXNDC5
CCL18
WDR46
FMN1
NUAK2
KRT8
C19orf33
PARD6B
EPS8L2
DMTN
JUP
PTPN6
PPP2R2C
TRIM59
-0.2
0.0
0.2
Correlation (GDC-0152)
E
% Viability
100
75
50
25
0
TCCSUP
KU1919
UMUC6
UMUC14
SCABER
CTRL
0.01
0.02
0.04
0.08
0.16
0.3
0.63
1.25
2.5
Birinapant - Dose (µM)
AUC
.95
TCCSUP
.95
UMUC6
.94
KU1919
.75
UMUC14
.43
SCABER
RIPK1
BIRC2
RIPK1 expression
5
4
3
2
BIRC2 alteration
Amplification
Drug AUC
1
0.8
0.6
0.4
F
Birinapant
Control
SCABER
UMUC14
*
*
1
2
3
4
Relative caspase-3/7 activity
G
SCABER
Birinapant
Control
Volume
600
400
200
0
***
1
6
9
13
18
25
32
Day
H
UMUC14
Birinapant
Control
Volume
1250
1000
750
500
250
0
1
6
9
13
18
25
Day
UMUC14
Volume (after dissection)
400
300
200
100
0
**
Ctrl
Birinapant
Treatment

Sup FIG 1

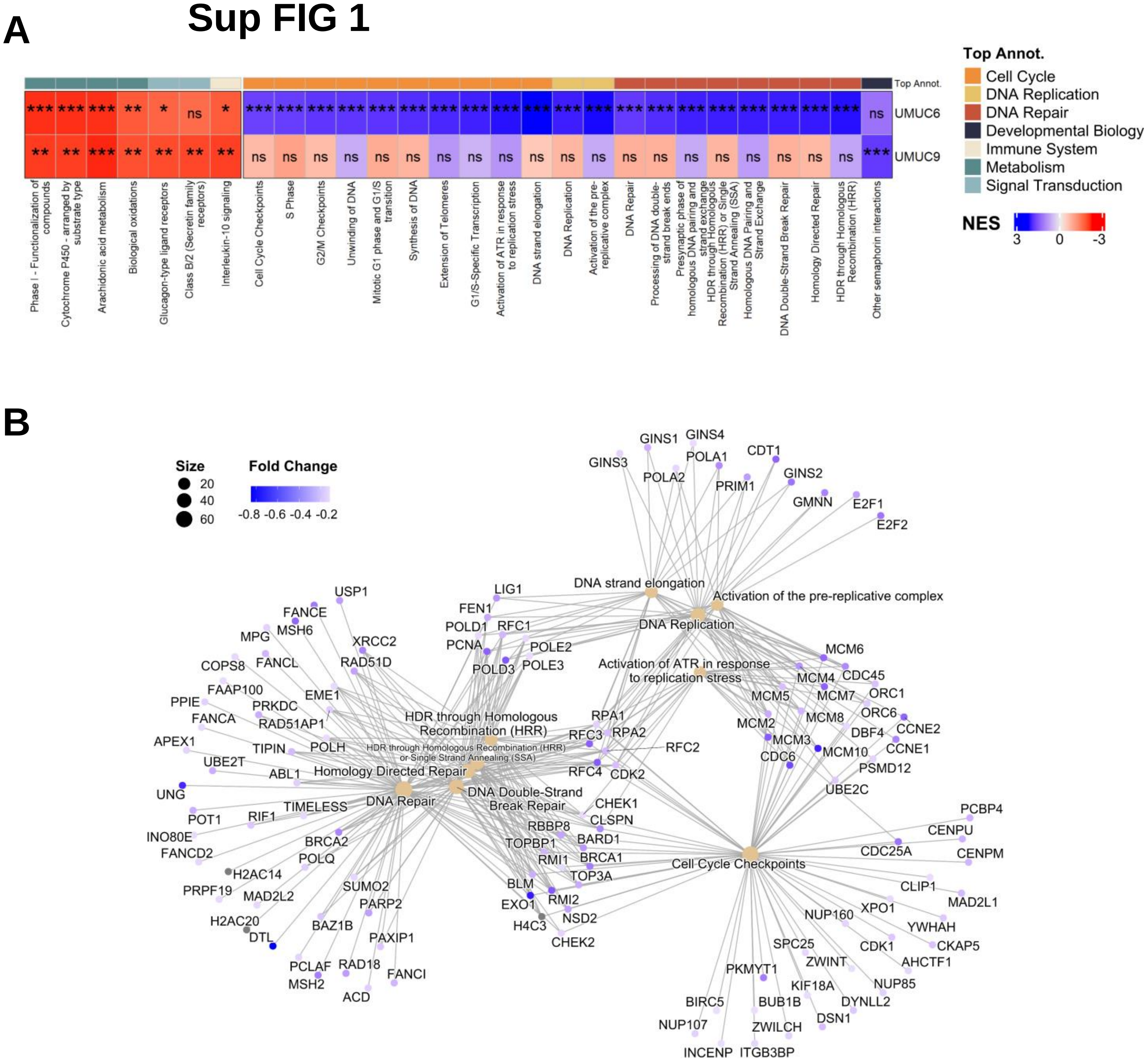
A
Top Annot.
UMUC6
UMUC9
*** *** *** ** * ns * *** ns
** ** *** ** ** ** ** ns ns ns ns ns ns ns ns ns ns ns ns ns ns ns ns ns ns ns ns ***
Phase I - Functionalization of compounds
Cytochrome P450 - arranged by substrate type
Arachidonic acid metabolism
Biological oxidations
Glucagon-type ligand receptors
Class B/2 (Secretin family receptors)
Interleukin-10 signaling
Cell Cycle Checkpoints
S Phase
G2/M Checkpoints
Unwinding of DNA
Mitotic G1 phase and G1/S transition
Synthesis of DNA
Extension of Telomeres
G1/S-Specific Transcription
Activation of ATR in response to replication stress
DNA strand elongation
DNA Replication
Activation of the pre-replicative complex
DNA Repair
Processing of DNA double-strand break ends
Presynaptic phase of homologous DNA pairing and strand exchange
HDR through Homologous Recombination (HRR) or Single Strand Annealing (SSA)
Homologous DNA Pairing and Strand Exchange
DNA Double-Strand Break Repair
Homology Directed Repair
HDR through Homologous Recombination (HRR)
Other semaphorin interactions
Top Annot.
Cell Cycle
DNA Replication
DNA Repair
Developmental Biology
Immune System
Metabolism
Signal Transduction
NES
3
0
-3
B
Size
20
40
60
Fold Change
-0.8 -0.6 -0.4 -0.2
GINS1
GINS4
GINS3
POLA1
CDT1
POLA2
PRIM1
GINS2
GMNN
E2F1
E2F2
DNA strand elongation
Activation of the pre-replicative complex
DNA Replication
LIG1
FEN1
POLD1
RFC1
PCNA
POLE2
POLD3
POLE3
USP1
FANCE
MSH6
MPG
XRCC2
RAD51D
COPS8
FANCL
FAAP100
PPIE
EME1
PRKDC
FANCA
RAD51AP1
APEX1
TIPIN
POLH
UBE2T
ABL1
UNG
HDR through Homologous Recombination (HRR)
HDR through Homologous Recombination (HRR) or Single Strand Annealing (SSA)
Homology Directed Repair
DNA Repair
DNA Double-Strand Break Repair
Activation of ATR in response to replication stress
RPA1
RFC3
RPA2
RFC2
RFC4
CDK2
MCM6
MCM4
CDC45
MCM5
MCM7
ORC1
MCM8
ORC6
MCM2
DBF4
CCNE2
MCM3
MCM10
CCNE1
CDC6
PSMD12
UBE2C
POT1
RIF1
TIMELESS
INO80E
FANCD2
BRCA2
POLQ
H2AC14
PRPF19
MAD2L2
SUMO2
PARP2
H2AC20
DTL
BAZ1B
PAXIP1
PCLAF
RAD18
MSH2
FANCI
ACD
CHEK1
CLSPN
RBBP8
BARD1
TOPBP1
RMI1
BRCA1
TOP3A
BLM
RMI2
EXO1
NSD2
H4C3
CHEK2
Cell Cycle Checkpoints
PCBP4
CENPU
CDC25A
CENPM
CLIP1
MAD2L1
XPO1
NUP160
YWHAH
CDK1
CKAP5
SPC25
ZWINT
AHCTF1
PKMYT1
KIF18A
NUP85
BIRC5
BUB1B
DYNLL2
DSN1
NUP107
ZWILCH
INCENP
ITGB3BP

11.1.3 Discussion et Perspectives

Dans cet article, nous avons montré un nouveau rôle de RARγ dans les lignées de cancers urothéliaux, ainsi que l'intérêt des Smac-mimétiques comme le biririnapant dans une partie de ces tumeurs, avec l'expression de *RIPK1* comme biomarqueur potentiel ainsi que les amplifications de *BIRC2*.

Concernant le birinapant et les Smac-mimétiques, nous allons tester sur des PDXs caractérisées dans l'**Article 1** son efficacité dans des PDXs amplifiées pour *BIRC2* (n=2) et présentant une expression élevée de *RIPK1,* avec comme contrôle deux PDXs non amplifiées pour-*BIRC2* et avec une faible expression de *RIPK1*. Ceci pourra permettre de confirmer les amplifications de *BIRC2* comme biomarqueur de réponse aux Smac-mimétiques dans les cancers urothéliaux, et dans des PDXs. Le birinapant étant un agent pro-apoptotique, le combiner avec des agents induisant l'apoptose comme la chimiothérapie a été privilégié dans d'autres cancers, et cette association pourrait être testée dans ces modèles PDX (éventuellement via des organoïdes dérivés de ces PDXs).

La base DepMap est extrêmement riche et de nombreux autres gènes et voies de signalisation sont à explorer. Par exemple, le complexe COMMANDER (16 protéines) qui joue de multiples rôles notamment dans le transport intracellulaire (cargos endosomales), dans la régulation de l'homéostasie cellulaire, du cycle cellulaire et de la réponse immunitaire [160], et est essentiel à la viabilité cellulaire d'un certain nombre de lignées tumorales urinaires.

L'inhibition à large échelle de gènes par CRISPR-Cas9 peut également être appliquée à des organoïdes. Ainsi des études de criblage à large échelle des organoïdes dérivés de la cohorte PDX pourrait permettre de découvrir des léthalités synthétiques dues à certaines altérations génomiques récurrentes sur des modèles plus proches du *vivo*. La difficulté, en dehors du coût, étant le faible nombre de modèles encore disponibles pour arriver à des conclusions statistiquement satisfaisantes.

11.2 Article 4 : Multi-stage expression in BBN mouse model reveals progression-associated molecular changes in basal/squamous and sarcomatoid bladder carcinogenesis

11.2.1 Introduction

L'exposition de souris au mutagène et carcinogène N-butyl-N-(4-hydroxybutyl)-nitrosamine (BBN) permet l'induction de tumeurs de la vessie de phénotype basal, et est donc un modèle très intéressant d'étude de la carcinogénèse de ces tumeurs [161].

Le travail de thèse du Dr Fontugne avait pour but d'étudier cette évolution tumorale dans ce modèle murin au niveau histologique et transcriptomique.

Mon étude des régulons des cancers de vessie m'a permis de constater que les tumeurs murines BBN basales devenant sarcomatoïdes présentaient une perte d'expression/diminution du régulon d'EGFR avec un switch phénotype vers une expression/activité élevée du régulon de FGFR1.

En utilisant la base Achilles de DepMap comme validation, il a été montré dans cet **Article 4**, dans la partie à laquelle j'ai participé, que les lignées urinaires sarcomatoïdes étaient effectivement dépendantes de FGFR1 (baisse de la viabilité cellulaire lors de l'inhibition de ce récepteur par CRISPR-Cas9).

11.2.2 Article 4 : Multi-stage expression in BBN mouse model reveals progression-associated molecular changes in basal/squamous and sarcomatoid bladder carcinogenesis

TITLE PAGE

Title

Multi-stage expression in BBN mouse model reveals progression-associated molecular changes in basal/squamous and sarcomatoid bladder carcinogenesis

Running title

Bladder carcinogenesis study through mouse model multi-stage RNA-seq

Authors

Jacqueline Fontugne[1,2,3], Jennifer Wong[1,4], Luc Cabel[1], Hélène Neyret-Kahn[1], Narjesse Karboul[1], Pascale Maillé[2], Audrey Rapinat[5], David Gentien[5], André Nicolas[6], Sylvain Baulande[7], Mathilde Sibony[8], Isabelle Bernard-Pierrot[1#], François Radvanyi[1#], Yves Allory[1,2,3#]

Author affiliations

1. Institut Curie, CNRS, UMR144, Equipe labellisée Ligue Contre le Cancer, PSL Research University, Paris, France

2. Institut Curie, Department of Pathology, F-92210, Saint-Cloud, France

3. Université Versailles St-Quentin, Université Paris-Saclay, F-78180, Montigny-le-Bretonneux, France

4. Institut Curie, Department of Genetics, Paris, France

5. Genomics Core Facility, Translational Research Department, PSL Research University, Institut Curie, Paris, France

6. Institut Curie, Department of Pathology, Paris, France

7. Genomics of Excellence (ICGex) Platform, Institut Curie, PSL Research University, Paris, France

8. Department of Pathology, Hôpital Cochin, Paris, France

# These authors co-supervised the study

Corresponding author

Pr Yves Allory

Address: Département de Pathologie / UMR 144, Équipe Oncologie Moléculaire

Institut Curie – site Saint Cloud

35 Rue Dailly, 92210 Saint-Cloud France

Email: yves.allory@curie.fr

Phone: +33 01 47 11 15 06

Conflict of interest statement

The authors have no conflict of interest to declare.

Word count

3991 words

ABSTRACT

The aggressive basal/squamous (Ba/Sq) bladder cancer (BLCA) subtype is often diagnosed at the muscle-invasive stage and can progress to the sarcomatoid variant. Identification of molecular changes occurring during progression from non-muscle-invasive BLCA (NMIBC) to Ba/Sq muscle-invasive BLCA (MIBC) is thus challenging in human disease. We used the N-butyl-N-(4-hydroxybutyl)-nitrosamine (BBN) mouse model of Ba/Sq MIBC to longitudinally study molecular changes leading to the Ba/Sq phenotype and to the sarcomatoid variant using IHC, microdissection followed by RNA-seq at all stages of progression. A shift to Ba/Sq phenotype started in early progression stages. Pathway analysis of gene clusters with coordinated expression changes revealed Shh signalling loss and a shift from fatty acid metabolism to glycolysis. An upregulated cluster, appearing early in carcinogenesis, showed relevance to human disease, identifying NMIBC patients at risk of progression. Similar to the human counterpart, sarcomatoid BBN tumours displayed a Ba/Sq phenotype and epithelial-mesenchymal transition (EMT) features. An EGFR/FGFR1 signalling switch occurred with sarcomatoid dedifferentiation and correlated with EMT. BLCA cell lines with high EMT were the most sensitive to FGFR1 knockout and resistant to EGFR knockout. Taken together, these findings provide insights into the underlying biology of Ba/Sq BLCA progression and sarcomatoid dedifferentiation with potential clinical implications.

KEY WORDS

Urothelial carcinoma, carcinogenesis, molecular evolution of bladder cancer, immunohistochemistry, sarcomatoid variant, EGFR, FGFR1, BBN mouse model

INTRODUCTION

Bladder cancer (BLCA) is the 10th most common cancer type worldwide, and caused nearly 200 000 deaths in 2018 (1). The vast majority of BLCAs are urothelial carcinomas, characterized by two clinically distinct forms of disease (2). Non-muscle-invasive bladder cancer (NMIBC) – papillary pTa, flat carcinoma *in situ* (CIS) and pT1 stage tumours – often recur, leading to a significant burden on patients' quality of life (3). In contrast, muscle-invasive bladder cancer (MIBC, ≥pT2) represents the lethal form of disease. Most patients with MIBC show no history of precursor NMIBC, challenging the study of carcinogenesis and progression in human disease. Overlaps in genomic alterations and lineage tracing studies in mice suggest that CIS represents a major precursor of MIBCs (4–6). However, the precise relationships between the different forms of NMIBC and MIBC have not been fully elucidated.

Transcriptomic classifications distinguish molecular subtypes of MIBC, with different clinical characteristics (7–11). The major molecular subtypes oppose luminal subtypes to the basal/squamous (Ba/Sq) subtype. The consensus Ba/Sq subtype of MIBC is a frequent (~35%) and aggressive subtype with poor survival. Histologically, nearly half of Ba/Sq MIBCs harbor squamous divergence and may eventually progress to the aggressive sarcomatoid variant, often composed of tumor cells of spindle morphology (12–14). Ba/Sq tumours are characterized by the overexpression of basal cell markers, such as KRT5, KRT6, and KRT14 and underexpression of luminal markers, such as KRT20, FOXA1, GATA3 or PPARG. They display high EGFR activity, with EGFR dependence *in vitro* and *in vivo* (7,15). Since most NMIBCs are considered to display a luminal phenotype, and the vast majority of CIS show aberrant high expression of KRT20, one could assume that a subtype switch is required during the progression from NMIBC to Ba/Sq MIBC (16). However, Ba/Sq tumours are often diagnosed at the muscle-invasive stage, rarely preceded by NMIBC tumours, hindering the longitudinal study of molecular alterations from early-stage carcinoma to Ba/Sq MIBC (15,17).

N-butyl-N-(4-hydroxybutyl)-nitrosamine (BBN) carcinogen specifically induces bladder tumours in mice and represents an attractive model of MIBC (18). We and others have demonstrated that BBN-induced MIBC is a model of the Ba/Sq transcriptomic subtype, and can harbour squamous divergence, or more rarely sarcomatoid features (15,19). We thus hypothesized that the BBN-induced model represents a stable means to longitudinally study Ba/Sq BLCA progression.

In this study, we aimed to identify the molecular changes occurring during the carcinogenesis of Ba/Sq MIBC. We report histological, immunohistochemical and RNA-seq profiles of lesions of all stages of progression in a carcinogen-induced murine model of the Ba/Sq subtype of MIBC. We showed that early-stage tumours already displayed Ba/Sq features and identified sets of genes with coordinated changes during progression. One cluster of co-expressed genes, which increased early in Ba/Sq MIBC carcinogenesis, showed relevance to human tumours, identifying patients with NMIBC at risk of progression. A focus on BBN-induced sarcomatoid tumours showed similarities with the human counterpart, such as epithelial-mesenchymal transition features, and revealed that an EGFR to FGFR1 signalling switch occurs with sarcomatoid dedifferentiation, with potential therapeutic implications.

MATERIAL AND METHODS

BBN-induced mouse model

Forty 8-week-old male C57BL/6 mice were exposed to N-butyl-N-(4-hydroxybutyl)-nitrosamine (BBN) 0.05% in drinking water *ad libitum* for a maximum of 14 weeks. Mice were sacrificed at different time points to obtain tumours of all stages. Five control mice received non-treated drinking water. See Supplementary methods for details.

Tissue processing

Mouse bladders were formalin-fixed, paraffin-embedded (FFPE) then sectioned at 3µm thickness. Slides at 3 different levels were stained with haematoxylin, eosin and saffron (HES) for morphological analysis and 10 unstained slides from flanking sections between each level were reserved at 4°C for immunohistochemistry (IHC).

Immunohistochemistry

For IHC assessment of luminal and basal markers, we used KRT5, KRT6A, KRT14, FOXA1 and KRT20 rabbit polyclonal antibodies on an Autostainer 480 (Lab Vision). Subtype markers were quantified using quickscore method. See Supplementary methods for details. For vimentin IHC, we used a monoclonal anti-vimentin antibody (clone EPR3776, ab92547, Abcam), an HRP-conjugated goat anti-rabbit IgG polymer detection kit (ImmPRESS MP-7451), DAB chromogen and Mayer's Hematoxylin counterstain.

Morphological analysis

The three levels of HES-stained slides for each FFPE block were reviewed by uropathologists (JF, MS, YA) for morphological analysis, in combination with IHC subtype markers. The highest stage lesion for each mouse bladder was documented regarding presence of variant morphology and stage according to the WHO 2016 classification of urothelial tumours and TNM 8th edition UICC staging (2). In two cases harbouring several lesions of identical stage with discordant IHC profiles, each lesion was documented individually regarding the aforementioned morphological parameters.

Tissue microdissection

Large MIBC tumours (n=3) were manually microdissected by scraping five 6µm-thick sections with visual control under a stereomicroscope, using corresponding H&E-stained slide for reference. For all other cases, we performed laser-capture microdissection (LMD7000, Leica Microsystems) (Supplementary methods).

RNA extraction, library preparation and sequencing

RNA was extracted from microdissected BBN-induced lesions and non-exposed urothelia using the RNeasy FFPE kit (Qiagen). Libraries were prepared using Ovation SoLo RNA-Seq system (NuGEN) and sequenced on a HiSeq2500 (Illumina). Reads were mapped to the mouse reference genome (mm10) using STAR (version 2.6.1a) and counted with Rsubreads (version 1.24.2). See Supplementary methods for details.

Identification of sample groups

Principal component analysis (PCA) was performed using prcomp function in R. Unsupervised clustering iterations were performed using ConsensusClusterPlus R package (v1.48.0) (20) (Supplementary methods).

Sample molecular classification

Mouse samples were classified using corresponding human homolog genes, obtained using biomaRt R package (v2.40.5, genome assemblies GRCm38.p6 and GRCh38.p13). LundTax and BASE47 classes were obtained using BLCAsubtyping (v2.1.1). Consensus subtypes were determined with ConsensusMIBC (v1.1.0) R package (7). The UROMOL study NMIBC classes were obtained using the online application (21).

Gene expression changes during progression

To identify significant expression changes during progression, we used an R package designed for RNA-seq time-course data, Next maSigPro (v1.56.0) (Supplementary methods). Genes with significant temporal changes were grouped into k=2 to k=8 clustering solutions. Functional enrichment was evaluated in each k solution using ClusterProfiler (v 3.12.0) and ReactomePA (v1.28.0) R packages. The lowest k solution capturing the most patterns of co-expression changes and grouping biologically related genes was selected as the final clustering solution (k=5).

Differential gene expression analyses

Pairwise differentially expressed genes were determined using DESeq2 (v1.24.0) in the BBN RNA-seq data, and Limma (v3.40.6) package for the array expression profiling data of human sarcomatoid cases from Guo *et al.* (12) (Supplementary methods).

Epithelial-mesenchymal transition (EMT) scores

We used a previously published signature combining 206 epithelial and 132 mesenchymal genes (23). EMT scores were calculated by subtracting the mean log2-normalized expression of the epithelial genes from that of the mesenchymal genes in each sample.

Regulon activity

In our BBN and in the Guo *et al.* cohorts, we determined the activity of 22 regulators reported to play a role in BLCA, as previously described (11) (see Supplementary methods).

Study approval

Animal experiments were performed in accordance with recommendations of the European Community (2010/63/UE) for the care and use of laboratory animals. Experimental procedures were approved by the ethics committee of Institut Curie CEEA-IC #118 (Authorization APAFiS #26671-2020072108262352-v2 given by National Authority) in compliance with international guidelines.

Statistical analysis

Details are provided in Supplementary methods.

Data Availability

Generated RNA-seq data was deposited in Gene Expression Omnibus (GEO) under accession GSE197016**.** Details on the public data analysed are provided in Supplementary methods.

RESULTS

BBN-exposed mice develop the full tumour spectrum of bladder carcinogenesis

To study disease progression, forty mice were exposed to BBN and sacrificed at different time points (Figure 1A). As previously described (24), histopathological analysis of mouse bladders after increasing durations of BBN exposure revealed a spectrum of lesions, including hyperplasia, dysplasia, CIS, papillary pTa, pT1 and muscle-invasive tumours, confirming the model progresses along stages similar to those found in human urothelial carcinogenesis (Figures 1B, 1C, 1D and 1E) (2). Flat neoplastic lesions and high-grade papillary pTa tumours arose week 8 and week 12, respectively. Infiltrating carcinoma, defined hereafter as breaching the basement membrane, was seen starting week 12, and involved the lamina propria (pT1) or the bladder muscle (MIBC). Most infiltrating tumours showed squamous differentiation (Figures 1D and 1F). However, four infiltrating tumours lacked squamous features and displayed spindle morphology, suggestive of the sarcomatoid variant of human urothelial carcinoma (Figures 1D and 1F).

Distinct transcriptomic groups reflect histological stages of progression

We performed laser-capture microdissection (Supplementary Figure 1) followed by RNA-sequencing of 37 samples, including 29 lesions from 27 BBN-exposed mice, representative of all stages of carcinogenesis - hyperplasia (n=4), dysplasia (n=5), CIS (n=3), pTa (n=5), pT1 (n=7), MIBC (n=5) - 3 BBN-exposed urothelia of normal morphology and 5 unexposed control urothelia. To assess the transcriptomic similarity between samples, we performed PCA, which showed a separation of samples according to stage and differentiation along the first and the second component, respectively (Figure 2A). To further confirm that progression groups were related to morphological stage, unsupervised clustering iteration was performed (20). The k = 3 clustering solution was the most robust in all tested clustering and linkage methods (Figures 2B and 2C). The three clusters were associated with stage, essentially grouping 1) normal and premalignant stages, 2) early neoplastic stages, and 3) infiltrating stages (pT1 and MIBCs). Interestingly, higher k solutions further divided the infiltrating group according to differentiation (squamous vs. sarcomatoid), regardless of stage (pT1 or MIBC) (Figure 2D). Sarcomatoid variant is suggested to develop by progression of conventional basal tumours in human MIBCs (12,13). PCA and clustering results indicated that BBN sarcomatoid cases may similarly represent a distinct group of progression. For our downstream analyses regarding molecular changes during progression, we thus considered the following sequential progression groups: 1) controls, 2) BBN-exposed urothelia with normal histology, 3) hyperplasia, 4) dysplasia, 5) CIS, 6) pTa, 7) infiltrating with squamous differentiation (≥pT1) and 8) infiltrating with pure sarcomatoid features (≥pT1).

Evolution of molecular subtyping during progression

We analysed the evolution of molecular classifications during progression in our model using 3 classifiers (7,9,25). As expected, all BBN-induced MIBC tumours, with squamous or sarcomatoid morphology, classified as consensus Ba/Sq and BASE47 basal subtypes (15,19). Strikingly, correlation to basal classes gradually increased during progression, transitioning to a full basal phenotype starting from early stages of carcinogenesis (Figure 3A). LundTax confirmed and refined these observations. Most pTa tumours were assigned to LundTax UroB group, which shares features of both urothelial-like (UroA) and Ba/Sq subtypes and is suggested to represent progression towards the basal phenotype (25,26). Most infiltrating sarcomatoid cases (3/4) classified as mesenchymal-like (Mes-like), indicating a distinct molecular phenotype.

Basal marker expression increased starting from the pre-malignant dysplasia stage, reaching maximum levels in infiltrating squamous samples (Figure 3B). However, infiltrating sarcomatoid cases had significantly lower expression of basal markers compared to cases with squamous divergence (p= 8.1 x 10^{-3}) (Figure 3C). Conversely, luminal marker expression progressively decreased during progression, with a significant drop at basement membrane infiltration (p= 0.01) (Figures 3B and 3C). LundTax Mes-like infiltrating sarcomatoid cases displayed the highest levels of typical markers of human Mes-like tumours, *Vim* and *Zeb2*, with low expression of *Epcam* (Figures 3B and 3C) (8). At the protein level, vimentin was expressed by tumour cells in sarcomatoid samples, whereas expression was identified in the stromal cells of non-sarcomatoid tumours with high *Vim* expression (Figure 3D). We also confirmed the sequential changes of basal and luminal markers at the protein level by IHC on the complete cohort (n=40 BBN-exposed mice) (Supplementary figures 2A and 2B).

Overall, these findings indicated that early-stage tumours already exhibit basal characteristics and suggest that infiltrating sarcomatoid cases represent a distinct group of basal infiltrating BBN tumours with mesenchymal features.

Analysis of gene expression dynamics during progression identifies clusters of co-expressed genes with biological relevance

To identify patterns of gene expression changes during progression, we applied a time-course approach to our RNA-seq data using the Next maSigPro algorithm (22). Setting our 8 predefined progression stages as analysis time points, we identified 946 genes with significant temporal changes. Clustering of the significant genes distinguished 5 groups with similar patterns of expression changes during progression (Figure 4A and 4B). Clusters 1-3 of downregulated genes included genes known to play a role in urothelial differentiation (*Pparg, Grhl3*, Uroplakins, *Krt20, Gata3*). The fourth cluster of genes with a coordinated increase starting from dysplasia stage, comprised basal markers (*Krt6a, Krt6b, Krt14, Cd44, Egfr)* as well as transcription factors reported to be active in the basal subtype (*Myc, Foxm1, Hif1a*) (7,11). Cluster 5 grouped genes with low expression in early stages, such as *Vim and Cdkn2a*, which increased at infiltration and were highest in sarcomatoid cases.

We performed functional overrepresentation analysis of each cluster to identify implicated biological pathways (Figure 4C). Among expected processes, cell cycle and tissue remodeling terms were enriched in increasing clusters 4 and 5. Conversely, in downregulated clusters during progression, we identified genes of the canonical Hedgehog signaling pathway (*Gli1, Hhip, Ptch1, Shh*), and of xenobiotic detoxifying glucoronidation, in particular UDP-glucuronosyltransferase enzymes (*Ugt1a* genes in cluster 3), as previously reported (5,27). Clusters 2 and 3 were both enriched in genes involved in fatty acid metabolism, in particular in oxidation (*Hadhb, Phyh, Abcd3, Pparg*). Concomitantly, glycolysis terms were enriched in cluster 4, linked to the upregulation of key enzymes or transporters of the glycolysis pathway (*Hk2, Pfkp, Pgk1, Eno1, Ldha, Slc16a1*). Cluster 4 also included *Hif1a* and *Myc*, known master regulators of glycolysis. These findings suggest an important energy rewiring during Ba/Sq bladder carcinogenesis.

A gene set with increasing expression during Ba/Sq carcinogenesis identifies NMBIC patients at risk of progression

We then explored the clinical relevance of cluster 4, a set of genes with a coordinated upregulation starting in early carcinogenic stages. We first investigated the expression of cluster 4 genes in different stages of human BLCA, using a publicly available dataset combining both NMIBC (n=213) and MIBC (n=95) samples (26). Unsupervised hierarchical clustering using the expression of all human orthologs of cluster 4 genes distinguished 2 groups with distinct cluster 4 metagene scores (mean-centered expression of all cluster 4 genes), which were associated with stage (Figure 5A). Further investigation confirmed that cluster 4 metagene score significantly increased in a stepwise manner with stage in human tumours (Figure 5B). We then classified all NMIBC tumours in this cohort using a recent NMIBC classification scheme, comprising classes 1, 2a, 2b and 3 (21). Interestingly, nearly half (10/22) of the pTa tumours assigned to the cluster 4 metagene “high” group were classified as NMIBC class 2a, which is associated with the highest risk of progression (Figure 5C). These findings were confirmed in an additional cohort of both NMIBCs and MIBCs (CIT cohort, n = 177, Supplementary figures 2A, 2B and 2C) (15). In another NMIBC cohort (n = 535, UROMOL project) (21), progression cluster 4 metagene score was significantly higher in pT1 compared to pTa tumours ($p = 1.7 \times 10^{-10}$, Supplementary figure 3D). Cluster 4 gene expression level was associated with progression-free survival in this cohort and patients with the highest score had the worst outcome (log-rank $p < 0.0001$, Figure 5D).

BBN sarcomatoid tumours show relevance to human sarcomatoid variant

Since sarcomatoid BBN-induced tumours in mice have not been extensively described in the literature, we further explored their transcriptomes. We first performed differential gene expression analysis between infiltrating sarcomatoid and non-sarcomatoid samples (Supplementary figure 4A). Top enriched terms in the upregulated genes included migration, matrix adhesion and mesenchymal cell differentiation, whereas downregulated genes were enriched in terms associated with epithelial cell differentiation and cell-cell adhesion (Supplementary figure 4B), suggesting epithelial-mesenchymal transition (EMT) features. Supporting these findings, the Hallmark EMT gene set was within the top enriched pathways in GSEA (Supplementary figure 4C and

4D). To test if BBN-induced sarcomatoid cases recapitulate the gene expression profile of the sarcomatoid variant of human MIBCs, we explored the gene expression profiles of a cohort of 112 patients with urothelial carcinoma, including 28 of the sarcomatoid variant (12). Guo *et al.* human sarcomatoid cases were similar to BBN sarcomatoid samples regarding molecular classification (Figure 6A). We then sought to compare the candidate mechanisms involved in BBN sarcomatoid phenotype to that of human sarcomatoid samples. We thus classified all 112 human samples using the consensus classifier, identifying 50 Ba/Sq tumours. We then performed differential gene expression analysis between Ba/Sq sarcomatoid (n=21) and Ba/Sq non-sarcomatoid cases (n=29). A significant overlap was found between the dysregulated genes identified in BBN compared to human samples (Figure 6B). Comparison of functional enrichment associated with the observed dysregulated genes revealed common biological processes (Figure 6C). Both datasets pointed to terms related to EMT as well as to downregulation of EGFR signaling in sarcomatoid samples. To compare the changes in EMT in mouse and human tumours, we calculated a previously published EMT score (23) in both our BBN and Ba/Sq human samples. Sarcomatoid cases had a significantly higher EMT score than non-sarcomatoid samples in both datasets (Supplementary figure 5A), further demonstrating the EMT profile of sarcomatoid tumours in our model and its relevance to the human sarcomatoid variant.

An EGFR to FGFR1 signaling switch occurs with sarcomatoid dedifferentiation

To further confirm the downregulation of EGFR signaling in sarcomatoid samples in our BBN cohort, we calculated the activity of 22 regulators associated with BLCA, including EGFR (Supplementary figure 5B) (11). EGFR regulon was significantly downregulated in BBN sarcomatoid compared to non-sarcomatoid infiltrating cases (Figure 6D). By computing all 22 regulons, we observed that FGFR1 displayed high activity in sarcomatoid cases (Supplementary figure 5B). GSEA using ranked fold changes of FGFR1 target genes between BBN sarcomatoid and non-sarcomatoid samples confirmed the significant enrichment of FGFR1 regulon in sarcomatoid cases (adj. $p = 2.4 \times 10^{-3}$) (Supplementary figure 5C). However, mean FGFR1 regulon activity score was not significantly higher in infiltrating sarcomatoid compared to non-sarcomatoid cases, potentially owing to the low number of BBN samples (Figure 6D). We thus similarly calculated regulon activity scores in Guo cohort (n=112) and confirmed the EGFR/FGFR1 switch in human Ba/Sq sarcomatoid samples, but not in non-Ba/Sq sarcomatoid cases (Figure 6D and Supplementary figure 5D).

Given the previously reported role of FGFR1 in EMT (28), we interrogated the association of FGFR1 activity and EMT score in BBN and human tumours. Interestingly, FGFR1 regulon activity was positively correlated with EMT score in both Ba/Sq and non Ba/Sq samples ($R = 0.83$, $p = 9.1 \times 10^{-14}$ in Ba/Sq and $R = 0.88$, $p < 2.2 \times 10^{-16}$ in non-Ba/Sq from Guo cohort; $R = 0.82$, $p = 0.001$ in our BBN cohort). In contrast, EGFR regulon activity was negatively correlated with EMT in both mouse and Ba/Sq human cohorts, but not in non-Ba/Sq human samples (Supplementary figures 5E and 5F). FGFR1 expression alone was also highly correlated with EMT score in a larger MIBC dataset (TCGA, n = 408, $R = 0.82$, $p < 2.2 \times 10^{-16}$) as well as in BLCA cell lines (CCLE, n = 36, $R = 0.85$, $p = 6.9 \times 10^{-11}$), suggesting a stroma-independent FGFR1 expression (Supplementary figures 5G and 5H).

Sensitivity to FGFR1 knockout was significantly correlated with both FGFR1 expression and EMT score in BLCA cell lines (Supplementary figures 5I and 5J) in a genome-wide CRISPR screen (n= 29, Achilles project, Broad Institute). As previously suggested (29,30), EGFR knockout had no effect on viability in cell lines with the highest EMT scores, including in cells with the highest sensitivity to FGFR1 inhibition

(Figure 6E). Of note, EMT-high cell lines that were not sensitive to FGFR1 inhibition harbour activating *RAS* mutations, suggesting potentially overlapping downstream pathways.

Taken together, these data show that sarcomatoid dedifferentiation, characterized by EMT, is associated with an EGFR to FGFR1 signaling switch, with potential sensitivity to FGFR1 inhibition.

DISCUSSION

The inherent natural history of the aggressive Ba/Sq subtype of BLCA hampers the study of progression from early-stage carcinoma to Ba/Sq MIBC in human samples. Here, were performed laser-capture microdissection and RNA-seq of lesions at all stages of carcinogenesis in a murine model of Ba/Sq MIBC to study gene expression dynamics during progression.

In human carcinogenesis, changes in molecular subtype during progression from NMIBC to MIBC have not been fully elucidated, in particular in the Ba/Sq subtype. To address this question, Sjödhal *et al*. built a cohort of 73 patients with NMIBC who eventually progressed to MIBC (17). Only 6 patients had recurring NMIBC that eventually progressed to Ba/Sq MIBC, illustrating the challenge of studying molecular dynamics during progression in this subtype particularly. In our study, gene expression-based classifications revealed that early stages already displayed basal/squamous features. Using single-cell transcriptome profiling and FACS analysis of pre-sorted and cultured BBN-induced tumour cells, Sfakianos *et al*. identified co-expression of luminal and basal genes at the single-cell level, and demonstrate cell lineage plasticity (31). These observations suggest that a subtype switch could occur with progression.

In contrast to BBN-induced mouse CIS, human CIS with basal features is a rare finding. In fact, the majority of human CIS are characterized by the aberrant overexpression of the luminal marker KRT20. However, cases of CIS expressing basal markers or squamous CIS have been reported (16,32). While it is likely that human Ba/Sq MIBCs may arise after a molecular phenotype switch, this study suggests that a subset could evolve from true basal/squamous CIS. This hypothesis is supported by a study suggesting that basal subtype commitment already occurs at the stage of CIS (33).

Functionally related genes tend to show correlated expression patterns across multiple conditions or perturbations (34). To investigate the gene expression changes during progression, we thus used a unique approach by deriving a time-course RNA-seq data algorithm. The time-course approach identified sets of genes with similar co-expression patterns during progression. Validating this method, we identified previously reported pathway dysregulations, such as Sonic Hedghog and glucoronidation pathway downregulation (5,27), or expected pathways such as cell cycle upregulation. This analysis also suggested that a rewiring of metabolism occurs in the early steps of Ba/Sq carcinogenesis, towards anaerobic glycolysis. Fantini *et al.* performed RNA-seq of 5 BBN-induced MIBC and 3 pre-tumoural tumours at 4 weeks of exposure and identified metabolic changes in established tumours but not in pre-tumoural samples (19). However, by using laser microdissection of pre-tumoural lesions in our study, the enrichment in tumour-cell RNA likely allowed to capture such changes with more sensitivity.

We acknowledge certain limitations related to our study design. We are aware that this analysis represents a pseudo time-series, where each sample is in fact a snapshot of a static state. However, the BBN-induced carcinogenesis is a stable model in which mice, with the same genetic background, inevitably develop muscle-invasive BLCA as carcinogenic exposure increases. Additionally, in order to preserve the tissue, we did not exhaust each mouse bladder FFPE block, and thus could not control whether the laser-capture microdissected area was in fact the highest stage lesion in the entire bladder.

Finally, we also report here, to our best knowledge, the first molecular characterization of BBN-induced sarcomatoid tumours in mice. BBN-induced sarcomatoid tumours, like human sarcomatoid BLCA, were assigned to the Ba/Sq subtype and harboured features of EMT (12,13), suggesting that BBN-induced sarcomatoid tumours recapitulate the transcriptional features of human sarcomatoid BLCA, broadening the utility of the BBN model to studies focusing on this aggressive variant.

Through differential analysis between sarcomatoid and non-sarcomatoid tumours, we demonstrated that an EGFR/FGFR1 switch occurs with sarcomatoid dedifferentiation in both BBN-induced and human basal/squamous tumours. FGFR1-mediated EMT has been shown in other cancer types, such as prostate or head and neck squamous cell carcinoma (35,36). In BLCA, FGFR1 overexpression has previously been reported in a subset of cases (37,38) and others have demonstrated that FGFR1 expression in BLCA cell lines induced EMT phenotypic changes (28). Here, we show that BLCA cell lines with highest EMT scores and FGFR1 expression were the most sensitive to FGFR1 inhibition. Similar to our findings, Tomlinson *et al.* showed that EMT-high JMSU1 cells were sensitive to an FGFR inhibitor. Further *in vivo* studies should investigate whether FGFR inhibitors alone or in combination with other therapies could tackle the biological complexity of sarcomatoid BLCA.

Overall, our findings provide insights into the underlying biology of Ba/Sq BLCA progression and sarcomatoid dedifferentiation with potential clinical implications.

ACKNOWLEDGMENTS

We could like to thank Elodie Chapeaublanc for her assistance in data management and GEO submission. This work was supported by a grant from Ligue Nationale Contre le Cancer (JF, LC, YA, FR, IBP) as an associated team (Equipe labellisée), the "Carte d'Identité des Tumeurs" program initiated, developed and funded by Ligue Nationale Contre le Cancer, and by the French Institut National du Cancer INCa (PRT- K 2013, Programme de Recherche Translationnelle en Cancérologie, “DIATRIBBE”). JF was supported by the Fondation ARC pour la recherche sur le cancer and by Groupe Pasteur Mutualité. LC was supported by the Fondation Médicale pour la Recherche. High-throughput sequencing was performed by the ICGex NGS platform of the Institut Curie supported by the grants ANR-10-EQPX-03 (Equipex) and ANR-10-INBS-09-08 (France Génomique Consortium) from the Agence Nationale de la Recherche ("Investissements d’Avenir" program), by the ITMO-Cancer Aviesan (Plan Cancer III) and by the SiRIC-Curie program (SiRIC Grant INCa-DGOS- 465 and INCa-DGOS-Inserm_12554).

STATEMENT OF AUTHOR CONTRIBUTIONS

Study concept and design: Fontugne, Wong, Bernard-Pierrot, Radvanyi, Allory

Data acquisition: Fontugne, Wong, Karboul, Maille, Neyret-Kahn, Rapinat, Gentien

Pathology review: Fontugne, Sibony, Allory

RNA-seq data pre-processing: Wong, Baulande

Data analysis: Fontugne, Cabel

Manuscript writing: Fontugne, Bernard-Pierrot, Radvanyi, Allory

Critical revision of the manuscript: all authors

Supervision: Bernard-Pierrot, Radvanyi, Allory

REFERENCES

1. Bray F, Ferlay J, Soerjomataram I, Siegel RL, Torre LA, Jemal A. Global cancer statistics 2018: GLOBOCAN estimates of incidence and mortality worldwide for 36 cancers in 185 countries. CA Cancer J Clin. 2018;68(6):394–424.
2. Humphrey PA, Moch H, Cubilla AL, Ulbright TM, Reuter VE. The 2016 WHO Classification of Tumours of the Urinary System and Male Genital Organs—Part B: Prostate and Bladder Tumours. Eur Urol [Internet]. 2016 Jul;70(1):106–19. Available from: https://linkinghub.elsevier.com/retrieve/pii/S0302283816002050
3. Babjuk M, Burger M, Compérat EM, Gontero P, Mostafid AH, Palou J, et al. European Association of Urology Guidelines on Non-muscle-invasive Bladder Cancer (TaT1 and Carcinoma In Situ) - 2019 Update. Eur Urol. 2019;76(5):639–57.
4. Knowles MA, Hurst CD. Molecular biology of bladder cancer: New insights into pathogenesis and clinical diversity. Nat Rev Cancer [Internet]. 2015;15(1):25–41. Available from: http://dx.doi.org/10.1038/nrc3817
5. Shin K, Lim A, Odegaard JI, Honeycutt JD, Kawano S, Hsieh MH, et al. Cellular origin of bladder neoplasia and tissue dynamics of its progression to invasive carcinoma. Nat Cell Biol. 2014;16(5):469–78.
6. Van Batavia J, Yamany T, Molotkov A, Dan H, Mansukhani M, Batourina E, et al. Bladder cancers arise from distinct urothelial sub-populations. Nat Cell Biol. 2014;16(10):982–91.
7. Kamoun A, de Reyniès A, Allory Y, Sjödahl G, Robertson AG, Seiler R, et al. A Consensus Molecular Classification of Muscle-invasive Bladder Cancer[Formula presented]. Eur Urol. 2020;77(4):420–33.

8. Sjödahl G, Eriksson P, Liedberg F, Höglund M. Molecular classification of urothelial carcinoma: global mRNA classification versus tumour-cell phenotype classification. J Pathol. 2017;242(1):113–25.

9. Damrauer JS, Hoadley KA, Chism DD, Fan C, Tignanelli CJ, Wobker SE, et al. Intrinsic subtypes of high-grade bladder cancer reflect the hallmarks of breast cancer biology. Proc Natl Acad Sci U S A. 2014;111(8):3110–5.

10. Choi W, Porten S, Kim S, Willis D, Plimack ER, Hoffman-Censits J, et al. Identification of Distinct Basal and Luminal Subtypes of Muscle-Invasive Bladder Cancer with Different Sensitivities to Frontline Chemotherapy. Cancer Cell [Internet]. 2014;25(2):152–65. Available from: http://dx.doi.org/10.1016/j.ccr.2014.01.009

11. Robertson AG, Kim J, Al-Ahmadie H, Bellmunt J, Guo G, Cherniack AD, et al. Comprehensive Molecular Characterization of Muscle-Invasive Bladder Cancer. Cell. 2017;171(3):540-556.e25.

12. Guo CC, Majewski T, Zhang L, Yao H, Bondaruk J, Wang Y, et al. Dysregulation of EMT Drives the Progression to Clinically Aggressive Sarcomatoid Bladder Cancer. Cell Rep. 2019;27(6):1781-1793.e4.

13. Genitsch V, Kollár A, Vandekerkhove G, Blarer J, Furrer M, Annala M, et al. Morphologic and genomic characterization of urothelial to sarcomatoid transition in muscle-invasive bladder cancer. Urol Oncol. 2019;37(11):826–36.

14. Lopez-Beltran A, Henriques V, Montironi R, Cimadamore A, Raspollini MR, Cheng L. Variants and new entities of bladder cancer. Histopathology. 2019;74(1):77–96.

15. Rebouissou S, Bernard-Pierrot I, De Reyniès A, Lepage ML, Krucker C,

Chapeaublanc E, et al. EGFR as a potential therapeutic target for a subset of muscle-invasive bladder cancers presenting a basal-like phenotype. Sci Transl Med. 2014;6(244).

16. Barth I, Schneider U, Grimm T, Karl A, Horst D, Gaisa NT, et al. Progression of urothelial carcinoma in situ of the urinary bladder: a switch from luminal to basal phenotype and related therapeutic implications. Virchows Arch. 2018;472(5):749–58.

17. Sjödahl G, Eriksson P, Patschan O, Marzouka NAD, Jakobsson L, Bernardo C, et al. Molecular changes during progression from nonmuscle invasive to advanced urothelial carcinoma. Int J Cancer. 2020;146(9):2636–47.

18. Vasconcelos-Nóbrega C, Colaço A, Lopes C, Oliveira PA. BBN as an urothelial carcinogen. In Vivo (Brooklyn). 2012;26(4):727–39.

19. Fantini D, Glaser AP, Rimar KJ, Wang Y, Schipma M, Varghese N, et al. A Carcinogen-induced mouse model recapitulates the molecular alterations of human muscle invasive bladder cancer. Oncogene [Internet]. 2018;37(14):1911–25. Available from: http://dx.doi.org/10.1038/s41388-017-0099-6

20. Wilkerson MD, Hayes DN. ConsensusClusterPlus: A class discovery tool with confidence assessments and item tracking. Bioinformatics. 2010;26(12):1572–3.

21. Lindskrog SV, Prip F, Lamy P, Taber A, Groeneveld CS, Birkenkamp-Demtröder K, et al. An integrated multi-omics analysis identifies prognostic molecular subtypes of non-muscle-invasive bladder cancer. Nat Commun [Internet]. 2021;12(1):1–18. Available from: http://dx.doi.org/10.1038/s41467-021-22465-w

22. Nueda MJ, Tarazona S, Conesa A. Next maSigPro: Updating maSigPro bioconductor package for RNA-seq time series. Bioinformatics. 2014;30(18):2598–602.

23. De Reynies A, Jaurand MC, Renier A, Couchy G, Hysi I, Elarouci N, et al. Molecular classification of malignant pleural mesothelioma: Identification of a poor prognosis subgroup linked to the epithelial-to-mesenchymal transition. Clin Cancer Res. 2014;20(5):1323–34.

24. Ohtani M, Kakizoe T, Nishio Y, Sato S, Sugimura T, Fukushima S, et al. Sequential changes of mouse bladder epithelium during induction of invasive carcinomas by n-butyl-n-(4-hydroxybutyl)nitrosamine. Cancer Res. 1986;46:2001–4.

25. Marzouka NAD, Eriksson P, Rovira C, Liedberg F, Sjödahl G, Höglund M. A validation and extended description of the Lund taxonomy for urothelial carcinoma using the TCGA cohort. Sci Rep. 2018;8(1):1–12.

26. Sjödahl G, Lauss M, Lövgren K, Chebil G, Gudjonsson S, Veerla S, et al. A molecular taxonomy for urothelial carcinoma. Clin Cancer Res. 2012;18(12):3377–86.

27. Iida K, Mimura J, Itoh K, Ohyama C, Fujii-Kuriyama Y, Shimazui T, et al. Suppression of AhR signaling pathway is associated with the down-regulation of UDP-glucuronosyltransferases during BBN-induced urinary bladder carcinogenesis in mice. J Biochem. 2010;147(3):353–60.

28. Tomlinson DC, Baxter EW, Loadman PM, Hull MA, Knowles MA. FGFR1-induced Epithelial to mesenchymal transition through MAPK/PLCγ/COX-2-mediated mechanisms. PLoS One. 2012;7(6).

29. Black PC, Brown GA, Inamoto T, Shrader M, Arora A, Siefker-Radtke AO, et al. Sensitivity to epidermal growth factor receptor inhibitor requires E-cadherin expression in urothelial carcinoma cells. Clin Cancer Res. 2008;14(5):1478–86.

30. Shrader M, Pino MS, Brown G, Black P, Adam L, Bar-Eli M, et al. Molecular correlates of gefitinib responsiveness in human bladder cancer cells. Mol Cancer Ther. 2007;6(1):277–85.

31. Sfakianos JP, Daza J, Hu Y, Anastos H, Bryant G, Bareja R, et al. Epithelial plasticity can generate multi-lineage phenotypes in human and murine bladder cancers. Nat Commun [Internet]. 2020;11(1):1–16. Available from: http://dx.doi.org/10.1038/s41467-020-16162-3

32. Guo CC, Fine SW, Epstein JI. Noninvasive Squamous Lesions in the Urinary Bladder. Am J Surg Pathol [Internet]. 2006 Jul;30(7):883–91. Available from: http://journals.lww.com/00000478-200607000-00014

33. Wullweber A, Strick R, Lange F, Sikic D, Taubert H, Wach S, et al. Bladder tumor subtype commitment occurs in carcinoma in situ driven by key signaling pathways including ECM Remodeling. Cancer Res. 2021;81(6):1552–66.

34. Stuart JM, Segal E, Koller D, Kim SK. A gene-coexpression network for global discovery of conserved genetic modules. Science (80-). 2003;302(5643):249–55.

35. Acevedo VD, Gangula RD, Freeman KW, Li R, Zhang Y, Wang F, et al. Inducible FGFR-1 Activation Leads to Irreversible Prostate Adenocarcinoma and an Epithelial-to-Mesenchymal Transition. Cancer Cell. 2007;12(6):559–71.

36. Nguyen PT, Tsunematsu T, Yanagisawa S, Kudo Y, Miyauchi M, Kamata N, et al. The FGFR1 inhibitor PD173074 induces mesenchymal-epithelial transition

through the transcription factor AP-1. Br J Cancer. 2013;109(8):2248–58.

37. Tomlinson DC, Lamont FR, Shnyder SD, Knowles MA. Fibroblast growth factor receptor 1 promotes proliferation and survival via activation of the mitogen-activated protein kinase pathway in bladder cancer. Cancer Res. 2009;69(11):4613–20.

38. Lim S, Koh MJ, Jeong HJ, Cho NH, Choi YD, Cho DY, et al. Fibroblast growth factor receptor 1 overexpression is associated with poor survival in patients with resected muscle invasive urothelial carcinoma. Yonsei Med J. 2016;57(4):831–9.

FIGURE LEGENDS

Figure 1. Mice develop a spectrum of bladder lesions with increasing BBN exposure, comparable to human carcinogenesis

A. Study design and workflow: 40 mice were exposed to BBN for a maximum of 14 weeks and sacrificed and different time points. Highest stage lesions in each bladder were morphologically and immunohistochemically characterized. RNA-seq was performed on a subset of cases of all stages of progression following laser-capture microdissection. Five non-exposed mice were used as controls. Representative haematoxylin, eosin, saffron-stained images of the spectrum of lesions identified during BBN exposure: pre-carcinomatous (B), early carcinomatous (C) and infiltrating tumours (D). Infiltrating tumours either harboured areas of squamous differentiation (purple insets) or had pure sarcomatoid morphology (pink insets). Scale bars: 100µm. E. Total number of each lesion type according to the time point of sacrifice after the start of BBN exposure, reporting the highest stage lesion in each bladder. F. Proportion of squamous or sarcomatoid differentiation in all observed infiltrating cases.

BBN: N-butyl-N-(4-hydroxybutyl)-nitrosamine; LCM: laser-capture microdissection; MIBC: muscle-invasive bladder cancer

Figure 2. Transcriptomic progression groups in BBN-exposed mice are associated with morphological stage and differentiation

A. Principal component analysis using the top 2000 genes with most varying expression shows separation of samples according to stage along component 1 and according to differentiation along component 2. B. Iterative hierarchical consensus clustering using the top 2000 genes with most varying expression identified the k=3 solution as the most stable grouping of BBN samples (”pam” clustering, “ward.D2” linkage). C. Silhouette plot metric shows high cohesion of each sample to its group. D. Sample tracking plot showing grouping of BBN samples according to k=3 to k=8 solutions. In k=3 solution, samples are roughly grouped in control and pre-carcinogenic stages (green), non-infiltrating carcinogenic stages (yellow) and infiltrating tumours (purple). Starting at k=5, infiltrating tumours were always separated according to differentiation (squamous vs. sarcomatoid), regardless of stage (pT1 or MIBC).

BBN: N-butyl-N-(4-hydroxybutyl)-nitrosamine; CIS: carcinoma *in situ*; MIBC: muscle-invasive bladder cancer

Figure 3. Molecular classification of BBN-induced lesions switches from luminal to basal during progression

A. Molecular classification of each sample according to three classification systems: consensus, BASE47 and LundTax. A gradual increase in correlation to basal subtypes in consensus and BASE47 systems was observed during progression. B. Gene expression heatmap of markers of basal, luminal and mesenchymal-like markers during progression. Colour key represents row mean-centered values of log2-transformed normalized expression. C. Dynamic expression profiles of mean basal keratins (Krt6a, Krt6b, Krt5, Krt14), luminal markers and mesenchymal-like markers during progression. *p*-values: two-sided Kruskal-Wallis test. D. Representative images of vimentin IHC staining (brown) with hematoxylin counterstain. Vimentin staining is observed in the stroma of squamous tumours (left). In contrast, vimentin is expressed by the tumour cells in sarcomatoid tumours (right).

BBN: N-butyl-N-(4-hydroxybutyl)-nitrosamine; CIS: carcinoma *in situ*; IHC: immunohistochemistry

Figure 4. RNA-seq analysis using a time-course approach reveals distinct dynamic profiles of co-expressed genes during progression

A. The 924 genes with significant temporal changes (Next maSigPro algorithm) were clustered into 5 distinct profiles of dynamic changes during progression. Clusters 1-3 (green, blue and teal) represented successive waves of downregulation. Cluster 4 (orange) grouped genes with an upregulation in early stages of carcinogenesis leading to Ba/Sq invasive tumours. Genes in cluster 5 (pink) were upregulated at infiltration and were highest in sarcomatoid tumours. B. Heatmap representation of the 5 clusters of genes with significant temporal changes during progression. Symbols of potential genes of interest in each cluster are shown. Colour key represents row mean-centered values of log2-transformed normalized expression. C. Over-representation analysis of the genes in each progression cluster using terms from GO-BP and KEGG databases.

Figure 5. BBN progression cluster 4 shows relevance to human disease and identifies NMIBC patients at risk of progression

A. Unsupervised consensus clustering using the expression of all human orthologs of BBN progression cluster 4 genes in a large dataset combining NMIBCs and MIBCs (Sjödahl 2012 cohort, n=308) separates cluster 4 metagene-“low” samples, essentially composed of pTa tumours, from cluster 4 metagene-“high” tumours, mostly composed of pT1 and MIBCs. B. Mean progression cluster 4 metagene score increases with stage in human tumours from the Sjödahl 2012 dataset (n=308). ***: *p*-value < 0.001, two-sided Wilcoxon test. C. Proportion of NMIBC tumours (Sjödahl 2012 cohort, n= 213) in each NMIBC class according to BBN cluster 4 metagene score group. ***: *p*-value < 0.001, two-sided Fisher’s exact test. D. Kaplan-Meier curves of progression-free survival (PFS) probability when stratifying patients according to tertiles of cluster 4 metagene score values in the UROMOL NMIBC cohort (n=535).

Figure 6. BBN-induced sarcomatoid tumours resemble the human counterpart and reveal an EGFR to FGFR1 switch with sarcomatoid dedifferentiation

A. Molecular classes of BBN and human sarcomatoid tumours (Guo *et al.* cohort, n = 28) according to consensus and LundTax systems. B. Significant overlap in differentially expressed genes (DEGs) between BBN sarcomatoid (n=4) vs. non-sarcomatoid (n=8) infiltrating samples and human Ba/Sq sarcomatoid (n= 21) vs. Ba/Sq non-sarcomatoid samples (n=29). *p*-value: one-sided Fisher's exact test using all orthologs identified in the BBN cohort as background genes. C. Functional over-representation analysis with GO-BP gene sets, using up- (red) or downregulated (blue) genes between sarcomatoid vs. non-sarcomatoid samples shows common dysregulated pathways in BBN and human sarcomatoid tumours, which are related to epithelial-mesenchymal transition (EMT). D. Comparison of EGFR and FGFR1 regulon activity between sarcomatoid and non-sarcomatoid samples in our BBN cohort and in human samples (Guo *et al*. with Ba/Sq (n=50) and non-Ba/Sq (n=62) tumours). *p*-value: two-sided Wilcoxon test. E. Effect of FGFR1 and EGFR knockdown in bladder cancer cell lines (n=29, Achilles Project, Broad Institute) is associated with EMT score.

SUPPLEMENTARY FIGURE LEGENDS

Supplementary figure 1. Representative images of BBN-induced bladder lesions of different stages of carcinogenesis before (top) and after (bottom) laser capture microdissection.

Supplementary figure 2. Transcriptomic progression groups in BBN-exposed mice are associated with morphological stage and differentiation

A. Principal component analysis using the top 2000 genes with most varying expression shows separation of samples according to stage along component 1 and according to differentiation along component 2. B. Iterative hierarchical consensus clustering using the top 2000 genes with most varying expression identified the k=3 solution as the most stable grouping of BBN samples (”pam” clustering, “ward.D2” linkage). C. Silhouette plot metric shows high cohesion of each sample to its group. D. Sample tracking plot showing grouping of BBN samples according to k=3 to k=8 solutions. In k=3 solution, samples are roughly grouped in control and pre-carcinogenic stages (green), non-infiltrating carcinogenic stages (yellow) and infiltrating tumours (purple). Starting at k=5, infiltrating tumours were always separated according to differentiation (squamous vs sarcomatoid), not stage (pT1 vs MIBC).

BBN: N-butyl-N-(4-hydroxybutyl)-nitrosamine; CIS: carcinoma in situ; MIBC: muscle-invasive bladder cancer

Supplementary figure 3. BBN progression cluster 4 shows relevance to human disease

A. Unsupervised consensus clustering of a dataset combining NMIBCs and MIBCs (CIT cohort, n=177) using the human orthologs of BBN progression cluster 4 genes separates cluster 4-“low” samples, essentially composed of pTa tumours, from cluster

4-“high” tumours, mostly composed of pT1 and MIBCs. B. Mean progression cluster 4 metascore significantly increases with stage in human tumours from the CIT dataset (n=177). *p*-value: Kruskal-Wallis test. C. Proportion of NMIBC tumours from the CIT cohort (n= 90) in each NMIBC class according to BBN cluster 4 metascore group. *p*-value: two-sided Fisher’s exact test. D. Mean progression cluster 4 metascore increases with stage in human tumours in another NMIBC cohort (UROMOL, n=535). *p*-value: Kruskal-Wallis test.

Supplementary figure 4. Differential gene expression analysis between sarcomatoid and non-sarcomatoid infiltrating BBN samples

A. Volcano plot representation of differentially expressed genes (DEGs) showing 369 up- and 630 down-regulated genes with a | log2FC | ≥0.58 and an adjusted *p*-value <0.05. B. Top GO-BP terms found enriched in the up- or down-regulated genes between sarcomatoid (sarc.) and non-sarcomatoid (non-sarc.) infiltrating BBN samples. C and D. In Gene Set Enrichment Analysis using ranked DEGs between sarcomatoid and non-sarcomatoid infiltrating BBN samples, Hallmark epithelial-mesenchymal transition pathway was among the significantly enriched pathways (adjusted *p*-value <0.05).

Supplementary figure 5. FGFR1 regulon, expression and knockout effect are associated with EMT, which is increased in sarcomatoid tumours

A. Comparison of EMT scores between sarcomatoid and non-sarcomatoid samples in both BBN and human Ba/Sq samples (Guo *et al*. cohort). *p*-value: two-sided Wilcoxon test. B. Heatmap of regulon activity profiles during progression in BBN-induced tumours, focusing on 22 regulators previously shown to play a role in bladder cancer. C. and D. GSEA of EGFR and FGFR1 regulons using ranked DEGs between sarcomatoid and non-sarcomatoid infiltrating BBN samples (C) and ranked DEGs between sarcomatoid and non-sarcomatoid infiltrating Ba/Sq Guo cohort samples (D). E. and F. Pearson correlation between EGFR or FGFR1 regulon activity and EMT score in our BBN cohort (E) and in the Guo *et al.* cohort (F). G and H. Pearson correlation of FGFR1 expression and EMT score in a large transcriptomic dataset of MIBCs (G, TCGA, n=408) and in bladder cancer cell lines (H, CCLE, n=36). I and J. Pearson correlations between FGFR1 KO CERES score (Achilles Project, Broad institute) and FGFR1 expression (I) or EMT score (J) in CCLE bladder cancer cell lines (n=29).

Sarc: sarcomatoid; CIS: carcinoma *in situ*

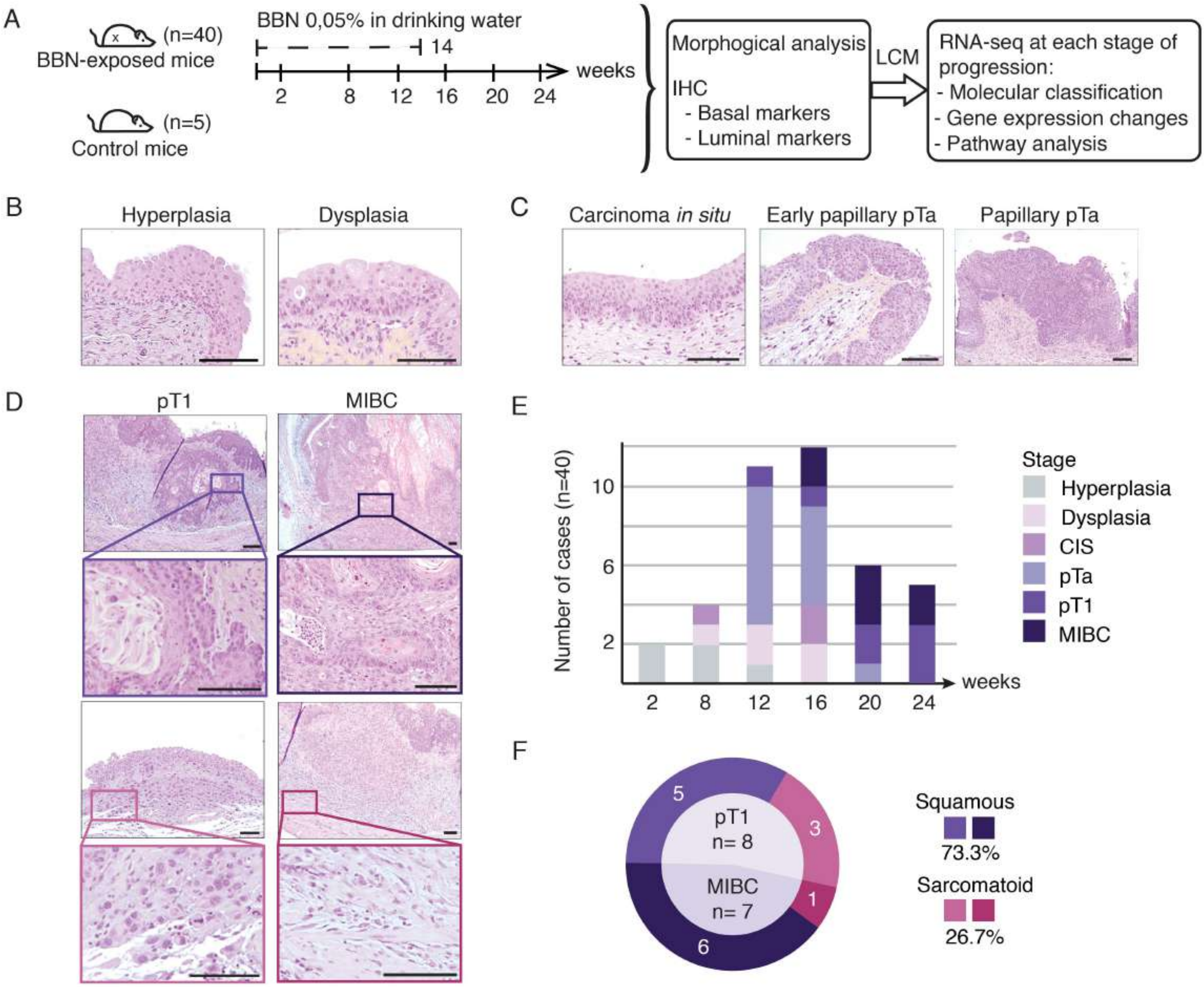
A
(n=40)
BBN-exposed mice
(n=5)
Control mice
BBN 0,05% in drinking water
14
weeks
2
8
12
16
20
24
Morphogical analysis
IHC
- Basal markers
- Luminal markers
LCM
RNA-seq at each stage of progression:
- Molecular classification
- Gene expression changes
- Pathway analysis
B
Hyperplasia
Dysplasia
C
Carcinoma in situ
Early papillary pTa
Papillary pTa
D
pT1
MIBC
E
Number of cases (n=40)
2
6
10
weeks
2
8
12
16
20
24
Stage
Hyperplasia
Dysplasia
CIS
pTa
pT1
MIBC
F
5
3
1
6
pT1
n= 8
MIBC
n= 7
Squamous
73.3%
Sarcomatoid
26.7%

Figure 1

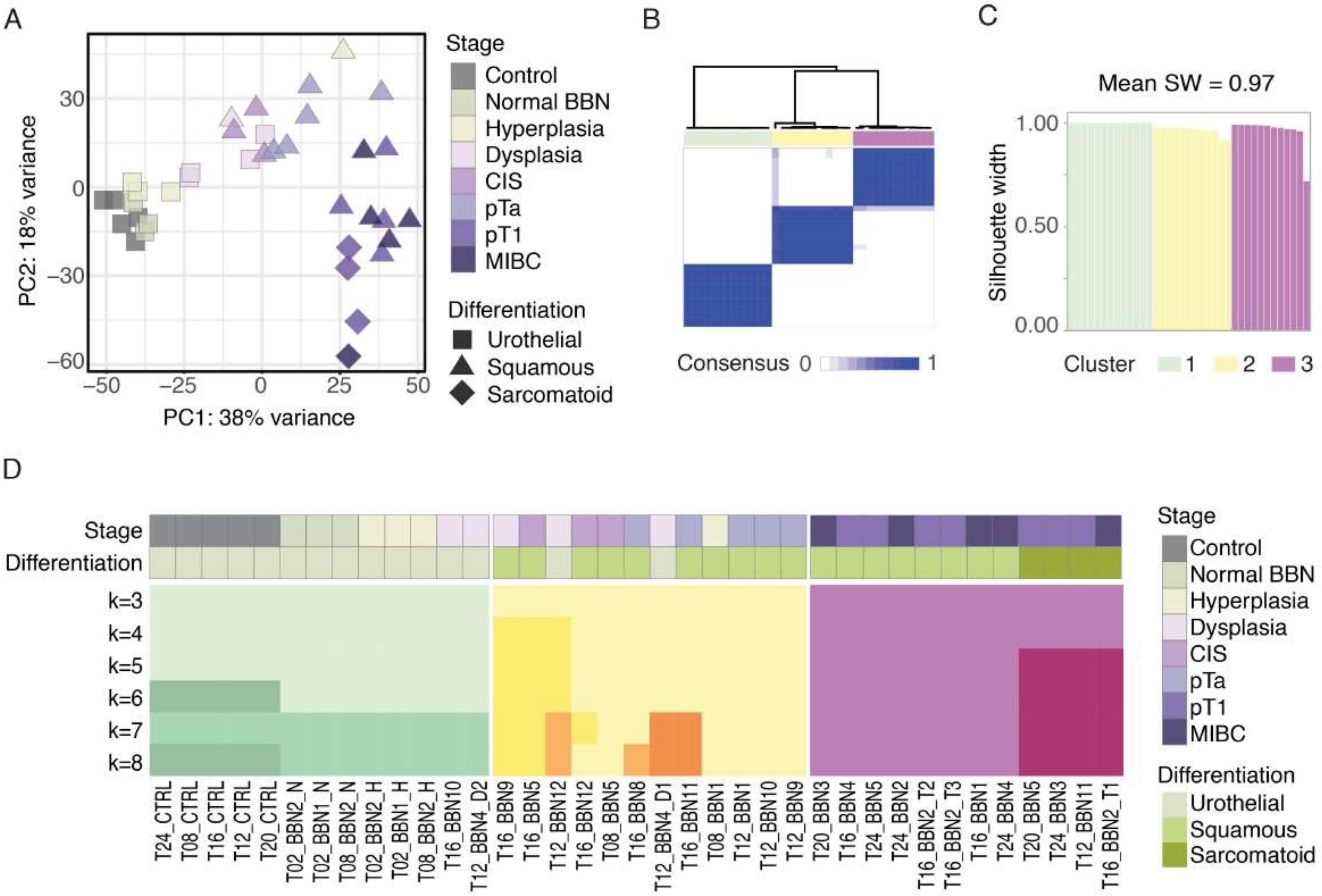
A
PC2: 18% variance
30
0
−30
−60
−50
−25
0
25
50
PC1: 38% variance
Stage
Control
Normal BBN
Hyperplasia
Dysplasia
CIS
pTa
pT1
MIBC
Differentiation
Urothelial
Squamous
Sarcomatoid
B
Consensus 0
1
C
Mean SW = 0.97
Silhouette width
1.00
0.50
0.00
Cluster
1
2
3
D
Stage
Differentiation
k=3
k=4
k=5
k=6
k=7
k=8
T24_CTRL
T08_CTRL
T16_CTRL
T12_CTRL
T20_CTRL
T02_BBN2_N
T02_BBN1_N
T08_BBN2_N
T02_BBN2_H
T02_BBN1_H
T08_BBN2_H
T16_BBN10
T12_BBN4_D2
T16_BBN9
T16_BBN5
T12_BBN12
T16_BBN12
T08_BBN5
T16_BBN8
T12_BBN4_D1
T16_BBN11
T08_BBN1
T12_BBN1
T12_BBN10
T12_BBN9
T20_BBN3
T16_BBN4
T24_BBN5
T24_BBN2
T16_BBN2_T2
T16_BBN2_T3
T16_BBN1
T24_BBN4
T20_BBN5
T24_BBN3
T12_BBN11
T16_BBN2_T1
Stage
Control
Normal BBN
Hyperplasia
Dysplasia
CIS
pTa
pT1
MIBC
Differentiation
Urothelial
Squamous
Sarcomatoid

Figure 2

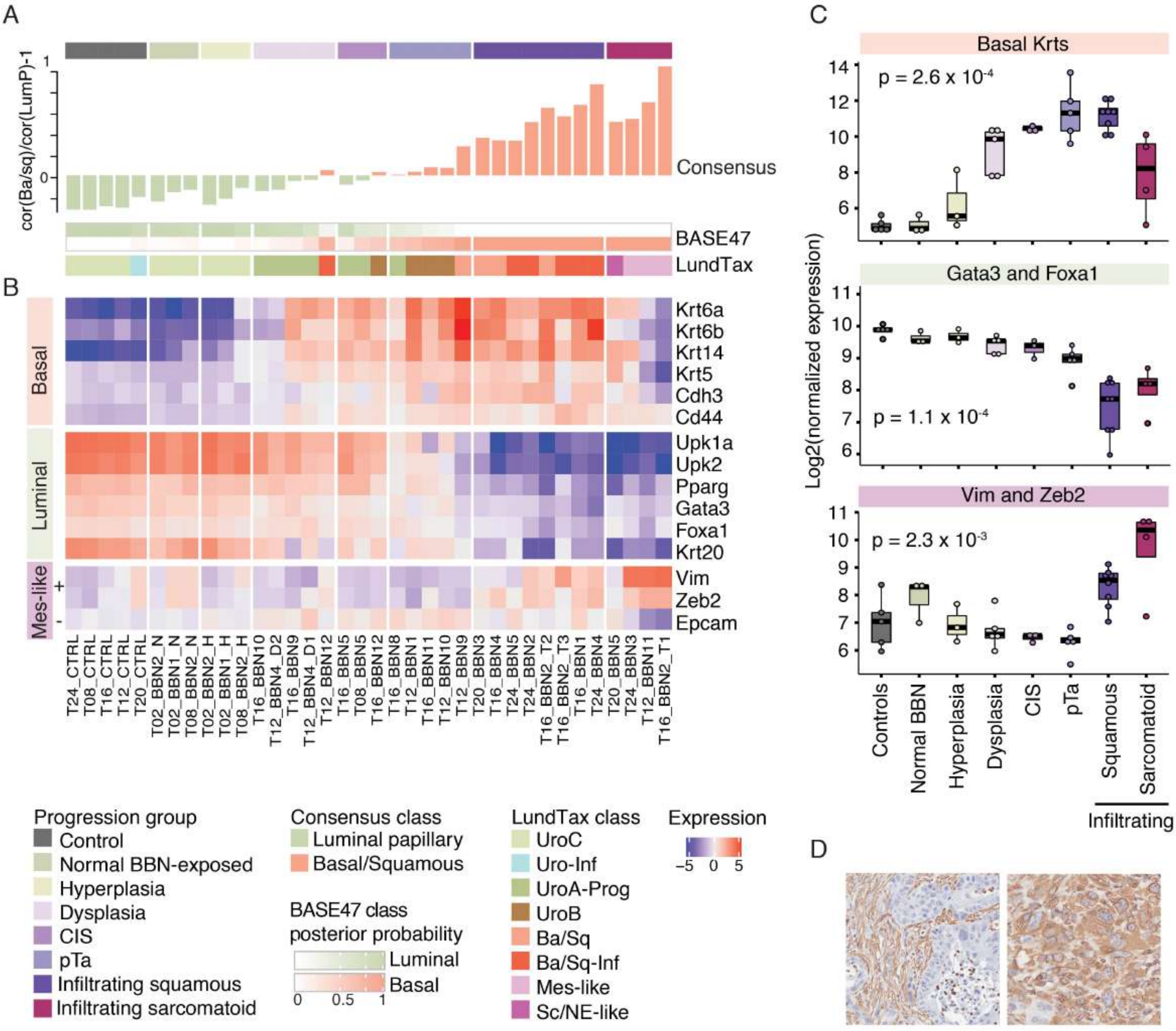
A
cor(Ba/sq)/cor(LumP)-1
1
0
Consensus
BASE47
LundTax
B
Basal
Luminal
Mes-like
+
-
Krt6a
Krt6b
Krt14
Krt5
Cdh3
Cd44
Upk1a
Upk2
Pparg
Gata3
Foxa1
Krt20
Vim
Zeb2
Epcam
T24_CTRL
T08_CTRL
T16_CTRL
T12_CTRL
T20_CTRL
T02_BBN2_N
T02_BBN1_N
T08_BBN2_N
T02_BBN2_H
T02_BBN1_H
T08_BBN2_H
T16_BBN10
T12_BBN4_D2
T16_BBN9
T12_BBN4_D1
T12_BBN12
T16_BBN5
T08_BBN5
T16_BBN12
T16_BBN8
T12_BBN1
T16_BBN11
T12_BBN10
T12_BBN9
T20_BBN3
T16_BBN4
T24_BBN5
T24_BBN2
T16_BBN2_T2
T16_BBN2_T3
T16_BBN1
T24_BBN4
T20_BBN5
T24_BBN3
T12_BBN11
T16_BBN2_T1
C
Log2(normalized expression)
Basal Krts
p = 2.6 x 10-4
14
12
10
8
6
Gata3 and Foxa1
p = 1.1 x 10-4
11
10
9
8
7
6
Vim and Zeb2
p = 2.3 x 10-3
11
10
9
8
7
6
Controls
Normal BBN
Hyperplasia
Dysplasia
CIS
pTa
Squamous
Sarcomatoid
Infiltrating
Progression group
Control
Normal BBN-exposed
Hyperplasia
Dysplasia
CIS
pTa
Infiltrating squamous
Infiltrating sarcomatoid
Consensus class
Luminal papillary
Basal/Squamous
BASE47 class
posterior probability
Luminal
Basal
0
0.5
1
LundTax class
UroC
Uro-Inf
UroA-Prog
UroB
Ba/Sq
Ba/Sq-Inf
Mes-like
Sc/NE-like
Expression
-5
0
5
D

Figure 3

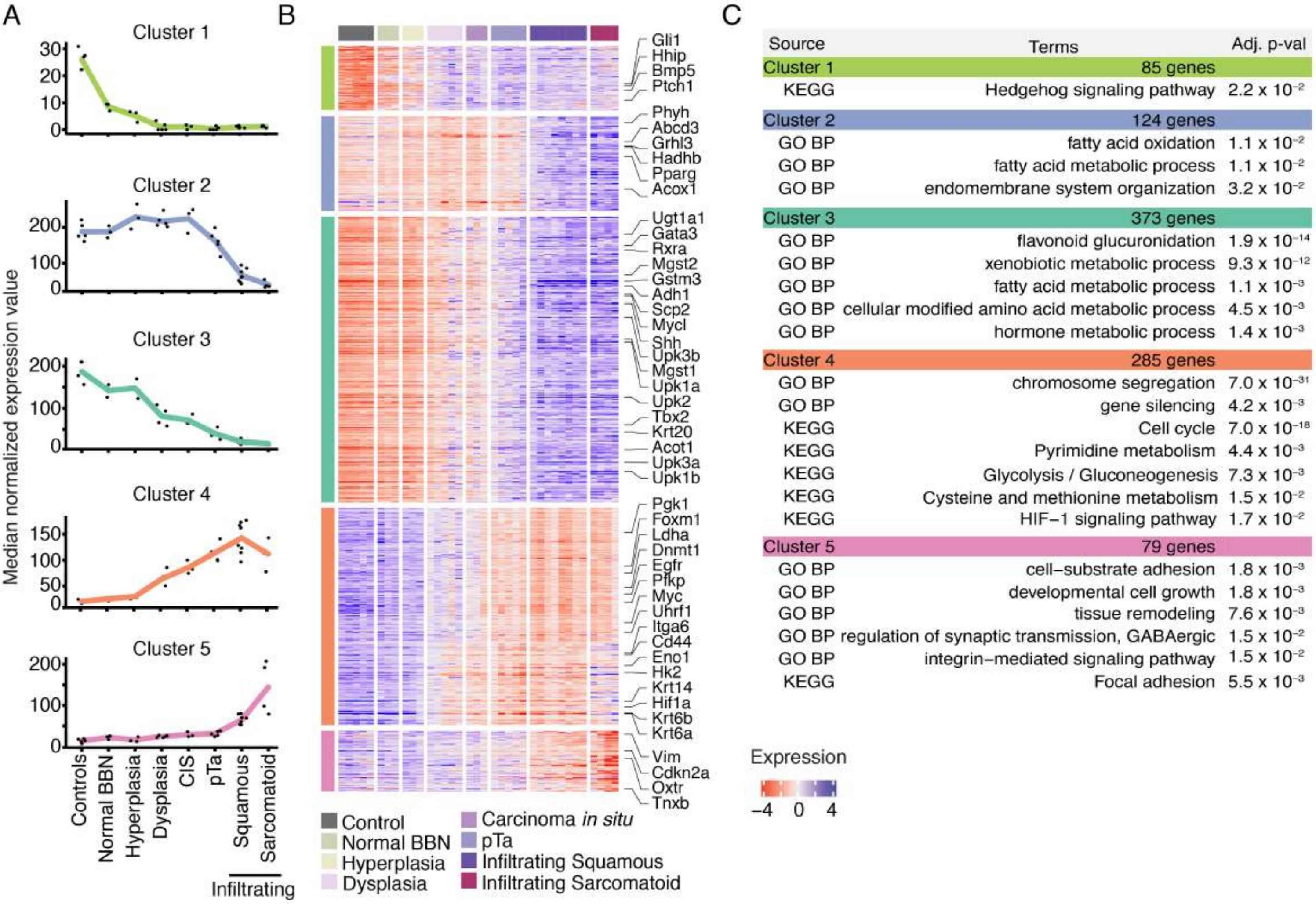

Source	Terms	Adj. p-val
Cluster 1	85 genes	
KEGG	Hedgehog signaling pathway	2.2×10^{-2}
Cluster 2	124 genes	
GO BP	fatty acid oxidation	1.1×10^{-2}
GO BP	fatty acid metabolic process	1.1×10^{-2}
GO BP	endomembrane system organization	3.2×10^{-2}
Cluster 3	373 genes	
GO BP	flavonoid glucuronidation	1.9×10^{-14}
GO BP	xenobiotic metabolic process	9.3×10^{-12}
GO BP	fatty acid metabolic process	1.1×10^{-3}
GO BP	cellular modified amino acid metabolic process	4.5×10^{-3}
GO BP	hormone metabolic process	1.4×10^{-3}
Cluster 4	285 genes	
GO BP	chromosome segregation	7.0×10^{-31}
GO BP	gene silencing	4.2×10^{-3}
KEGG	Cell cycle	7.0×10^{-18}
KEGG	Pyrimidine metabolism	4.4×10^{-3}
KEGG	Glycolysis / Gluconeogenesis	7.3×10^{-3}
KEGG	Cysteine and methionine metabolism	1.5×10^{-2}
KEGG	HIF−1 signaling pathway	1.7×10^{-2}
Cluster 5	79 genes	
GO BP	cell−substrate adhesion	1.8×10^{-3}
GO BP	developmental cell growth	1.8×10^{-3}
GO BP	tissue remodeling	7.6×10^{-3}
GO BP	regulation of synaptic transmission, GABAergic	1.5×10^{-2}
GO BP	integrin−mediated signaling pathway	1.5×10^{-2}
KEGG	Focal adhesion	5.5×10^{-3}

Figure 4

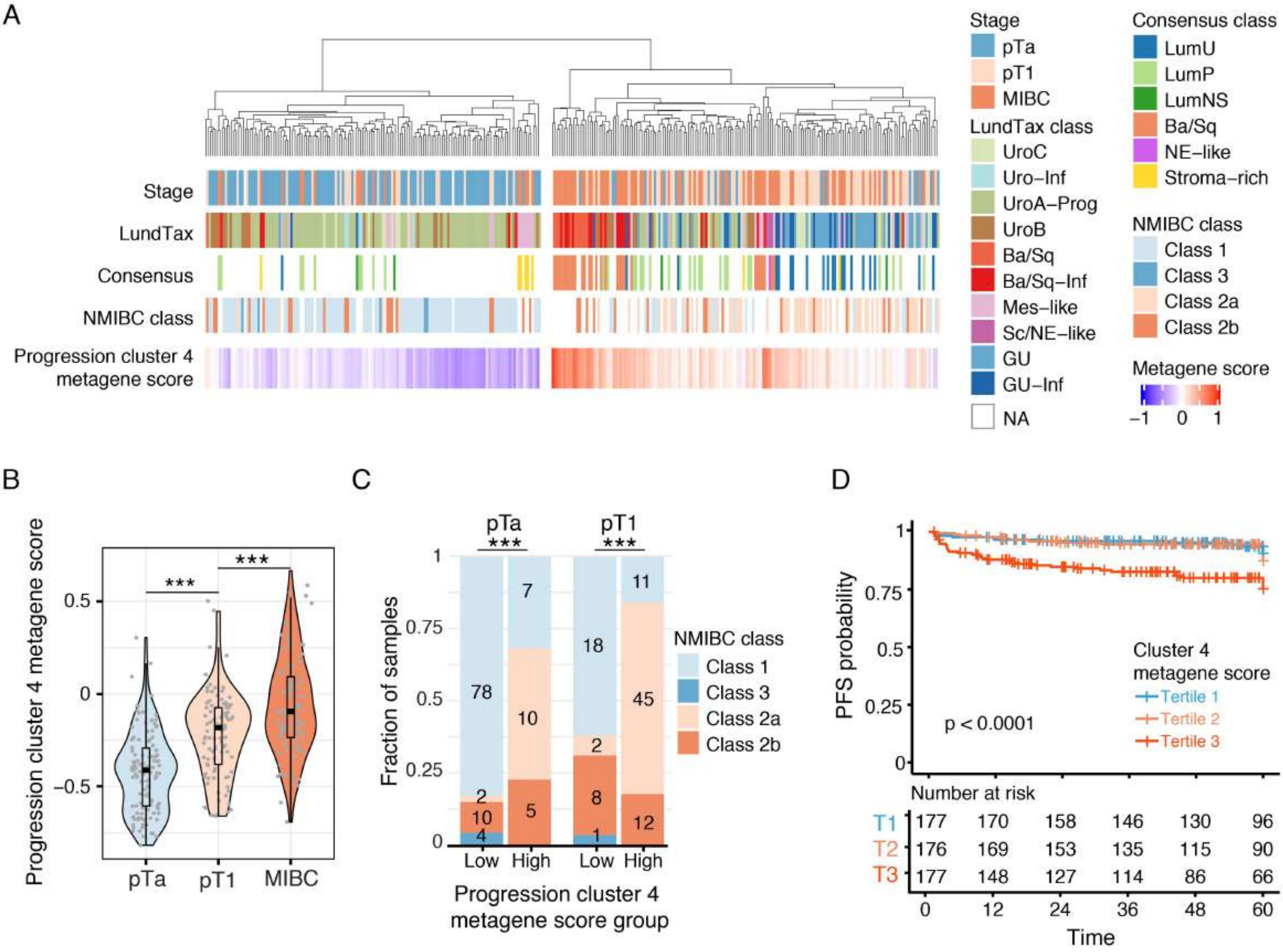
A
Stage
LundTax
Consensus
NMIBC class
Progression cluster 4 metagene score
Stage
pTa
pT1
MIBC
LundTax class
UroC
Uro−Inf
UroA−Prog
UroB
Ba/Sq
Ba/Sq−Inf
Mes−like
Sc/NE−like
GU
GU−Inf
NA
Consensus class
LumU
LumP
LumNS
Ba/Sq
NE−like
Stroma−rich
NMIBC class
Class 1
Class 3
Class 2a
Class 2b
Metagene score
−1
0
1
B
Progression cluster 4 metagene score
0.5
0
−0.5
***
***
pTa
pT1
MIBC
C
Fraction of samples
1
0.75
0.5
0.25
0
pTa
***
pT1
***
78
2
10
4
7
10
5
18
2
8
1
11
45
12
Low
High
Low
High
Progression cluster 4 metagene score group
NMIBC class
Class 1
Class 3
Class 2a
Class 2b
D
PFS probability
1
0.75
0.5
0.25
0
p < 0.0001
Cluster 4 metagene score
Tertile 1
Tertile 2
Tertile 3
Number at risk
T1 177 170 158 146 130 96
T2 176 169 153 135 115 90
T3 177 148 127 114 86 66
0
12
24
36
48
60
Time

Figure 5

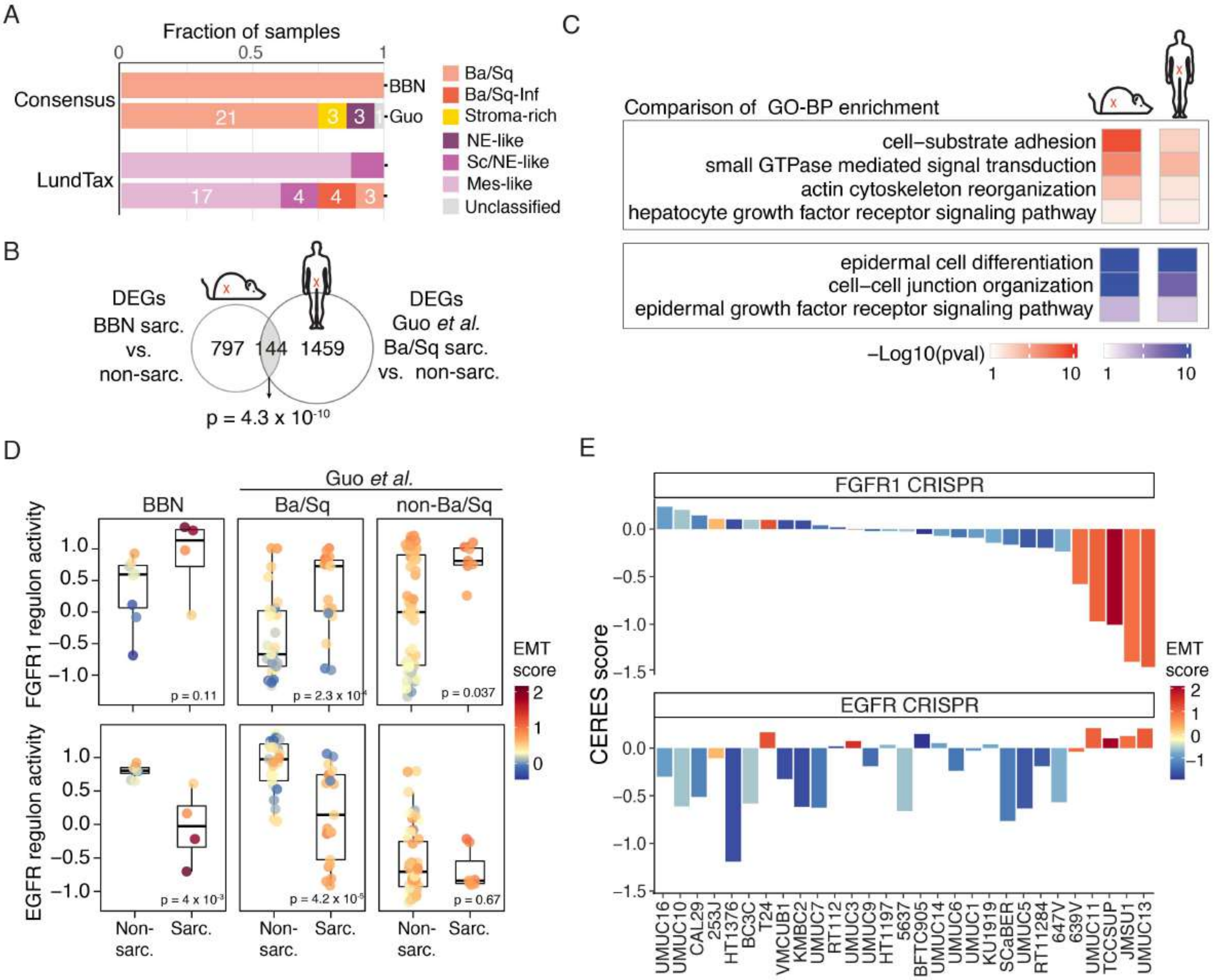
A
Fraction of samples
0
0.5
1
Consensus
LundTax
BBN
Guo
21
3
3
17
4
4
3
Ba/Sq
Ba/Sq-Inf
Stroma-rich
NE-like
Sc/NE-like
Mes-like
Unclassified
B
DEGs BBN sarc. vs. non-sarc.
797
144
1459
DEGs Guo et al. Ba/Sq sarc. vs. non-sarc.
p = 4.3 x 10-10
C
Comparison of GO-BP enrichment
cell−substrate adhesion
small GTPase mediated signal transduction
actin cytoskeleton reorganization
hepatocyte growth factor receptor signaling pathway
epidermal cell differentiation
cell−cell junction organization
epidermal growth factor receptor signaling pathway
−Log10(pval)
1
10
1
10
D
BBN
Guo et al.
Ba/Sq
non-Ba/Sq
FGFR1 regulon activity
EGFR regulon activity
1.0
0.5
0.0
−0.5
−1.0
p = 0.11
p = 2.3 x 10-4
p = 0.037
p = 4 x 10-3
p = 4.2 x 10-5
p = 0.67
Non-sarc.
Sarc.
EMT score
2
1
0
E
FGFR1 CRISPR
EGFR CRISPR
CERES score
0.0
−0.5
−1.0
−1.5
EMT score
2
1
0
−1
UMUC16
UMUC10
CAL29
253J
HT1376
BC3C
T24
VMCUB1
KMBC2
UMUC7
RT112
UMUC3
UMUC9
HT1197
5637
BFTC905
UMUC14
UMUC6
UMUC1
KU1919
SCaBER
UMUC5
RT11284
647V
639V
UMUC11
TCCSUP
JMSU1
UMUC13

Figure 6

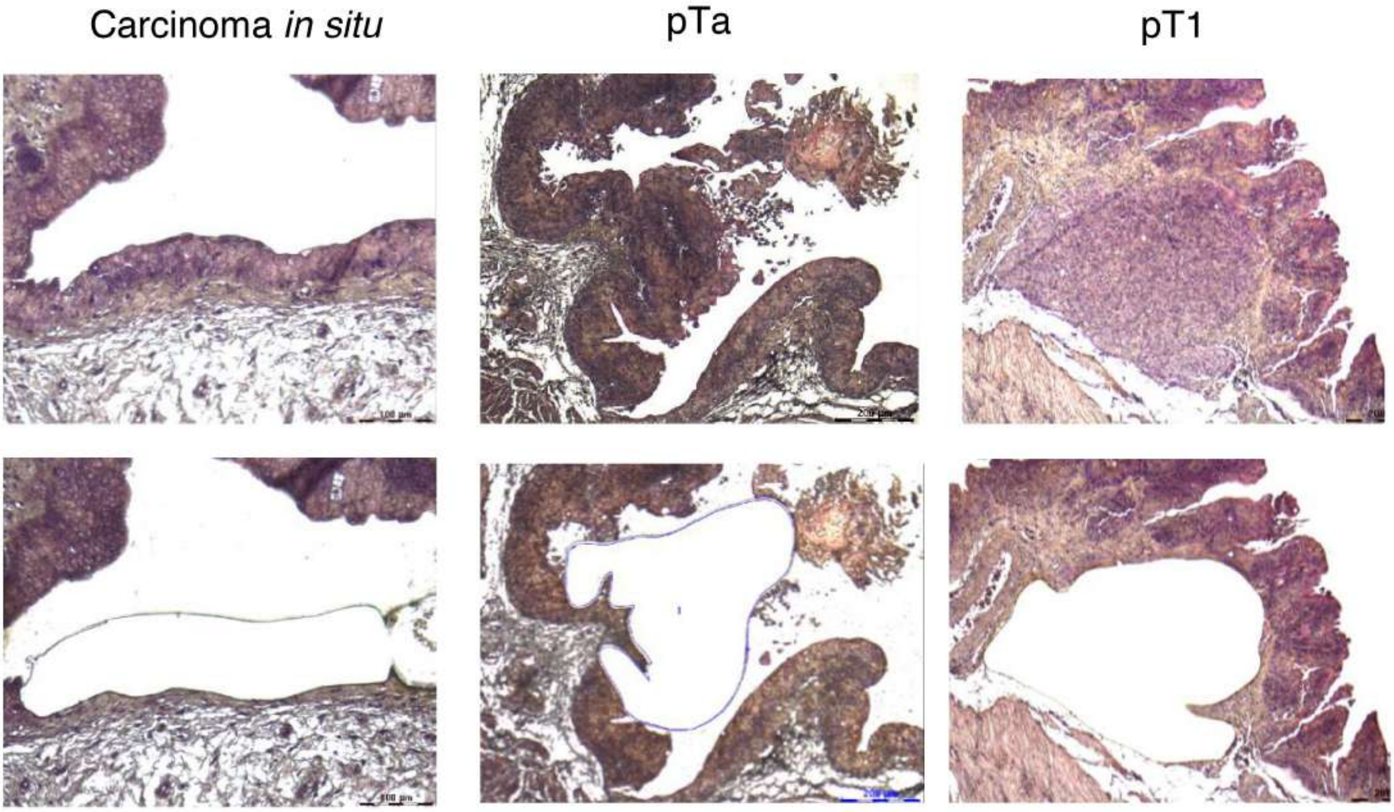

Carcinoma *in situ*

pTa

pT1

Supplementary figure 1

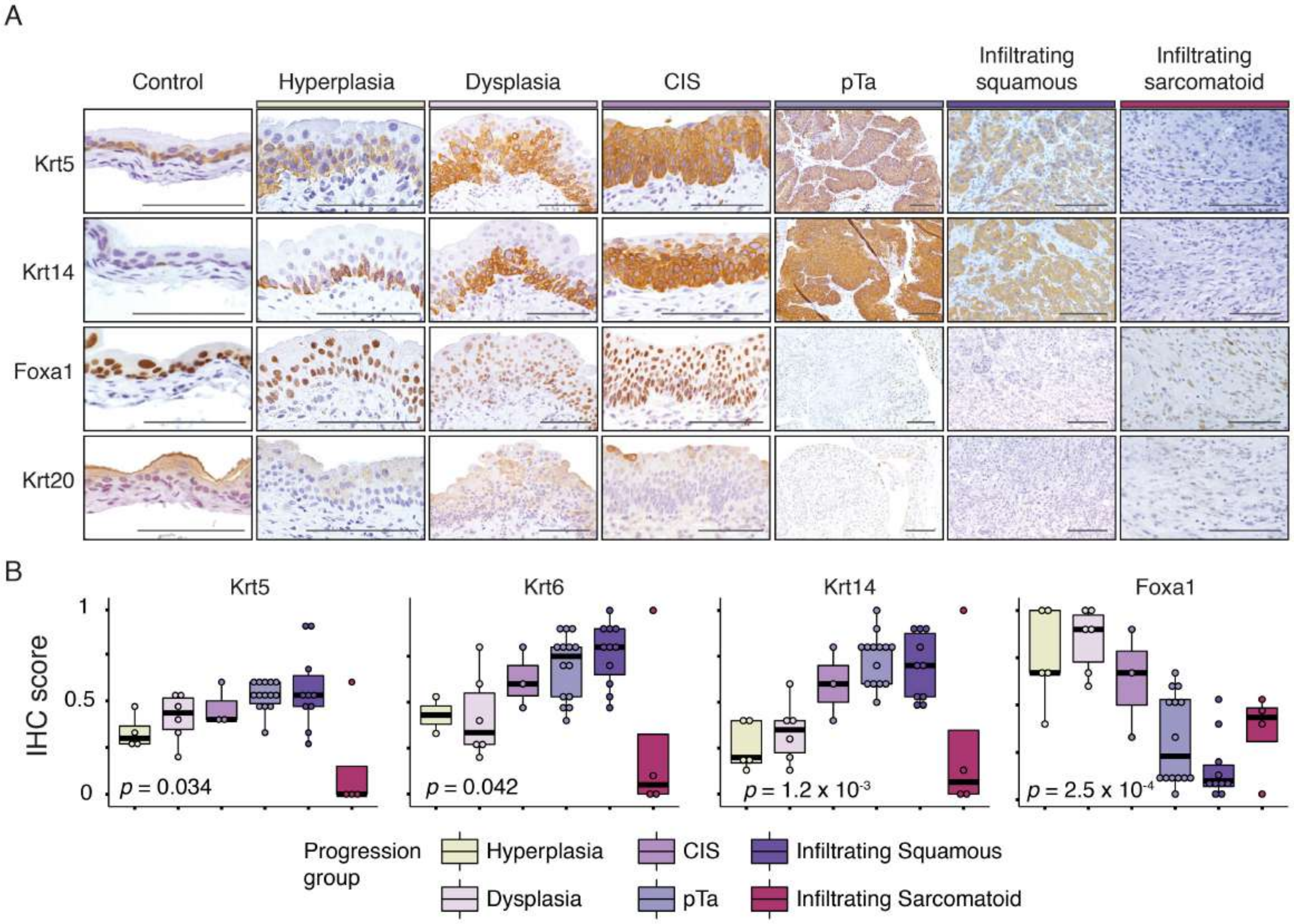

Supplementary figure 2

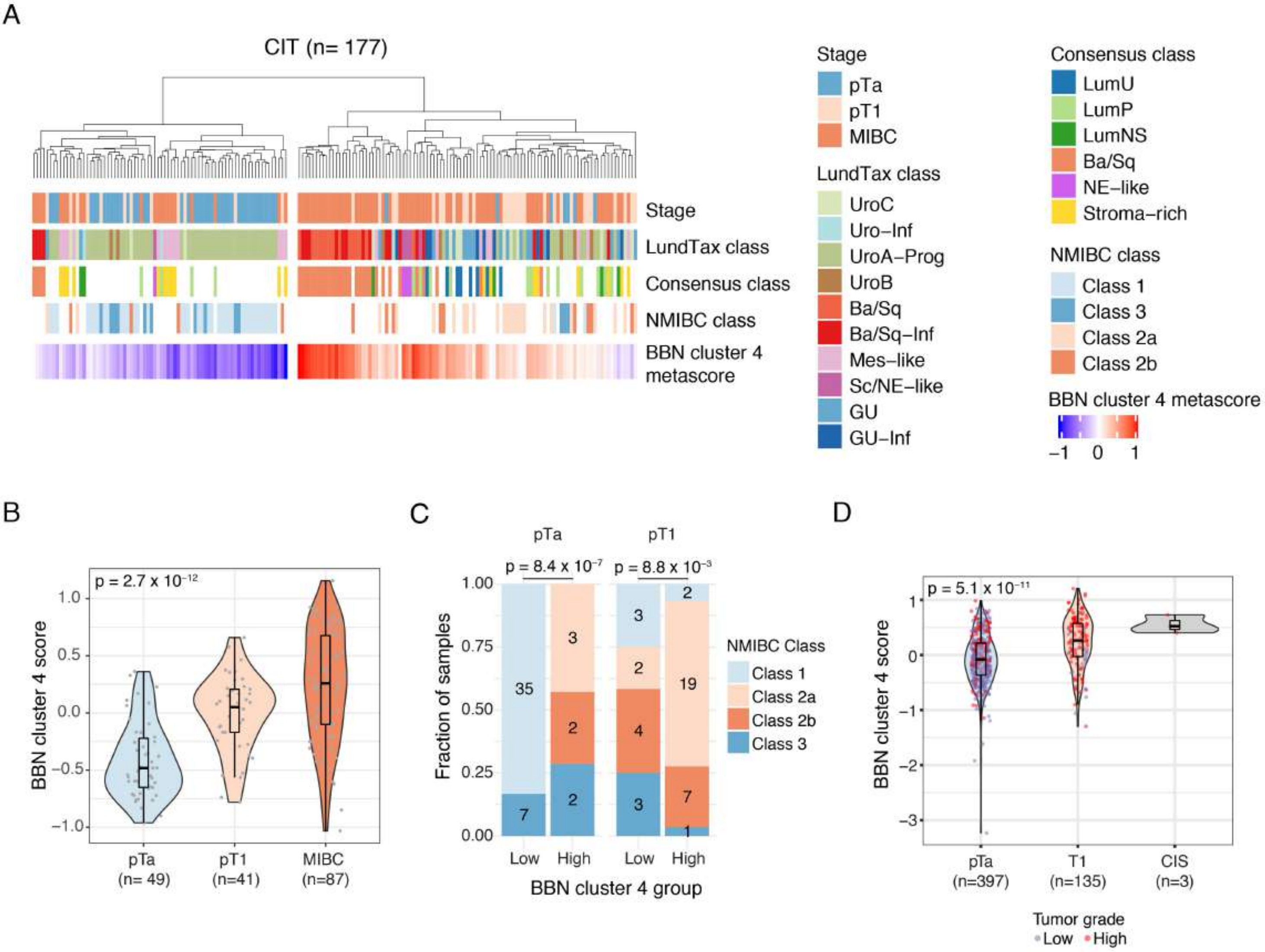

Supplementary figure 3

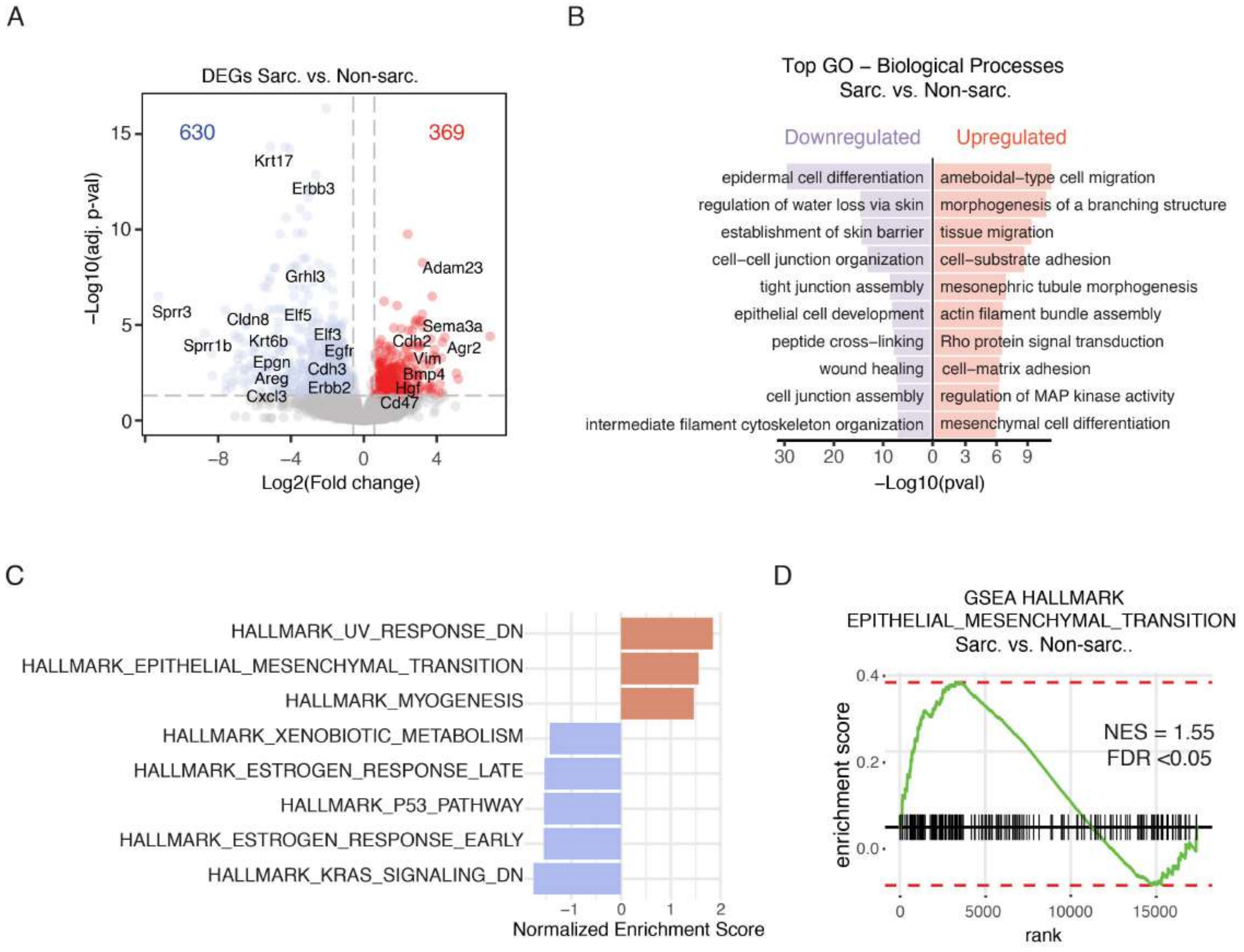

Supplementary figure 4

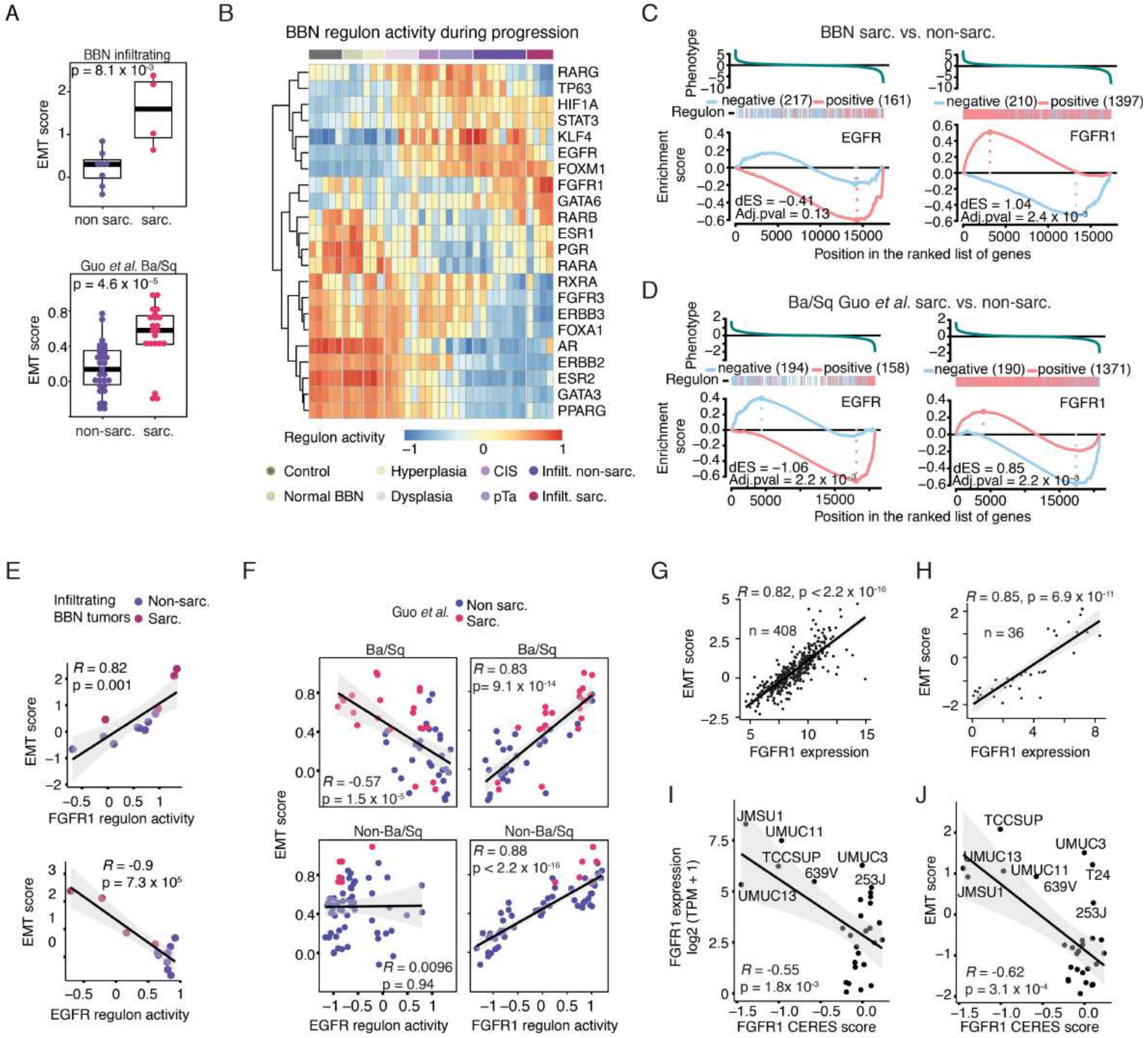

Supplementary figure 5

Multi-stage expression in BBN mouse model reveals progression-associated molecular changes in basal/squamous and sarcomatoid bladder carcinogenesis

SUPPLEMENTARY METHODS

BBN-induced mouse model

Forty 8-week-old male C57BL/6 mice were exposed to N-butyl-N-(4-hydroxybutyl)-nitrosamine (BBN) 0.05% in drinking water *ad libitum* for a maximum of 14 weeks. After 14 weeks, drinking water was switched to regular tap water. To obtain tumors of all stages of carcinogenesis, groups of mice were sacrificed at different time points: at 4, 10, 14, 16 and 24 weeks after the start of BBN exposure. The exposed mice from weeks 4, 10 and 14 were withdrawn from BBN exposure 2 weeks prior to sacrifice (at weeks 2, 8 and 12 from start of BBN exposure) and switched to untreated tap water in order to ensure elimination of all carcinogenic metabolites before sacrifice. In parallel, 5 control mice received only non-treated drinking water. Controls were sacrificed at different time points in order to obtain controls of ages similar to that of the treated group. Bladders were removed, cut in half sagittaly and fixed in 10% formalin before paraffin embedding.

Immunohistochemistry

For immunohistochemical assessment of luminal and basal markers, we used KRT5 (1:6000, Poly19055 clone, Biolegend), KRT6A (1:5000, Cusabio CSB-PA224586), KRT14 (1:20000, Poly19053, Biolegend), FOXA1 (1:4000, ab23738, Abcam) and KRT20 (1:500, ab118574, Abcam) rabbit polyclonal antibodies on the Autostainer 480 (Lab Vision). Subtype markers were quantified using quickscore method, in which a semi-quantitative assessment of the intensity of KRT5, KRT6A, KRT14 cytoplasmic stainings and FOXA1 nuclear staining (0: absent, 1: weak, 2: moderate, 3: strong staining) was performed. To calculate the staining score (quickscore), the mean global intensity was multiplied by the percentage of positive cells and then divided by 300 to normalize scores between 0 and 1.

Tissue microdissection

We performed laser-capture microdissection (LCM) of morphologically and immunohistochemically characterized lesions using a UV laser-based microscopy system. FFPE blocks were freshly cut and 12 flanking 6µm-thick sections were mounted on polyethylene-naphthalate (PEN) membrane-coated glass slides (Leica Microsystems 11505158). Dried PEN-membrane slides were stained using a previously published LCM-compatible hematoxylin and eosin (H&E) staining protocol (1). H&E-stained lesions were immediately microdissected using a UV laser-based microscopy system (LMD7000, Leica Microsystems). UV laser-cut fragments from 3 to 12 flaking sections were collected in the cap of 0.2ml tubes. Successful capture of fragments for each case was visually verified by focusing the microscope of the cap collector. Tubes were immediately frozen at -80°C before nucleotide extraction.

RNA extraction, library preparation and sequencing

RNA was extracted from microdissected BBN-induced lesions and non-exposed urothelia using the RNeasy FFPE kit (Qiagen). RNA quality was assessed using the Bioanalyzer 2100 system (Agilent) with RNA 6000 Pico kits (Agilent). Libraries were prepared with a low input-appropriate kit, Ovation SoLo RNA-Seq system (NuGEN), from 4ng of total RNA. The resulting libraries were qualified with the High Sensitivity DNA Kit (Agilent) using the Bioanalyzer 2100 system (Agilent), then sequenced on a HiSeq2500 (Illumina) with the Rapid Run mode and paired-end 100bp read length. Reads were mapped to the mouse reference genome (mm10) using STAR (version 2.6.1a). Reads were counted with the *featureCounts* function from Rsubreads (version 1.24.2). The resulting count table was normalized using DESeq2 method and log2-transformed for downstream analyses.

Identification of sample groups

Iterative unsupervised clustering analysis was performed into k=2 to k=10 clustering solutions using ConsensusClusterPlus R package (v1.48.0) (2), testing the top 1000 to 5000 genes (in increments of 1000) with the most varying expression, ranked by median absolute deviation. To test the robustness of each cluster solution, we compared the assignment of each sample to each k using multiple clustering ("pam" and "hc") and linkage methods ("ward.D2", "average", "complete"). Silhouette metrics were plotted to identify and select the most robust clustering solution. For all figure representations, we chose the k=3 solution using the top 2000 most varying genes, with "pam" clustering, "ward.D2" linkage and "pearson" correlation as distance metric. Represented results show the top 2000 genes with most varying expression, "pam" clustering and "ward.D2" linkage.

Of note, one hyperplasia was distant from all other hyperplastic lesions in the PCA (Figure 2) and was assigned to cluster 2. Considered an outlier, this hyperplasia case was excluded from downstream transcriptomic analyses. Histological review of the hyperplastic lesions revealed that the outlier case was the only one with squamous metaplasia.

Gene expression changes during progression

To identify significant expression changes during progression, we used an R package designed for RNA-seq time-course data, Next maSigPro (v1.56.0) (22). We used progression stages as time points in the experimental design matrix. Next maSigPro two-step regression algorithm was applied to normalized counts using degree 4, goodness-of-fit R^2=0.7 and FDR=0.05 parameters. Genes with significant temporal changes were grouped into k=2 to k=8 clustering solutions. Functional enrichment was evaluated for each k solution with ClusterProfiler (v 3.12.0) (using GO-Biological processes and KEGG databases) and ReactomePA (v1.28.0) R packages. The lowest k solution capturing the most patterns of co-expression changes and grouping biologically related genes was selected as the final clustering solution (k=5).

Pairwise differential gene expression analyses in sarcomatoid samples

Genes with a |log2FC| >0.58 and a Benjamini-Hochberg adjusted *p*-value <0 .05 were considered significantly differentially expressed. Functional enrichment of the differentially expressed genes was evaluated using clusterProfiler (v3.12.0) with terms from GO-biological processes and KEGG datatbases. Gene set enrichment analysis (GSEA) was performed using human orthologs with fgsea (v1.10.1) R package using Hallmark v7.1 gene sets.

Regulon activity

We first performed a Transcriptional Network Inference from the TCGA MIBC RNA-seq data (n= 414, obtained using GDC query, project "TCGA-BLCA"), using the RTN R package (version 2.12.0) (3). We used this regulatory network (TNI class object) to calculate a regulon activity score for each sample in our BBN samples (n=36) et and the Guo *et al.* (n=112) cohort using the *tni.gsea2* function, which calculates two-tailed GSEA tests. The regulon activity profiles represent each sample's regulon activity relative to other samples in each cohort. The individual GSEA plots for FGFR1 and EGFR regulons were performed with the *tna.plot.gsea2* function, using the fold changes of each of the 2 regulon target genes, obtained from pairwise differential analyses, as described above (infiltrating sarcomatoid vs. infiltrating non-sarcomatoid in the BBN cohort, Ba/Sq sarcomatoid vs. Ba/Sq non sarcomatoid in the Guo cohort).

Statistical analysis

All statistical and bioinformatics analyses were conducted in R software version 3.6.1. The association between a continuous and a categorical variable was determined using two-sided Wilcoxon (2 categories) or Kruskal-Wallis (>2 categories) tests. Pearson correlation was used for all calculated correlation coefficients. Proportions were compared using two sided Fisher's exact test, except for the overrepresentation analysis of the overlap in differentially expressed genes between BBN and human sarcomatoid cases, where one-sided Fisher's exact test was applied, using all detected genes with human orthologs as the background gene set. For Kaplan Meier analyses testing the association of the progression cluster 4 metagene score and progression-free survival, we divided the UROMOL samples based on tertile segmentation of the metagene score values (calculated as the mean expression of the human orthologs of cluster 4 genes). Log-rank *P* values were calculated to test the association between progression-free survival and low, intermediate and high metagene expression groups using survminer R package (v0.4.7). A *p*-value < 0.05 was set to be statistically significant in all analyses. All gene expression heatmaps show mean-centered log2-transformed normalized counts of each represented gene. For all clusterings shown with heatmaps, we used default parameters of complexHeatmap R package (Complete clustering method and Euclidean distance).

Public data

Expression data for Guo *et al.* sarcomatoid (4) and Sjödahl 2012 (5) cohorts were obtained from Gene Expression Omnibus (GSE128192 and GSE32894) using the GEOquery R package (v2.52.0). Expression data and clinical information regarding NMIBC samples from the UROMOL project were obtained from the supplementary material of the original publication (6). CCLE bladder cancer cell line expression and CERES scores were downloaded from the DepMap repository (https://depmap.org/portal/download/) (7).

REFERENCES

1. Espina V, Wulfkuhle JD, Calvert VS, VanMeter A, Zhou W, Coukos G, et al. Laser-capture microdissection. Nat Protoc. 2006;1(2):586–603.

2. Wilkerson MD, Hayes DN. ConsensusClusterPlus: A class discovery tool with confidence assessments and item tracking. Bioinformatics. 2010;26(12):1572–3.

3. Castro MAA, De Santiago I, Campbell TM, Vaughn C, Hickey TE, Ross E, et al. Regulators of genetic risk of breast cancer identified by integrative network analysis. Nat Genet. 2015;48(1):12–21. Available from: http://dx.doi.org/10.1038/ng.3458

4. Guo CC, Majewski T, Zhang L, Yao H, Bondaruk J, Wang Y, et al. Dysregulation of EMT Drives the Progression to Clinically Aggressive Sarcomatoid Bladder Cancer. Cell Rep. 2019;27(6):1781-1793.e4.

5. Sjödahl G, Lauss M, Lövgren K, Chebil G, Gudjonsson S, Veerla S, et al. A molecular taxonomy for urothelial carcinoma. Clin Cancer Res. 2012;18(12):3377–86.

6. Lindskrog SV, Prip F, Lamy P, Taber A, Groeneveld CS, Birkenkamp-Demtröder K, et al. An integrated multi-omics analysis identifies prognostic molecular subtypes of non-muscle-invasive bladder cancer. Nat Commun. 2021;12(1):1–18. Available from: http://dx.doi.org/10.1038/s41467-021-22465-w

7. Meyers RM, Bryan JG, McFarland JM, Weir BA, Sizemore AE, Xu H, et al. Computational correction of copy number effect improves specificity of CRISPR-Cas9 essentiality screens in cancer cells. Nat Genet. 2017;49(12):1779–84.

11.2.3 Discussion et Perspectives

Dans cet article, l'évolution histologique et moléculaires des souris traitées par le BBN a montré qu'à un stade précoce, les tumeurs présentaient déjà des caractéristiques Ba/Sq, et il a été identifié un ensemble de gènes présentant des changements coordonnés au cours de la progression. L'étude des tumeurs sarcomatoïdes induites par le BBN a montré des similitudes avec les tumeurs humaines, et a révélé qu'un passage de la signalisation de l'EGFR au FGFR1 se produit avec la dédifférenciation sarcomatoïdes, avec des implications thérapeutiques potentielles.

Une expérience d'inhibition de FGFR *in vivo* sur un modèle PDX sarcomatoïde n'a pas montré d'efficacité en monothérapie, suggérant une différence d'efficacité in vitro et in vivo dont le(s) mécanisme(s) reste(nt) à explorer. Cette transition épithélio-mésenchymateuse et la dépendance possible à FGFR1 pourraient aussi être étudiées dans des tumeurs sarcomatoides non urinaires.

11.3 Criblage de cibles thérapeutiques potentielles modulées par PPARG

11.3.1 Introduction et objectif

Bien que le rôle protumorogénique de PPARG ait été démontré dans les tumeurs luminales de vessie *in vitro*, son rôle biologique est encore mal compris, même si un rôle dans l'immuno-évasion de ces tumeurs a été montré [55,60,61]. Néanmoins, dans notre laboratoire, il a été montré un effet des siRNA PPARG sur la viabilité, mais pas d'effet des drogues inhibitrices de PPARγ tel le T0070907 (données non montrées). Un effet des inhibiteurs de PPARγ avaient été observés dans la littérature, mais l'effet sur la prolifération n'est visible qu'après un traitement long (> 96 heures)[60]. Dans l'hypothèse où les drogues auraient un effet inhibiteur insuffisant, la recherche de cibles clés oncogéniques régulées par PPARγ et leur inhibition pourrait conduire à de nouvelles thérapies.

L'objectif de cette partie du travail était de mieux comprendre le rôle oncogénique de PPARγ en étudiant l'effet de l'inhibition des gènes cibles clés de PPARγ sur la prolifération de lignées dérivées de cancers de vessie, et ainsi potentiellement de permettre de déterminer de nouvelles cibles dans les tumeurs PPARγ-dépendantes.

11.3.2 Méthode de sélection des gènes

Pour sélectionner les gènes candidats cibles directs de PPARγ, plusieurs étapes avaient été utilisées et décrites dans le travail de Laure Coutos-Thévenot [63] que je résume ici (**Figure 1**) :

1. Sélection de gènes modulés par le siRNA PPARG et siRXRA dans la lignée SD48 (ayant un gain de *PPARG* et une forte expression/signature d'activation de PPARγ).
2. Sélection de gènes dont l'expression ARN était élevée dans les tumeurs avec une signature PPARγ « élevée » comparée aux tumeurs ayant une signature PPARγ « basse ».
3. Sélection de gènes ayant un site de liaison dans leur zone promotrice à *PPARG* et à *RXRA* (réalisation de 2 ChIP-seq de chacun des 2 partenaires dans la lignée SD48, en réplicat).
4. Parmi ces gènes, sélection de gènes ayant des altérations génomiques dans les tumeurs luminales par rapport aux tumeurs basales et/ou surexprimées (ARN) dans les lignées cellulaires dépendantes de PPARγ (SD48/UMUC9/RT4) par rapport à des lignées ayant une signature d'activation de PPARγ basse (UMUC3/VMCUB1/UMUC6).

L'intégration des gènes modulés par un siPPARG et siRXRA, des données de transcriptomique du TCGA des tumeurs de vessie, de ChIP-seq de PPARγ/RXRα et des données transcriptomiques ou génomiques des lignées cellulaires urinaires avait permis de sélectionner 25 gènes cibles directes de PPARγ.

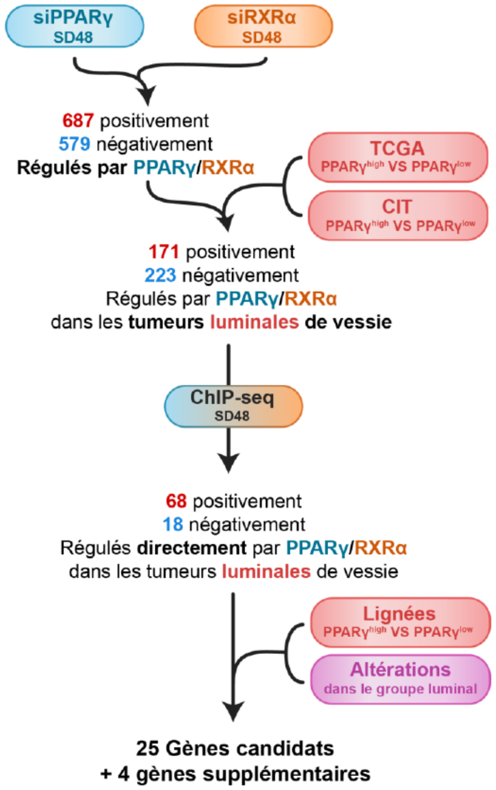

Figure 1 : Schéma récapitulant la méthode pour déterminer les gènes cibles candidats ayant un rôle potentiel majeur dans l'action de PPARγ (source [63]).

Parmi ces gènes, plusieurs étaient reliés au métabolisme lipidique (*ACSL5*, *FABP4*), au métabolisme (*PDK4*), au peroxysome (*PEX19*, PPARγ étant un promoteur du peroxysome), de la réponse anti-oxydante (*GPX2*), permettant de cibler des voies biologiques variées.

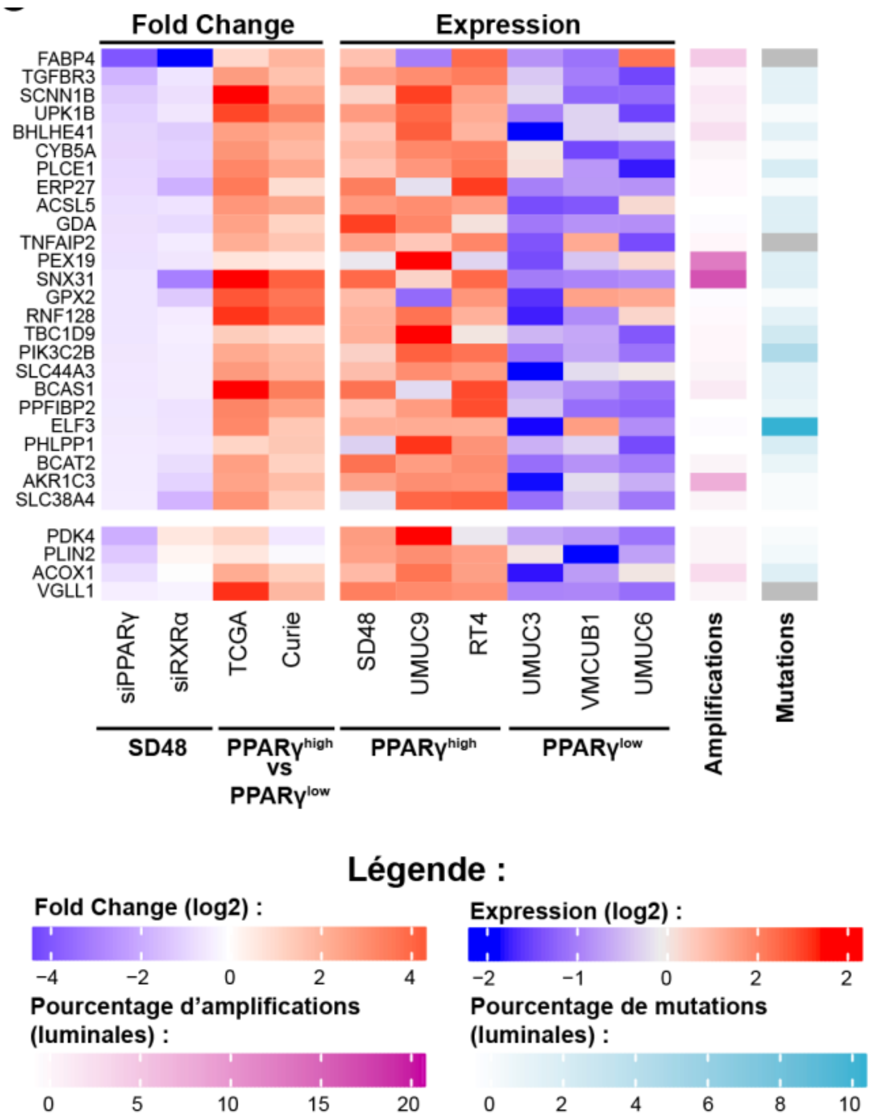

Figure 2 : Liste des 25 gènes sélectionnés, ainsi que leur modulation sous siRNA PPARG et RXRA, leur expression dans les données du TCGA ou du CIT-Curie [57], dans des lignées cellulaires ayant une signature élevée ou non de PPARγ, et selon la présence ou non d'une altération génomique (amplification/mutation). Source [63].

11.3.3 Résultats

Pour déterminer si ces 25 gènes avaient bien un effet protumorigénique, j'ai réalisé un screening de viabilité cellulaire (par Celltiter Glo après 96h de transfection) en utilisant un pool de 4 siRNA par gène (provenant de Dharmacon, concentration de 20nM) dans des lignées luminales de vessie (SD48, RT4, UMUC9, cultivées dans du FBS 5%).

J'ai ensuite déconvolué ce pool pour les gènes ayant eu un effet d'au moins 20% sur la viabilité cellulaire sur une des expériences réalisée, en me basant particulièrement sur la lignée SD48 qui a été la plus utilisée dans le processus de sélection des gènes (N=10 : *ACSL5, ERP27, TNFAIP2, SLC44A3, ELF3, TBC1D9, PLIN2, PEX19, SCNN1B, SLC38A4, VGLL1*) (Ex d'une expérience dans la lignée SD48 **Figure 3**).

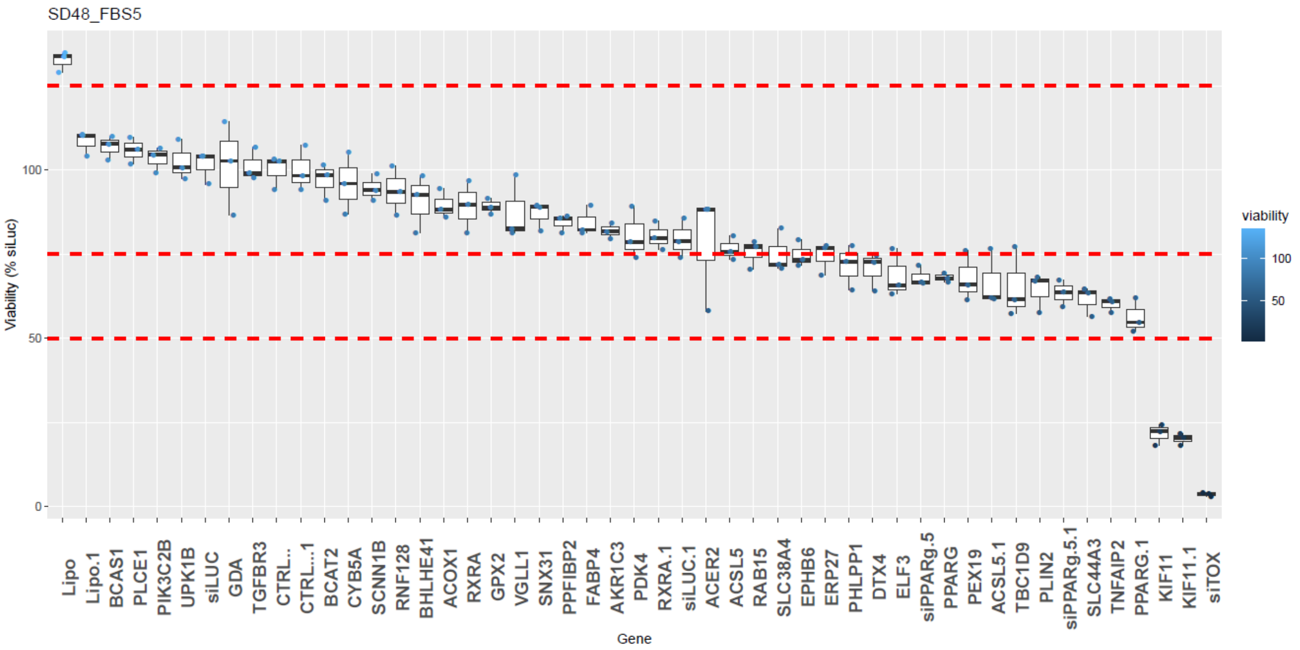

Figure 3 : Viabilité par rapport au contrôle (siLUC) du screening de pool de siRNA (20nM), exemple d'une expérience dans la lignée SD48 (culture FBS5%, lecture de la viabilité à 96h par CelltiterGlo).

Note : certains gènes sont en double car présents sur chacune des 2 plaques (ex PPARG/PPARG1). Le siRNA « PPARG » provient du pool de siRNA de Dharmacon, le siPPARG5 est un siRNA testé et connu du laboratoire provenant de Qiagen). Contrôles positifs = siTOX, Contrôles négatifs = siCTRL.

Je n'ai pas retrouvé lors de la déconvolution dans la lignée SD48 au moins 2 siRNA, pour un gène donné, entrainant une baisse de la viabilité de plus de 25% (avec contrôle positif PPARG ~25-50% de baisse de la viabilité, SD48 N=2) (**Figure 4**).

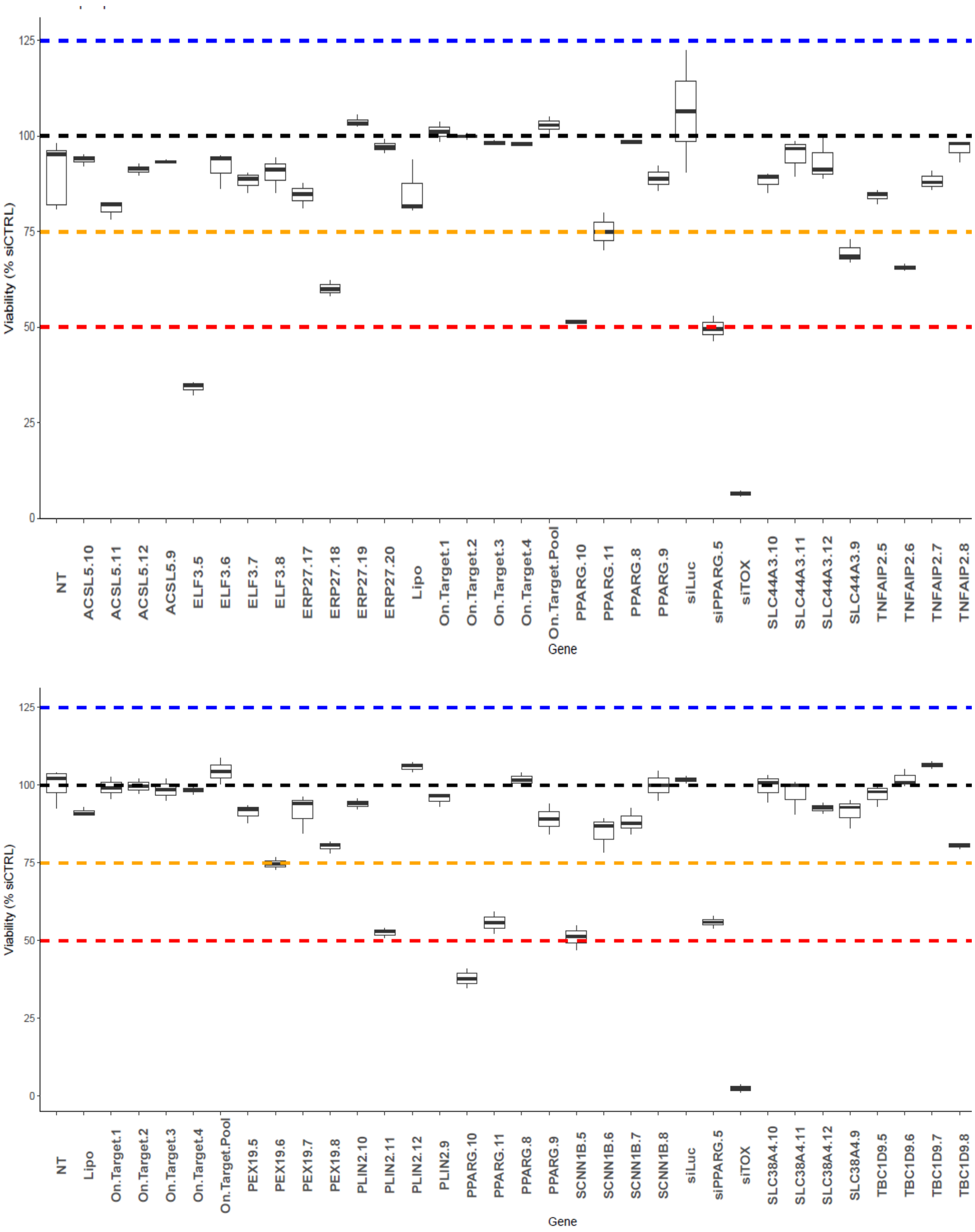

Figure 4 : Viabilité par rapport au contrôle (siCTRL) de la déconvolution du pool de siRNA des gènes sélectionnés après le screening du pool (20nM), exemple d'une expérience dans la lignée SD48 (culture FBS5%, lecture de la viabilité à 96h par CelltiterGlo). Note le .X représente le numéro du siRNA de Dharmacon, NT : non-traité, lipo= lipofectamine.

11.3.4 Discussion et Perspectives

Cette expérience n'a donc pas permis de déterminer, parmi ces 25 gènes cibles directes de PPARγ sélectionnés, une cible clé ayant un effet important sur la viabilité.

De plus l'étude systématique des données d'Achilles pour rechercher des gènes modulés par PPARγ (modulation par des siRNA ciblant *PPARG*), cibles directes de PPARγ (ChIP-seq de *PPARG*) et dont l'inactivation avait un effet sur la viabilité n'a pas non plus permis d'identifier des cibles intéressantes.

Notre hypothèse est donc que l'effet protumorigénique de PPARγ *in vivo* serait lié soit : i) à une combinaison de gènes modulés, ii) à un gène non présent dans le screening, iii) à une absence d'inhibition du gène de par la méthode de transfection (pas de contrôle par RT-PCR), ou/et iv) à l'effet sur le microenvironnement de l'activation de PPARγ entrainant une immuno-évasion.

Pour essayer de mieux caractériser le réseau de gènes autour de PPARγ et identifier des redondances entre certains facteurs de transcription, une expérience utilisant la technologie du Pertub-seq dans la lignée RT112 est en cours dans le laboratoire, avec inhibition d'une vingtaine de gènes clés des tumeurs luminales dont *PPARG* (ex *GATA3*, *FOXA1*…)[162]. Cela pourrait permettre d'identifier les mécanismes biologiques contrôlés par PPARγ par rapport à ceux contrôlés par les autres facteurs de transcription du réseau, et ainsi de mieux comprendre son rôle protumorigénique.

12 Articles en annexe

12.1 Article 5 : Epigenomic mapping identifies a super-enhancer repertoire that regulates cell identity in bladder cancers through distinct transcription factor networks

Epigenomic mapping identifies a super-enhancer repertoire that regulates cell identity in bladder cancers through distinct transcription factor networks

Authors

Hélène Neyret-Kahn*[1,2], Jacqueline Fontugne*[1,3], Xiang Yu Meng[1,2,5], Clarice S. Groeneveld[1,2,6], Luc Cabel[1,2], Tao Ye[7], Elodie Guyon[1,4], Clémentine Krucker[1,2], Florent Dufour[1,2], Elodie Chapeaublanc[1,2], Audrey Rapinat[8], Daniel Jeffery[9], Yann Neuzillet[10], Thierry Lebret[10], David Gentien[8], Irwin Davidson[11], Yves Allory[1,2,3], Isabelle Bernard-Pierrot [#,1,2], François Radvanyi [#,1,2].

* These authors contributed equally to this work

[#] These authors co-supervised this work

Correspondance to helene.neyret-kahn@curie.fr

Affiliations

[1] Molecular Oncology, PSL Research University, CNRS, UMR 144, Institut Curie, Equipe Labellisée Ligue Nationale Contre le Cancer, Paris, France

[2] Sorbonne Universités, UPMC Université Paris 06, CNRS, UMR144, 75005, Paris, France.

[3] Department of Pathology, Institut Curie, Saint-Cloud, France.

[4] Department of Pathology, Institut Curie, Paris, France.

[5] Department of Urology, Zhongnan Hospital of Wuhan University

[6] Université de Paris, Centre de Recherche des Cordeliers, Paris, France

[7] Institut de Génétique et de Biologie Moléculaire et Cellulaire (IGBMC), Institut National de la Santé et de la Recherche Médicale (INSERM) U1258, Centre National de Recherche Scientifique (CNRS) UMR7104, Université de Strasbourg,1 rue Laurent Fries, 67404 Illkirch, France

[8] Department of Translational Research, Genomics Platform, Institut Curie, PSL Research University, Paris, France

[9] Urology Medico-Scientific Program, Department of Translational Research, Institut Curie, PSL Research University, Paris, France

[10] Urology Department, Hôpital Foch, Suresnes, France

[11] Department of Functional Genomics and Cancer, Institut de Genétique et de Biologie Moleculaire et Cellulaire, CNRS/INSERM/UDS, 67404 Illkirch Cedex, France.

Abstract

Muscle-invasive bladder cancer (BLCA) is an aggressive disease. Consensus BLCA transcriptomic subtypes have been proposed, with two major Luminal and Basal subgroups, presenting distinct molecular and clinical characteristics. However, how these distinct subtypes are regulated remains unclear. We hypothesized that epigenetic activation of distinct super-enhancers could drive the transcriptional programs of BLCA subtypes.

Through integrated RNA-sequencing and epigenomic profiling of histone marks in primary tumours, cancer cell lines, and normal human urothelia, we established the first integrated epigenetic map of BLCA and demonstrated the link between subtype and epigenetic control. We identified the repertoire of activated super-enhancers and highlighted Basal, Luminal and Normal-associated SEs. We revealed the super-enhancer-regulated networks of candidate master transcription factors for Luminal and Basal subgroups including FOXA1 and ZBED2 respectively. FOXA1 CRISPR-Cas9 mutation triggered a shift from Luminal to Basal phenotype, confirming its role in Luminal identity regulation and induced ZBED2 overexpression. In parallel, we showed that both FOXA1 and ZBED2 play concordant roles in preventing inflammatory response in cancer cells through STAT2 inhibition.

Our study furthers the understanding of epigenetic regulation of muscle-invasive BLCA and identifies a co-regulated network of super-enhancers and associated transcription factors providing potential targets for the treatment of this aggressive disease.

Abbreviation

SE, Super-enhancer
TF, Transcription Factor
NMIBC, non-muscle-invasive bladder carcinoma
MIBC, muscle-invasive bladder carcinoma
BLCA, Bladder Cancer Carcinoma
Ba/Sq, basal/squamous
LumU, luminal unstable
LumNS, luminal non-specified
LumP, luminal papillary

Introduction

Bladder cancer is the tenth most common cancer worldwide, accounting for nearly two thousand cancer-related deaths globally in 2018 (1). Urothelial carcinoma is classified as non-muscle-invasive bladder cancer (NMIBC comprising carcinoma *in situ*, and the pTa and pT1 stages) or the aggressive muscle-invasive bladder cancer (MIBC, stages pT2 to pT4), depending on the level of invasion into the bladder wall (2). Molecular classifications of bladder carcinomas have been established using mainly gene expression profiling studies (3–8). A recent consensus classification of MIBC presents six subtypes, from which tumours can be coarsely divided into two subgroups: the Luminal and the non-Luminal subgroups. Luminal subgroup comprises three Luminal subtypes (LumU, LumNS and LumP) whereas Basal-Squamous subtype (Ba/Sq) constitutes the major part of the non-luminal subgroup (3). Luminal tumours, accounting for about 50% of MIBCs, present high expression of urothelial differentiation markers (GATA3, FOXA1, KRT20, uroplakins) and are enriched in activating mutations of *FGFR3*. Basal tumours also called Basal/Squamous are particularly aggressive and account for ~35% of MIBCs (3). They are characterized by the overexpression of markers of the basal layer of the urothelium (including KRT5, KRT6), the under-expression of markers of luminal differentiation and activation of EGFR (9). Concerning the NMIBC tumours, the recent UROMOL studies group them into 4 classes including Class 1 associated with luminal differentiation and good prognosis, and a Class 2a comprising high risk tumours (7, 8). One hypothesis to explain the establishment of the different subtypes and their potential plasticity, is that each subtype harbours a regulatory network in which various upstream genomic and epigenomic alterations lead to the activation of a core set of master transcription factors (TFs) that then determine a transcriptomic downstream program. While transcriptional regulators of urothelial differentiation, such as FOXA1, GATA3 and PPARG, have been established as key regulators of the Luminal phenotypes, the essential transcription regulators driving the Ba/Sq subtype have not been elucidated (10–14).

Recent studies have demonstrated that altered enhancer activity drives changes in cell identity and oncogenic transformation, notably through large clusters of highly active enhancers called super-enhancers (SEs) (15–17). Indeed, targeting SE-driven oncogenesis has become a novel therapeutic approach with the advent of BRD4 inhibitors, which inhibit SE activation (18). By regulating the expression of a small number of master TFs, SEs can orchestrate cell- or cancer-specific transcriptional programs. The gold standard for identifying SEs is histone mark profiling (17). The ENCODE roadmap, that profiled histone marks in normal and cancer cell lines, has become a valuable source of information to uncover chromatin organisation, alteration, and subsequent regulation of master regulators but did not include bladder models (19). Recently, two studies provided new insights with the profiling of particular histone marks in bladder cancer samples and cell lines (20, 21). Here, we further characterized bladder cancer epigenetic by integrating transcriptomic and epigenomic profiling of multiple histone marks in human bladder tumours, bladder cancer cell lines, and primary cultures from normal urothelia to produce a comprehensive bladder cancer epigenetic map. With this map, we demonstrated the link between molecular subtype and the underlying epigenetic landscape. Through H3K27ac analysis, we established a repertoire of SEs that are specific to distinct subgroups (Luminal, Ba/Sq subtypes, as well as Normal primary cells), highlighting SE-associated genes with subgroup-specific clinical relevance. From there, we identified the core SE-regulated networks of master TFs that distinguish luminal and basal subgroups, including known and new candidate master TFs. Finally, through functional knock-down and knock-out experiments, we revealed that one of these master TFs (FOXA1) is a key factor in subtype determination antagonized by ZBED2, and that both FOXA1 and ZBED2 present the ability to dampen inflammatory response. Overall, this work provides new data characterizing epigenetic regulation in bladder cancer. We reveal important genes that can be essentials for maintenance of bladder cancer cell identity and present potential new targets to treat aggressive bladder cancers.

Results

Integrated bladder cancer chromatin landscape

To elucidate the contribution of chromatin landscape in bladder cancer biology, we generated ChIP-seq for active (H3K27ac) and repressive histone marks (H3K27me3, H3K9me3) in 24 bladder samples (Fig.1). In order to distinguish features of the non-cancerous stromal cells and of normal urothelial cells, we used not only human primary tumours (n=15) from the CIT (*Carte d'Identité des Tumeurs*) cohort (9, 22), but also cellular models (7 bladder cancer cell lines) and patient-derived Normal Human Urothelium in proliferation (NHU, n=2). Of note, tumors were macrodissected to enrich for bladder cancer content (Fig. 1, Fig. S1A). Of the 15 primary tumours, we included 13 MIBCs and 2 NMIBCs to assess the stage-dependence of our results (Fig. 1A, Fig. S1A, and Table S1). With the aim of identifying subtype-specific epigenetic alterations/characteristics, we coupled our ChIP-seq with RNA-seq from the same extraction and classified them according to the current consensus subtypes (3). Of the 13 MIBCs, 2 classified as stroma-rich, 4 classified as basal/squamous (Ba/Sq) and 7 as luminal, including 1 luminal papillary (LumP), 3 luminal unstable (LumU) and 2 luminal non-specified (LumNS). Of the 7 cell lines, 3 were classified Ba/Sq, 3 LumP and one could not be classified (Table S1)(23). Using the recent UROMOL classifier, the two NMIBC samples classified as class 3 (7, 8). Further analysis using subtype deconvolution (WISP, (24)), and previously described regulatory signatures (3, 7), revealed that one of the tumours originally classified as Ba/Sq (T391) was composed of a mixed population of LumP and Ba/Sq cells (Fig. S1B, S1C). Knowing it's important intra-tumoral heterogeneity, tumour T391 was excluded from differential analyses between subgroups. Peak calling using MACS showed that ChIP-seq for H3K27ac gave the most homogeneous and highest number of peaks across the 24 samples (Fig. S1D).

We integrated our multi-factorial ChIP-seq profiles using ChromHMM (25), reporting the first integrated epigenetic map in bladder cancer in both primary tumour samples and cell lines (Fig. 2A). Six chromatin states (E1–E6) were assigned according to histone mark enrichments, as previously described (ENCODE, Roadmap project (19)), where H3K27ac-enriched regions correspond to active promoters and enhancers (E2), H3K27me3 and H3K9me3-enriched states associate with repression (E4) or heterochromatin (E6), and regions enriched in both active and repressive marks define bivalent enhancers or promoters (E3). Regions without any marks or only weak H3K9me3 enrichment were designated as quiescent/no marks (E1) or quiescent/weakly repressed (E5), respectively (Fig. 2A, Fig. S2A, B). Analysis of associated RNA-seq data confirmed that gene expression correlates with the expected chromatin states (Fig. 2B). Briefly, genes with transcription start sites (TSSs) in E2 states (active enhancers / promoters) have the highest expression levels, followed by those in E3 states (bivalent enhancers / promoters). Minimal expression was noted for genes with TSSs in the remaining states.

Chromatin states classify bladder cancers by transcriptomic subgroups

Next, we sought to classify our samples based on chromatin states for comparison with molecular subtypes. To do this we first performed an unsupervised analysis to select the most distinguishing features from the chromatin profiles (see methods, Fig. S2C) and plotted all samples by multiple correspondence analysis on the most varying regions (MCA, Fig. S2D). Similar to Principal Component Analysis (PCA), but adapted for categorical data, this method of dimensionality reduction separates samples in 2D space by proximity according to the primary (Dim 1) and secondary (Dim 2) dimensions. Thus, greater differences in chromatin profiles are represented by greater distances in the 2D plot. Dim 1 distinguished primary tumour samples from cell lines, which could be indicative of chromatin changes associated with cell culture or stroma content. Interestingly, Dim 2 distinguished Non-basal from Basal subgroups. To confirm this distinction of molecular subtypes, we re-assessed the data with an alternative dimensionality reduction method (MDS), coupled to a batch effect-like correction (MNN), which eliminated most of the cell line vs primary tumour differences while maintaining and strengthening the distinction between Non-Basal and Basal subgroups along Dim 2 (Fig. 2C). Therefore, we identified two clusters derived from differences in chromatin state that are associated with molecular subtypes; a “basal cluster” containing all Ba/Sq samples (except the mixed T391), and a “non-basal cluster” including all luminal, stroma-rich and NMIBC samples (Fig. 2C). Interestingly, NHU cells were located at the border between the two groups (Fig. 2C). To explore the biological pathways associated with the chromatin profiles that could distinguish Luminal from Basal bladder cancers, we ranked genes based on the MCA outputs for Dim 2 and performed Gene Set Enrichment Analysis (GSEA (26, 27), Fig. 2D). As expected, for the basal cluster, we found that active chromatin (E2) was strongly enriched at genes involved in decreased Luminal differentiation, while repressive chromatin (E4) was strongly depleted for these genes (Fig. 2D). Interestingly, genes involved in increased tumour aggressiveness, stemness, extracellular matrix, epithelial-mesenchymal transition and invasion were also enriched in active chromatin and depleted for repressive chromatin in the basal cluster (Fig. 2D). Taking an alternative approach, we derived Basal and Luminal gene signatures from an independent publicly available scRNA-seq dataset (GSM4307111) and compared these genes with the chromatin states associated with the basal and non-basal clusters identified in Fig. 2C (Fig. 2E, see methods). Luminal signature genes were enriched in active state in the non-basal chromatin cluster while Basal signature genes were enriched in active state in the basal chromatin cluster, suggesting epigenetic regulation of signature genes involved in urothelial differentiation. We further illustrate this relationship with two well-described markers of bladder cancer subtypes: *FOXA1* and *KRT6A* (Fig. 2F). FOXA1 expression is higher in Luminal than Basal tumours (11, 14, 28, 29). In agreement, our results showed that *FOXA1* was marked with active (E2) chromatin in Luminals (including LumP, LumNS and LumU), NMIBC samples, and even NHU cells, but harboured repressive chromatin in Ba/Sq tumour samples (Fig. 2F). On the other hand, *KRT6A*, commonly expressed in Basal tumours (3), had active chromatin marks in seven out of eight Ba/Sq samples, as well as NHU, but not in any Luminal sample. Taken together, these results demonstrate the importance of histone marks in the regulation of gene expression driving cell identity in bladder cancer.

Identification of the bladder super-enhancer repertoire and subtype specificities

To determine if chromatin profiles identify SEs that could control bladder cancer subtype, we determined and annotated typical enhancer and SE regions in our samples using the ROSE algorithm (Table S2), which calls enhancers and particularly super enhancers according to H3K27ac signal (18, 30). Despite signal correction using input, the number of called SEs was notably lower in samples with gene amplification, owing to very high H3K27ac signal in amplified regions, thus creating a bias in the ranked enhancer plot (Fig. S3A). To correct for the copy-number bias, we set a threshold and defined the top 1000 enhancer regions in each sample as SEs for all downstream analyses, approximately representing the mean number of SEs per sample (mean = 956 SEs, Table S2).

To gain insight into subtype-specific enhancer alterations and assess sample similarity based on these SE profiles, we determined the global repertoire of SEs in bladder by extracting a consensus set of 2887 SEs present in at least 2 of our 24 samples (Table S3). Using PCA of

H3K27ac signal corresponding only to the consensus SE regions, we again found that samples were grouped according to molecular subgroup, separating Basals from Luminals, NMIBC segregating with differentiated tumors (Fig. 3A). This reveals that the variability in SE profiles reflects the differences in Basal and Luminal transcriptional programs. We also performed PCA using H3K27ac, H3K27me3 and H3K9me3 independently for peaks located inside the SE consensus regions for the tumour samples alone (Fig. S3B). Interestingly, all three profiles separated the Ba/Sq tumors from the other samples, indicating that all three histone marks are likely linked to SE regulation of bladder cancer molecular subtypes.

We sought to further explore the functional pathway enrichment of SE-regulated genes. We first assigned SEs to their closest and most transcriptionally correlated genes (see methods). For example, a large SE mapped close to *KLF5*, whose expression was correlated with SE activity mostly in Luminal samples, as previously reported (31) (Fig. 3B). In contrast, *KLF7* was regulated by a SE mostly active in Basal samples (Fig. 3B). We then performed pairwise differential analyses between subtypes (Fig. 3C, S3C). The comparison between Basal and Luminal samples identified 369 subgroup-specific SEs (Fig. 3C, Table S3). By comparing the differential SEs to RNA-seq differential expression analysis, we confirmed that luminal-gained SEs showed significantly higher expression levels in Luminal samples relative to Basal samples and vice-versa for basal-gained SEs (Fig. 3D). We then validated the subgroup-specific SE-associated genes identified in our samples in a larger dataset, leveraging the gene expression profiles of the TCGA-BLCA MIBC cohort across molecular subtypes (n=406) (32, 33). Hierarchical clustering of TCGA samples using the genes associated to the most differentially regulated SEs in our consensus repertoire recovered the molecular classification (Fig. S3D, Table S3). Strikingly, differential analysis between Basal and Luminal SEs revealed that Luminal-specific SEs were attributed to known transcriptional drivers of the luminal phenotype, namely *GATA3*, *PPARg*, *FOXA1* (14, 22). Luminal-gained SEs were associated with “Signalling by TGF-beta family members”, notably due to SEs annotated close to negative regulators of TGF-beta signalling such as the E3 Ubiquitin ligase *SMURF1* or *SMAD6 (*Fig. 3C, E, Table S4). In contrast, SE regions significantly bound at higher levels in the Basal tumours were associated with genes known to contribute to Basal cancer biology such as *EGFR*, but also less characterized genes with regards to bladder cancer biology, such as genes related to inflammation and FOXO signalling (*IL7R*, *FBX032*), signalling by Interleukin or signalling by MET, the activation of which is often correlated with BLCA progression (34) (Fig. 3E). We also identified genes encoding membrane receptors (*IL7R*, *OSMR*, *EGFR*) and transcriptional regulators (*BNC2*, *HMGA2*, *KLF7*, *NR3C1*) as enriched in Basal tumours (Fig. 3C). Taking advantage of the NHU samples in our cohort, we extracted differential SEs in three comparisons (Ba/Sq *vs* NHU *vs* Luminals, Fig. S3C, Fig. 3F). This analysis validated the identification of genes that could be specific to cancer biology, such as *IL7R*, *OSMR*, *JUN*, *NR3C1* in Ba/Sq subtype, or *NPAS2*, *FOXQ1*, *GRHL3* in Luminal samples (Fig. 3F). Overall, we established a first SE repertoire for bladder cancer, highlighting subgroup-specific, cancer-specific SE activation coupled with gene expression.

Super-enhancers regulate a network of candidate master transcription factors for bladder cancer subgroups

SEs often regulate the expression of master TFs, forming autoregulatory loops and correlated networks (35, 36). Having established the SE landscape in bladder cancer, we next sought to determine which master regulators control the subtype-specific transcriptional programs. To this end, we overlaid the genomic coordinates of subgroup-specific peaks inside SEs with publicly available ChIP-seq datasets (37, 38). Our analysis revealed that Luminal-specific SEs were significantly enriched in several TF binding sites (Fig. 4A, Table S5), including known regulators of Luminal subtypes FOXA1, GATA3, and ESR1 (3, 14, 32). Basal-specific SEs were enriched in binding sites of a different set of regulators, including components of the AP-1 complex (FOSL1, FOSL2, JUND, JUNB), as well as SMAD2/3, NFkB, and STAT3. Further DNA motif enrichment analysis comparing Basal differential peaks inside subgroup-specific SEs over Luminal ones, again identified AP-1 as a potential regulator of Basal SEs, as well as FOXA1, FOXA1:AR, GATA, and GRHL1/2/3 for Luminal SEs (Fig. 4B, Table S5, Homer (39)).

However, motif binding and ChIP-seq data are not available for all known TFs. To overcome this issue, we designed a method to identify subgroup-associated TFs and their co-regulated networks based on our differential SEs and the large transcriptomic cohort from the TCGA (32) (Fig. 4C). We selected TFs that were regulated by differential SEs (Basal vs Luminal), according to annotations from Lambert *et al*. (40), and that were differentially expressed in TCGA Ba/Sq vs Luminal subgroups. Then, we used ARACNe (41) and VIPER (42) analysis to identify and evaluate the regulons (group of genes regulated in response to one transcription regulator) of the 75 resulting TFs. Hierarchical clustering of the resulting TF regulons clustered scores into three groups, which were respectively associated with Luminal, Ba/Sq or Stroma-Rich subtypes (Fig. 4D, E). Since master TFs form interconnected networks with highly correlated levels of expression, we selected only TFs whose expression was correlated with that of at least one of the other TF in TCGA-BLCA data (Pearson correlation coefficient ≥0.5, n=55), and built the top correlated network based on subtype-specific SE-associated TFs (Fig. 4F) (see methods). This strategy identified a large module of Luminal TFs, including known Luminal-associated TFs (e.g., FOXA1/GATA3/PPARG), as well as TFs with yet unexplored roles in Luminal bladder cancer biology (e.g., HES1, FOXQ1, ZBTB7C, MECOM, GRHL2/3 and TBX3). Unlike for Luminals, few TFs have been characterized as key regulators of Basal tumours. Our analysis revealed a network of TFs whose activity could be essential to Basal bladder cancer biology, including HMGA2, KLF7, NR3C1 and ZBED2. Notably, ZBED2 has recently been associated with basal identity in keratinocytes (43) and regulation of inflammation in pancreatic cancer (44). Combining analyses of tumour and cell lines SEs should avoid the identification of master TFs expressed by the stroma. In fact, we found that TFs associated with the Luminal network showed strong expression correlation in TCGA-BLCA and in CCLE bladder cell cohorts (45) (Fig. S4A, B) while expression correlations of Stroma-Rich or Basal-associated TFs (e.g., ZEB1, SPI1) in the TCGA were lower for urothelial cell lines in the CCLE (46) (Fig. S4A, B). This indicates that expression of those TFs could be dependent on growing conditions and/or interactions with the tumour microenvironment.

To validate our Luminal- and Basal-specific TF networks, we analysed public single-cell RNA-seq data of a tumour presenting both a Luminal and a Basal cell population (GSM4307111, Fig. S4C). The Luminal-associated TFs FOXA1, GATA3 and PPARG were mostly expressed in the Luminal cell cluster, whereas ZBED2, HMGA2, and KLF7, newly identified as part of the Basal TF network, were mostly expressed in the Basal cell clusters (Fig. 4G), validating our subgroup-specific networks. Together, these analyses identified a targeted subset of interconnected candidate master TFs that could represent key regulators of bladder cancer subgroup identity.

FOXA1 binds subgroup-specific bladder super-enhancers and correlates with their activation

We identified FOXA1 as one of our candidate master TFs for the Luminal bladder cancer subgroup. FOXA1 is a known pioneer factor with a demonstrated impact on Luminal bladder cancer biology (29, 32, 47), though the mechanism for how FOXA1 regulates cell identity is unknown. To better assess the role of FOXA1 in the regulation of bladder cancer SEs, we mapped FOXA1, CTCF (Insulator/enhancers) and H3K4me3 (Promoter) binding by ChIP-seq in two bladder cancer cell lines: SD48 (LumP) and 5637 (Ba/Sq). FOXA1 binding was mostly found outside promoters (Fig. S5A), with 61,083 FOXA1 peaks detected in SD48 cells and 39,445 in 5637, an expected variation as FOXA1 was more abundant in Luminal cells. Despite such differences, we identified three classes of FOXA1 peaks: SD48-specific peaks, peaks overlapping in the two cell lines, and 5637-specific peaks (Fig. 5A, Fig. S5B), which suggests that FOXA1 has specific targets in each cell line and subtype. Interestingly, when analysing TF binding sites from publicly available ChIP-seq data, SD48-specific FOXA1 peaks were highly enriched not only for FOXA1 binding sites, but also GATA3 binding sites (Fig. 5B), which could indicate a functional partnership between FOXA1 and GATA3 for regulation of the Luminal program, as suggested by Warrick *et al.* and described in breast cancer (14, 48). Surprisingly, 5637-specific FOXA1 peaks were mostly enriched at AP-1 binding sites and not FOXA1 sites (Fig. 5B, Fig. S5B). Both enrichments were confirmed by Homer motif analysis of SD48-specific peaks versus 5637-specific peaks or vice and versa (Fig. S5C and D, (39)). Ontology comparison of genes associated with the three classes of FOXA1 peaks showed that 5637-specific peaks were enriched in terms associated with Ba/Sq super-enhancers (e.g. Signalling by Tyrosine Kinase, Signalling by MET, Signalling by Interleukin), indicating that FOXA1 might be involved in the regulation of both Luminal and Basal bladder cancer subtypes (Fig. 5C). Indeed, FOXA1 binding in the two cell lines overlapped with most (87%) of the total repertoire of bladder SEs (Fig. 5D) and correlated strongly with H3K27ac levels at these loci (Fig. 5E, F), in line with a role for its regulation of these SEs. Notably, FOXA1 bound at SEs associated with genes involved in regulating urothelial differentiation and strongly correlated with increased H3K27ac at these loci. This could clearly be observed for the Luminal-specific SEs associated with *GATA3* or *PPARG* in the Luminal SD48 cells and in both cell lines for the non-specific *PPARG* SE. But we also found FOXA1 binding associated with high H3K27ac at certain Basal-specific SEs in the Basal 5637 cells, such as *TGFB2* (Fig. 5G). This implies that FOXA1, even if expressed at a low level as in Ba/Sq cells, could play an important role in BLCA biology, through enhancer/SE regulation. In summary, FOXA1 may regulate bladder cell identity through binding of subgroup-specific bladder SEs with partners such as GATA3 in Luminal cells and AP-1 in Basal cells.

FOXA1 regulates inflammation and cellular identity

To better understand FOXA1 function, we performed short-term (<72h) knock-down in both Luminal and Basal models. Knock-down of FOXA1 by siRNA decreased clonogenicity and proliferation of both Luminal and Basal cells (Fig. S6A, B) and it reduced cell viability in both RT112 (LumP subtype) and SCaBER (Ba/Sq) cells, with a stronger impact in RT112 (Fig. 6A). Furthermore, FOXA1 knock-down in RT112 and SCaBER cell lines dramatically altered gene expression (Fig. 6B, Table S6). The downregulated genes were related to cell cycle and checkpoint pathways, consistent with the reductions in viability and proliferation upon FOXA1 knock-down. Surprisingly, the upregulated genes in both cell lines were strongly associated with inflammatory signalling and interferon response (Fig. 6C, Fig. S6D). Notably, FOXA1 knock-down induced upregulation of master interferon response TFs, STAT1 and STAT2, and key genes involved in the regulation of inflammation in human cancer, including the immune checkpoint modulator *CD274* (PD-L1) (Fig. 6D), which we also identified as a downregulated SE in both Luminal and Basal *vs* NHU cells (see earlier Fig. 3F). While our FOXA1 ChIP-seq in Luminal and Basal cell lines showed FOXA1 binding at many interferon responsive genes, we did not observe strong FOXA1 enrichment on *STAT1, STAT2* or *CD274* promoters or enhancers (Fig. S6E). This suggests that the upregulation of these genes upon FOXA1 knock-down is independent of FOXA1 binding of their regulatory elements, in agreement with recent work showing that FOXA1 directly binds and inhibits the STAT2 protein to dampen inflammation in a chromatin-independent manner (49). Interestingly, if FOXA1 knock down triggered interferon response in both Luminal and Basal models, its depletion affected the Luminal network of co-regulated TFs only in RT112 cells and not in SCaBER (Fig. 6E). PCA projection of TCGA-BLCA transcriptomes together with that of our knock down cells on our scRNA-seq-derived Basal/Luminal signature space confirmed that FOXA1 acute depletion induced a small but consistent shift from Luminal towards Basal subtype only in RT112 cells (Fig. S6F, see methods). Therefore, in agreement with a previous study (14), short-term knock-down of FOXA1 showed a consistent but mild impact on cell identity, not sufficient to majorly alter the subtype of the luminal cells.

Altering the epigenetic landscape could indeed take a longer time. To determine if FOXA1, through its binding to the SE repertoire, regulates the bladder cancer epigenetic landscape and subsequently cellular identity, we produced *FOXA1* CRISPR mutant clones allowing long-term FOXA1 inactivation in two Luminal cell lines (SD48 and RT112, Fig. S6G). Despite fundamental differences between RT112 and SD48 cellular models and heterogeneity between clones due to clonal selection, transcriptomic analysis of 3' RNA-seq data by PCA distinguished CRISPR *FOXA1* mutant clones from wildtype (WT) (Fig. S6H). Importantly, PCA projection of TCGA-BLCA transcriptomes together with that of our WT and mutant clones on the Basal/Luminal signature space showed that mutation of *FOXA1* induced a strong shift from the Luminal cluster to the Basal cluster (Fig. 6F). GSEA analysis confirmed that *FOXA1* mutants were enriched for our Basal signature and depleted for our Luminal signature (Fig. S6I)(26, 27). GSVA analysis further revealed that *FOXA1* mutant clones were less differentiated than WT controls (Fig. 6G, (11)) and tended to express higher levels of TFs associated with the Basal TF network (Fig. 6H, Fig. 4F). Differential gene expression analysis revealed 1040 and 1102 Differentially Expressed Genes (DEGs) in RT112 and SD48, respectively, when comparing *FOXA1* mutant clones to WT (Fig. S6J). *FOXA1* mutant DEGs were associated with EMT, KRAS signalling and the inflammatory response pathway (Fig. 6I), all linked to Basal phenotypes. Intriguingly, differential analysis of *FOXA1* mutants vs WT revealed increased expression of NR3C1 and ZBED2 in the mutants, two of the candidate master TFs identified in our Basal TF network (Fig. 6J, Table S7). In summary, our results demonstrate that loss of *FOXA1* promotes a clear shift from Luminal to Basal cell identity.

ZBED2, a novel Basal-associated TF involved in inflammation dampening

To further explore the interconnected network of candidate master TFs, we chose to examine ZBED2 as one of the TFs in the Basal network since it was upregulated by *FOXA1* CRispR inactivation, and because of recent work in keratinocytes that identified a role for ZBED2 in the basal phenotype (43). ZBED2 expression in the TCGA-BLCA cohort is upregulated in the Ba/Sq subtype (Fig. 7A) and correlates with poor survival prognosis (Fig. S7A). ZBED2 expression is negatively correlated with FOXA1 expression in the TCGA cohort (Fig. 7B), but more interestingly scRNA-seq in CCLE bladder cell lines shows that FOXA1 and ZBED2 expression are often mutually exclusive (Fig. 7C). As little is known about the ZBED2 TF, we used ARACNE/VIPER algorithms to identify the ZBED2 regulon based on TCGA-BLCA expression data. Interestingly, FOXA1 was predicted as a ZBED2 target, with the most negative weight, whereas two genes associated with Basal-specific SEs (*IL7R* and *CAV1*) were in the top 10 positive ZBED2 regulon weights (Fig. S7B). Using ZBED2 ChIP-seq data from pancreatic cancer cell lines (44) (the only ZBED2 ChIP-seq reported so far), we found a high confidence ZBED2 peak in the *FOXA1* promoter (Fig. 7D, left). Analysis of the RNA-seq data from the same study revealed that ZBED2 overexpression triggered downregulation of FOXA1 (Fig. S7C, p=0.004). In our data, we found that the *ZBED2* SE was highly enriched in FOXA1 binding in SD48 luminal cells, whereas FOXA1 binding was significantly decreased in 5637 Ba/Sq cells, and negatively correlated with ZBED2 expression (Fig. 7D, right). Overall, these findings suggest that FOXA1 and ZBED2 could negatively regulate each other to promote or maintain Luminal or Basal identity, respectively.

On the other hand, ZBED2 has been shown to inhibit STAT2 and dampen inflammation by direct competition with IRF1 for Interferon Responsive Element binding in the pancreas (44). We therefore sought to determine if ZBED2 is involved in the downregulation of interferon signalling in bladder cancer, potentially through interfering with FOXA1-activated pathways. Intriguingly, *ZBED2* expression in the TCGA-BLCA cohort positively correlated with interferon gamma associated gene expression (Fig. S7D), which could be an indication that ZBED2 increases in response to inflammation at the cell population level, or vice versa. We then examined the correlation between ZBED2 expression and different cellular pathways at the single-cell level using publicly available scRNA-seq data (50). Our analysis revealed that *ZBED2* expression anti-correlates with interferon response and positively correlates with cell cycle progression and *E2F* targets within the same cell (Fig. 7E), suggesting that the positive correlation with interferon response in the bulk RNA-seq data reflects increased levels of *ZBED2* expression and interferon response genes in different subpopulations of cells. To test this association further, we knocked down *ZBED2* by siRNA and performed bulk 3' RNA-seq in two BLCA cell lines. Strikingly, downregulation of *ZBED2* increased expression of interferon response genes and decreased expression of cell cycle progression and *E2F* target genes (Fig. 7F). Furthermore, siZBED2 in both RT112 and SCaBER cells increased gene expression of *STAT2* and *CD274* (Fig. 7G) and tended towards decreased cell viability (Fig. S7E). Therefore, ZBED2 directly dampens interferon response in bladder cancer, in agreement with its reported role in the pancreas (44). Notably, siRNA of *FOXA1* induced strong *STAT2* and *CD274* expression, while double knock-down of both *FOXA1* and *ZBED2* partially dampened this response compared to siFOXA1 alone (Fig. 7G), suggesting that the inflammatory response resulting from FOXA1 knock-down is partially dependant on ZBED2 target genes. In conclusion, both FOXA1 and ZBED2 inhibit inflammatory response and promote bladder cancer cell survival.

Discussion:

Epigenetic mechanisms are essential for the establishment and maintenance of cellular identity notably through SE regulation of master transcriptional regulators (17). Bladder cancer has been extensively studied at the transcriptomic level, but until two recent studies, very little was known about its epigenetic landscape (21).

Here, we report a large epigenetic profiling of both bladder cancer primary tumours and bladder cancer cell lines representative of the main molecular subtypes, as well as NHU cultures, using three histone marks ChIP-seq and paired RNA-seq. Using integrative analyses, we established a comprehensive chromatin state map of bladder cancer and showed that Basal and Luminal subgroups can be distinguished by their chromatin profiles. This map can be used to identify new genes or regulatory regions for diagnostic, prognostic or pharmacological targeting.

We characterized the bladder SE repertoire, and through differential analysis identified subgroup-specific and cancer-specific SE activation. Our study corroborates and expands the two recently reported enhancer landscapes of bladder cancer (20, 21). Consistent with prior reports, Luminal-activated SEs were located in proximity to known key regulators of the Luminal phenotype, namely *FOXA1*, *GATA3*, and *PPARG* (3, 14, 21), and to new Luminal-associated genes, such as *NPAS2 and GRHL2* – also identified by Iyyanki *et al.* (20) – or *KLF5*, recently characterized as activated through super-enhancer amplification in various squamous cell carcinomas (31). Importantly, based on our data for 7 Ba/Sq samples, we were able to identify higher enhancer activity associated with potential key genes in Basal tumour biology, including cell surface receptors (*IL7R*, *OSMR*, *EGFR*, *MET*) and transcriptional regulators (*BNC2*, *HMGA2*, *KLF7*, *NR3C1*).

We further characterized subgroup-associated master regulators and co-regulated networks for both Luminal and Ba/Sq subgroups using two complementary approaches, in order to overcome issues linked to low expression, unknown binding motifs or multi-partner complexes. First, we identified TFs with enriched binding sites or DNA motifs in subgroup-specific SEs. Second, we combined SE activity in our cohort with regulon analysis of TCGA data to identify master regulator networks for Luminal and Basal subgroups. The first approach, based on public ChIP-seq data, validated the role of TFs involved in urothelial differentiation in Luminal SE activity, namely FOXA1 and GATA3, but also revealed that the AP-1 complex regulates Basal SEs. AP-1 has been shown to drive reprogramming of breast cancer cells from a Luminal to a Basal phenotype during treatment resistance acquisition through high-order assemblies of transcription factors (48). Thus, a role for AP-1 in driving Basal enhancers and cell identity in bladder cancer suggests AP-1 inhibitors as potential therapeutic options for this aggressive disease. Interestingly, our mapping of FOXA1 binding sites in two different cell models indicated that the pioneer factor binds most bladder-associated SEs, even if its DNA binding motif is mostly found in the Luminal-specific SEs. The mapping of FOXA1 binding also confirmed that FOXA1 binding sites in Basal enhancers are associated with AP-1 localisation, suggesting that AP-1 could play an important role in the regulation of Basal regulatory regions through FOXA1 recruitment—or trapping—at discrete chromatin loci. By combining the ChIP-seq approach with regulon analysis, we were able to highlight new Luminal-associated TFs, in addition to known Luminal master regulators (FOXA1, GATA3, PPARG) and the recently identified NPAS2 (20). Importantly, we also identified a Basal TF network, including ZBED2, KLF7, HMGA2, NR3C1 as major regulators, whose expression was restricted to the basal component of tumours, according to scRNA-seq data. To our knowledge, the role of these TFs has not been investigated in bladder cancer biology.

With regards to ZBED2, a scRNA-seq study revealed that it promotes basal cell identity of keratinocytes (43). Another study demonstrated that in pancreatic cancer, ZBED2 represses differentiation and dampens STAT2-mediated inflammatory response through IRES binding competition with IRF1 (44). Previous work showed that the three master Luminal TFs (FOXA1, GATA3, and PPARG) had to be perturbed simultaneously to induce a cell identity switch from luminal to basal (14). However, we found that while short term knock-down of FOXA1 had a mild effect on cell identity, the long-term inactivation of FOXA1 alone through CRISPR mutation was sufficient to induce a shift from Luminal to Basal subgroup in luminal cells, highlighting the role of FOXA1 in the regulation of cell fate. Moreover, we demonstrated that this major shift is accompanied by activation of one of our newly identified Basal network TFs, ZBED2. Despite its known role as an activator of transcription, FOXA1 has also been associated to direct repression of transcription (51). ZBED2 is described as a transcriptional repressor (44). Therefore, FOXA1 and ZBED2 could repress each other, defining a new cell identity regulatory loop. Through functional knock-down and knock-out experiments, we verified that FOXA1 and ZBED2 have antagonistic but interconnected functions in cell identity. However, ZBED2 is expressed at a very low level and additional experiments, including overexpression models are needed to validate its repressive function on FOXA1, or vice versa, and its potential role in Luminal to Basal plasticity.

Finally, our work also uncovers a role for both FOXA1 and ZBED2 in the regulation of inflammation in bladder cancer. While they play antagonistic roles in the regulation of cell identity, we found that they share a common function in inhibiting inflammation. Short term loss of either FOXA1 or ZBED2 triggers an inflammatory response, identified through STAT2 overexpression, in agreement with the study of ZBED2 function in the pancreas [44]. The low FOXA1 binding enrichment at STAT2 in our FOXA1 ChIP-Seq experiments suggest that FOXA1 could have a repressive function of inflammation presumably independent of its chromatin binding. These conclusions are in accordance with the recent work of He et *al.* [57] characterizing a chromatin independent function of FOXA1, which, by direct binding of STAT2 protein, inhibited STAT2-mediated inflammation. This could explain the limited infiltrate of luminal tumours, expressing high levels of FOXA1.

Therefore, given the dual role of FOXA1 and ZBED2 in the regulation of cell identity and inflammation, it will be important to study their link with tumour plasticity and in response to immunotherapy. Although direct inhibitors do not yet exist, targeting FOXA1/ZBED2 or the upstream or downstream signaling pathways, may improve sensitivity to immune-based therapies. Similarly, it will be worth studying the effect of interferon treatment on FOXA1 and ZBED2 inhibited inflammation as it could be used to overcome the inflammation inhibition induced by these two master regulators.

If FOXA1 and ZBED2 revealed promising features, our study identified numerous other super enhancers, associated genes and master regulators that could be explored for pharmacological targeting.

General targeting of SEs with BRD4 inhibitors has shown efficiency, in particular in cancers with specific SE single mutation alterations or with the activation of MYC SE in leukemia or lymphoma (18, 52, 53). However, those treatments show mild efficiency in solid tumours and enhancer rewiring has been associated to resistance to treatment. Identification of SEs associated with bladder cancer and subgroups may pave the way for further research into targeting activated master regulators, upstream/downstream activated pathways or even with the advent of RNA and CRISPR technology, directly targeting SEs.

Conclusions

We provide an integrated epigenomic and transcriptomic map of bladder cancer constituting a new comprehensive tool to study epigenetic regulation of muscle-invasive bladder cancer. We revealed Luminal and Basal coregulated networks of super-enhancers and associated transcription factors as new potential targets with important clinical relevance. Our findings and functional assays on FOXA1 and ZBED2 demonstrate that the SEs and TF networks identified herein represent prime targets for further pre-clinical investigation for bladder cancer treatment.

MATERIALS and METHODS

Biological Resources

Cell lines and culture

The human bladder cancer derived cell lines RT112, 5637, KK47, and SCaBER were obtained from DSMZ (Heidelberg, Germany). MGH-U3, KK47 and SD48 cell lines were provided by Yves Fradet (CRC, Quebec), Jennifer Southgate laboratory (previously of Cancer Research Unit, St James's University Hospital, Leeds, UK), and Henri Mondor Hospital (Créteil, France), respectively. The L1207 cell line was derived from tumour T1207 (25). RT112 and 5637 cells were cultured in RPMI medium, L1207 were cultured in DMEM-F12 and all the other cell lines were cultured in DMEM medium. All cell media were supplemented with 10% fetal bovine serum (FBS). Normal human urothelium (NHU) cells were obtained from normal ureter urothelium from healthy kidney donors from Foch hospital and were cultured as previously described (26). All cells were cultured at 37°C in an atmosphere of 5% CO2 and were routinely tested for mycoplasma contamination.

Patient tumour tissue processing

We selected human tumours with an available OCT-compound frozen block from our CIT (Carte d'Identité des Tumeurs) cohort (9, 22). Each block was frozen-sectioned and stained with hematoxylin and eosin. Pathology review was performed to confirm the tumour stage and to select tumour areas, in order to enhance neoplastic content (estimated at 30 to 95%, median tumour cell content = 65%). For tumours with sufficient material, tumour-enriched areas were macrodissected from the frozen block and manually finely ground in a mortar. Frozen ground tumour tissue was kept at -80°C until further processing.

The characteristics of the tumours are shown in Table 1.

CRispR vectors, siRNA

siRNA and CrispR vectors used in the study are referenced in supplemental information file.

Chromatin immunoprecipitation and sequencing

Tumour chromatin cross-linking and extraction

In order to obtain efficiently disrupted tissue, the frozen ground material (15mg) was further homogenized using a tube pestle or the TissueLyser II system (Qiagen). Disrupted tissue was then processed using the reagents from the iDeal ChIP-seq Kit for Histones (Diagenode), according to the manufacturer's instructions. Briefly, the tissue was homogenized and washed in 1ml PBS-protease inhibitor cocktail. DNA-protein cross-linking was ensured with an 8-minute incubation in 1% formaldehyde then quenched with 0.125 M glycine for 5 minutes. Cells were then washed and lysed. Centrifuged cell lysates were resuspended in shearing buffer and sonicated using the Pico Bioruptor device (Diagenode) for 15 minutes (30s ON/30s OFF). Following a centrifugation at 16000g for 10 minutes, an aliquot was reserved to control the sonication and the remaining supernatant was stored at -80°C. Sonication efficiency was controlled for each sample on the aliquot of sheared chromatin by overnight reverse cross-linking, DNA was purified using the phenol-chloroform method and 2% agarose gel electrophoresis was used to determine DNA fragment size.

Tumours ChIP-seq

Tumour samples with optimal chromatin fragment size (200-500 bp) were immunoprecipitated using the iDeal ChIP-seq Kit for Histones (Diagenode). Magnetic immunoprecipitation of sheared DNA-chromatin complexes (500ng) was performed overnight using a rabbit polyclonal histone H3K27acetyl ChIP Grade antibody (ab4729, Abcam), H3K27me3 (Active Motif, ref. 39155), and H3K9me3 (Active Motif, ref. 39161). Magnetic immunoprecipitation beads were washed the following day. The captured chromatin as well as non-immunoprecipitated input chromatin underwent elution and reverse cross-linking steps. DNA purification was performed using iPure magnetic beads. Immunoprecipitation (IP) efficiency was verified by qPCR according to the manufacturer's protocol. Library preparation from IP DNA and input DNA was performed using the Diagenode MicroPlex Library Preparation kit v2. The resulting amplified libraries were assessed using the Bioanalyzer system 2100 (Agilent) and sequenced using the HiSeq 4000 platform (Illumina) as single-read 50 base reads, following Illumina's instructions. Reads were aligned to the reference genome (Hg19) using Bowtie 1.0.0.

Cell line ChIP-seq

Cell lines cultures were crosslinked directly in the growing medium with formaldehyde 1% for 10 minutes at room temperature. The reaction was stopped by adding Glycine with a final concentration of 0.125M for 10 minutes at room temperature. Fixed cells were rinsed 3 times with PBS containing protease inhibitors, pelleted, and resuspended in lysis buffer (10mM EDTA, pH8, 50mM Tris-HCl pH8, SDS 1%). After centrifugation, the ChIP was performed using ChIP-

IT High Sensitivity kit (Active Motif, Carlsbad, CA, USA), following the manufacturer's instructions. Chromatin was sonicated in a bioruptor Pico device (Diagenode) for 10 min (30s ON/30s OFF). Sheared chromatin was immunoprecipitated using an H3K27ac antibody (Abcam ab4729). Sheared chromatin was used as input-DNA control.

ChIP-seq libraries were prepared using NEXTflex ChIP-Seq Kit (#5143-02, Bioo Scientific) following the manufacturer's protocol (V12.10) with some modifications. Briefly, 10 ng of ChIP enriched DNA were end-repaired using T4 DNA polymerase, Klenow DNA polymerase and T4 PNK, then size selected and cleaned-up using Agencourt AMPure XP beads (#A63881, Beckman). A single 'A' nucleotide was added to the 3' ends of the blunt DNA fragments with a Klenow fragment (3' to 5'exo minus). The ends of the DNA fragments were ligated to double stranded barcoded DNA adapters (NEXTflex ChIP-Seq Barcodes - 6, #514120, Bioo Scientific) using T4 DNA Ligase. The ligated products were enriched by PCR and cleaned-up using Agencourt AMPure XP beads. Prior to sequencing, DNA libraries were checked for quality and quantified using a 2100 Bioanalyzer (Agilent). The libraries were sequenced on the Illumina Hi-Seq 2500 as single-end 50 base reads following Illumina's instructions. Sequence reads were mapped to reference genome hg19 using Bowtie 1.0.0.

ChIP-seq data analysis and integration

Peak detection was performed using MACS2 (model-based analysis for ChIP-seq v2.1.0.20140616) software under settings where input samples were used as a negative control. We used a default cutoff and -B option for broad peaks.

To identify enhancer regions in each tumour we used ROSE (Ranked Ordering of Super-Enhancers) algorithm (18, 30), with the following parameters: 12.5kb stitching distance, exclusion of promoter regions 2500 bp around TSS. For each sample, stitched enhancer regions are normalized, ranked and plotted. The regions above the inflexion point are considered super-enhancers by the algorithm. However, the number of called super-enhancers was notably lower in cases with a known amplified gene. The very high H3K27ac signal in the amplified region likely created a bias in the plot of ranked enhancers. To correct for this bias, we set a threshold to the top 1000 ranked enhancers to select candidate super-enhancer regions.

Heatmaps and PCA of ChIP-seq signal were performed using Diffbind R package (version 2.16.0) or Easeq (54). For super-enhancers analysis, the top 1000 SE regions of either tumours or cell lines were merged for a consensus using Diffbind. Then, H3K27ac signal was calculated in the consensus peak for each sample. Differential analysis between molecular subtypes was performed with Diffbind and DESeq2 default parameters using both IP and input bam files, and a file containing the consensus super enhancer regions evaluated for differential analysis as input. Regions with an pval <0.05 were considered differentially bound.

Genomic annotation and pathway enrichment analyses were performed using ChIPseeker, clusterProfiler and GREAT (28).

Chromatin Binding enrichment analysis

Factor binding analyses were performed using public data available in Cistrome DB Toolkit (37, 38). DNA binding motif analysis was performed using HOMER known motif function (39).

Genomic annotation of the SE regions and cis-regulatory genes

SE activity and gene expression was jointly analysed to determine the cis-regulatory between the SE and genes on proximity. In brief, the overlap / proximal genes corresponding to each SE were annotated using GREAT/ROSE tools, as the candidate proximal genes regulated by the SE (30, 55). The spearman correlation coefficients between SE activity (H3K27ac read counts, log2RPKM normalized) and the expression of the candidate genes (RLE normalized) were calculated in the tumours. The gene whose expression showing the highest correlation with the activity of the corresponding SE was determined as the gene most likely regulated by the SE. The SE-gene relationships within the top 1% were also given, not limited to the proximal genes. The number of germline single nucleotide polymorphisms (SNPs) within a given SE as well as their association with bladder cancer (median –log10 p-value) was provided based on the UK biobank GWAS summary statistics (Neale lab Round 2, ukb-d-C67, extracted from the MRC IEU OpenGWAS database) (56). The germline SNPs falling within the SEs and with published GWAS-level association with BCa or with –log10P.value > 5 in GWAS summary statistics (PhenoScanner v2 database) were provided as GWAS SNPs within the SEs (57). For the genes most likely regulated by a given SE, we provided their median CERES dependency score of all and urothelial cancer cells from the Cancer Dependency Map database (45), as well as the p-value for difference between the two. We checked if any bias compared to the background in mutation type (missense, non-sense, synonymous, etc.) for the protein coding genes by Chi-square test. We checked if they were within the list of established cancer genes, including the COSMIC Cancer Gene Census and Network of Cancer Genes 6 (58, 59).

Chromatin state analysis and correlation with expression

ChromHMM was used to identify chromatin states. The genome was analyzed at 1000 bp intervals and the tool was used to learn models from the 3 histone marks ChIP-seq reads files and corresponding Input controls. A model of 6 states was selected and applied on all samples. The 6 states identified were then given functional annotation based on histone marks enrichment and ENCODE published chromatin states.

We checked the genome-wide association between gene expression and chromatin states of the TSS, in both tumour and cell line samples. In each tumour / cell line, we classified the genes according to the chromatin states of the TSS. For genes with multiple TSS, the chromatin states showing frequency dominance was considered. We then calculated the median expression of the genes by their TSS categories in each sample, and assessed the distribution of the median expression by chromatin state across all tumour and cell line samples.

ChromHMM output files were concatenated using the unionbed function from BEDTools, by which a consensus sample-by-states matrix was created, where in each cell the chromatin state corresponding to the column's chromosome region in the row's sample, excluding regions from sexual chromosomes, with all samples included (n = 24, including 15 tumours and 9 cell lines).

We next performed unsupervised analysis of the integrated chromatin states in tumour and cell line samples.

Selection of most informative features

We first looked for the most informative features in the consensus sample-by-states matrix where in each cell the chromatin state corresponding to the column's chromosome region in the row's sample, excluding regions from sexual chromosomes, with all samples included (n = 24, including 15 tumours and 9 cell lines). We excluded genome regions of 'no mark' state to enrich our feature selection with active regions and filtered features with top 1% Shannon's entropy. Then to further select informative feature, we signed-rank transformed the data: For each state, given the constitution of the histone marks and association with gene expression, we performed a numeric transformation of the categorical states by assigning numeric values to categorical states, as 3 to E2 (Active Enhancer / Promoter), -3 to E4 (Repressed Chromatin), 2 to E3 (Bivalent Enhancer / Promoter), -2 to E6 (Heterochromatin / ZNF/ Repeats), 1 to E1 (Quiescent / No mark), and -1 to E5 (Quiescent / Weak repression). This allow to further increased the selection power as the top 1% features by variance ranking. We then used these top 1% variable features for subsequent analysis.

Dimension reduction and functional ontology analysis

We performed dimension reduction and visualization taking directly the categorical format of the above described selected features using multiple correspondence analysis (MCA). To explore the biological significance of the regions that contributed to the dimension that distinguishes the non-basal and basal clusters, the chromosome segments' loading estimates to the Dim 2 were extracted from the MCA outputs and regions with a p-value < 0.05 for the loading estimate were included (n = 12,198). Genes mapped to Dim 2 contributing regions were pre-ranked by loading estimates for gene-set enrichment analysis (GSEA) by which we identified multiple biological gene sets / ontologies associated with Dim 2. The gene sets collections were retrieved from the Broad Institute Molecular Signature Database, spanning the H (hall mark gene sets), C2 (curated gene sets, eg. pathways), C3 (regulatory target gene sets), C5 (ontology gene sets, eg. Gene Ontology), C6 (oncogenic signature gene sets), and C8 (cell type signature gene sets) categories, using the msigdbr R package (27, 60).

As complementary exploration, we in the meantime performed dimensional reduction to the numeric transformed data of the selected features, using MDS. Similar to what was observed in MCA, the Dim 2 represents the dimension that distinguishes the basal versus non-basal samples, and Dim 1 separates cell lines from tumours, suggesting potential batch effect and/or *in vitro* culture-specific effect. We then adjusted for these latent effects to obtain a refined clustering (basically on Dim 2), using the MNN algorithm implemented in the fastMNN function of the batchelor R Bioconductor package (61).

We then calculated for the chromosomal segments (ie. features of the consensus sample-by-states matrix), the difference in the numeric chromatin state scores between basal and non-basal groups, named chromatin state score difference basal vs non-basal. A negative score difference indicates stronger activation in the non-basal group, and a positive one indicates stronger activation in the basal group. For subsequent function analysis, we performed expression quantitative trait locus (eQTL) mapping to refine the segments to the ones significantly linked with associated gene expression, and limited the analysis to the significant eQTL pairs (p-value < 0.05, n = 4,377). We then analysed the distribution of the chromatin state score difference of the segments corresponding to the luminal and basal cell type signature genes.

Cell treatments, cell viability assay

For siRNA treatments, cells were reverse transfected using Lipofectamine RNAi max (Invitrogen) using 10 ng of siRNA (siRNA table in additional information).

For CRispR mutant cell lines production, RT112 and SD48 cells were plated at 80% confluence and the day after transfected with vectors expressing Cas9 an gRNA (VectorBuilder, see additional information) using Fugene HD transfection reagent. 48h post transfection, cells were selected using Puromycin (2µg/µL) during 4 days. After 2 weeks, clonal selection was performed using clonal dilution. FOXA1 mutation was assessed by Western Blot (anti-FOXA1 Abcam ab23738), PCR and genomic DNA sequencing.

Cell Viability was assessed in 96 well plates using CellTiter-Glo® Luminescent Cell Viability Assay (Promega).

RNA extraction and sequencing

RNA extraction

Cell lines RNA were extracted using Qiagen RNeasy kit coupled with DNAse treatment. Tumours RNA were extracted using Triple extraction protocol.

Tumours RNA sequencing

RNA sequencing libraries: Kit Nugen. The pool of libraries was quantified using a qPCR method (KAPA library quantification kit, Roche). The sequencing was carried out using paired-end mode (PE100) on a Illumina Novaseq 6000 instrument, using a custom primer (provided into the Nugen kit) to initiate the Read 1 sequencing. The target number of reads was about 50 million paired-reads per sample.

Cell lines RNA sequencing

RNA sequencing libraries were prepared from 1µg of total RNA using the Illumina TruSeq Stranded mRNA Library preparation kit (Illumina) which allows to perform a strand specific RNA sequencing. A first step of polyA selection using magnetic beads is done to focus sequencing on polyadenylated transcripts. After fragmentation, cDNA synthesis was performed and resulting fragments were used for dA-tailing and then ligated to the TruSeq indexed adapters. PCR amplification was finally achieved to create the final cDNA library (12 cycles). The resulting barcoded libraries were then equimolarly pooled and quantified using a qPCR method

(KAPA library quantification kit, Roche). The sequencing was carried out using paired-end mode (PE100) on a Illumina HiSeq2000 instrument. The sequencing configuration was set to reach an average of 100 million paired-reads per sample.

Cell lines 3'RNA-seq (Lexogen 3'Seq)

RNA sequencing libraries were prepared from 200ng of total RNA using the QuantSeq FWD 3'mRNA Seq LEXOGEN Standard (CliniSciences). Libraries were prepared according to the manufacturer's recommendations. The first step enables the synthesis of double strand cDNA, by revers transcription, using oligo dT priming. A qPCR optimization step was performed in order to estimate the most appropriate number of PCR cycles for library amplification. The resulting amplified and barcoded libraries were then equimolarly pooled and quantified using a qPCR method (KAPA library quantification kit, Roche). The sequencing was carried out using single-read mode (SR100) on an Illumina Novaseq 6000 instrument. The sequencing configuration was set to reach an average of 10 million reads per sample.

RNA-seq analysis

RNAseq were aligned on genome hg19 using STAR with default parameters. Our RNA-seq as well as RNA-seq from public data repository integrated using Deseq2 default parameters and VST normalisation. 3'RNA-seq were analysed with Deseq2 and RPM normalisation.

Assignment of MIBC and NMIBC subtypes

Gene expression data of the most tumour cases was previously generated and published (9, 22). We assigned consensus classes using the previously generated gene expression data using ConsensusMIBC (v1.1.0) R package (3) (Table S1). Given potential intra-tumour molecular heterogeneity, we also to verify the subtype in our ChIP-seq sampled tumour area using RNAseq from the same powder using the same ConsensusMIBC (v1.1.0) R package.

NMIBC samples (n=2) were classified using classifyNMIBC R Package (7).

Regulons

The regulatory network was reverse engineered by ARACNe-AP (41) from human urothelial cancer tissue datasets profiled by RNA-seq from TCGA. ARACNe was run with 100 bootstrap iterations using all probe-clusters mapping to a set of 1,740 transcription factors. Parameters used were standard parameters, with Mutual Information p-value threshold of 10^{-8}.

The VIPER (Virtual Inference of Protein-activity by Enriched Regulon analysis) (42) (R package viper 1.24), using the regulatory network obtained from ARACNE on urothelial cancer, and we computed the enrichment of each regulon on the gene expression signature using different implementations of the analytic Rank-based Enrichment Analysis algorithm.

SE Correlation Network

To build SE driven correlation network, we first selected genes regulated by SE defined as TF in Lambert *et al.* (40). Next using TCGA regulon VIPER score, we calculated the mean regulon score by subtype (Luminal, Ba/Sq or Stroma-Rich and kept TFs with mean regulon > 2 or < -2 (n=75). We further restricted the list to TFs with a minimum expression correlation of 0.5 in TCGA to build correlation network using igraph.

General bioinformatics, statistical analyses and public data

Plots and statistical analyses were performed in R software version 3.6.1, using ggpubr package. Wilcoxon and Kruskal-Wallis tests were used to test the association between continuous and categorical variables, for 2 categories or >2 categories, respectively. P-values <0.05 were considered statistically significant. Pairwise correlation of gene expression was calculated using Pearson coefficient and plotted using complexHeatmap R package. All gene expression heatmaps show mean-centered log2-transformed normalized counts of each represented gene.

TCGA-BLCA MIBC RNA-seq data were downloaded from TCGA data portal using TCGAbiolinks package (R), raw counts were normalized to account for different library size and the variance was stabilized with VST function in the DESeq2 R-package (62). TCGA-BLCA samples (n=404) were classified using the consensus system using consensusMIBC R package.

CCLE urinary tract cell line gene expression were downloaded from the DepMap portal (*https://depmap.org/portal/download/*). For consensus classification of CCLE bladder cancer cell lines, we adapted this classification considering only genes expressed by both tumours and cell lines. Ten cell lines were classified as Ba/Sq, all other were grouped as non-Ba/Sq.

MGHU3 RNA-seq bulk data were download from GEO (accession number, GSE171129).

Survival analysis

For Kaplan Meier survival analyses testing the association of gene expression and overall survival, we used http://tumorsurvival.org/index.html tool and divided the samples based on mean +/- sd. Log-rank P values were calculated to test the association between overall survival and low vs high expression groups.

Public scRNA-seq and Basal/Luminal signature

We downloaded the log2 TPM normalized gene expression of single cells from a Ba/Sq subtype MIBC tumour from the GEO database (accession number, GSM4307111). Initial quality control excluded genes expressed in less than 3 cells and cells with less than 200 genes. The top 2000 variable genes were used as features for subsequent PCA and the first 9 principal components were used for cell clustering and visualization by uniform manifold approximation and projection (UMAP) embedding. The marker genes of the luminal and basal tumour cells were calculated with Wilcoxon test based approach. The single cell RNA-seq data analyses were performed using the Seurat v4 package with default parameters unless otherwise specified.

Given the single-cell derived luminal and basal tumour cell signature was based on single-cell sequencing of primary *in vivo* tumour sample, and the *FOXA1* knock-out perturbation signature is likely limited to the genes regulated by *FOXA1* in an *in vitro* setting, it is important to adopt the cell subtype signatures to refine to the marker genes regulated by *FOXA1*, as a *FOXA1*-depdent luminal-basal plasticity signature which could be then used for further analyses involving *in vitro* transcriptomes. We first compared the perturbation and single-cell signatures by GSEA (perturbation DEG effect for ranking, and luminal / basal signatures as gene sets of interest) and found that in RT112 cell line, there was both significant enrichment of luminal signature in genes down-regulated in *FOXA1 KO* clones and significant enrichment of basal signature in genes up-regulated in *FOXA1 KO* clones. We then took the leading edge genes as the adopted *FOXA1*-depdent plasticity signature. As validation, this adopted signature showed similar enrichment in RT112 *FOXA1* KD assays and SD48 *FOXA1* KO assays, while the original cell type signature failed.

Data Availability

The datasets supporting the conclusions of this article are available in the GEO repository under accession numbers:

GSEXXXXX for Tumours ChIP-seq
GSEXXXXX for Normal and Cancer cell culture ChIP-seq
GSEXXXXX for Tumours RNAseq
GSEXXXXX for Normal and Cancer cell culture RNA-seq
GSEXXXXX for functional assays 3'RNAseq

Ethics approval and consent to participate

All patients provided written informed consent. All research in this study conformed to the principles of the Helsinki Declaration. All patients consent to participate

Funding

The work was supported by grants from Ligue Nationale Contre le Cancer: (H.N-K., J.F., C.G., X-Y.M., L.C., F.D., C.K., Y.A., F.R., I. B-P.) as an associated team (Equipe labellisée), the "Carte d'Identité des Tumeurs" program initiated, developed and funded by Ligue Nationale Contre le Cancer, and a post-doctoral fellowship supporting H.N-K. J.F. was supported by the Fondation ARC pour la recherche sur le cancer, L.C. by FRM (Fondation Recherche Médicale) and X-Y.M. was supported by a fellowship from ITMO Cancer AVIESAN, within the framework of Cancer Plan. The work was also supported by a "PL-Bio" project funded by INCa (2016-146), the French Ministry of Education and Research, the CNRS, and the Institut Curie. ChIP-sequencing was performed by the GenomEast platform, a member of the 'France Genomique' consortium (ANR-10-INSB-0009).

Conflict of Interest

The authors declare that they have no competing interests

Acknowledgements

We thank the NGS platform of Institut Curie, directed by Sylvain Baulande

Authors' contributions

H. N-K., J. F, performed the ChIP-seq and RNA-seq experiments.

C.K. established the NHU primary cells cultures.

Y. N. and T. L. provided clinical insight for analysis of the CIT cohort.

J.F. under Y.A. supervision performed histo-pathological analysis and E.G. the macrodissection of the tumors.

A.R. under D.G. supervision optimized RNA sequencing of primary tumour samples.

H. N-K. performed the functional experiments, siRNA, CRispR, cellular assays.

H. N-K, X-Y.M., C.G., J.F, T.Y., L.C., F.D, E.C. carried out the bioinformatics analysis. In particular, H.N-K. analysed ChIP-seq data, performed ChromHMM integration, SE identification with J.F., differential analysis, ontology/GSEA analysis, 3'RNA-seq analyses, and established coregulatory network with the help of J.F., F.D. and D.J. C.G. designed R scripts and participated to several analyses (GSVA, SE differential analysis, classifications). L.C. performed the regulon analysis. X-Y. M. analysed ChromHMM output, publicly available scRNA-seq, derived Basal/Luminal signature, 3'RNA-seq, performed GSEA analysis, optimized SE annotation. T.Y. under I.D. supervision processed the ChIPseq data. E.C. processed RNA-seq data of cell lines and centralized the data for bioinformatics analyses.

H. N-K., J.F., X-Y.M., C.G., D.J., I. B-P., F.R. wrote the manuscript.

The study was conceived by H. N-K., J.F. and supervised by Y.A., I.B-P. and F.R.

All authors gave critical insights and approved the final version for publication.

.

References:

1. Bray F et al. Global cancer statistics 2018: GLOBOCAN estimates of incidence and mortality worldwide for 36 cancers in 185 countries [Internet]. *CA. Cancer J. Clin.* 2018;68(6):394–424.

2. Humphrey PA, Moch H, Cubilla AL, Ulbright TM, Reuter VE. The 2016 WHO Classification of Tumours of the Urinary System and Male Genital Organs—Part B: Prostate and Bladder Tumours [Internet]. *Eur. Urol.* 2016;70(1):106–119.

3. Kamoun A et al. A Consensus Molecular Classification of Muscle-invasive Bladder Cancer[Formula presented] [Internet]. *Eur. Urol.* 2020;77(4):420–433.

4. Marzouka NAD et al. A validation and extended description of the Lund taxonomy for urothelial carcinoma using the TCGA cohort [Internet]. *Sci. Rep.* 2018;8(1). doi:10.1038/s41598-018-22126-x

5. Choi W et al. Identification of Distinct Basal and Luminal Subtypes of Muscle-Invasive Bladder Cancer with Different Sensitivities to Frontline Chemotherapy. *Cancer Cell* 2014;25(2):152–165.

6. Rebouissou S et al. CDKN2A homozygous deletion is associated with muscle invasion in FGFR3-mutated urothelial bladder carcinoma. [Internet]. *J. Pathol.* 2012;227(3):315–24.

7. Viborg Lindskrog S et al. An integrated multi-omics analysis identifies prognostic molecular subtypes of non-muscle-invasive bladder cancer [Internet] doi:10.1038/s41467-021-22465-w

8. Hedegaard J et al. Comprehensive Transcriptional Analysis of Early-Stage Urothelial Carcinoma. *Cancer Cell* 2016;30(1):27–42.

9. Rebouissou S et al. EGFR as a potential therapeutic target for a subset of muscle-invasive bladder cancers presenting a basal-like phenotype. [Internet]. *Sci. Transl. Med.* 2014;6(244):244ra91.

10. Fishwick C et al. Heterarchy of transcription factors driving basal and luminal cell phenotypes in human urothelium [Internet]. *Cell Death Differ.* 2017;24(5):809–818.

11. Eriksson P et al. Molecular subtypes of urothelial carcinoma are defined by specific gene regulatory systems [Internet]. *BMC Med. Genomics* 2015;8(1). doi:10.1186/s12920-015-0101-5

12. Yamashita H et al. Repression of transcription factor AP-2 alpha by PPARγ reveals a novel transcriptional circuit in basal-squamous bladder cancer [Internet]. *Oncogenesis* 2019;8(12). doi:10.1038/s41389-019-0178-3

13. Karni-Schmidt O et al. Distinct expression profiles of p63 variants during urothelial

development and bladder cancer progression [Internet]. *Am. J. Pathol.* 2011;178(3):1350–1360.

14. Warrick JI et al. FOXA1, GATA3 and PPARIγ Cooperate to drive luminal subtype in bladder cancer: A molecular analysis of established human cell lines [Internet]. *Sci. Rep.* 2016;6(December):1–15.

15. Chapuy B et al. Discovery and Characterization of Super-Enhancer-Associated Dependencies in Diffuse Large B Cell Lymphoma [Internet]. *Cancer Cell* 2013;24(6):777–790.

16. Ott CJ et al. Enhancer Architecture and Essential Core Regulatory Circuitry of Chronic Lymphocytic Leukemia [Internet]. *Cancer Cell* 2018;34(6):982-995.e7.

17. Hnisz D et al. Super-enhancers in the control of cell identity and disease [Internet]. *Cell* 2013;155(4):934.

18. Lovén J et al. Selective inhibition of tumor oncogenes by disruption of super-enhancers. [Internet]. *Cell* 2013;153(2):320–34.

19. Dunham I et al. An integrated encyclopedia of DNA elements in the human genome [Internet]. *Nature* 2012;489(7414):57–74.

20. Iyyanki T et al. Subtype-specific epigenomic landscape and 3D genome structure in bladder cancer2020;1–20.

21. van der Vos KE et al. Epigenetic profiling demarcates molecular subtypes of muscle-invasive bladder cancer [Internet]. *Sci. Rep.* 2020;10(1):1–10.

22. Biton A et al. Independent Component Analysis Uncovers the Landscape of the Bladder Tumor Transcriptome and Reveals Insights into Luminal and Basal Subtypes [Internet]. *Cell Rep.* 2014;9(4):1235–1245.

23. Shi MJ et al. Identification of new driver and passenger mutations within APOBEC-induced hotspot mutations in bladder cancer [Internet]. *Genome Med.* 2020;12(1):85.

24. Blum Y et al. Dissecting heterogeneity in malignant pleural mesothelioma through histo-molecular gradients for clinical applications [Internet]. *Nat. Commun.* 2019;10(1):1–12.

25. Ernst J, Kellis M. ChromHMM: Automating chromatin-state discovery and characterization [Internet]. *Nat. Methods* 2012;9(3):215–216.

26. Mootha VK et al. PGC-1α-responsive genes involved in oxidative phosphorylation are coordinately downregulated in human diabetes [Internet]. *Nat. Genet.* 2003;34(3):267–273.

27. Subramanian A et al. *Gene set enrichment analysis: A knowledge-based approach for interpreting genome-wide expression profiles [Internet]*. 2005:

28. Parolia A et al. Distinct structural classes of activating FOXA1 alterations in advanced prostate cancer [Internet]. *Nature* 2019;571(7765):413–418.

29. Kim E et al. Creation of bladder assembloids mimicking tissue regeneration and cancer [Internet]. *Nature* 2020;588(7839):664–669.

30. Whyte WA et al. Master transcription factors and mediator establish super-enhancers at key cell identity genes [Internet]. *Cell* 2013;153(2):307–319.

31. Zhang X et al. Somatic superenhancer duplications and hotspot mutations lead to oncogenic activation of the KLF5 transcription factor [Internet]. *Cancer Discov.* 2018;8(1):108–125.

32. Robertson AG et al. Comprehensive Molecular Characterization of Muscle-Invasive Bladder Cancer. *Cell* 2017;171(3):540-556.e25.

33. Weinstein JN et al. Comprehensive molecular characterization of urothelial bladder carcinoma [Internet]. *Nature* 2014;507(7492):315–322.

34. Sim WJ et al. c-Met activation leads to the establishment of a TGFβ-receptor regulatory network in bladder cancer progression [Internet]. *Nat. Commun.* 2019;10(1). doi:10.1038/s41467-019-12241-2

35. Chen L et al. Master transcription factors form interconnected circuitry and orchestrate transcriptional networks in oesophageal adenocarcinoma [Internet]. *Gut* 2020;69(4):630–640.

36. Saint-André V et al. Models of human core transcriptional regulatory circuitries. *Genome Res.* 2016;26(3):385–396.

37. Zheng R et al. Cistrome Data Browser: Expanded datasets and new tools for gene regulatory analysis [Internet]. *Nucleic Acids Res.* 2019;47(D1):D729–D735.

38. Mei S et al. Cistrome Data Browser: A data portal for ChIP-Seq and chromatin accessibility data in human and mouse [Internet]. *Nucleic Acids Res.* 2017;45(D1):D658–D662.

39. Heinz S et al. Simple Combinations of Lineage-Determining Transcription Factors Prime cis-Regulatory Elements Required for Macrophage and B Cell Identities [Internet]. *Mol. Cell* 2010;38(4):576–589.

40. Lambert SA et al. The Human Transcription Factors [Internet]. *Cell* 2018;172(4):650–665.

41. Lachmann A, Giorgi FM, Lopez G, Califano A. ARACNe-AP: gene network reverse engineering through adaptive partitioning inference of mutual information [Internet]. *Bioinformatics* 2016;32(14):2233–2235.

42. Alvarez MJ et al. Functional characterization of somatic mutations in cancer using network-

based inference of protein activity [Internet]. *Nat. Genet.* 2016;48(8):838–847.

43. Finnegan A et al. Single-cell transcriptomics reveals spatial and temporal turnover of keratinocyte differentiation regulators. *Front. Genet.* 2019;10(JUL):1–14.

44. Somerville TDD et al. ZBED2 is an antagonist of interferon regulatory factor 1 and modifies cell identity in pancreatic cancer [Internet] doi:10.1073/pnas.1921484117/-/DCSupplemental

45. Barretina J et al. The Cancer Cell Line Encyclopedia enables predictive modelling of anticancer drug sensitivity. *Nature* 2012;483(7391):603–607.

46. Ghandi M et al. Next-generation characterization of the Cancer Cell Line Encyclopedia. *Nature* 2019;569(7757):503–508.

47. Choi W et al. Intrinsic basal and luminal subtypes of muscle-invasive bladder cancer. [Internet]. *Nat. Rev. Urol.* 2014;11(7):400–10.

48. Bi M et al. Enhancer reprogramming driven by high-order assemblies of transcription factors promotes phenotypic plasticity and breast cancer endocrine resistance [Internet]. *Nat. Cell Biol.* 2020;22(6):701–715.

49. He Y et al. FOXA1 overexpression suppresses interferon signaling and immune response in cancer [Internet]. *J. Clin. Invest.* 2021;131(14). doi:10.1172/JCI147025

50. Lee HW et al. Single-cell RNA sequencing reveals the tumor microenvironment and facilitates strategic choices to circumvent treatment failure in a chemorefractory bladder cancer patient [Internet] doi:10.1186/s13073-020-00741-6

51. Song B et al. Targeting FOXA1-mediated repression of TGF-β signaling suppresses castration-resistant prostate cancer progression. *J. Clin. Invest.* 2019;129(2):569–582.

52. Mansour MR et al. An oncogenic super-enhancer formed through somatic mutation of a noncoding intergenic element [Internet]. *Science (80-.).* 2014;346(6215):1373–1377.

53. Chapuy B et al. Discovery and Characterization of Super-Enhancer-Associated Dependencies in Diffuse Large B Cell Lymphoma [Internet]. *Cancer Cell* 2013;24(6):777–790.

54. Lerdrup M, Johansen JV, Agrawal-Singh S, Hansen K. An interactive environment for agile analysis and visualization of ChIP-sequencing data [Internet]. *Nat. Struct. Mol. Biol.* 2016;23(4):349–357.

55. McLean CY et al. GREAT improves functional interpretation of cis-regulatory regions [Internet]. *Nat. Biotechnol.* 2010;28(5):495–501.

56. Elsworth B et al. The MRC IEU OpenGWAS data infrastructure [Internet]

doi:10.1101/2020.08.10.244293

57. Kamat MA et al. Databases and ontologies PhenoScanner V2: an expanded tool for searching human genotype-phenotype associations [Internet] doi:10.1093/bioinformatics/btz469

58. Tate JG et al. COSMIC: The Catalogue Of Somatic Mutations In Cancer [Internet]. *Nucleic Acids Res.* 2019;47(D1):D941–D947.

59. Sondka Z et al. The COSMIC Cancer Gene Census: describing genetic dysfunction across all human cancers [Internet]. *Nat. Rev. Cancer* 2018;18(11):696–705.

60. Liberzon A et al. The Molecular Signatures Database Hallmark Gene Set Collection [Internet]. *Cell Syst.* 2015;1(6):417–425.

61. Haghverdi L, Lun ATL, Morgan MD, Marioni JC. Batch effects in single-cell RNA-sequencing data are corrected by matching mutual nearest neighbors [Internet]. *Nat. Biotechnol.* 2018;36(5):421–427.

62. Love MI, Huber W, Anders S. Moderated estimation of fold change and dispersion for RNA-seq data with DESeq2 [Internet]. *Genome Biol.* 2014;15(12):550.

Figures legends

Figure 1: Methodology/Workflow

Figure 2: Chromatin states classify bladder cancers by subgroups

A. ChromHMM principle example and emission order dividing genome in 6 states based on combination of H3K27ac, H3K27me3 and H3K9me3 marks.
B. Expression level association with each chromatin state and each sample.
C. Two chromatin state clusters revealed by unsupervised analysis of top 1% varying regions using MDS for dimension reduction plus MNN for batch effect correction.
D. GSEA functional enrichment analysis of the genes mapped to the MCA Dim2 contributing features. A negative NES indicates significant enrichment in lower Dim2 coordinates (basal direction), and the reverse is in higher Dim2 coordinates (Luminal direction).
E. Luminal versus basal tumour cell signature genes identified with single cell RNA-seq analysis showing concordant enrichment in chromatin state clusters.
F. Genome Browser view of chromatin states at *FOXA1* and *KRT6* loci with corresponding RNAseq (VST normalized scaled expression).

Figure 3: Identification of the bladder super-enhancer repertoire and subtype specificities

A. PCA of H3K27ac signal inside ROSE consensus SE (n=2887) for all samples.
B. Representative examples of H3K27ac signal in Ba/Sq, Stroma-Rich, Luminal and NMIBC tumors with corresponding RNA-seq gene expression. Orange boxes represent SE localisation.
C. Fold Change plots for differentially bound SEs between Ba/Sq and Luminals samples. Significance by p-value <0.05.
D. Plot comparing expression LogFC between Ba/Sq and Luminal samples for genes assigned to subgroup-enriched SE.
E. Reactome pathway enrichment analysis of genes associated with Ba/Sq vs Luminal SEs.
F. Venn diagram comparing 3 differential analyses of SE. NHU-enriched SEs are enriched in NHU vs Luminal or NHU vs Basal (pink circle). Basal-enriched SEs are enriched in Basal vs NHU or Basal vs Luminal (red circle). Luminal-enriched SEs are enriched in Luminal vs NHU or Luminal vs Basal (green circle).

Figure 4: Super-enhancers regulate a network of candidate master transcription factors for bladder cancer subgroups

A. Cistrome analysis of LumP and Ba/Sq specific SE.
B. Homer motif enrichment analysis in H3K27ac differential peaks inside differential SE in Luminal vs Basal and Basal vs Luminal.
C. Methodology to identify key coregulated SE-associated TFs.
D. Heatmap of the top 75 TFs with high regulon score. Clustering identified 3 major clusters.

E. Heatmap of the top 75 TFs expression in TCGA-BLCA.
F. Correlation network of the top 55 TFs with an expression correlation coefficient of min 0.5 in TCGA-BLCA cohort.
G. Single cell RNA-seq analysis of one Bladder Cancer tumors with both Basal and Luminal Population (GSM4307111) Right panel, associated expression for key TF in each compartment.

Figure 5: FOXA1 binds subgroup-specific bladder super-enhancers and correlates with their activation

A. Venn diagram comparing FOXA1 ChIP-seq peaks in SD48 and 5637 cell line. Heatmap for 3 categories of peaks and associated mean profiles.
B. Cistrome analysis of motif enrichment analysis in SD48-specific and 5637-specific FOXA1 peaks.
C. Reactome pathway analysis of genes associated to the 3 categories of FOXA1 peaks.
D. Pie chart showing proportion of SE with an overlapping FOXA1 peak (merge of FOXA1 peaks in SD48 and 5637).
E. Correlation between H3K27ac peaks versus FOXA1 peaks inside SE.
F. Heatmap of FOXA1 and H3K27ac reads on FOXA1 peaks overlapping Super-enhancers ranked by FOXA1 reads ration in SD48 vs 5637.
G. Genome browser view of GATA3, PPARg and TGFB2 associated SE. SE are highlighted with orange boxes.

Figure 6: FOXA1 regulates inflammation and cellular identity

A. Cell viability in RT112 and SCaBER under siRNA treatment against FOXA1
B. Venn diagram comparing differentially expressed genes in RT112 and SCaBER FOXA1 KD.
C. GSEA plot of Msig Hallmark GSEA Analysis of genes differentially regulated in RT112 and SCaBER cell lines upon FOXA1 siRNA (2 independent siRNA, 2 replicates)
D. Heatmap of genes in Hallmark interferon gamma response genes that are differentially regulated in FOXA1 KD *vs* Ct (min Fold Change = 1,5).
E. Heatmap of Top Luminal TFs expression in RT112 and SCaBER cell lines upon FOXA1 KD.
F. PCA projection of TCGA tumors and CRispR mutant clones on the Basal/Luminal signatures.
G. GSVA analysis of FOXA1 CRispR mutant clones on Urothelial differentiation signature from Eriksson et al.
H. GSVA analysis of FOXA1 CRispR mutant clones on Basal TFs identified in Fig. 4F
I. Overrepresentation analysis of DEG in FOXA1 mutant *vs* Controls.
J. Volcano plot of Deseq2 RNA-seq analysis comparing pooled CRispR mutant FOXA1 clones in SD48 and RT112 *versus* controls.

Figure 7: ZBED2, a novel Basal-associated TF also involved inflammation dampening

A. TCGA expression of ZBED2 by Subtypes.
B. TCGA expression Heatmap of ZBED2 and FOXA1 and TCGA correlation between ZBED2 and FOXA1.
C. Expression of FOXA1 and ZBED2 in single-cell transcriptomics from bladder cancer cell lines in the Cancer Cell Line Encyclopedia (CCLE), highlighting the nearly mutually exclusive expression of these genes.
D. Genome browser view of ZBED2 and FOXA1 loci in SD48 and 5637 cell lines
E. GSEA analysis (Hallmarlk) of ZBED2 correated genes in basal cells population of GSM4307111 scRNAseq tumor.
F. GSEA analysis (Hallmarlk) of gene expression upon siZBED2 KD in RT112 (siZBED2-1 and siZBED2-2).
G. 3’seq STAT2 and CD274 (PD-L1) expression in RT112 and SCaBER after siZBED2 and siFOXA1.

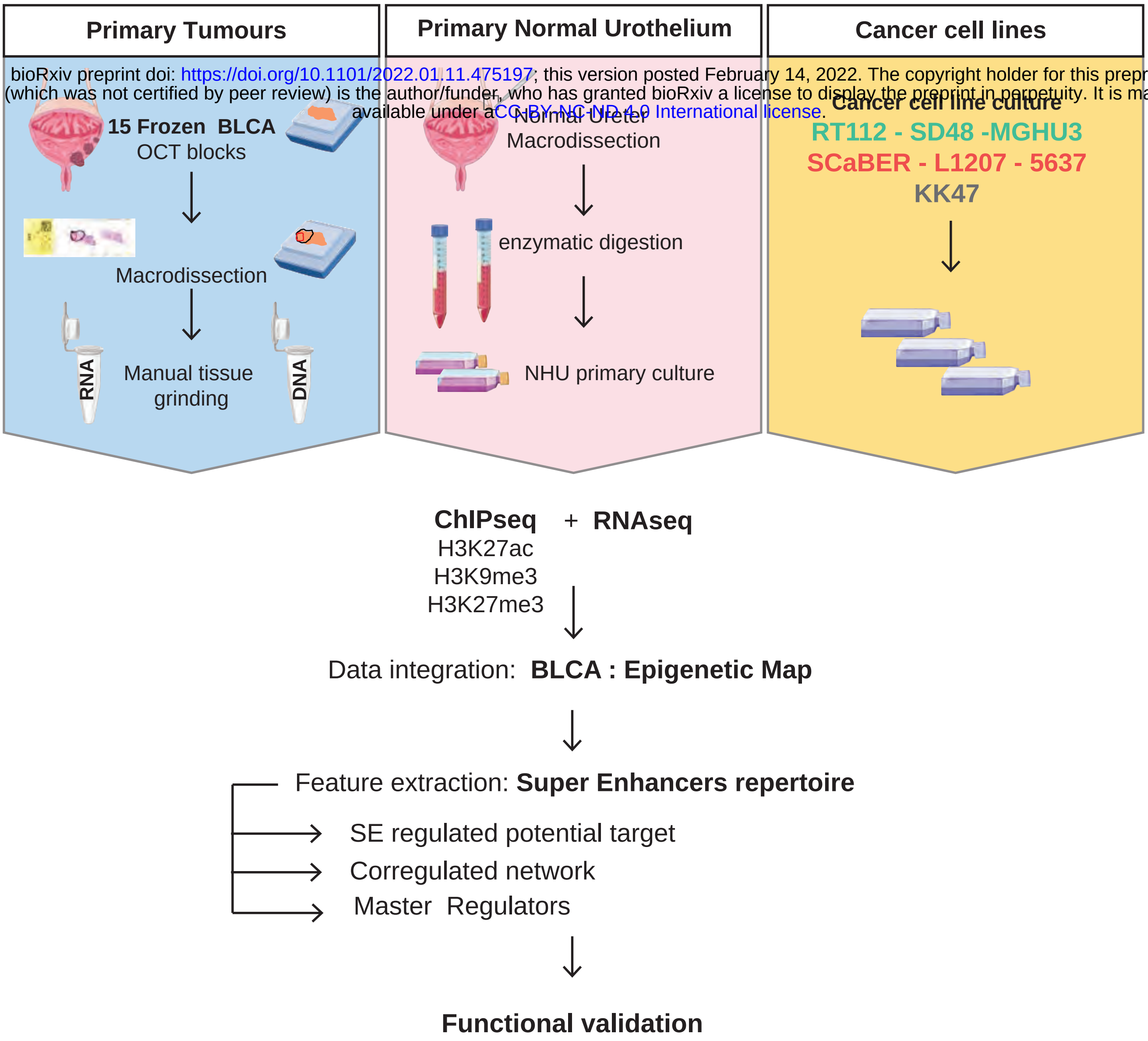

Figure 1: Methodology/Workflow

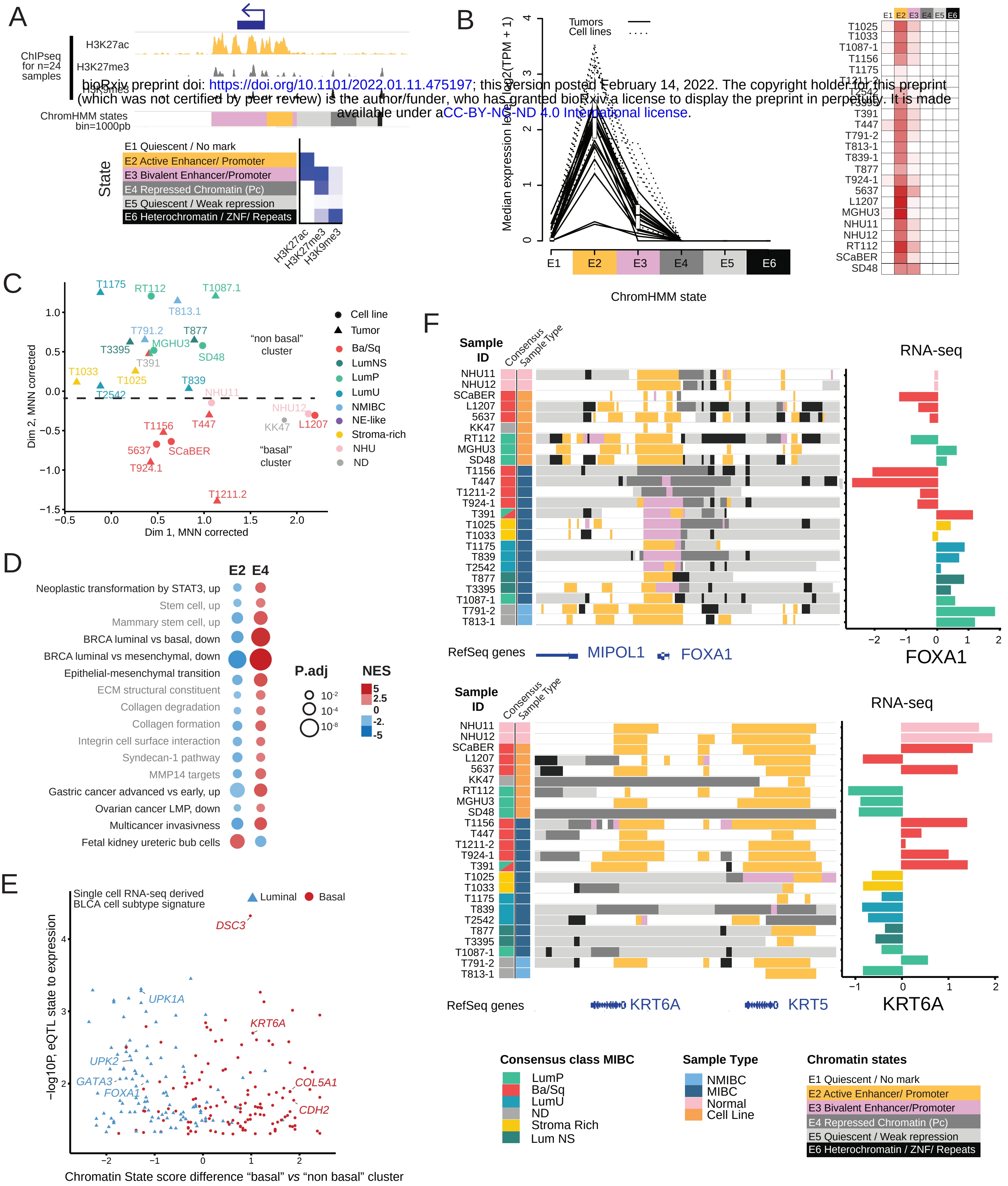

Figure 2: Chromatin states classify bladder cancers by subgroups
(A) ChromHMM principle example and emission order dividing genome in 6 states based on combination of H3K27ac, H3K27me3 and H3K9me3 marks. (B) Expression level association with each chromatin state and each sample. (C) Two chromatin state clusters revealed by unsupervised analysis of top 1% varying regions using MDS for dimension reduction plus MNN for batch effect correction. (D) GSEA functional enrichment analysis of the genes mapped to the MCA Dim2 contrib-uting features. A negative NES indicates significant enrichment in lower Dim2 coordi-nates (basal direction), and the reverse is in higher Dim2 coordinates (Luminal direction). (E) Luminal versus basal tumour cell signature genes identified with single cell RNA-seq analysis showing concordant enrichment in chromatin state clusters. (F) Genome Browser view of chromatin states at FOXA1 and KRT6 loci with corresponding RNAseq (VST normalized scaled expression).

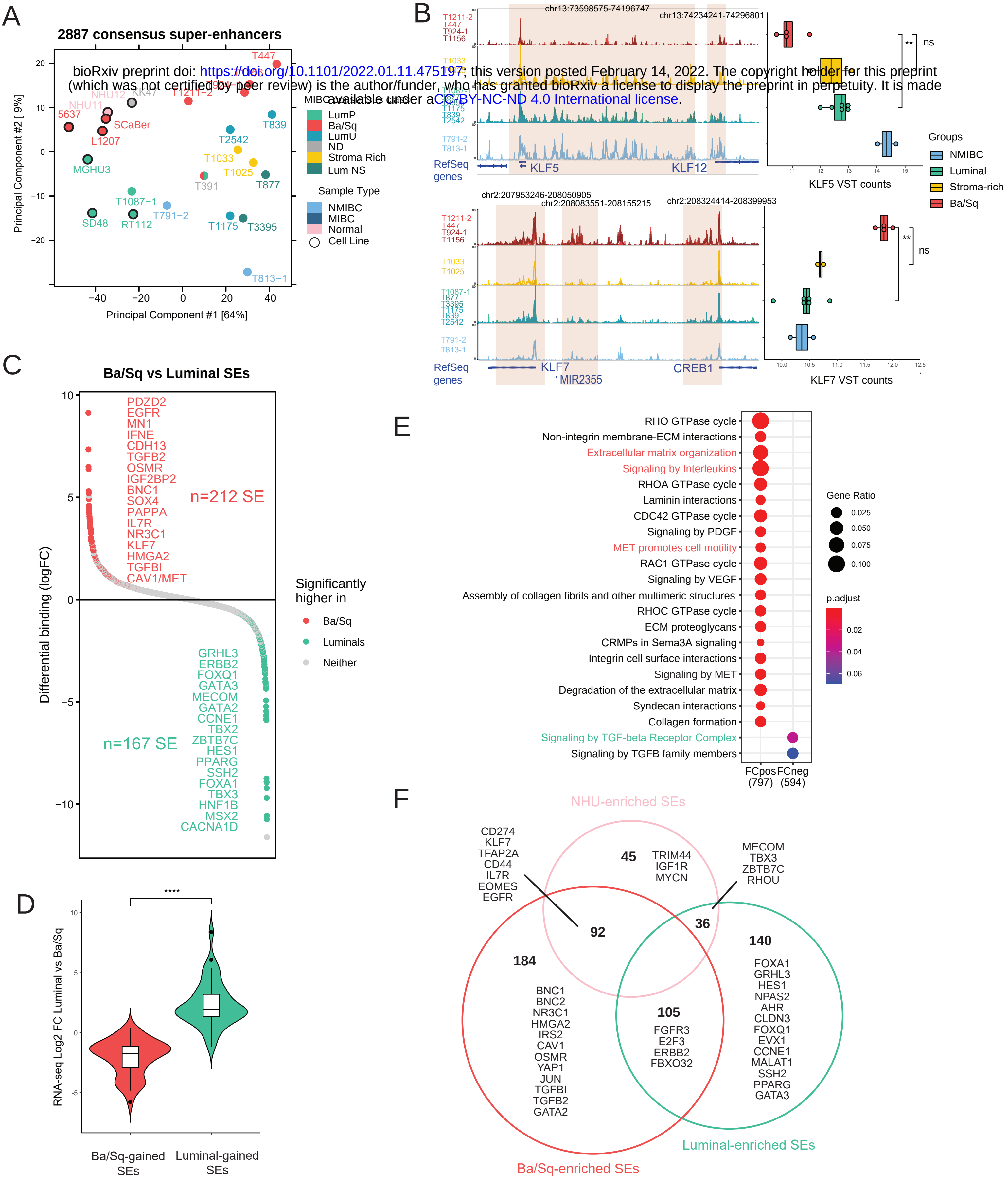

Figure 3: Identification of the bladder super-enhancer repertoire and subtype specificities
(A) PCA of H3K27ac signal inside ROSE consensus SE (n=2887) for all samples.(B) Representative examples of H3K27ac signal in Ba/Sq, Stroma-Rich, Luminal and NMIBC tumors with corresponding RNA-seq gene expression. Orange boxes represent SE localisation.(C) Fold Change plots for differentially bound SEs between Ba/Sq and Luminals samples. Significance by p-value <0.05.(D) Plot comparing expression LogFC between Ba/Sq and Luminal samples for genes as-signed to subgroup-enriched SE.(E) Reactome pathway enrichment analysis of genes associated with Ba/Sq vs Luminal SEs.(F) Venn diagram comparing 3 differential analyses of SE. NHU-enriched SEs are enriched in NHU vs Luminal or NHU vs Basal (pink circle). Basal-enriched SEs are enriched in Basal vs NHU or Basal vs Luminal (red circle). Luminal-enriched SEs are enriched in Luminal vs NHU or Luminal vs Basal (green circle).

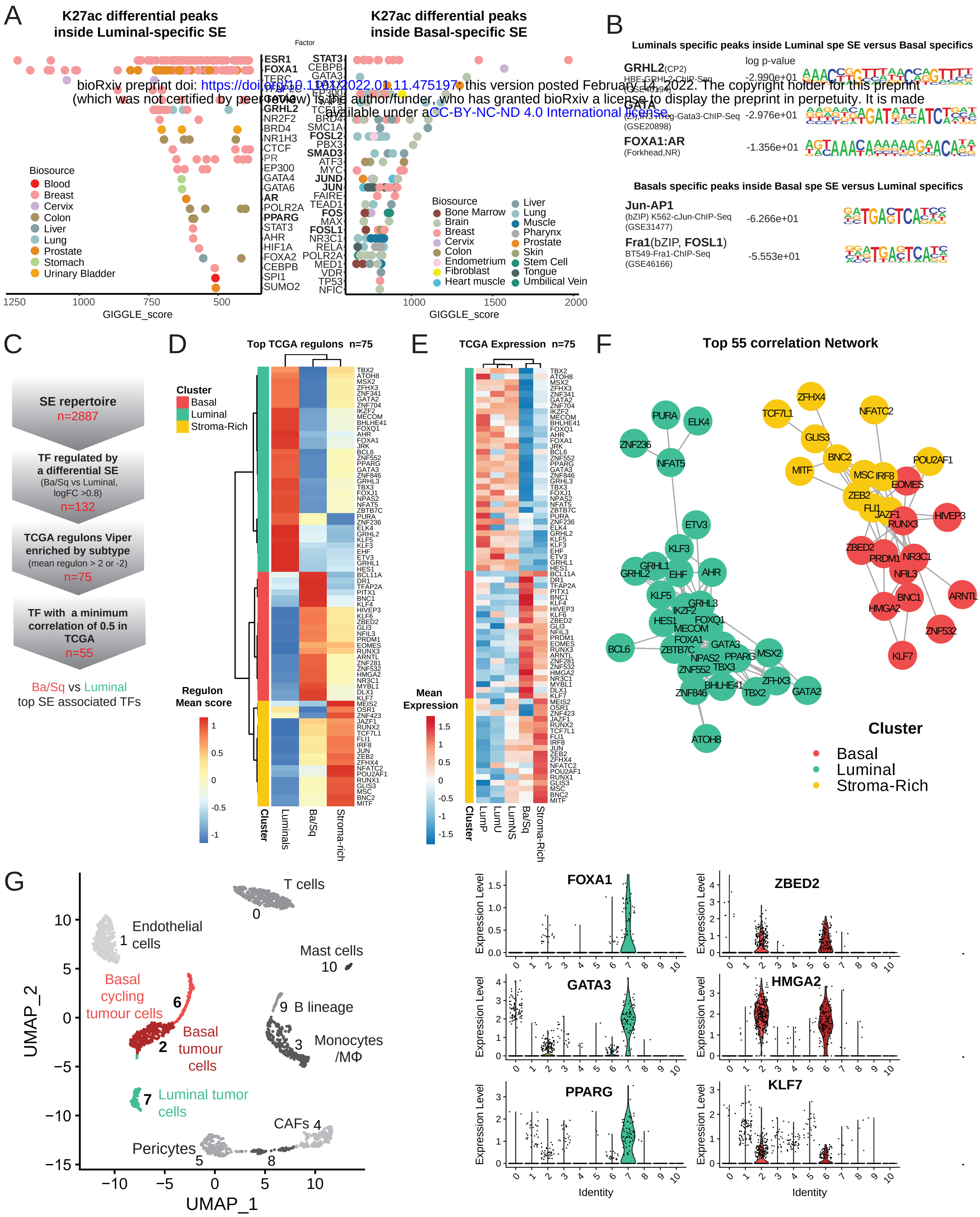

Figure 4: SE regulate a network of candidate master transcription factors for bladder cancer subgroups
(A) Cistrome analysis of LumP and Ba/Sq specific SE.(B) Homer motif enrichment analysis in H3K27ac differential peaks inside differential SE in Luminal vs Basal and Basal vs Luminal.(C) Methodology to identify key coregulated SE-associated TFs.(D) Heatmap of the top 75 TFs with high regulon score. Clustering identified 3 major clusters.(E) Heatmap of the top 75 TFs expression in TCGA-BLCA.(F) Correlation network of the top 55 TFs with an expression correlation coefficient of min 0.5 in TCGA-BLCA cohort.(G) Single cell RNA-seq analysis of one Bladder Cancer tumors with both Basal and Luminal Population (GSM4307111) Right panel, associated expression for key TF in each compartment.

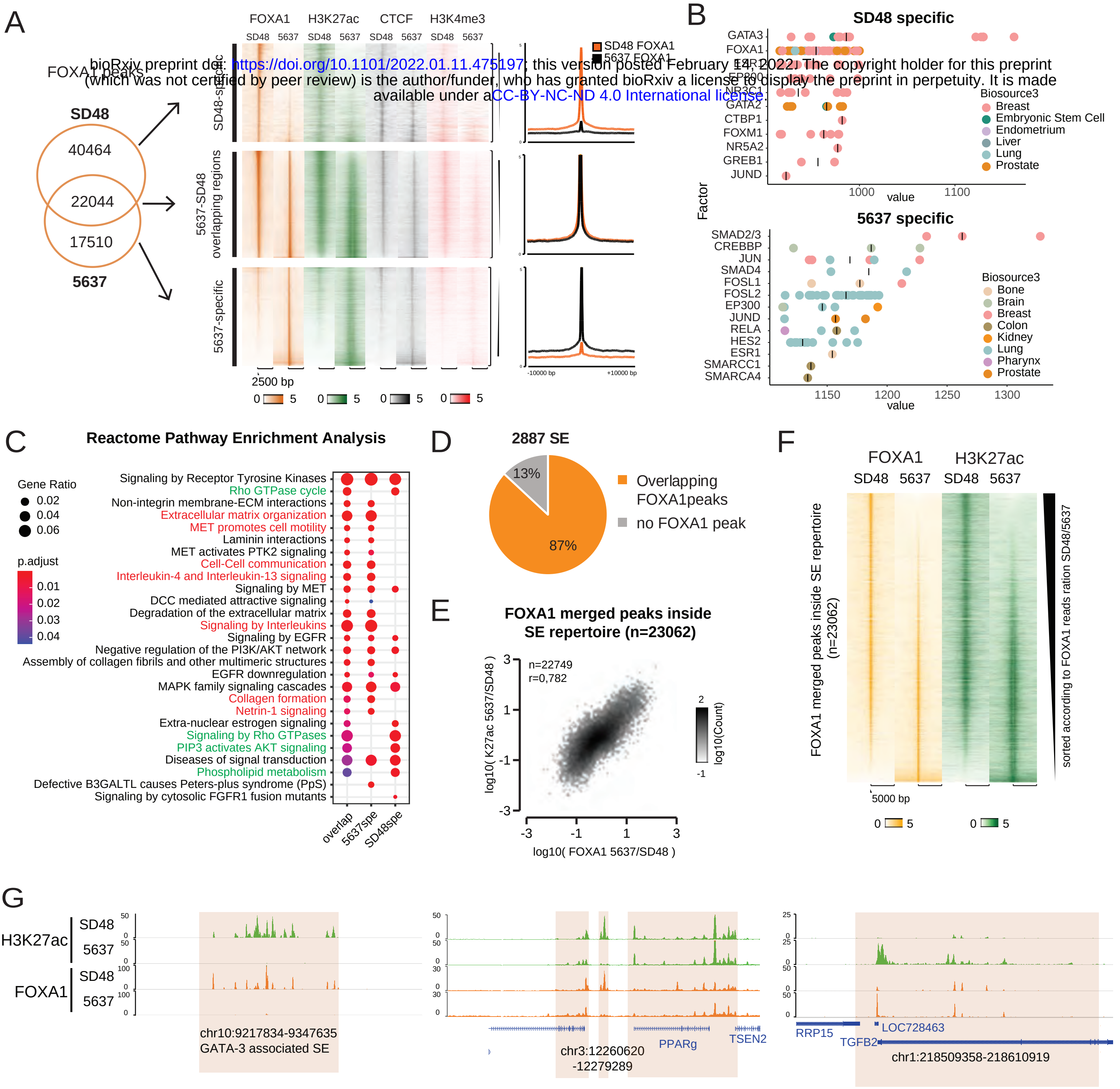

Figure 5: FOXA1 binds subgroup-specific bladder super-enhancers and correlates with their activation

(A) Venn diagram comparing FOXA1 ChIP-seq peaks in SD48 and 5637 cell line. Heatmap for 3 categories of peaks and associated mean profiles. (B) Cistrome analysis of motif enrichment analysis in SD48-specific and 5637-specific FOXA1 peaks.(C) Reactome pathway analysis of genes associated to the 3 categories of FOXA1 peaks.(D) Pie chart showing proportion of SE with an overlapping FOXA1 peak (merge of FOXA1 peaks in SD48 and 5637).(E) Correlation between H3K27ac peaks versus FOXA1 peaks inside SE. (F) Heatmap of FOXA1 and H3K27ac reads on FOXA1 peaks overlapping Super-enhancers ranked by FOXA1 reads ration in SD48 vs 5637.(G) Genome browser view of GATA3, PPARg and TGFB2 associated SE. SE are highlighted with orange boxes.

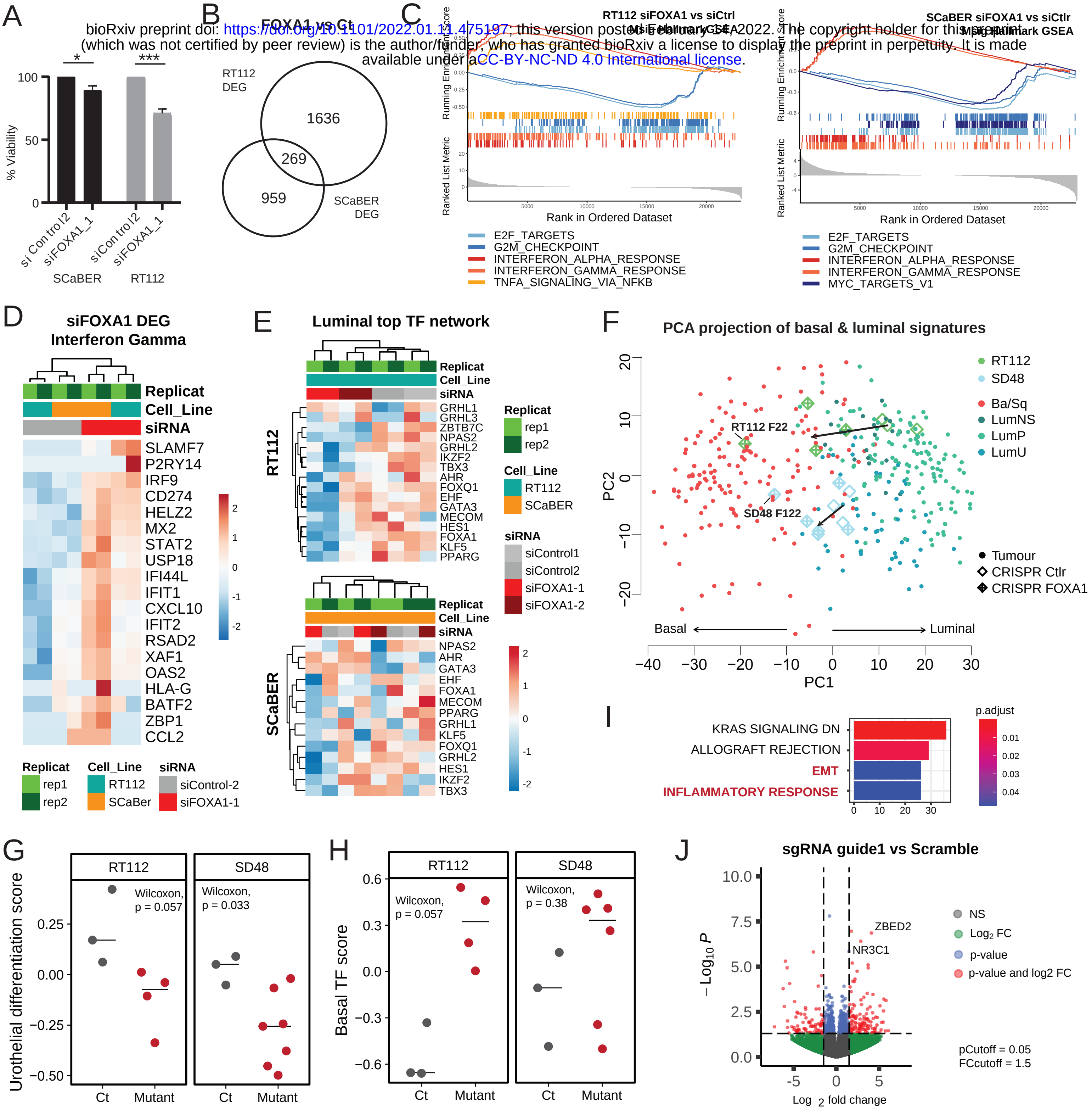

Figure 6: FOXA1 regulates inflammation and cellular identity
(A) Cell viability in RT112 and SCaBER under siRNA treatment against FOXA1. (B) Venn diagram comparing differentially expressed genes in RT112 and SCaBER FOXA1 KD.(C) GSEA plot of Msig Hallmark GSEA Analysis of genes differentially regulated in RT112 and SCaBER cell lines upon FOXA1 siRNA (2 independent siRNA, 2 replicates) (D) Heatmap of genes in Hallmark interferon gamma response genes that are differentially regulated in FOXA1 KD vs Ct (min Fold Change = 1,5). (E) Heatmap of Top Luminal TFs expression in RT112 and SCaBER cell lines upon FOXA1 KD. (F) PCA projection of TCGA tumors and CRispR mutant clones on the Basal/Luminal signatures.(G) GSVA analysis of FOXA1 CRispR mutant clones on Urothelial differentiation signature from Eriksson et al. (H) GSVA analysis of FOXA1 CRispR mutant clones on Basal TFs identified in Fig. 4F . (I) Overrepresentation analysis of DEG in FOXA1 mutant vs Controls. (J) Volcano plot of Deseq2 RNA-seq analysis comparing pooled CRispR mutant FOXA1 clones in SD48 and RT112 versus controls.

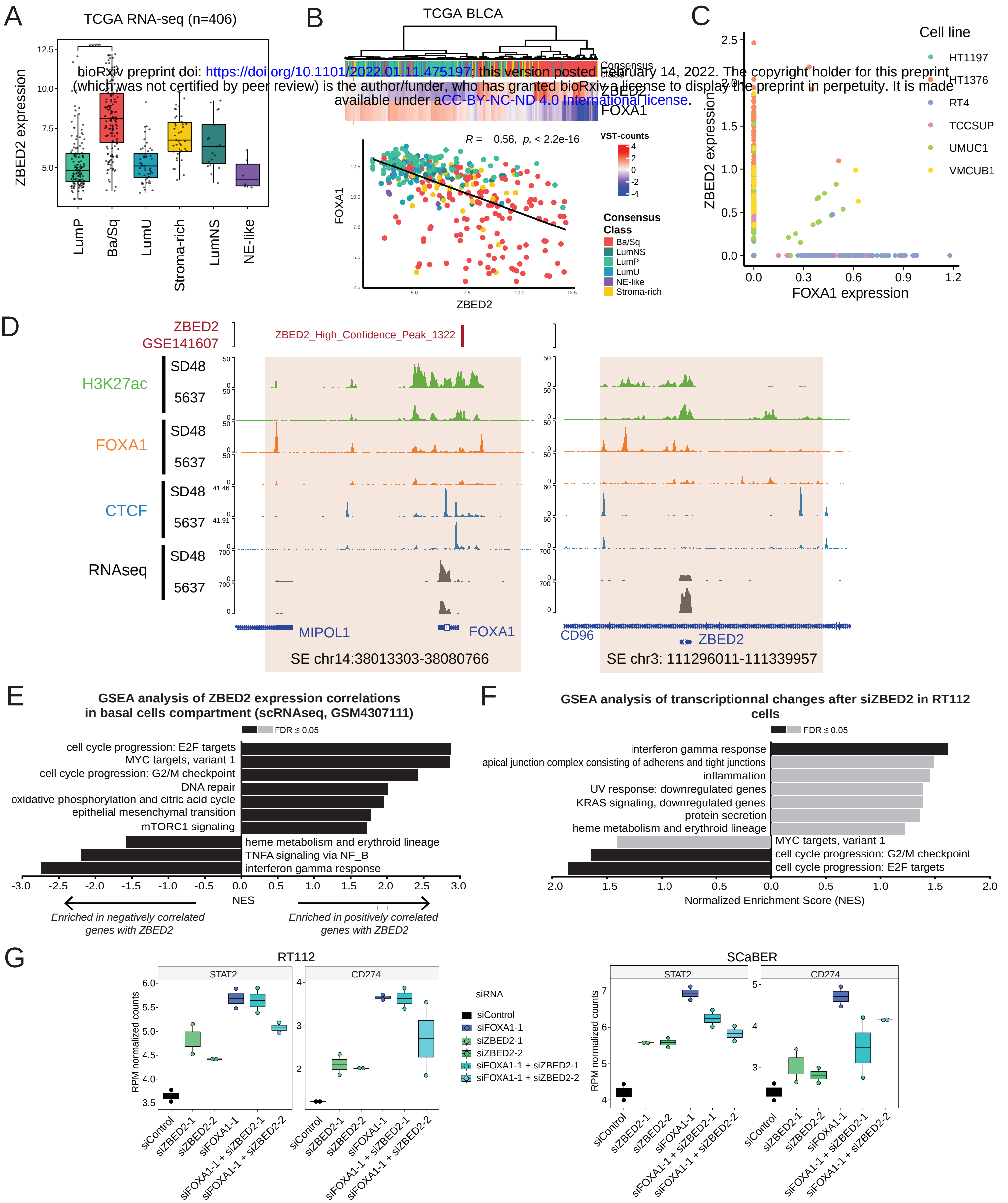

Figure 7: ZBED2, a novel Basal-associated TF also involved inflammation dampening
(A) TCGA expression of ZBED2 by Subtypes. (B) TCGA expression Heatmap of ZBED2 and FOXA1 and TCGA correlation between ZBED2 and FOXA1. (C) Expression of FOXA1 and ZBED2 in single-cell transcriptomics from bladder cancer cell lines in the Cancer Cell Line Encyclopedia (CCLE), highlighting the nearly mutually ex-clusive expression of these genes. (D) Genome browser view of ZBED2 and FOXA1 loci in SD48 and 5637 cell lines. (E) GSEA analysis (Hallmarlk) of ZBED2 correated genes in basal cells population of GSM4307111 scRNAseq tumor. (F) GSEA analysis (Hallmarlk) of gene expression upon siZBED2 KD in RT112 (siZBED2-1 and siZBED2-2). (G) 3'seq STAT2 and CD274 (PD-L1) expression in RT112 and SCaBER after siZBED2 and siFOXA1.

12.2 Article 6 : FGFR3 mutational activation can induce luminal-like papillary bladder tumor formation and favors a male sex bias

EUROPEAN UROLOGY xxx (xxxx) xxx–xxx

available at www.sciencedirect.com
journal homepage: www.europeanurology.com

European Association of Urology

Bladder Cancer

FGFR3 Mutational Activation Can Induce Luminal-like Papillary Bladder Tumor Formation and Favors a Male Sex Bias

Ming-Jun Shi [a,b,c,†], *Jacqueline Fontugne* [b,c,d,e,†], *Aura Moreno-Vega* [b,c,†], *Xiang-Yu Meng* [b,c,f,†], *Clarice Groeneveld* [b,g,†], *Florent Dufour* [b,c,h], *Aurélie Kamoun* [g], *Sia Viborg Lindskrog* [i], *Luc Cabel* [b,c], *Clémentine Krucker* [b,c], *Audrey Rapinat* [j], *Claire Dunois-Larde* [b,c], *May-Linda Lepage* [b,c], *Elodie Chapeaublanc* [b,c], *Olivier Levrel* [k], *Victoria Dixon* [b,e], *Thierry Lebret* [l], *Anna Almeida* [j], *Aurélien De Reynies* [g], *Natacha Rochel* [m,n,o,p], *Lars Dyrskjøt* [i], *Yves Allory* [b,d,e], *François Radvanyi* [b,c], *Isabelle Bernard-Pierrot* [b,c,*]

[a] *Department of Urology, Beijing Friendship Hospital, Capital Medical University, Beijing, China;* [b] *Institut Curie, PSL Research University, CNRS, UMR144, Equipe Labellisée Ligue contre le Cancer, Paris, France;* [c] *Sorbonne Universités, UPMC Université Paris 06, CNRS, UMR144, Paris, France;* [d] *Université Versailles St-Quentin, Université Paris-Saclay, Montigny-le-Bretonneux, France;* [e] *Institut Curie, Department of Pathology, Saint-Cloud, France;* [f] *Department of Urology, Zhongnan Hospital of Wuhan University, Wuhan, China;* [g] *La Ligue contre le Cancer, Paris, France;* [h] *Inovarion, Paris, France;* [i] *Department of Molecular Medicine, Aarhus University Hospital, Aarhus, Denmark;* [j] *Department of Translational Research, Institut Curie, Paris, France;* [k] *MEDIPATH Les Jalassières, Eguilles, France;* [l] *Service d'Urologie, Hôpital Foch, Suresnes, France;* [m] *Institut de Génétique et de Biologie Moléculaire et Cellulaire (IGBMC), Illkirch, France;* [n] *Institut National de La Santé et de La Recherche Médicale (INSERM), Illkirch, France;* [o] *U1258/Centre National de Recherche Scientifique (CNRS), Illkirch, France;* [p] *UMR7104/Université de Strasbourg, Illkirch, France*

Article info

Article history:
Accepted September 29, 2022

Associate Editor:
James Catto

Keywords:
Bladder cancer
Fibroblast growth factor receptor 3
Androgen receptor
Estrogen receptor
Sex bias
Mouse model
Luminal tumors
Tyrosine kinase receptor

Abstract

Background: Bladder cancer (BCa) is more common in men and presents differences in molecular subtypes based on sex. Fibroblast growth factor receptor 3 (*FGFR3*) mutations are enriched in the luminal papillary muscle-invasive BCa (MIBC) and non-MIBC subtypes.

Objective: To determine whether *FGFR3* mutations initiate BCa and impact BCa male sex bias.

Design, setting, and participants: We developed a transgenic mouse model expressing the most frequent *FGFR3* mutation, FGFR3-S249C, in urothelial cells. Bladder tumorigenesis was monitored in transgenic mice, with and without carcinogen exposure. Mouse and human BCa transcriptomic data were compared.

Intervention: Mutant *FGFR3* overexpression in mouse urothelium and siRNA knockdown in cell lines, and N-butyl-N(4-hydroxybutyl)-nitrosamine (BBN) exposure.

Outcome measurements and statistical analysis: Impact of transgene dosage on tumor frequency, synergy with BBN treatment, and FGFR3 pathway activation were analyzed. The sex-specific incidence of *FGFR3*-mutated tumors was evaluated in mice and humans. *FGFR3* expression in FGFR3-S249C mouse urothelium and in various human epithelia

---

[†] These authors contributed equally to the work.

[*] Corresponding author. Institut Curie, 26 rue d'Ulm, 75005 Paris, France. Tel. +33 1 42 34 63 40; Fax: +33 1 42 34 63 49.
E-mail address: ibernard@curie.fr (I. Bernard-Pierrot).

https://doi.org/10.1016/j.eururo.2022.09.030
0302-2838/

Please cite this article as: M.-J. Shi, J. Fontugne, A. Moreno-Vega et al., FGFR3 Mutational Activation Can Induce Luminal-like Papillary Bladder Tumor Formation and Favors a Male Sex Bias, Eur Urol (2022), https://doi.org/10.1016/j.eururo.2022.09.030

Tumor microenvironment

was measured. Mutant *FGFR3* regulation of androgen (*AR*) and estrogen (*ESR1*) receptor activity was evaluated, through target gene expression (regulon) and reporter assays.

Results and limitations: FGFR3-S249C expression in mice induced low-grade papillary BCa resembling human luminal counterpart at histological, genomic, and transcriptomic levels, and promoted BBN-induced basal BCa formation. Mutant FGFR3 expression levels impacted tumor incidence in mice, and mutant *FGFR3*–driven human tumors were restricted to epithelia presenting high normal *FGFR3* expression levels. BCa male sex bias, also found in our model, was even higher in human *FGFR3*-mutated tumors compared with wild-type tumors and was associated with higher AR and lower ESR1 regulon activity. Mutant *FGFR3* expression inhibited both ESR1 and AR activity in mouse tumors and human cell lines, demonstrating causation only between FGFR3 activation and low ESR1 activity in tumors.

Conclusions: Mutant *FGFR3* initiates luminal papillary BCa formation and favors BCa male sex bias, potentially through FGFR3-dependent ESR1 downregulation. Patients with premalignant lesions or early-stage BCa could thus potentially benefit from FGFR3 targeting. *FGFR3* expression level in epithelia could account for FGFR3-driven carcinoma tissue specificity.

Patient summary: By developing a transgenic mouse model, we showed that gain-of-function mutations of *FGFR3* receptor, among the most frequent genetic alterations in bladder cancer (BCa), initiate BCa formation. Our results could support noninvasive detection of *FGFR3* mutations and FGFR3 targeting in early-stage bladder lesions.

1. Introduction

Bladder cancer (BCa) is the sixth most common cancer in men worldwide [1]. At diagnosis, most tumors are non–muscle-invasive urothelial carcinomas (NMIBC; 75%). NMIBCs have a high recurrence rate (70%), and a subset (10–15%) progresses to the aggressive form of disease—muscle-invasive bladder cancer (MIBC). Molecular classifications have been established in both NMIBC and MIBC to identify different biological processes to support patient treatment stratification [2–7].

Fibroblast growth factor receptor 3 (FGFR3), a receptor tyrosine kinase, is frequently genetically altered in BCa [3,5,8,9]. Point mutations (observed in 70% of NMIBCs and enriched in classes 1 and 3, and in 15% of MIBCs, mostly in the luminal papillary [LumP] subtype [2–7]) or chromosomal translocations resulting in protein fusions (affecting 5% of MIBCs) lead to a constitutively active FGFR3. The transforming properties of genetically altered *FGFR3* have been shown in vitro, and FGFR3 oncogenic dependency for tumor growth has been demonstrated both in vitro and in vivo [10–14]. Recently, the FGFR inhibitor erdafitinib received US Food and Drug Administration approval for patients with locally advanced or metastatic BCa with *FGFR3/2* alterations [15].

To determine the functional role of *FGFR3* mutations in BCa in vivo, several teams have developed *FGFR3*-altered genetically engineered mice (GEMs) through transgene insertion (mouse mutant K644E [16] or S243C [17], and human S249C [18]). So far, results suggest that FGFR3 activation alone is not sufficient to induce tumorigenesis [16,18,19], but can promote tumor formation when associated with other molecular alterations (p53/pRB deficiency [17] or PTEN loss [19]) or with carcinogen treatment [18].

Here, we report for the first time a GEM model overexpressing the human *FGFR3*b-S249C mutant in the urothelium, in which mice develop low-grade papillary BCa, resembling the human counterpart at histological, genomic, and transcriptomic levels. The impact of FGFR3-S249C expression on tumor formation penetrance led us to investigate *FGFR3* expression levels in different normal human epithelia and its role in the tissue specificity of *FGFR3*-driven tumors. The higher incidence of tumors in male mice prompted us to explore sex distribution and to investigate sex hormone receptors (androgen receptor [AR] and estrogen receptor 1 [ESR1]) activation in *FGFR3*-mutated human BCa and cell lines.

2. Materials and methods

All the materials and methods are described in the Supplementary material.

3. Results

3.1. *FGFR3-S249C expression in uroplakin II–expressing cells induces urothelial hyperplasia and low-grade papillary NMIBC*

We generated transgenic mice expressing a human mutant *FGFR3* in the urothelium. We focused on the most common *FGFR3* mutation in both NMIBC and MIBC, S249C [8], and used the mouse uroplakin II (UII) gene promoter to specifically target its expression to urothelial cells (Fig. 1A) [20]. We selected two founders for our UII-hFGFR3-S249C model, numbers 569 and 538, which expressed high levels of the transgene in the urothelium (mostly in the suprabasal and intermediate cell layers; Supplementary Fig. 1). These two founders were viable and fertile, and transmitted the transgene to their offspring in a Mendelian fashion. Following the

Please cite this article as: M.-J. Shi, J. Fontugne, A. Moreno-Vega et al., FGFR3 Mutational Activation Can Induce Luminal-like Papillary Bladder Tumor Formation and Favors a Male Sex Bias, Eur Urol (2022), https://doi.org/10.1016/j.eururo.2022.09.030

propagation of founder lines, we examined the bladder of heterozygous or homozygous transgenic mice (one or two alleles of the transgene, respectively) aged 1–18 mo. Macroscopically, papillary lesions were observed in both lines after 15 mo. Tumor incidence was further studied in mouse 569 line, which showed higher hFGFR3-S249c expression level and higher phenotype penetrance. The overall penetrance at 18 mo was low (~10%), and tumor incidence was impacted by both sex and zygosity (Fig. 1B). Males developed more tumors than females, and homozygous mice developed more tumors than heterozygous mice in both sexes. The tumors corresponded histologically to NMIBCs (stage pTa) of papillary architecture with exophytic or mixed (exophytic and inverted) growth patterns and low-grade cytological atypia (Fig. 1C). Similar to human low-grade pTa BCa, mouse tumor proliferation rate was low, with <5% of Ki67-labeled nuclei by immunohistochemistry (Fig. 1D). A systematic histological analysis of UII-hFGFR3-S249C mice bladders also identified hyperplastic lesions, defined by a thickened urothelium without cytological atypia, with an increase to up to 20 cell layers (Fig. 1C). The penetrance of the hyperplastic phenotype was complete from 6 mo of age in both lines.

3.2. *FGFR3-induced mouse tumors harbor copy number alterations and transcriptomic modulation of hallmark cancer pathways*

We performed genomic and transcriptomic characterization of tumors obtained from line 569. Whole-exome sequencing did not reveal any recurrent mutations but showed recurrent copy number alterations (CNAs), the most common being chromosome 16 gains in five out of seven sequenced tumors (Fig. 2A). We confirmed the chromosomal gains by quantitative polymerase chain reaction (qPCR) of three selected genes of gained regions (*Trat1*, *Erbb4*, and *Fkbp5* located inchr16, chr1, and chr17, respectively) in six sequenced tumors and four additional tumors (Supplementary Fig. 2A), but not in hyperplasia (n = 6; Supplementary Fig. 2B). Gene expression profiles of hyperplastic lesions (n = 6) from UII-hFGFR3-S249C mice were more similar to normal samples (n = 3 control littermate urothelia) than tumors (n = 6) in the principal component analysis (Fig. 2B). Fewer than 200 significantly differentially expressed genes (DEGs) were found between hyperplasia and normal controls (Fig. 2C and Supplementary Table 1). In contrast, 1118 DEGs were identified between hFGFR3-S249C mouse tumors and controls (Fig. 2C and Supplementary Table 1). Furthermore, genes dysregulated in hyperplasia were enriched in the DEGs found in tumors (Fig. 2D).

A gene set enrichment analysis using DEGs in mouse tumors and hyperplasia (when compared with controls) and upon FGFR3 siRNA knockdown in human FGFR3-dependent BCa cell lines (see DEGs in Supplementary Tables 1 and 2) highlighted common enriched pathways (with NES in opposite directions), suggesting direct FGFR3 modulation. Specifically, we identified an increase in “cell cycle” and “DNA replication,” and a decrease of “inflammation” and “interferon gamma” terms (Fig. 2E and Supplementary Table 3). Alterations in “mitotic spindle” and “sister chromatid segregation” pathways (Fig. 2E) could contribute to CNAs observed in FGFR3-S249C–induced tumors (Fig. 2A). As previously demonstrated in human BCa, MYC activation could also contribute to FGFR3 oncogenic properties in mice (Fig. 2E) [14]. Further supporting an FGFR3-dependent alteration of cell cycle regulation, a Western blot analysis showed a decrease in p27 and p53 expression in hyperplasia and tumors from UII-hFGFR3-S249C mice compared with the normal urothelium from controls (Fig. 2F). Of note, no recurrent mutations of *TP53* were observed in mice tumors.

3.3. *UII-hFGFR3-S249C model is a model of human luminal papillary BCa, but BBN-induced tumors in UII-hFGFR3-S249C mice retain a basal/squamous phenotype*

We and others have previously shown that N-butyl-N(4-hydroxybutyl) nitrosamine (BBN)-induced bladder tumors in mice represent a model of the basal subtype of MIBC [21–23]. Given the papillary nature of hFGFR3-S249C–induced murine tumors, we hypothesized that these recapitulate the LumP consensus subtype of human BCa, which is enriched in *FGFR3* mutations.

We first identified genomic-level similarities, with a significant overlap in genes with CNAs between the mouse model and human pTa *FGFR3*-mutated tumors (our CIT cohort, n = 44; Fig. 3A) [24]. Then, we classified hFGFR3-S249C tumors (n = 6) using a recently proposed NMIBC transcriptomic classifier [7]. The hFGFR3-S249C–induced tumors showed high correlations with NMIBC class 1 and 3 centroids, which are classes enriched in *FGFR3* mutations in humans (Fig. 3B) [5,7]. Using the BASE47 classifier [25], *FGFR3*-induced mice tumors were defined as luminal, whereas previously obtained BBN-induced tumors [21] were classified as basal (Fig. 3C). To further validate these findings, we performed a cross-species comparison by coclustering hFGFR3-S249C and BBN mice tumors with human tumors from our CIT-BLCA cohort (n = 96 MIBCs and 99 NMIBCs) [24], using corresponding orthologues of genes from the consensus classifier for the basal/squamous (Ba/Sq), LumP, and neuroendocrine-like subtypes [2]. BBN mice tumors clustered with human Ba/Sq tumors and hFGFR3-S249C with LumP human tumors (Fig. 3D).

We confirmed, as previously described [18], that hFGFR3-S249C expression promoted BBN-induced carcinogenesis (Supplementary Fig. 3A and 3B). Of note, BBN-induced FGFR3-mutated tumors retained Ba/Sq features, with frequent squamous differentiation and similar immunohistochemical expression patterns to that of BBN-induced tumors from littermate control mice, when considering basal marker CK5/6 and luminal marker FOXA1 (Supplementary Fig. 3C).

Human FGFR3-mutated tumors are characterized by low immune infiltration compared with other subtypes [2,5,7]. In line with this observation, a comparison of mouse tumor immune population abundance, inferred with the murine Microenvironment Cell Population counter (mMCP-counter) [26], with that of The Cancer Genome Atlas (TCGA)

Please cite this article as: M.-J. Shi, J. Fontugne, A. Moreno-Vega et al., FGFR3 Mutational Activation Can Induce Luminal-like Papillary Bladder Tumor Formation and Favors a Male Sex Bias, Eur Urol (2022), https://doi.org/10.1016/j.eururo.2022.09.030

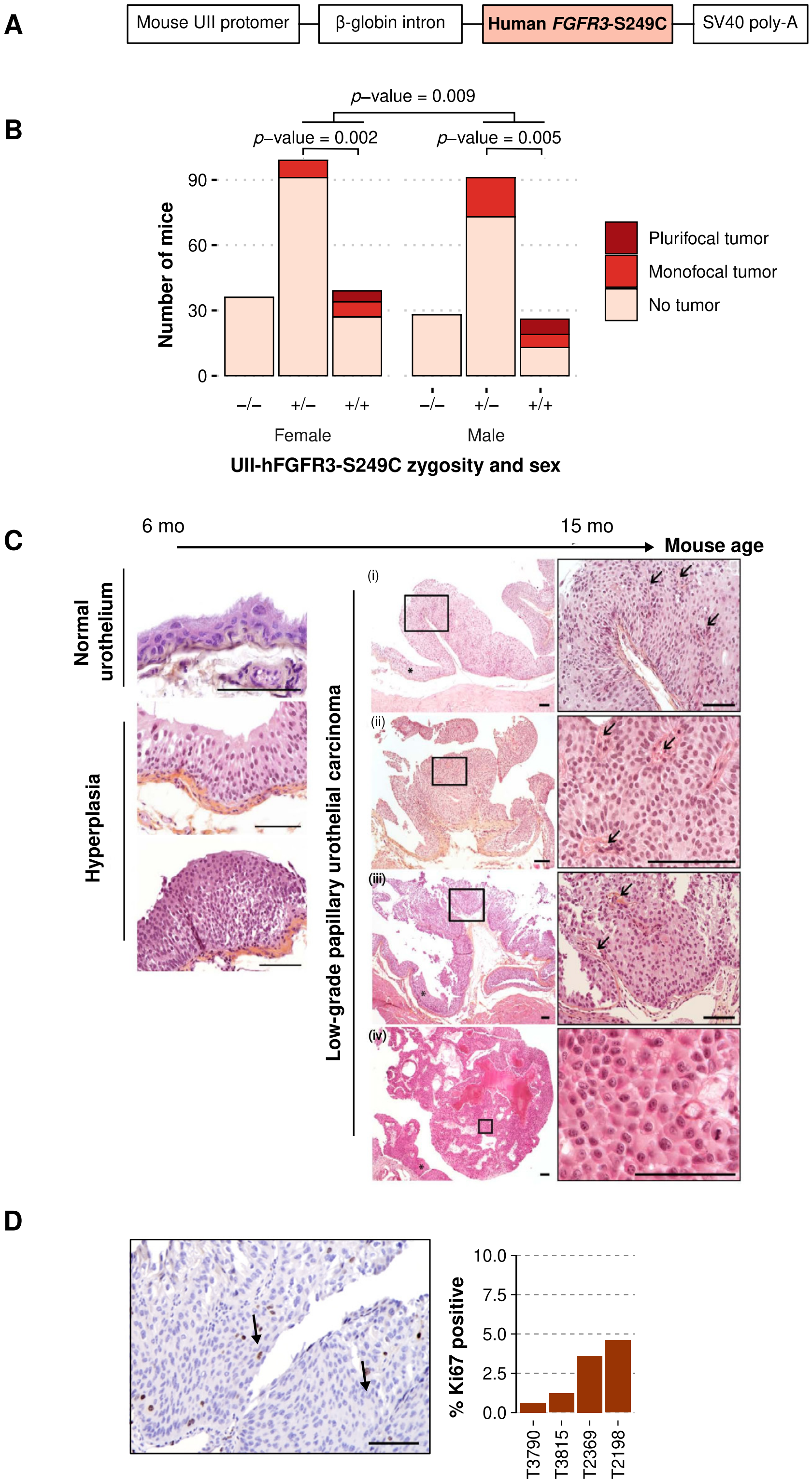

Fig. 1 – UPII-FGFR3-S249C transgenic mice develop urothelial hyperplasia and non–muscle-invasive low-grade urothelial carcinoma. (A) Chimeric construct used to generate transgenic mice, consisting of a 3.6-kb mouse *UPII* gene promoter and a 2.1-kb human *FGFR3b* cDNA carrying the mutation S249C. (B) Frequency of mono- or plurifocal bladder tumor development in homozygous (+/+) or heterozygous (+/–) hFGFR3-S249C mice versus control littermates (–/–) at 18 mo. Proportions of mice developing either mono- or plurifocal tumors between homozygous (+/+) and heterozygous (+/–) mice were compared using Fisher's exact tests within each sex. We also found that male mice developed more tumors than female tumors, controlling for zygosity, using a Cochran-Mantel-Haenszel chi-square test. (C) Representative H&E histology of urothelial lesions in hFGFR3-S249C mice compared with normal mouse urothelium. Hyperplastic lesions (left panel) or low-grade papillary urothelial carcinomas (right panel) developed in hFGFR3-S249C mice from 6 or 15 mo of age, respectively. Asterisks show tumor-adjacent urothelial hyperplasia. Arrows point to papillae fibrovascular cores. Scale bar: 100 µm. (D) Ki67 staining of hFGFR3-S249C mouse tumors. A representative stained slide is shown on the left; arrows indicate Ki67-positive cells. The proportion of Ki67-positive tumor cells was evaluated in four tumors; all were classified as low grade with <5% Ki67-positive cells. Scale bar: 100 µm. FGFR3 = fibroblast growth factor receptor 3; H&E = hematoxylin and eosin; UII = uroplakin II.

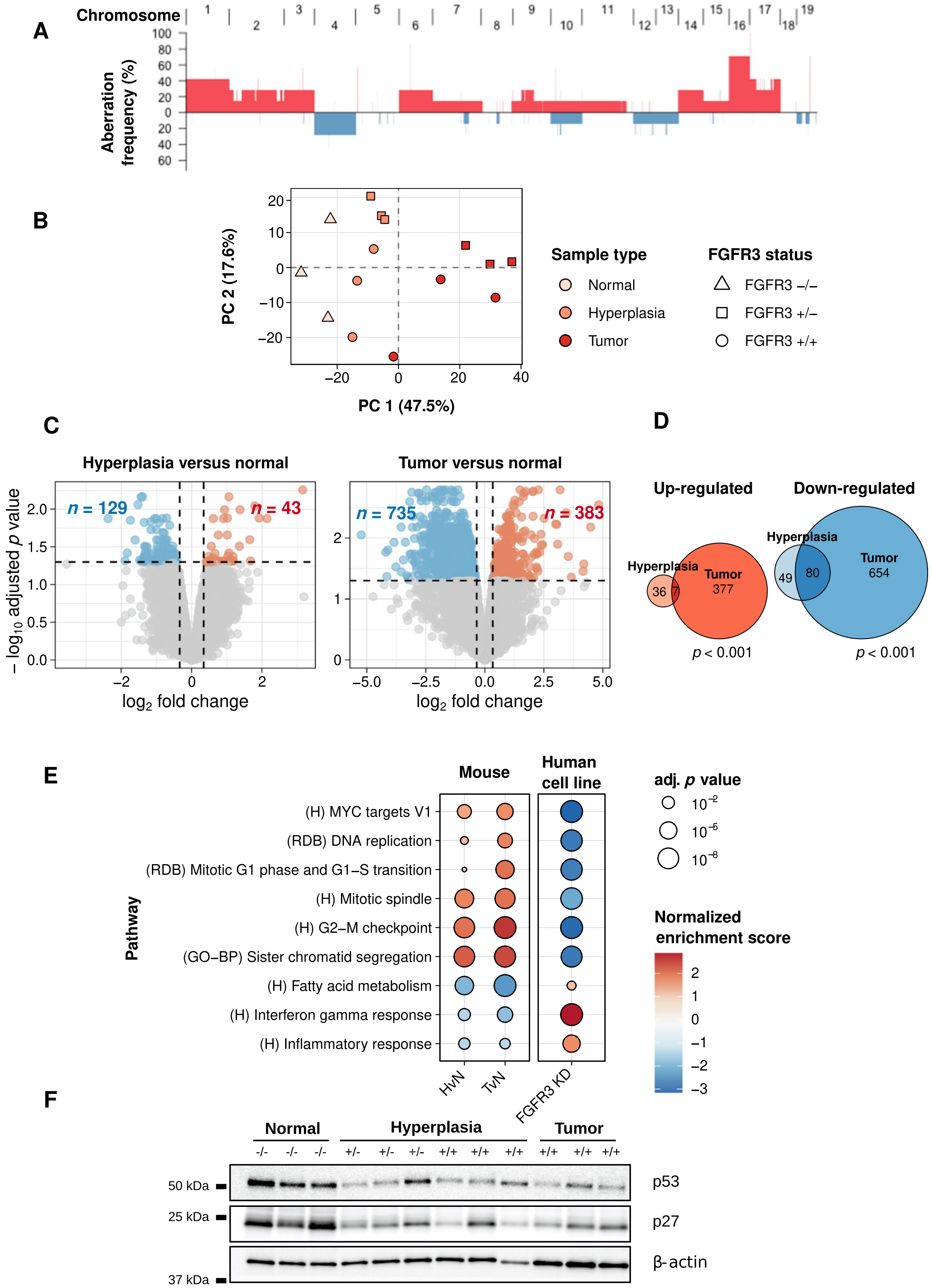

Fig. 2 – Mouse hFGFR3-S249C tumors present copy number alterations and transcriptomic modulation of some key cancer hallmarks pathways. (A) Frequency of chromosomal copy number alterations in UII-hFGFR3-S249C tumors. (B) Principal component analysis of the 1000 most varying genes expressed on the Affymetrix Mouse Exon 1.0 ST array from tumor, and hyperplastic urothelium from UPII-hFGFR3-S249C mice and normal urothelial samples from control littermates. (C) Volcano plot of the differentially expressed genes (|log2FC| > 0.35; adj. $p < 0.05$) between hFGFR3-S249C mice hyperplasia and littermate normal control urothelia (left panel, 172 DEGs) and between hFGFR3-S249C mice tumors and controls (right panel, 1118 DEGs). Lists of DEGs are provided in Supplementary Table 1. (D) Comparison of up- and downregulated genes between hFGFR3-S249C hyperplastic urothelium and normal urothelium from littermates (controls) and hFGFR3-S249C tumors versus controls. Overlap was evaluated using Fisher's exact test. (E) Gene set enrichment analysis of deregulated pathways in (left) hFGFR3-S249C hyperplastic urothelium compared with normal urothelium from control littermates (HvN), (center) hFGFR3-S249 tumors compared with controls (TvN), and (right) *FGFR3* knockdown compared with control in three *FGFR3*-dependent bladder cancer cell lines (RT-112, UM-UC-14, and MGH-U3). Normalized enrichment scores and FDRs of curated significantly enriched terms are displayed. A list of DEGs in cell lines is provided in Supplementary Table 2. (F) Western blot analysis of p53 and p27 protein levels in normal urothelium of control littermate mice and in hyperplastic urothelium and bladder tumors from either heterozygous (+/–) or homozygous (+/+) hFGFR3-S249C mice. Β-actin was used as loading control. DEG = differentially expressed gene; FDR = false discovery rate; FGFR3 = fibroblast growth factor receptor 3; UII = uroplakin II.

Please cite this article as: M.-J. Shi, J. Fontugne, A. Moreno-Vega et al., FGFR3 Mutational Activation Can Induce Luminal-like Papillary Bladder Tumor Formation and Favors a Male Sex Bias, Eur Urol (2022), https://doi.org/10.1016/j.eururo.2022.09.030

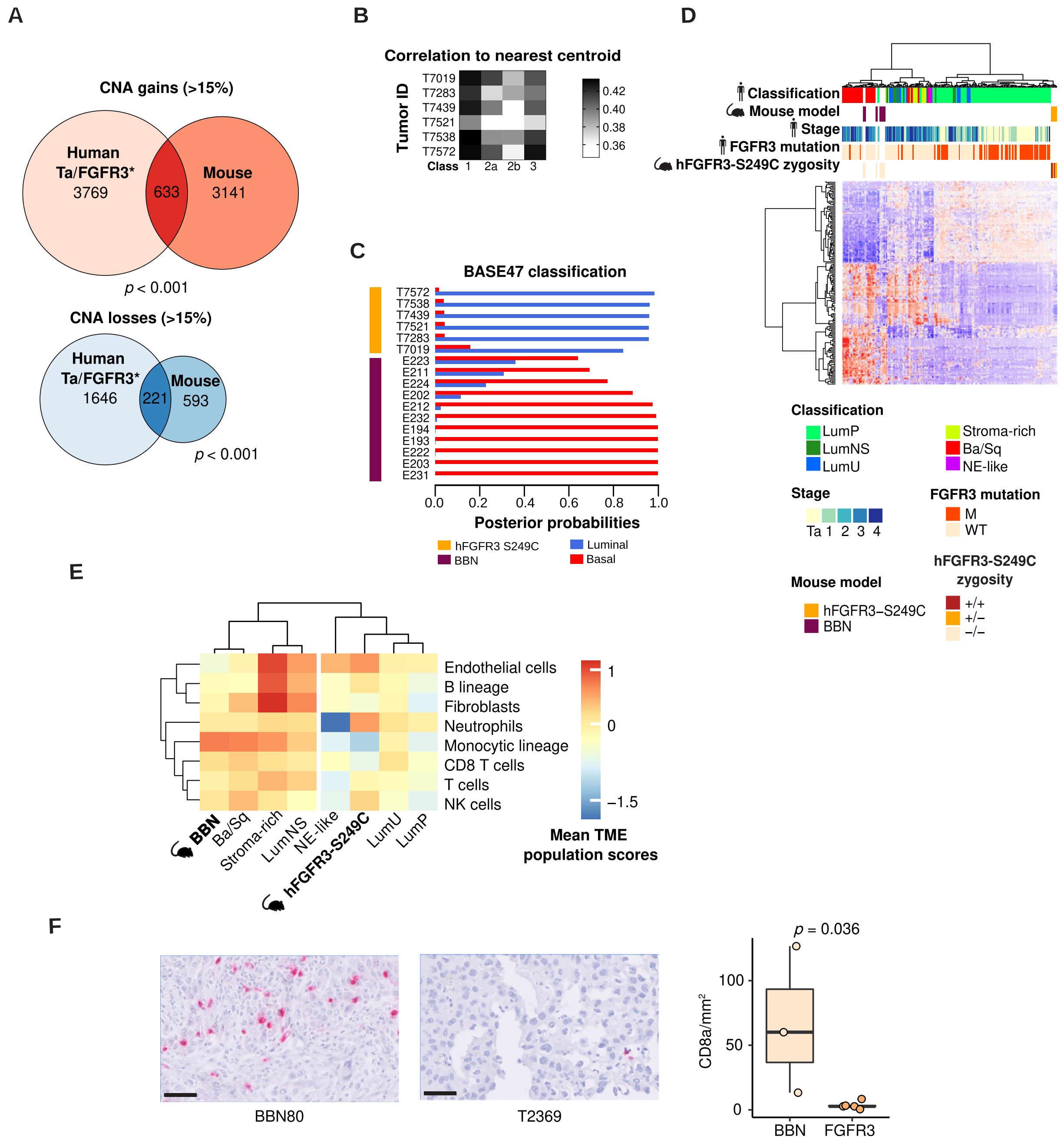

Fig. 3 – Mouse *hFGFR3*-S249C bladder tumors resemble human luminal papillary tumors. (A) Comparison of genes with frequent (>15%) copy number gains (top) and losses (bottom) between pTa *FGFR3*-mutated human tumors and *hFGFR3*-S249C mouse tumors. Overlap was evaluated using Fisher's exact tests. (B) Correlation with the nearest centroid of the four classes of UROMOL non–muscle-invasive carcinoma classification scheme [5,7] and (C) the BASE47 classifier [25] for tumors of *hFGFR3*-S249C mice. Muscle-invasive tumors derived from N-butyl-N-(4-hydroxybutyl)nitrosamine (BBN)-treated mice are used for comparison [21]. (D) Cross-species unsupervised hierarchical clustering of *hFGFR3*-S249C mice tumors (*n* = 6), BBN-induced tumors (*n* = 11), and human bladder tumors (*n* = 193 from the CIT series) considering genes from the consensus classifier for basal/squamous and luminal-papillary human BCa [2]. (E) Cross-species unsupervised hierarchical clustering using microenvironment cellular compositions estimated with mMCP-counter and MCP-counter scores, for BBN (*n* = 11) and *hFGFR3*-S249C (*n* = 6) models and TCGA MIBCs according to consensus subtype (*n* = 408). (F) Representative CD8 IHC staining (left panel) and quantification of CD8-positive lymphocytes per millimeter square of tumor surface in BBN-induced and *hFGFR3*-induced mouse bladder carcinoma (right panel). Differences were assessed using Wilcoxon rank-sum test. Ba/Sq = basal/squamous; BCa = bladder cancer; CNA = copy number alteration; FGFR3 = fibroblast growth factor receptor 3; IHC = immunohistochemical; LumNS = luminal nonspecified; LumP = luminal papillary; LumU = luminal unstable; MCP-counter = Microenvironment Cell Population counter; MIBC = muscle-invasive bladder cancer; mMCP-counter = murine Microenvironment Cell Population counter; NE-like = neuroendocrine-like; NK cell = natural killer cell; TCGA = The Cancer Genome Atlas; TME = tumor microenvironment.

MIBC tumors (*n* = 408), estimated with MCP-counter, found similar clustering results, suggesting that both BBN and FGFR3 models are relevant to study tumor microenvironment in basal and luminal bladder tumors, respectively (Fig. 3E). CD8a immunostaining confirmed these results (Fig. 3E), showing lower infiltration of CD8+ lymphocytes in FGFR3-mutated mice tumors than in BBN-induced mice tumors.

Please cite this article as: M.-J. Shi, J. Fontugne, A. Moreno-Vega et al., FGFR3 Mutational Activation Can Induce Luminal-like Papillary Bladder Tumor Formation and Favors a Male Sex Bias, Eur Urol (2022), https://doi.org/10.1016/j.eururo.2022.09.030

3.4. *FGFR3 expression levels impact tumor formation in UII-hFGFR3-S249C mice and could account for tissue specificity of mutant FGFR3–induced tumors*

We further explored the impact of hFGFR3-S249C zygosity on tumorigenesis, given the increased frequency and tumor multifocality in homozygous mice (Fig. 1B). We confirmed that the transgene expression was higher in the hyperplastic urothelium of homozygous mice than in that of heterozygous mice at mRNA and protein levels (Fig. 4A and 4B, respectively). The same difference was observed in tumors at the mRNA level (Fig. 4A). We also analyzed FGFR3 protein expression in tumors from homozygous mice and observed similar expression levels to the hyperplastic urothelium of homozygous hFGFR3-S249C mice (Fig. 4B). Using DEGs upon *FGFR3* knockdown in FGFR3-dependent BCa cell lines (Supplementary Table 2) and genes overexpressed in *FGFR3*-mutated MIBC tumors from the TCGA-BLCA cohort, we developed an FGFR3-activation signature (area under the curve = 0.9 for detecting *FGFR3*-mutated tumors in CIT data; Supplementary material and Supplementary Fig. 4). We observed a gradual increase in FGFR3 signature scores with gene dosage and tumor development stages (Fig. 4C and 4D). We therefore hypothesized that higher h*FGFR3* expression level in homozygous than in heterozygous mice urothelium (Fig. 4A and 4B) could increase tumor development susceptibility. We thus measured FGFR3b (main isoform expressed in epithelial cells) expression levels in different normal human epithelia, including the urothelium, obtained after laser microdissection. Interestingly, epithelia presenting high *FGFR3b* expression levels were those in which *FGFR3*-mutated tumors are described (bladder, skin, and exocervix; Fig. 4E) [3,27–29]. Our data suggest that high epithelial expression of *FGFR3* is required for *FGFR3* mutations to induce tumor formation. Nevertheless, although *FGFR3* gene dosage in mice influenced tumor frequency, it did not impact tumor latency or induce progression toward MIBC.

3.5. *Mutant FGFR3 induces a higher BCa male sex bias and represses ESR1 transcriptional activity*

BCa is a sex-biased cancer occurring three times more in men than in women [30]. The distribution of molecular subtypes is sex dependent, males being enriched with tumors of the LumP and neuroendocrine-like subtypes and females with the Ba/Sq subtype [31]. A male sex bias in luminal tumors induced by the constitute activation of β-catenin was also observed in mice [32]. Given the higher proportion of males developing *FGFR3*-S249C–induced tumors (Fig. 1B), we explored the relationship between sex and *FGFR3* mutation status in human tumors (Fig. 5A). Since *FGFR3* mutations other than S249C display the same or a higher oncogenic potential [8,30,31], we considered all *FGFR3* mutations and not only S249C for further analysis. Considering all tumors, we observed a significantly higher male/female ratio in *FGFR3*-mutated tumors than in *FGFR3* wild-type tumors (Fig. 5A). *FGFR3* mutation enrichment in males was driven by MIBCs, in particular by the LumP subtype, for which the male/female ratio was significantly higher (around 3.5-fold) in *FGFR3*-mutated than in *FGFR3* wild-type (not mutated) tumors. Class 3 NMIBCs also presented a trend for such a bias, albeit not significant, potentially due to low numbers of *FGFR3* wild-type tumors. These observations suggested that sex-specific pathways could synergize with *FGFR3* mutations to induce BCa, in particular in LumP MIBC. We thus investigated sex hormone receptor activation in association with *FGFR3* mutations. Using AR and ESR1 regulon gene sets defined for MIBC and NMIBC [2,7] and filtered for direct target genes using ChIP-seq data (Supplementary material), we calculated AR and ESR1 filtered regulon activity in both NMIBCs from UROMOL and MIBCs from TCGA cohorts using a gene set variation analysis. Considering gender as a covariate for adjustment, we observed significantly higher AR (Fig. 5B) and lower ESR1 (Fig. 5C) filtered regulon activity in *FGFR3*-mutated tumors than in *FGFR3* wild-type tumors in different subtypes in both MIBC and NMIBC, including LumP for ESR1 regulon. We then investigated whether the association of *FGFR3* mutation with higher AR and lower ESR1 activity was linked to FGFR3 activity/expression in our mouse model and BCa cell lines. We observed, contrarily to FGFR3 pathway activation (Fig. 4C), a gradual decrease of ESR1 filtered regulon activity with tumor progression in our FGFR3-induced mouse model (Fig. 5D). We also observed an enrichment of both ESR1 and AR filtered regulons in the DEGs upon FGFR3 siRNA knockdown in human FGFR3-dependent BCa cell lines (Fig. 5E). We further confirmed the inhibition of ESR1 and AR activity by FGFR3-S249C using reporter assays in HEK293FT cells (Fig. 5F). A reporter plasmid comprising the firefly luciferase gene under the control of a promoter containing an AR-response element (PGL4-ARE-X2-PSA-luc) or an ESR1-response element (PsG5-17M-ERE-bGlob-LUC) was coexpressed in HEK293FT cells with a plasmid encoding AR or ESR1, respectively (Fig. 5F, upper panel). FGFR3-S249C expression induced a significantly lower transcriptional activity of AR and ESR1 than transfection with the empty plasmid, in the presence of an AR agonist (2 nM 2-hydroxytestosterone) and phenol red mimicking estrogen, respectively. The FGFR3-S249C–dependent repression of AR and ESR1 transcriptional activity was significantly reduced in the presence of the FGFR inhibitor erdafitinib, demonstrating that the receptor kinase activity was required to modulate hormone receptor activity (Fig. 5F, lower panel). Taken together, our data suggest a causal link between FGFR3 activation and ESR1 activity downregulation but not for AR activity upregulation in *FGFR3*-mutated compared with wild-type tumors. This finding highlights a potential role of an FGFR3-dependent regulation of ESR1 in the sex bias of *FGFR3*-mutated tumors, particularly in the LumP subtype.

4. Discussion

We describe here the first transgenic mouse model demonstrating the tumorigenic role of *FGFR3* mutations in the bladder in vivo. Expression of hFGFR3-S249C in UII-expressing cells induced spontaneous low-grade papillary tumor formation and favored BBN-induced carcinogenesis. In two different transgenic lines, hFGFR3-S249C induced tumorigenesis, indicating an effect of the expression of the

Please cite this article as: M.-J. Shi, J. Fontugne, A. Moreno-Vega et al., FGFR3 Mutational Activation Can Induce Luminal-like Papillary Bladder Tumor Formation and Favors a Male Sex Bias, Eur Urol (2022), https://doi.org/10.1016/j.eururo.2022.09.030

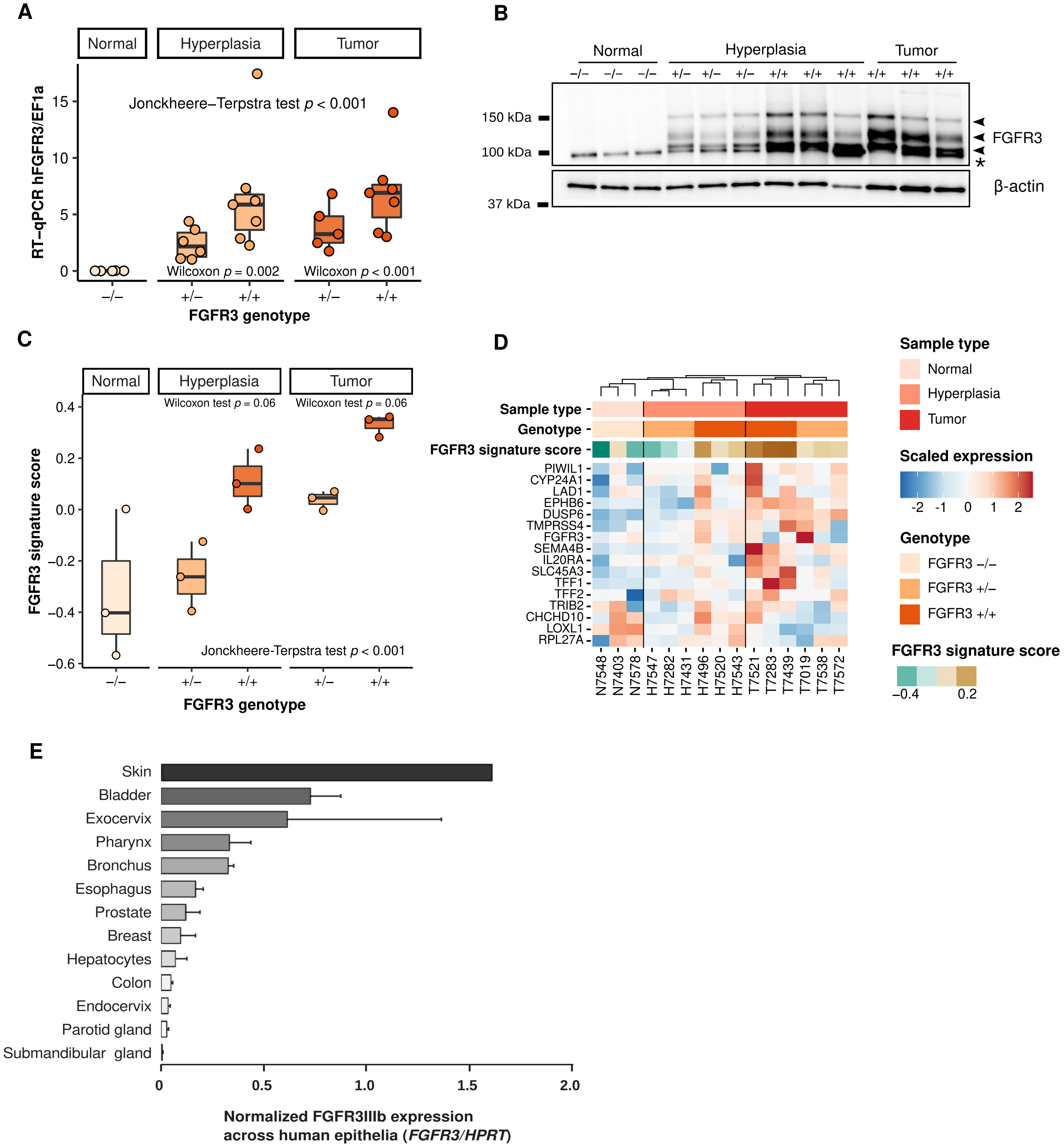

Fig. 4 – *FGFR3*-induced tumor development is dependent on FGFR3 expression levels. (A) *hFGFR3-IIIb* mRNA expression evaluated by RT-qPCR in hyperplastic urothelium or bladder tumors of hFGFR3-S249C homozygous (+/+) or heterozygous (+/–) mice and in normal urothelium of control littermate mice (–/–). Results were normalized using Ef1a expression levels. The statistical difference across all groups was assessed using Jonckheere-Terpstra test and differences between –/+ and +/+ groups were assessed using Wilcoxon rank-sum test. (B) Western blot analysis of hFGFR3 protein levels in normal urothelium of control littermate mice and in hyperplastic urothelium and bladder tumors from either heterozygous (+/–) or homozygous (+/+) hFGFR3-S249C mice. The three bands corresponding to different FGFR3-glycosylation patterns are indicated by an arrow. The asterisk shows a nonspecific band; β-actin was used as a loading control. (C) Comparison of FGFR3 modulation signature scores in normal, hyperplastic, or tumor urothelium from *FGFR3* wild-type mice (normal), or heterozygous and homozygous *hFGFR3*-S249C mice. GSVA-derived FGFR3 signature scores were compared between heterozygous and homozygous hFGFR3-S249C within hyperplastic and tumor tissues using Student *t* tests. The overall increase in *FGFR3* signature scores in tumor development (normal urothelium < hyperplasia < tumor) was confirmed using Jonckheere-Terpstra test. (D) Heatmap of normalized expression values of the FGFR3 modulation signature genes in normal urothelium, hyperplastic urothelium, and tumors. Samples were clustered separately by sample type, grouping genotype in an unsupervised manner. (E) *FGFR3-IIIb* expression levels assessed by RT-qPCR in different normal human epithelia obtained after laser microdissection of surgical biopsies obtained from organ donors. Results are presented as the mean ± SD (n = 2 for all samples except skin, n = 1, and bladder n = 3). FGFR3 = fibroblast growth factor receptor 3; GSVA = gene set variation analysis; RT-qPCR = reverse transcription quantitative polymerase chain reaction; SD = standard deviation.

transgene itself, rather than the alteration of an endogenous key gene resulting from nonspecific transgene insertion. Surprisingly, a mutated FGFR3 has already been targeted to urothelial cells using the same promoter without any spontaneous tumor formation being reported [16–19]. Nonetheless, in some of these studies, mutated receptor expression promoted bladder tumor development when combined with carcinogen exposure [18] or in association

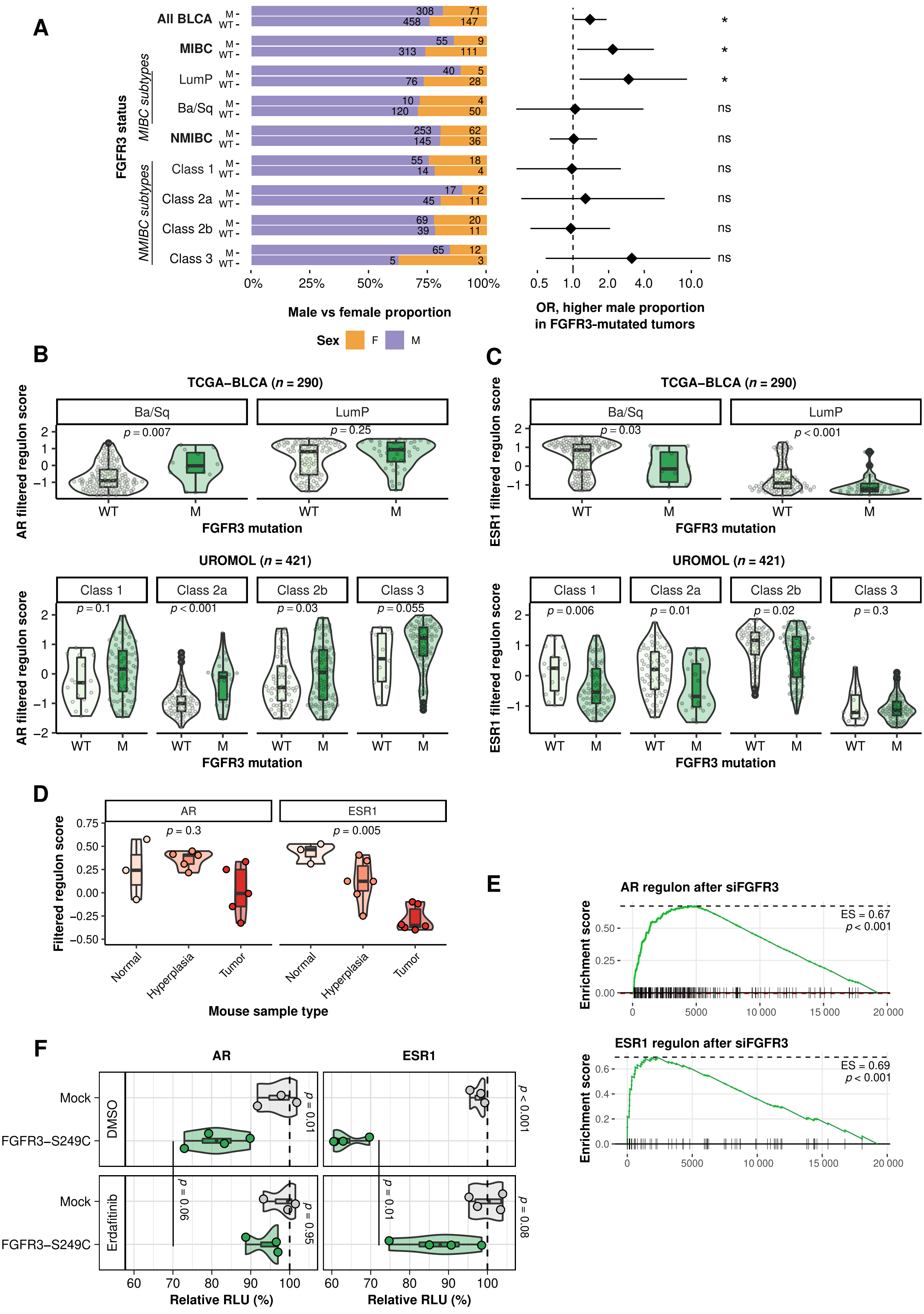

Please cite this article as: M.-J. Shi, J. Fontugne, A. Moreno-Vega et al., FGFR3 Mutational Activation Can Induce Luminal-like Papillary Bladder Tumor Formation and Favors a Male Sex Bias, Eur Urol (2022), https://doi.org/10.1016/j.eururo.2022.09.030

with *Pten* loss [19] or P53/pRB deficiency [17]. The discrepancy between the previously developed GEM models and ours could be linked to the specifically studied *FGFR3* mutation (S249C here and K644E in two previous studies [16,19]) or to the use of an inducible model for FGFR3-S249C expression in other studies [17,18]. We additionally showed that FGFR3-S249C expression levels impact tumor formation frequency, suggesting that lower transgene expression in former GEM models could also account for the absence of tumorigenesis.

FGFR3 mutations are found in very few tumor types. FGFR3-S249C in particular, which is likely induced by APOBEC mutagenesis [8], is rarely found in other APOBEC-related cancer types, such as breast or lung cancers, which suggests that the mutation brings little selective advantage. Our model reveals that a sufficient level of mutant FGFR3 expression is critical to induce tumor formation and that weak FGFR3 expression level in lung and breast normal epithelial cells could explain the absence of *FGFR3* mutation–driven tumor formation in these tissues.

Considering the increasing interest of targeting FGFR3 for BCa treatment, a model resembling the human counterpart at histological, genomic, and transcriptomic levels may have a clinical translational value to evaluate new treatment combinations to prevent resistance. The model we present here is the first immunocompetent model of mutant *FGFR3*–induced low-grade luminal papillary carcinoma, with a tumor microenvironment resembling the human counterpart. *FGFR3*-mutated tumors are non–T cell inflamed and have been associated with a poor immune microenvironment, therefore being less likely to respond to immunotherapy [3,33,34]. Allografts obtained from this model (latency and penetrance of the phenotype will not allow a direct use of the model) should allow an evaluation of combined therapies using both FGFR and checkpoint inhibitors.

Our model should also allow for a better understanding of the signaling pathways activated by FGFR3 in NMIBC. The tumor formation latency and the stage-dependent increase in FGFR3 activation score suggest that a tumor-suppressor pathway and/or a negative regulator of FGFR3 pathways might be activated in normal and hyperplastic urothelia. However, so far our analysis did not reveal such a pathway but confirmed the activation of MYC [14], and highlighted a repression of ER and AR activity by FGFR3. Previous studies using carcinogen-induced mouse models and in vitro transformation assay using normal urothelial cells supported inhibitory functions of ESR1 in urothelial carcinogenesis [35]. Further elucidating whether FGFR3-dependent repression of ESR1 activity could contribute to FGFR3-induced urothelial carcinogenesis and to the male-biased ratio of FGFR3-induced tumors will be of interest. Finally, an additional analysis of the signaling pathway leading to ESR1 repression by FGFR3 is worth further investigation.

5. Conclusions

FGFR3 mutations initiate luminal papillary bladder tumor formation in vivo and favor a male sex bias potentially through inhibition of ESR1 activity. Our findings suggest a potential benefit of FGFR inhibitors in early stages of BCa and premalignant lesions. Our results also suggest that the expression level of FGFR3 in epithelial tissue accounts for the tissue-specificity of FGFR3-driven carcinomas.

Author contributions: Isabelle Bernard-Pierrot had full access to all the data in the study and takes responsibility for the integrity of the data and the accuracy of the data analysis.

Study concept and design: Shi, Fontugne, Moreno-Vega, Meng, Groeneveld, Radvanyi, Bernard-Pierrot.
Acquisition of data: Shi, Fontugne, Moreno-Vega, Meng, Groeneveld, Dufour, Rapinat, Cabel, Krucker, Dunois-Larde, Lepage, Levrel, Dixon, Bernard-Pierrot.
Analysis and interpretation of data: Shi, Fontugne, Moreno-Vega, Meng, Groeneveld, Dufour, Kamoun, Lindskrog, Cabel, Dunois-Larde, Chapeaublanc, Levrel, Radvanyi, Bernard-Pierrot.
Drafting of the manuscript: Shi, Fontugne, Moreno-Vega, Meng, Groeneveld, Bernard-Pierrot.
Critical revision of the manuscript for important intellectual content: All authors.
Statistical analysis: Meng, Groeneveld.
Obtaining funding: Bernard-Pierrot, Radvanyi.
Administrative, technical, or material support: None.

Fig. 5 – *FGFR3* mutations are associated with a higher male sex bias in human tumors and repress *ESR1* transcriptional program. (A) Comparison of sex distribution between *FGFR3*-mutated and wild-type human bladder tumors of different subgroups. Molecular classifications for both NMIBC (UROMOL, CIT) and MIBC (TCGA, CIT), as described previously, in which NMIBC class 3 and MIBC luminal papillary (MIBC LumP) subtypes are known to be enriched for *FGFR3* mutations [3,5,7]. Odds ratios (ORs), corresponding 95% confidence intervals (95% CIs), and Z test–based *p* values were calculated (Materials and methods). OR > 1 represents a higher male proportion in *FGFR3* mutated tumors. (B) AR and (C) ESR1 activity scores for NMIBC and MIBC, calculated using GSVA using AR and ESR1 regulon target gene sets, which were filtered for direct targets identified by CHIP-seq in different tumor types (Supplementary material). The *p* values for comparisons of AR and ESR1 filtered regulon activity between *FGFR3* mutated and wild type by NMIBC or MIBC subtype were calculated using linear regression with gender as a covariate for adjustment. (D) AR and ESR1 filtered regulon scores between UPII-hFGFR3-S249C mouse bladder hyperplasia and tumors compared with control urothelium from littermates. The *p* values were calculated using linear regression with sex as a covariate to control for possible sex bias. (E) GSEA scores for AR (top) and ESR1 (bottom) filtered regulon genes calculated from $\log_2$ fold-change of gene expression upon *FGFR3* knockdown in FGFR3-dependent bladder cancer–derived cell lines (UM-UC-14 [FGFR3-S249C], MGH-U3 [FGFR3-Y375C], and RT112 [FGFR3-TACC3] cells) [8,14]. (F) A reporter plasmid containing the firefly luciferase gene under the control of a promoter containing an AR-response element (PGL4-ARE-X2-PSA-luc) or an ESR1-response element (PsG5-17M-ERE-bGlob-LUC) was coexpressed in HEK293FT cells with a plasmid encoding AR or ESR1, respectively, and a mock pcDNA3 vector or pcDNA encoding hFGFR3-S249C. Cells were treated for 24 h with DMSO or with 100 nM erdafitinib 24 h later, in the presence of 2 nM 2-hydroxytestosterone for an AR reporter assay. Renilla luciferase, expressed under the control of the CMV promoter, was used to normalize the signal (relative light units [RLU]). The data shown are the means ± SD of one representative experiment out of at least three independent ones conducted in quadruplicate. The statistical differences between each condition for AR (left) and ESR1 (right) transcriptional activity were assessed using *t* test. AR = androgen receptor; Ba/Sq = basal/squamous; BLCA = bladder cancer; DMSO = dimethyl sulfoxide; ES = enrichment score; ESR1 = estrogen receptor 1; FGFR3 = fibroblast growth factor receptor 3; GSEA = Gene set enrichment analysis; GSVA = gene set variation analysis; LumP = luminal papillary; M = mutated; MIBC = muscle-invasive bladder cancer; NMIBC = non–muscle-invasive bladder cancer; SD = standard deviation; TCGA = The Cancer Genome Atlas; UII = uroplakin II; WT = wild type.

Please cite this article as: M.-J. Shi, J. Fontugne, A. Moreno-Vega et al., FGFR3 Mutational Activation Can Induce Luminal-like Papillary Bladder Tumor Formation and Favors a Male Sex Bias, Eur Urol (2022), https://doi.org/10.1016/j.eururo.2022.09.030

Supervision: Almeida, De Reynies, Rochel, Dyrskjøt, Allory, Radvanyi, Bernard-Pierrot.

Other: Lebret provided samples and helped with clinical data analysis.

Financial disclosures: Isabelle Bernard-Pierrot certifies that all conflicts of interest, including specific financial interests and relationships and affiliations relevant to the subject matter or materials discussed in the manuscript (eg, employment/affiliation, grants or funding, consultancies, honoraria, stock ownership or options, expert testimony, royalties, or patents filed, received, or pending), are the following: None.

***Funding/Support and role of the sponsor*:** This work was supported by a grant from Ligue Nationale Contre le Cancer (Aura Moreno-Vega, Ming-Jun Shi, Jacqueline Fontugne, Xiang-Yu Meng, Florent Dufour, Claire Dunois-Larde, Elodie Chapeaublanc, May-Linda Lepage, Yves Allory, François Radvanyi, and Isabelle Bernard-Pierrot) as an associated team (Equipe labellisée); the "Carte d'Identité des Tumeurs" program was initiated, developed, and funded by Ligue Nationale Contre le Cancer. Ming-Jun Shi was supported by National Natural Science Foundation of China (NSFC, 82002672). Aura Moreno-Vega was supported by a scholarship from the French Ministry of Research. Xiang-Yu Meng was supported by a fellowship from ITMO Cancer AVIESAN, within the framework of Cancer Plan. Jacqueline Fontugne was supported by the Fondation ARC pour la recherche sur le cancer.

***Data sharing*:** RNAseq data for a cohort of 476 tumors including 460 NMIBC were obtained from ArrayExpress E-MTAB-4321 [5]. RNAseq data and *FGFR3* mutational status for 407 TCGA MIBC were downloaded from cBioPortal for Cancer Genomics: http://www.cbioportal.org/. The microarray for MGH-U3, RT112, and UM-UC-14 cells treated with FGFR3 siRNA are available from GEO (https://www.ncbi.nlm.nih.gov/geo/) under accession number GSE84733 and GSE125547. All other publicly available data used in the current study can be found as described in the Materials and methods. Other data that support the findings of this study are available from the corresponding author upon reasonable request. The microarrays for mouse tumors and hyperplasia and the urothelium from control littermate are available on GEO under reference GSE151888.

Acknowledgments: We thank Xue-Ru Wu and Tung-Tien Sun (NYU) for providing the plasmid with the murine UII promoter, Jeanne-Marie Girault for the hFGFR3-S249C plasmid construct, Martine Blanche for establishing the UII-hFGFR3-S249C transgenic mice, David Gentien from the genomics platform, and the animal facility members of Institut Curie, particularly Celine Daviaud and Sonia Jannet. We thank Eric Letouzé and Geco (Integragen, Evry, France) for their analysis of mutations and copy number variation in mouse tumors. We thank Ellen Zwarthoff (Erasmus MC Cancer Institute, the Netherlands) for providing FGFR3 mutation status for her cohort of tumors for which transcriptomic data were publicly available. We thank Daniel Metzger (IGBMC, Strasbourg, France) and Francis Vacherot (Paris Est Créteil University, TRePCa, France) for providing plasmids for ESR1 and AR reporter assay, respectively. We thank Daniel Jeffery (Institut Curie, France) for his help in preparing the revised manuscript and the response to reviewers.

Peer Review Summary

Peer Review Summary and Supplementary data to this article can be found online at https://doi.org/10.1016/j.eururo.2022.09.030.

References

[1] Sung H, Ferlay J, Siegel RL, et al. Global cancer statistics 2020: GLOBOCAN estimates of incidence and mortality worldwide for 36 cancers in 185 countries. CA Cancer J Clin 2021;71:209–49.
[2] Kamoun A, de Reyniès A, Allory Y, et al. A consensus molecular classification of muscle-invasive bladder cancer. Eur Urol 2019;77:420–33.
[3] Robertson AG, Kim J, Al-Ahmadie H, et al. Comprehensive molecular characterization of muscle-invasive bladder cancer. Cell 2017;171:540–556.e25.
[4] Sjödahl G, Eriksson P, Liedberg F, Höglund M. Molecular classification of urothelial carcinoma: global mRNA classification versus tumour-cell phenotype classification. J Pathol 2017;242:113–25.
[5] Hedegaard J, Lamy P, Nordentoft I, et al. Comprehensive transcriptional analysis of early-stage urothelial carcinoma. Cancer Cell 2016;30:27–42.
[6] Kim W-J, Kim E-J, Kim S-K, et al. Predictive value of progression-related gene classifier in primary non-muscle invasive bladder cancer. Mol Cancer 2010;9:1–9.
[7] Lindskrog SV, Prip F, Lamy P, et al. An integrated multi-omics analysis identifies prognostic molecular subtypes of non-muscle-invasive bladder cancer. Nat Commun 2021;12:2301.
[8] Shi MJ, Meng XY, Lamy P, et al. APOBEC-mediated mutagenesis as a likely cause of FGFR3 S249C mutation over-representation in bladder cancer. Eur Urol 2019;76:9–13.
[9] Cappellen D, De OC, Ricol D, et al. Frequent activating mutations of FGFR3 in human bladder. Nat Genet 1999;23:18–20.
[10] Porębska N, Latko M, Kucińska M, Zakrzewska M, Otlewski J, Opaliński Ł. Targeting cellular trafficking of fibroblast growth factor receptors as a strategy for selective cancer treatment. J Clin Med 2018;8:7.
[11] Nakanishi Y, Akiyama N, Tsukaguchi T, et al. Mechanism of oncogenic signal activation by the novel fusion kinase FGFR3-BAIAP2L1. Cancer Res 2015;75:123.
[12] Williams SV, Hurst CD, Knowles MA. Oncogenic FGFR3 gene fusions in bladder cancer. Hum Mol Genet 2013;22:795–803.
[13] Bernard-Pierrot I, Brams A, Dunois-Lardé C, et al. Oncogenic properties of the mutated forms of fibroblast growth factor receptor 3b. Carcinogenesis 2006;27:740–7.
[14] Mahe M, Dufour F, Neyret-Kahn H, et al. An FGFR3/MYC positive feedback loop provides new opportunities for targeted therapies in bladder cancers. EMBO Mol Med 2018;10:e8163.
[15] Loriot Y, Necchi A, Park SH, et al. Erdafitinib in locally advanced or metastatic urothelial carcinoma. N Engl J Med 2019;381:338–48.
[16] Ahmad I, Singh LB, Foth M, et al. K-Ras and b-catenin mutations cooperate with Fgfr3 mutations in mice to promote tumorigenesis in the skin and lung, but not in the bladder. Dis Model Mech 2011;4:548–55.
[17] Zhou H, He F, Mendelsohn CL, Tang MS, Huang C, Wu XR. FGFR3b extracellular loop mutation lacks tumorigenicity in vivo but collaborates with p53/pRB deficiency to induce high-grade papillary urothelial carcinoma. Sci Rep 2016;6:1–11.
[18] Foth M, Ismail NFB, Kung JSC, et al. FGFR3 mutation increases bladder tumourigenesis by suppressing acute inflammation. J Pathol 2018;246:331–43.
[19] Foth M, Ahmad I, Van Rhijn BWG, et al. Fibroblast growth factor receptor 3 activation plays a causative role in urothelial cancer pathogenesis in cooperation with Pten loss in mice. J Pathol 2014;233:148–58.
[20] Zhang ZT, Pak J, Shapiro E, Sun TT, Wu XR. Urothelium-specific expression of an oncogene in transgenic mice induced the formation of carcinoma in situ and invasive transitional cell carcinoma. Cancer Res 1999;59:3512–7.
[21] Rebouissou S, Bernard-Pierrot I, de Reyniès A, et al. EGFR as a potential therapeutic target for a subset of muscle-invasive bladder cancers presenting a basal-like phenotype. Sci Transl Med 2014;6:244ra91.
[22] Saito R, Smith CC, Utsumi T, et al. Molecular subtype-specific immunocompetent models of high-grade urothelial carcinoma reveal differential neoantigen expression and response to immunotherapy. Cancer Res 2018;78:3954–68.
[23] Fantini D, Glaser AP, Rimar KJ, et al. A Carcinogen-induced mouse model recapitulates the molecular alterations of human muscle invasive bladder cancer. Oncogene 2018;37:1911–25.

Please cite this article as: M.-J. Shi, J. Fontugne, A. Moreno-Vega et al., FGFR3 Mutational Activation Can Induce Luminal-like Papillary Bladder Tumor Formation and Favors a Male Sex Bias, Eur Urol (2022), https://doi.org/10.1016/j.eururo.2022.09.030

[24] Biton A, Bernard-Pierrot I, Lou Y, et al. Independent component analysis uncovers the landscape of the bladder tumor transcriptome and reveals insights into luminal and basal subtypes. Cell Rep 2014;9:1235–45.

[25] Damrauer JS, Hoadley KA, Chism DD, et al. Intrinsic subtypes of high-grade bladder cancer reflect the hallmarks of breast cancer biology. PNAS 2014;111:3110–5.

[26] Becht E, Giraldo NA, Lacroix L, et al. Estimating the population abundance of tissue-infiltrating immune and stromal cell populations using gene expression. Genome Biol 2016;17:1–20.

[27] Logié A, Dunois-Lardé C, Rosty C, et al. Activating mutations of the tyrosine kinase receptor FGFR3 are associated with benign skin tumors in mice and humans. Hum Mol Genet 2005;14:1153–60.

[28] Hafner C, Van Oers JMM, Vogt T, et al. Mosaicism of activating FGFR3 mutations in human skin causes epidermal nevi. J Clin Invest 2006;116:2201–7.

[29] Rosty C, Aubriot MH, Cappellen D, et al. Clinical and biological characteristics of cervical neoplasias with FGFR3 mutation. Mol Cancer 2005;4:2–9.

[30] Yang A, Cannataro VL, Townsend JP. Re: Ming-Jun Shi, Xiang-Yu Meng, Philippe Lamy, et al. APOBEC-mediated mutagenesis as a likely cause of FGFR3 S249C mutation over-representation in bladder cancer. Eur Urol 2019;76:9–13. Eur Urol 2020;77:e24–5.

[31] Shi MJ, Meng XY, Chen CL, et al. Reply to Alexander Yang, Vincent L. Cannataro, Jeffrey P. Townsend's Letter to the Editor, re: Ming-Jun Shi, Xiang-Yu Meng, Philippe Lamy, et al. APOBEC-mediated mutagenesis as, a likely cause of FGFR3 S249C mutation over-representation in bladder cancer. Eur Urol 2020;77:e26–7.

[32] Lin C, Yin Y, Stemler K, et al. Constitutive β-catenin activation induces male-specific tumorigenesis in the bladder urothelium. Cancer Res 2013;73:5914–25.

[33] Kardos J, Chai S, Mose LE, et al. Claudin-low bladder tumors are immune infiltrated and actively immune suppressed. JCI Insight 2016;1:e85902.

[34] Sweis RF, Spranger S, Bao R, et al. Molecular drivers of the non-T cell-inflamed tumor microenvironment in urothelial bladder cancer. Cancer Immunol Res 2016;4:563–8.

[35] Goto T, Miyamoto H. The role of estrogen receptors in urothelial cancer. Front Endocrinol (Lausanne) 2021;12:643870.

Please cite this article as: M.-J. Shi, J. Fontugne, A. Moreno-Vega et al., FGFR3 Mutational Activation Can Induce Luminal-like Papillary Bladder Tumor Formation and Favors a Male Sex Bias, Eur Urol (2022), https://doi.org/10.1016/j.eururo.2022.09.030

13 Conclusion générale

J’ai pu durant cette thèse explorer, dans les cancers de vessie et de l’uretère, de nouveaux biomarqueurs de sensibilité et de résistance aux traitements, apporter de nouveaux éléments sur les réseaux de régulation transcriptionnelle ainsi qu’identifier de nouvelles pistes thérapeutiques.

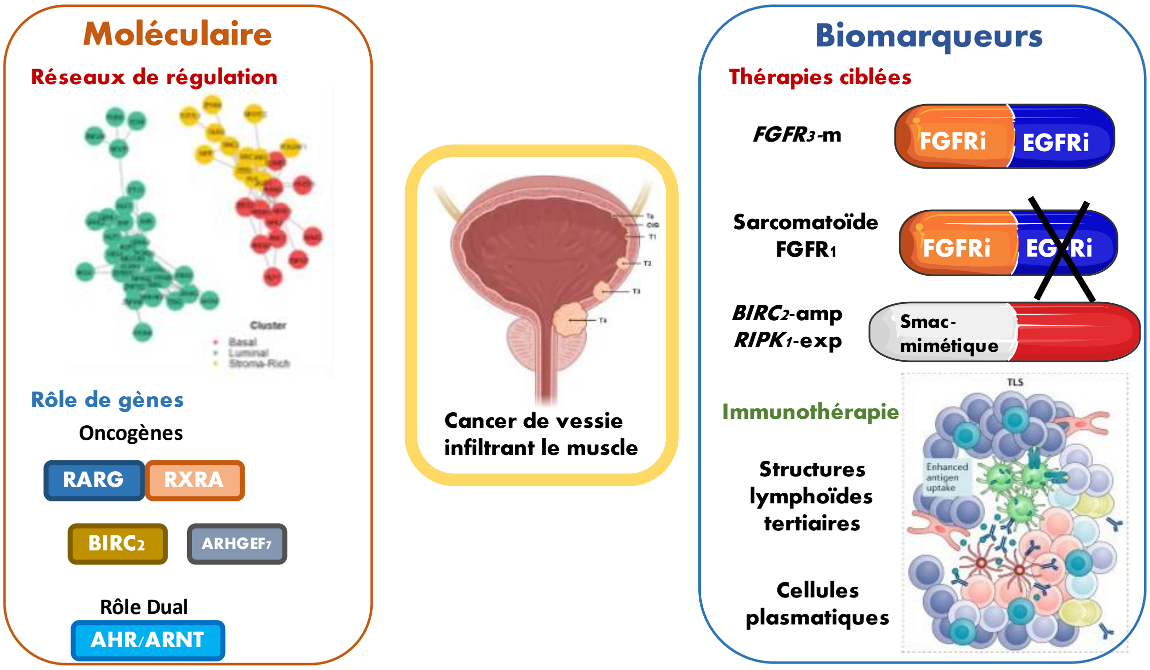

Résumé graphique des résultats obtenus pendant la thèse

Concernant les biomarqueurs de réponse, j’ai pu contribuer à identifier les tumeurs sarcomatoïdes comme résistantes aux thérapies anti-EGFR du fait d’un switch phénotypique d’expression d’EGFR vers FGFR1 dans certaines tumeurs Ba/Sq, ce qui pourrait avoir un impact thérapeutique qui reste à confirmer, via l’utilisation d’inhibiteur de FGFR (**Article 1 et 4**). Un projet dans le laboratoire vise à mieux comprendre ces tumeurs sarcomatoïdes et l’expression de FGFR1 par rapport aux tumeurs Ba/Sq non sarcomatoïdes. Une stratégie de criblage génétique ou de drogues dans les tumeurs sarcomatoïdes pourrait permettre de déterminer des thérapies ciblées.

Concernant les inhibiteurs de FGFR dans les TVIM *FGFR3* mutées, une combinaison d’inhibiteur de FGFR + anti-EGFR semble prometteuse dans ce contexte, du fait d’une augmentation d’expression d’*EGFR* mais aussi *ERBB2-3* après traitement par inhibiteur de FGFR dans ces tumeurs (**Article 1**). Il est nécessaire de confirmer cette surexpression d'*EGFR/ERBB2/ERBB3* sous inhibiteur de FGFR dans une plus large cohorte de patients traités par inhibiteur de FGFR pour une TVIM FGFR3-mutée, mais il est difficile de disposer d'échantillons pré et post thérapeutiques en clinique. Devant la toxicité probable de la combinaison inhibiteur tyrosine kinase FGFR/EGFR, d'autres associations inhibiteurs tyrosine kinase / anticorps ciblés pourraient être testées (ex inhibiteur FGFR + anticorps anti EGFR) dans des modèles tumoraux. Il est également nécessaire d'étudier l'inhibition d'ERBB2/3 associé à un inhibiteur de FGFR dans ce contexte, pour déterminer si une inhibition plus large des récepteurs ERBB/HER permettrait d'améliorer l'activité anti tumorale. Les tumeurs de vessie faisant parties des tumeurs solides les plus mutées du fait de l'exposition chronique à un carcinogène, l'hétérogénéité tumorale génomique est un facteur qui sera à prendre en compte car potentiellement pourvoyeur de résistance secondaire.

Concernant l'immunothérapie, j'ai pu contribuer à proposer les structures lymphoïdes tertiaires comme nouveau biomarqueur de réponse aux ICI (**Article 2**). Il reste à mieux comprendre le rôle de ces STL dans la réponse anti tumorale, en particulier le rôle de leur localisation par rapport à la tumeur, de leur type et/ou de leur nombre dans l'induction de cette réponse. Par rapport à certains biomarqueurs complexes à implémenter en pratique clinique, la caractérisation des STL pourrait être analysée en routine clinique sur des lames histologiques, et est en cours d'analyse dans un projet du laboratoire. Au niveau thérapeutique, une stratégie pourrait être d'induire au niveau local ces STL par des injections tumorales, mais cela nécessite une meilleure compréhension biologique de leur formation en regard de la tumeur pour déterminer une drogue qui permettrait de favoriser leur constitution.

En explorant la base de criblage CRISPR-Cas9 DepMap, j'ai pu découvrir un rôle pro-tumorigénique de RARγ dans des lignées cellulaires de cancer de vessie, dont le rôle semble plus important dans certaines tumeurs Ba/Sq. Il reste nécessaire de tester *in vivo* l'inhibition de de RARγ avec une drogue ciblée, ainsi que de mieux comprendre son rôle biologique, dans les tumeurs exprimant peu *PPARG* mais également dans celles exprimant *PPARG*, car un rôle compétitif entre PPARγ/RXRα et RARγ/RXRα pourrait exister (**Article 3**). L'alternative serait d'explorer l'inhibition thérapeutique de RXRα, mais qui en clinique risque d'être plus toxique du fait des différents partenaires et du rôle multiples de RXRα. Ceci montre l'importance de réaliser des criblages d'inhibition de gènes ou de drogues en parallèle de la caractérisation génomique des tumeurs, pour déterminer des dépendances qui ne sont pas toujours reliées à des altérations génomiques, mais qui dépendent d'un phénotype tumoral. J'ai pu aussi montrer via l'analyse de DepMap que le birinapant, un Smac mimétique, était efficace *in vitro* et *in vivo* dans certaines lignées de cancer de vessie, et que l'amplification de *BIRC2* (une des cibles des Smac mimétiques) pourrait être un biomarqueur prédictif dans les cancers de la vessie, en parallèle de l'expression de *RIPK1*, mais cela reste à confirmer sur plus de modèles *BIRC2*-amplifiés (expérience en cours) (**Article 3**). Il serait nécessaire ensuite de tester des combinaisons birinapant +/- chimiothérapie pour déterminer si le birinapant peut potentialiser l'effet de la chimiothérapie. Biologiquement, le rôle de MAP3K7 dans le mécanisme d'action des SMAC mimétiques reste à explorer dans les tumeurs de vessie. Il est intéressant de noter que les quelques études ayant étudier les SMAC mimétiques dans les lignées de cancer de vessie n'avaient pas montré un rôle antitumoral de ces traitements, mais ces études avaient analysé peu de modèles. Ceci montre l'importance lors de l'évaluation d'une drogue de disposer d'un nombre conséquent de modèles tumoraux, bien caractérisés au niveau clinique, histologique et moléculaire, pour ainsi identifier des réponses plus rares et/ou dépendantes d'une altération génomique peu récurrente.

Le laboratoire avait précédemment montré qu'AHR était un oncogène dans certaines lignées luminales de cancers urinaires, et j'ai pu identifier un rôle suppresseur de la prolifération d'AHR dans certaines lignées, en particulier Ba/Sq (**Article 3,**[73]). Il est nécessaire de comprendre biologiquement cet effet antagoniste d'AHR selon la tumeur, qui pose un problème thérapeutique avec le développement des inhibiteurs d'AHR. Cette notion d'effet dual est importante pour la clinique, car il n'est généralement pas possible d'identifier en cas de progression tumorale si celle-ci est liée à l'histoire naturelle de l'évolution tumorale ou à une progression tumorale plus rapide induite par un traitement, en particulier si cet effet protumoral est limité à une faible fréquence des cancers traités.

J'ai pu participer, en collaboration, à la proposition d'un réseau de régulation de gènes dans les tumeurs luminales et dans les tumeurs Ba/Sq ou stroma-rich, pour déterminer des points de contrôles tumoraux potentiels (**Article 5**). Il est nécessaire d'explorer le rôle biologique ainsi que l'effet thérapeutique de l'inhibition de ces potentiels points de contrôle tumoraux, seul ou en combinaison thérapeutique. Une étude de Pertub-seq dans une lignée luminale (RT112), en cours dans le laboratoire, pourra permettre d'étudier la redondance mais aussi les différences dans la modulation des gènes induites par l'inhibition de ces facteurs de transcription.

De manière plus générale, le développement de nouvelles technologies, comme les criblages à large échelle de gènes ou de drogues, les perturbations génomiques à large échelle (comme le Pertub-Seq), la création de nouveaux modèles d'études (comme les organoïdes) et le développement de nouvelles technologies d'analyses de cellule unique, dont l'analyse spatiale, va permettre, dans le futur proche, une meilleure compréhension des mécanismes biologiques tumoraux et du stroma ainsi que des écosystèmes impliqués dans les cancers, dont les cancers urothéliaux. Ceci va permettre de découvrir de nouvelles thérapies, ciblant le stroma et/ou la cellule tumorale. Ces approches, indispensables pour avoir un impact majeur sur le traitement du cancer, nécessitent néanmoins de plus en plus de collaborations interdisciplinaires ainsi que des moyens importants. En effet, les technologies précédemment citées sont très coûteuses et doivent être mutualisées pour permettre d'obtenir une caractérisation d'échantillons conséquents, avec des données multimodales, comme celles obtenues par le consortium DepMap ou par le TCGA. De nouvelles politiques de partage de données d'essais cliniques devraient également être discutées, l'essai IMVIGOR210 étant un modèle sur le partage de données translationnelles d'un essai clinique industriel[118]. Il est également nécessaire de pouvoir disposer d'échantillons dans des situations cliniques bien définies, la question des biomarqueurs étant généralement traitement et cancer dépendant. Il est donc de plus en nécessaire que chercheurs et cliniciens collaborent étroitement.

14 Références

1. Bray, F., Ferlay, J., Soerjomataram, I., Siegel, R.L., Torre, L.A., and Jemal, A. (2018). Global cancer statistics 2018: GLOBOCAN estimates of incidence and mortality worldwide for 36 cancers in 185 countries. CA. Cancer J. Clin. *68*, 394–424. 10.3322/caac.21492.

2. Powles, T., Bellmunt, J., Comperat, E., De Santis, M., Huddart, R., Loriot, Y., Necchi, A., Valderrama, B.P., Ravaud, A., Shariat, S.F., et al. (2021). Bladder cancer: ESMO Clinical Practice Guideline for diagnosis, treatment and follow-up. Ann. Oncol. Off. J. Eur. Soc. Med. Oncol., S0923-7534(21)04827-4. 10.1016/j.annonc.2021.11.012.

3. Sung, H., Ferlay, J., Siegel, R.L., Laversanne, M., Soerjomataram, I., Jemal, A., and Bray, F. (2021). Global Cancer Statistics 2020: GLOBOCAN Estimates of Incidence and Mortality Worldwide for 36 Cancers in 185 Countries. CA. Cancer J. Clin. *71*, 209–249. 10.3322/caac.21660.

4. Sanli, O., Dobruch, J., Knowles, M.A., Burger, M., Alemozaffar, M., Nielsen, M.E., and Lotan, Y. (2017). Bladder cancer. Nat. Rev. Dis. Primer *3*, 1–19. 10.1038/nrdp.2017.22.

5. Bladder Cancer NCCN Guidelines Version 6.2021 (2021).

6. Birrer, M.J., Moore, K.N., Betella, I., and Bates, R.C. (2019). Antibody-Drug Conjugate-Based Therapeutics: State of the Science. J. Natl. Cancer Inst. *111*, 538–549. 10.1093/jnci/djz035.

7. Santi, D.V., Cabel, L., and Bidard, F.-C. (2021). Does sacituzumab-govitecan act as a conventional antibody drug conjugate (ADC), a prodrug of SN-38 or both? Ann. Transl. Med. *9*, 1113. 10.21037/atm-21-1103.

8. Tagawa, S.T., Balar, A.V., Petrylak, D.P., Kalebasty, A.R., Loriot, Y., Fléchon, A., Jain, R.K., Agarwal, N., Bupathi, M., Barthelemy, P., et al. (2021). TROPHY-U-01: A Phase II Open-Label Study of Sacituzumab Govitecan in Patients With Metastatic Urothelial Carcinoma Progressing After Platinum-Based Chemotherapy and Checkpoint Inhibitors. J. Clin. Oncol. Off. J. Am. Soc. Clin. Oncol. *39*, 2474–2485. 10.1200/JCO.20.03489.

9. Powles, T., Rosenberg, J.E., Sonpavde, G.P., Loriot, Y., Durán, I., Lee, J.-L., Matsubara, N., Vulsteke, C., Castellano, D., Wu, C., et al. (2021). Enfortumab Vedotin in Previously Treated Advanced Urothelial Carcinoma. N. Engl. J. Med. *384*, 1125–1135. 10.1056/NEJMoa2035807.

10. Chu, C.E., Sjöström, M., Egusa, E.A., Gibb, E.A., Badura, M.L., Zhu, J., Koshkin, V.S., Stohr, B.A., Meng, M.V., Pruthi, R.S., et al. (2021). Heterogeneity in NECTIN4 Expression Across Molecular Subtypes of Urothelial Cancer Mediates Sensitivity to Enfortumab Vedotin. Clin. Cancer Res. *27*, 5123–5130. 10.1158/1078-0432.CCR-20-4175.

11. Chou, J., Trepka, K., Sjöström, M., Egusa, E.A., Chu, C.E., Zhu, J., Chan, E., Gibb, E.A., Badura, M.L., Contreras-Sanz, A., et al. (2022). TROP2 Expression Across Molecular Subtypes of Urothelial Carcinoma and Enfortumab Vedotin-resistant Cells. Eur. Urol. Oncol., S2588-9311(21)00215-7. 10.1016/j.euo.2021.11.005.

12. Boussiotis, V.A. (2016). Molecular and Biochemical Aspects of the PD-1 Checkpoint Pathway. N. Engl. J. Med. *375*, 1767–1778. 10.1056/NEJMra1514296.

13. Balar, A.V., Galsky, M.D., Rosenberg, J.E., Powles, T., Petrylak, D.P., Bellmunt, J., Loriot, Y., Necchi, A., Hoffman-Censits, J., Perez-Gracia, J.L., et al. (2017). Atezolizumab as first-line treatment in cisplatin-ineligible patients with locally advanced and metastatic urothelial carcinoma: a single-arm, multicentre, phase 2 trial. Lancet Lond. Engl. *389*, 67–76. 10.1016/S0140-6736(16)32455-2.

14. Balar, A.V., Castellano, D., O'Donnell, P.H., Grivas, P., Vuky, J., Powles, T., Plimack, E.R., Hahn, N.M., de Wit, R., Pang, L., et al. (2017). First-line pembrolizumab in cisplatin-ineligible patients with locally advanced and unresectable or metastatic urothelial cancer (KEYNOTE-052): a multicentre, single-arm, phase 2 study. Lancet Oncol. *18*, 1483–1492. 10.1016/S1470-2045(17)30616-2.

15. Bellmunt, J., de Wit, R., Vaughn, D.J., Fradet, Y., Lee, J.-L., Fong, L., Vogelzang, N.J., Climent, M.A., Petrylak, D.P., Choueiri, T.K., et al. (2017). Pembrolizumab as Second-Line Therapy for Advanced Urothelial Carcinoma. N. Engl. J. Med. *376*, 1015–1026. 10.1056/NEJMoa1613683.

16. Rosenberg, J.E., Hoffman-Censits, J., Powles, T., van der Heijden, M.S., Balar, A.V., Necchi, A., Dawson, N., O'Donnell, P.H., Balmanoukian, A., Loriot, Y., et al. (2016). Atezolizumab in patients with locally advanced and metastatic urothelial carcinoma who have progressed following treatment with platinum-based chemotherapy: a single-arm, multicentre, phase 2 trial. Lancet Lond. Engl. *387*, 1909–1920. 10.1016/S0140-6736(16)00561-4.

17. Sharma, P., Retz, M., Siefker-Radtke, A., Baron, A., Necchi, A., Bedke, J., Plimack, E.R., Vaena, D., Grimm, M.-O., Bracarda, S., et al. (2017). Nivolumab in metastatic urothelial carcinoma after platinum therapy (CheckMate 275): a multicentre, single-arm, phase 2 trial. Lancet Oncol. *18*, 312–322. 10.1016/S1470-2045(17)30065-7.

18. Powles, T., Park, S.H., Voog, E., Caserta, C., Valderrama, B.P., Gurney, H., Kalofonos, H., Radulović, S., Demey, W., Ullén, A., et al. (2020). Avelumab Maintenance Therapy for Advanced or Metastatic Urothelial Carcinoma. N. Engl. J. Med. *383*, 1218–1230. 10.1056/NEJMoa2002788.

19. Liu, H., Ye, T., Yang, X., Lv, P., Wu, X., Zhou, H., Lu, H., Tang, K., and Ye, Z. (2020). Predictive and Prognostic Role of PD-L1 in Urothelial Carcinoma Patients with Anti-PD-1/PD-L1 Therapy: A Systematic Review and Meta-Analysis. Dis. Markers *2020*, 8375348. 10.1155/2020/8375348.

20. Loriot, Y., Necchi, A., Park, S.H., Garcia-Donas, J., Huddart, R., Burgess, E., Fleming, M., Rezazadeh, A., Mellado, B., Varlamov, S., et al. (2019). Erdafitinib in Locally Advanced or Metastatic Urothelial Carcinoma. N. Engl. J. Med. *381*, 338–348. 10.1056/NEJMoa1817323.

21. Pal, S.K., Rosenberg, J.E., Hoffman-Censits, J.H., Berger, R., Quinn, D.I., Galsky, M.D., Wolf, J., Dittrich, C., Keam, B., Delord, J.-P., et al. (2018). Efficacy of BGJ398, a Fibroblast Growth Factor Receptor 1–3 Inhibitor, in Patients with Previously Treated Advanced Urothelial Carcinoma with *FGFR3* Alterations. Cancer Discov. *8*, 812–821. 10.1158/2159-8290.CD-18-0229.

22. Rebouissou, S., Bernard-Pierrot, I., de Reyniès, A., Lepage, M.-L., Krucker, C., Chapeaublanc, E., Hérault, A., Kamoun, A., Caillault, A., Letouzé, E., et al. (2014). EGFR as a potential therapeutic target for a subset of muscle-invasive bladder cancers presenting a basal-like phenotype. Sci. Transl. Med. *6*, 244ra91. 10.1126/scitranslmed.3008970.

23. Marzouka, N.-A.-D., Eriksson, P., Rovira, C., Liedberg, F., Sjödahl, G., and Höglund, M. (2018). A validation and extended description of the Lund taxonomy for urothelial carcinoma using the TCGA cohort. Sci. Rep. *8*, 3737. 10.1038/s41598-018-22126-x.

24. Choi, W., Porten, S., Kim, S., Willis, D., Plimack, E.R., Hoffman-Censits, J., Roth, B., Cheng, T., Tran, M., Lee, I.-L., et al. (2014). Identification of distinct basal and luminal subtypes of muscle-

invasive bladder cancer with different sensitivities to frontline chemotherapy. Cancer Cell *25*, 152–165. 10.1016/j.ccr.2014.01.009.

25. Mo, Q., Nikolos, F., Chen, F., Tramel, Z., Lee, Y.-C., Hayashi, K., Xiao, J., Shen, J., and Chan, K.S. (2018). Prognostic Power of a Tumor Differentiation Gene Signature for Bladder Urothelial Carcinomas. J. Natl. Cancer Inst. *110*, 448–459. 10.1093/jnci/djx243.

26. Damrauer, J.S., Hoadley, K.A., Chism, D.D., Fan, C., Tiganelli, C.J., Wobker, S.E., Yeh, J.J., Milowsky, M.I., Iyer, G., Parker, J.S., et al. (2014). Intrinsic subtypes of high-grade bladder cancer reflect the hallmarks of breast cancer biology. Proc. Natl. Acad. Sci. U. S. A. *111*, 3110–3115. 10.1073/pnas.1318376111.

27. Robertson, A.G., Kim, J., Al-Ahmadie, H., Bellmunt, J., Guo, G., Cherniack, A.D., Hinoue, T., Laird, P.W., Hoadley, K.A., Akbani, R., et al. (2017). Comprehensive Molecular Characterization of Muscle-Invasive Bladder Cancer. Cell *171*, 540-556.e25. 10.1016/j.cell.2017.09.007.

28. Kamoun, A., de Reyniès, A., Allory, Y., Sjödahl, G., Robertson, A.G., Seiler, R., Hoadley, K.A., Groeneveld, C.S., Al-Ahmadie, H., Choi, W., et al. (2020). A Consensus Molecular Classification of Muscle-invasive Bladder Cancer. Eur. Urol. *77*, 420–433. 10.1016/j.eururo.2019.09.006.

29. Alvarez, M.J., Shen, Y., Giorgi, F.M., Lachmann, A., Ding, B.B., Ye, B.H., and Califano, A. (2016). Functional characterization of somatic mutations in cancer using network-based inference of protein activity. Nat. Genet. *48*, 838–847. 10.1038/ng.3593.

30. Lachmann, A., Giorgi, F.M., Lopez, G., and Califano, A. (2016). ARACNe-AP: gene network reverse engineering through adaptive partitioning inference of mutual information. Bioinformatics *32*, 2233–2235. 10.1093/bioinformatics/btw216.

31. Huynh-Thu, V.A., Irrthum, A., Wehenkel, L., and Geurts, P. (2010). Inferring Regulatory Networks from Expression Data Using Tree-Based Methods. PLOS ONE *5*, e12776. 10.1371/journal.pone.0012776.

32. Mahe, M., Dufour, F., Neyret-Kahn, H., Moreno-Vega, A., Beraud, C., Shi, M., Hamaidi, I., Sanchez-Quiles, V., Krucker, C., Dorland-Galliot, M., et al. (2018). An FGFR3/MYC positive feedback loop provides new opportunities for targeted therapies in bladder cancers. EMBO Mol. Med. *10*. 10.15252/emmm.201708163.

33. Al-Obaidy, K.I., and Cheng, L. (2021). Fibroblast growth factor receptor (FGFR) gene: pathogenesis and treatment implications in urothelial carcinoma of the bladder. J. Clin. Pathol. *74*, 491–495. 10.1136/jclinpath-2020-207115.

34. Zengin, Z.B., Chehrazi-Raffle, A., Salgia, N.J., Muddasani, R., Ali, S., Meza, L., and Pal, S.K. (2022). Targeted therapies: Expanding the role of FGFR3 inhibition in urothelial carcinoma. Urol. Oncol. *40*, 25–36. 10.1016/j.urolonc.2021.10.003.

35. Billerey, C., Chopin, D., Aubriot-Lorton, M.H., Ricol, D., Gil Diez de Medina, S., Van Rhijn, B., Bralet, M.P., Lefrere-Belda, M.A., Lahaye, J.B., Abbou, C.C., et al. (2001). Frequent FGFR3 mutations in papillary non-invasive bladder (pTa) tumors. Am. J. Pathol. *158*, 1955–1959. 10.1016/S0002-9440(10)64665-2.

36. Cappellen, D., De Oliveira, C., Ricol, D., de Medina, S., Bourdin, J., Sastre-Garau, X., Chopin, D., Thiery, J.P., and Radvanyi, F. (1999). Frequent activating mutations of FGFR3 in human bladder and cervix carcinomas. Nat. Genet. *23*, 18–20. 10.1038/12615.

37. The Cancer Genome Atlas Research Network (2014). Comprehensive molecular characterization of urothelial bladder carcinoma. Nature *507*, 315–322. 10.1038/nature12965.

38. Williams, S.V., Hurst, C.D., and Knowles, M.A. (2013). Oncogenic FGFR3 gene fusions in bladder cancer. Hum. Mol. Genet. *22*, 795–803. 10.1093/hmg/dds486.

39. Bernard-Pierrot, I., Brams, A., Dunois-Lardé, C., Caillault, A., Diez de Medina, S.G., Cappellen, D., Graff, G., Thiery, J.P., Chopin, D., Ricol, D., et al. (2006). Oncogenic properties of the mutated forms of fibroblast growth factor receptor 3b. Carcinogenesis *27*, 740–747. 10.1093/carcin/bgi290.

40. Nakanishi, Y., Akiyama, N., Tsukaguchi, T., Fujii, T., Satoh, Y., Ishii, N., and Aoki, M. (2015). Mechanism of Oncogenic Signal Activation by the Novel Fusion Kinase FGFR3-BAIAP2L1. Mol. Cancer Ther. *14*, 704–712. 10.1158/1535-7163.MCT-14-0927-T.

41. Wu, Y.-M., Su, F., Kalyana-Sundaram, S., Khazanov, N., Ateeq, B., Cao, X., Lonigro, R.J., Vats, P., Wang, R., Lin, S.-F., et al. (2013). Identification of Targetable FGFR Gene Fusions in Diverse Cancers. Cancer Discov. *3*, 636–647. 10.1158/2159-8290.CD-13-0050.

42. Tomlinson, D.C., Hurst, C.D., and Knowles, M.A. (2007). Knockdown by shRNA identifies S249C mutant FGFR3 as a potential therapeutic target in bladder cancer. Oncogene *26*, 5889–5899. 10.1038/sj.onc.1210399.

43. Mahe, M., Dufour, F., Neyret-Kahn, H., Moreno-Vega, A., Beraud, C., Shi, M., Hamaidi, I., Sanchez-Quiles, V., Krucker, C., Dorland-Galliot, M., et al. (2018). An FGFR3/MYC positive feedback loop provides new opportunities for targeted therapies in bladder cancers. EMBO Mol. Med. *10*. 10.15252/emmm.201708163.

44. di Martino, E., L'Hôte, C.G., Kennedy, W., Tomlinson, D.C., and Knowles, M.A. (2009). Mutant fibroblast growth factor receptor 3 induces intracellular signaling and cellular transformation in a cell type- and mutation-specific manner. Oncogene *28*, 4306–4316. 10.1038/onc.2009.280.

45. Culine, S., Flechon, A., Gravis, G., Roubaud, G., Loriot, Y., Joly, F., Barthelemy, P., Assaf, E., Mahammedi, H., Beuzeboc, P., et al. (2017). Results of the GETUG-AFU 19 trial: A randomized phase II study of dose dense methotrexate, vinblastine, doxorubicin, and cisplatin (dd-MVAC) with or without anti-epidermal growth factor receptor (EGF-R) monoclonal antibody panitumumab (PANI) in advanced transitional cell carcinoma (ATCC). J. Clin. Oncol. *35*, 307–307. 10.1200/JCO.2017.35.6_suppl.307.

46. Philips, G.K., Halabi, S., Sanford, B.L., Bajorin, D., and Small, E.J. (2009). A phase II trial of cisplatin (C), gemcitabine (G) and gefitinib for advanced urothelial tract carcinoma: results of Cancer and Leukemia Group B (CALGB) 90102. Ann. Oncol. *20*, 1074–1079. 10.1093/annonc/mdn749.

47. Pruthi, R.S., Nielsen, M., Heathcote, S., Wallen, E.M., Rathmell, W.K., Godley, P., Whang, Y., Fielding, J., Schultz, H., Grigson, G., et al. (2010). A phase II trial of neoadjuvant erlotinib in patients with muscle-invasive bladder cancer undergoing radical cystectomy: clinical and pathological results. BJU Int. *106*, 349–354. 10.1111/j.1464-410X.2009.09101.x.

48. Gong, K., Guo, G., Panchani, N., Bender, M.E., Gerber, D.E., Minna, J.D., Fattah, F., Gao, B., Peyton, M., Kernstine, K., et al. (2020). EGFR inhibition triggers an adaptive response by co-opting antiviral signaling pathways in lung cancer. Nat. Cancer *1*, 394–409. 10.1038/s43018-020-0048-0.

49. Leonetti, A., Sharma, S., Minari, R., Perego, P., Giovannetti, E., and Tiseo, M. (2019). Resistance mechanisms to osimertinib in EGFR-mutated non-small cell lung cancer. Br. J. Cancer *121*, 725–737. 10.1038/s41416-019-0573-8.

50. Nagano, T., Tachihara, M., and Nishimura, Y. (2018). Mechanism of Resistance to Epidermal Growth Factor Receptor-Tyrosine Kinase Inhibitors and a Potential Treatment Strategy. Cells *7*, E212. 10.3390/cells7110212.

51. Westover, D., Zugazagoitia, J., Cho, B.C., Lovly, C.M., and Paz-Ares, L. (2018). Mechanisms of acquired resistance to first- and second-generation EGFR tyrosine kinase inhibitors. Ann. Oncol. Off. J. Eur. Soc. Med. Oncol. *29*, i10–i19. 10.1093/annonc/mdx703.

52. Mazaira, G.I., Zgajnar, N.R., Lotufo, C.M., Daneri-Becerra, C., Sivils, J.C., Soto, O.B., Cox, M.B., and Galigniana, M.D. (2018). The Nuclear Receptor Field: A Historical Overview and Future Challenges. Nucl. Recept. Res. *5*, 101320. 10.11131/2018/101320.

53. Peters, J.M., Shah, Y.M., and Gonzalez, F.J. (2012). The role of peroxisome proliferator-activated receptors in carcinogenesis and chemoprevention. Nat. Rev. Cancer *12*, 181–195. 10.1038/nrc3214.

54. Coutos-Thévenot, L., Beji, S., Neyret-Kahn, H., Pippo, Q., Fontugne, J., Osz, J., Krucker, C., Groeneveld, C.D.S., Dufour, F., Kamoun, A., et al. (2019). PPARγ is a tumor suppressor in basal bladder tumors offering new potential therapeutic opportunities. 868190. 10.1101/868190.

55. Rochel, N., Krucker, C., Coutos-Thévenot, L., Osz, J., Zhang, R., Guyon, E., Zita, W., Vanthong, S., Hernandez, O.A., Bourguet, M., et al. (2019). Recurrent activating mutations of PPARγ associated with luminal bladder tumors. Nat. Commun. *10*, 253. 10.1038/s41467-018-08157-y.

56. Lewis, J.D., Ferrara, A., Peng, T., Hedderson, M., Bilker, W.B., Quesenberry, C.P., Vaughn, D.J., Nessel, L., Selby, J., and Strom, B.L. (2011). Risk of bladder cancer among diabetic patients treated with pioglitazone: interim report of a longitudinal cohort study. Diabetes Care *34*, 916–922. 10.2337/dc10-1068.

57. Biton, A., Bernard-Pierrot, I., Lou, Y., Krucker, C., Chapeaublanc, E., Rubio-Pérez, C., López-Bigas, N., Kamoun, A., Neuzillet, Y., Gestraud, P., et al. (2014). Independent component analysis uncovers the landscape of the bladder tumor transcriptome and reveals insights into luminal and basal subtypes. Cell Rep. *9*, 1235–1245. 10.1016/j.celrep.2014.10.035.

58. Cancer Genome Atlas Research Network (2014). Comprehensive molecular characterization of urothelial bladder carcinoma. Nature *507*, 315–322. 10.1038/nature12965.

59. Harbeck, N., Penault-Llorca, F., Cortes, J., Gnant, M., Houssami, N., Poortmans, P., Ruddy, K., Tsang, J., and Cardoso, F. (2019). Breast cancer. Nat. Rev. Dis. Primer *5*, 1–31. 10.1038/s41572-019-0111-2.

60. Goldstein, J.T., Berger, A.C., Shih, J., Duke, F.F., Furst, L., Kwiatkowski, D.J., Cherniack, A.D., Meyerson, M., and Strathdee, C.A. (2017). Genomic Activation of PPARG Reveals a Candidate Therapeutic Axis in Bladder Cancer. Cancer Res. *77*, 6987–6998. 10.1158/0008-5472.CAN-17-1701.

61. Korpal, M., Puyang, X., Jeremy Wu, Z., Seiler, R., Furman, C., Oo, H.Z., Seiler, M., Irwin, S., Subramanian, V., Julie Joshi, J., et al. (2017). Evasion of immunosurveillance by genomic alterations of PPARγ/RXRα in bladder cancer. Nat. Commun. *8*, 103. 10.1038/s41467-017-00147-w.

62. Halstead, A.M., Kapadia, C.D., Bolzenius, J., Chu, C.E., Schriefer, A., Wartman, L.D., Bowman, G.R., and Arora, V.K. (2017). Bladder-cancer-associated mutations in RXRA activate peroxisome proliferator-activated receptors to drive urothelial proliferation. eLife *6*. 10.7554/eLife.30862.

63. Coutos-Thévenot, L. (2019). Rôle dual de PPARγ dans les tumeurs de la vessie.

64. Wang, Z., Snyder, M., Kenison, J.E., Yang, K., Lara, B., Lydell, E., Bennani, K., Novikov, O., Federico, A., Monti, S., et al. (2020). How the AHR Became Important in Cancer: The Role of Chronically Active AHR in Cancer Aggression. Int. J. Mol. Sci. *22*. 10.3390/ijms22010387.

65. Xue, P., Fu, J., and Zhou, Y. (2018). The Aryl Hydrocarbon Receptor and Tumor Immunity. Front. Immunol. *9*, 286. 10.3389/fimmu.2018.00286.

66. Madak-Erdogan, Z., and Katzenellenbogen, B.S. (2012). Aryl Hydrocarbon Receptor Modulation of Estrogen Receptor α-Mediated Gene Regulation by a Multimeric Chromatin Complex Involving the Two Receptors and the Coregulator RIP140. Toxicol. Sci. *125*, 401–411. 10.1093/toxsci/kfr300.

67. Rothhammer, V., and Quintana, F.J. (2019). The aryl hydrocarbon receptor: an environmental sensor integrating immune responses in health and disease. Nat. Rev. Immunol. *19*, 184–197. 10.1038/s41577-019-0125-8.

68. Larigot, L., Juricek, L., Dairou, J., and Coumoul, X. (2018). AhR signaling pathways and regulatory functions. Biochim. Open *7*, 1–9. 10.1016/j.biopen.2018.05.001.

69. Murray, I.A., Patterson, A.D., and Perdew, G.H. (2014). Aryl hydrocarbon receptor ligands in cancer: friend and foe. Nat. Rev. Cancer *14*, 801–814. 10.1038/nrc3846.

70. Nothdurft, S., Thumser-Henner, C., Breitenbücher, F., Okimoto, R.A., Dorsch, M., Opitz, C.A., Sadik, A., Esser, C., Hölzel, M., Asthana, S., et al. (2020). Functional screening identifies aryl hydrocarbon receptor as suppressor of lung cancer metastasis. Oncogenesis *9*, 102. 10.1038/s41389-020-00286-8.

71. Paris, A., Tardif, N., Galibert, M.-D., and Corre, S. (2021). AhR and Cancer: From Gene Profiling to Targeted Therapy. Int. J. Mol. Sci. *22*, E752. 10.3390/ijms22020752.

72. Ye, M., Zhang, Y., Gao, H., Xu, Y., Jing, P., Wu, J., Zhang, X., Xiong, J., Dong, C., Yao, L., et al. (2018). Activation of the Aryl Hydrocarbon Receptor Leads to Resistance to EGFR TKIs in Non-Small Cell Lung Cancer by Activating Src-mediated Bypass Signaling. Clin. Cancer Res. Off. J. Am. Assoc. Cancer Res. *24*, 1227–1239. 10.1158/1078-0432.CCR-17-0396.

73. Shi, M.-J., Meng, X.-Y., Fontugne, J., Chen, C.-L., Radvanyi, F., and Bernard-Pierrot, I. (2020). Identification of new driver and passenger mutations within APOBEC-induced hotspot mutations in bladder cancer. Genome Med. *12*, 85. 10.1186/s13073-020-00781-y.

74. Califano, A., and Alvarez, M.J. (2017). The recurrent architecture of tumour initiation, progression and drug sensitivity. Nat. Rev. Cancer *17*, 116–130. 10.1038/nrc.2016.124.

75. Paull, E.O., Aytes, A., Jones, S.J., Subramaniam, P.S., Giorgi, F.M., Douglass, E.F., Tagore, S., Chu, B., Vasciaveo, A., Zheng, S., et al. (2021). A modular master regulator landscape controls cancer transcriptional identity. Cell *184*, 334-351.e20. 10.1016/j.cell.2020.11.045.

76. Warrick, J.I., Walter, V., Yamashita, H., Chung, E., Shuman, L., Amponsa, V.O., Zheng, Z., Chan, W., Whitcomb, T.L., Yue, F., et al. (2016). FOXA1, GATA3 and PPARɣ Cooperate to Drive Luminal Subtype in Bladder Cancer: A Molecular Analysis of Established Human Cell Lines. Sci. Rep. *6*, 38531. 10.1038/srep38531.

77. Kang, H.W., Kim, W.-J., Choi, W., and Yun, S.J. (2020). Tumor heterogeneity in muscle-invasive bladder cancer. Transl. Androl. Urol. *9*, 2866–2880. 10.21037/tau.2020.03.13.

78. Meeks, J.J., Al-Ahmadie, H., Faltas, B.M., Taylor, J.A., Flaig, T.W., DeGraff, D.J., Christensen, E., Woolbright, B.L., McConkey, D.J., and Dyrskjøt, L. (2020). Genomic heterogeneity in bladder cancer: challenges and possible solutions to improve outcomes. Nat. Rev. Urol. *17*, 259–270. 10.1038/s41585-020-0304-1.

79. Warrick, J.I., Sjödahl, G., Kaag, M., Raman, J.D., Merrill, S., Shuman, L., Chen, G., Walter, V., and DeGraff, D.J. (2019). Intratumoral Heterogeneity of Bladder Cancer by Molecular Subtypes and Histologic Variants. Eur. Urol. *75*, 18–22. 10.1016/j.eururo.2018.09.003.

80. Sirab, N., Drubay, D., Maillé, P., Popova, T., Ngo, C., Gentien, D., Moktefi, A., Soyeux-Porte, P., Pelletier, R., Reyes, C., et al. Multilayer spectrum of intratumoral heterogeneity in basal bladder cancer. J. Pathol. *n/a*. 10.1002/path.5813.

81. Sjödahl, G., Eriksson, P., Lövgren, K., Marzouka, N.-A.-D., Bernardo, C., Nordentoft, I., Dyrskjøt, L., Liedberg, F., and Höglund, M. (2018). Discordant molecular subtype classification in the basal-squamous subtype of bladder tumors and matched lymph-node metastases. Mod. Pathol. Off. J. U. S. Can. Acad. Pathol. Inc *31*, 1869–1881. 10.1038/s41379-018-0096-5.

82. Groeneveld C.D.S. 1736MO - Pure or mixed basal/squamous tumours present decreased outcomes after neoadjuvant chemotherapy in the GETUG-AFU V05 VESPER trial. ESMO 2022.

83. Wei, W., Rong, Y., Sanhe, L., Chunxiu, Y., Thokerunga, E., Cui, D., and Wang, F. (2022). Single-cell sequencing and its applications in bladder cancer. Expert Rev. Mol. Med. *24*, e6. 10.1017/erm.2021.23.

84. Li, X., Yang, Y., Huang, Q., Deng, Y., Guo, F., Wang, G., and Liu, M. (2021). Crosstalk Between the Tumor Microenvironment and Cancer Cells: A Promising Predictive Biomarker for Immune Checkpoint Inhibitors. Front. Cell Dev. Biol. *9*.

85. Hanahan, D. (2022). Hallmarks of Cancer: New Dimensions. Cancer Discov. *12*, 31–46. 10.1158/2159-8290.CD-21-1059.

86. Ohue, Y., and Nishikawa, H. (2019). Regulatory T (Treg) cells in cancer: Can Treg cells be a new therapeutic target? Cancer Sci. *110*, 2080–2089. 10.1111/cas.14069.

87. Zheng, L., Qin, S., Si, W., Wang, A., Xing, B., Gao, R., Ren, X., Wang, L., Wu, X., Zhang, J., et al. (2021). Pan-cancer single-cell landscape of tumor-infiltrating T cells. Science *374*, abe6474. 10.1126/science.abe6474.

88. Sautès-Fridman, C., Petitprez, F., Calderaro, J., and Fridman, W.H. (2019). Tertiary lymphoid structures in the era of cancer immunotherapy. Nat. Rev. Cancer *19*, 307–325. 10.1038/s41568-019-0144-6.

89. Murphy, N., Shah, P., Shih, A., Khalili, H., Liew, A., Zhu, X., and Lee, A. (2020). Single-Cell Sequencing in Genitourinary Malignancies. Adv. Exp. Med. Biol. *1255*, 153–164. 10.1007/978-981-15-4494-1_13.

90. Zhang, P., Li, X., Pan, C., Zheng, X., Hu, B., Xie, R., Hu, J., Shang, X., and Yang, H. (2022). Single-cell RNA sequencing to track novel perspectives in HSC heterogeneity. Stem Cell Res. Ther. *13*. 10.1186/s13287-022-02718-1.

91. Bakken, T.E., Hodge, R.D., Miller, J.A., Yao, Z., Nguyen, T.N., Aevermann, B., Barkan, E., Bertagnolli, D., Casper, T., Dee, N., et al. (2018). Single-nucleus and single-cell transcriptomes compared in matched cortical cell types. PLOS ONE *13*, e0209648. 10.1371/journal.pone.0209648.

92. Lee, H.W., Chung, W., Lee, H.-O., Jeong, D.E., Jo, A., Lim, J.E., Hong, J.H., Nam, D.-H., Jeong, B.C., Park, S.H., et al. (2020). Single-cell RNA sequencing reveals the tumor microenvironment and facilitates strategic choices to circumvent treatment failure in a chemorefractory bladder cancer patient. Genome Med. *12*, 47. 10.1186/s13073-020-00741-6.

93. Wang, L., Sfakianos, J.P., Beaumont, K.G., Akturk, G., Horowitz, A., Sebra, R.P., Farkas, A.M., Gnjatic, S., Hake, A., Izadmehr, S., et al. (2021). Myeloid Cell-associated Resistance to PD-1/PD-L1 Blockade in Urothelial Cancer Revealed Through Bulk and Single-cell RNA Sequencing. Clin. Cancer Res. Off. J. Am. Assoc. Cancer Res. *27*, 4287–4300. 10.1158/1078-0432.CCR-20-4574.

94. Wang, H., Mei, Y., Luo, C., Huang, Q., Wang, Z., Lu, G.-M., Qin, L., Sun, Z., Huang, C.-W., Yang, Z.-W., et al. (2021). Single-Cell Analyses Reveal Mechanisms of Cancer Stem Cell Maintenance and Epithelial-Mesenchymal Transition in Recurrent Bladder Cancer. Clin. Cancer Res. Off. J. Am. Assoc. Cancer Res. 10.1158/1078-0432.CCR-20-4796.

95. Lai, H., Cheng, X., Liu, Q., Luo, W., Liu, M., Zhang, M., Miao, J., Ji, Z., Lin, G.N., Song, W., et al. (2021). Single-cell RNA sequencing reveals the epithelial cell heterogeneity and invasive subpopulation in human bladder cancer. Int. J. Cancer *149*, 2099–2115. 10.1002/ijc.33794.

96. Gouin, K.H., Ing, N., Plummer, J.T., Rosser, C.J., Ben Cheikh, B., Oh, C., Chen, S.S., Chan, K.S., Furuya, H., Tourtellotte, W.G., et al. (2021). An N-Cadherin 2 expressing epithelial cell subpopulation predicts response to surgery, chemotherapy and immunotherapy in bladder cancer. Nat. Commun. *12*, 4906. 10.1038/s41467-021-25103-7.

97. Chen, Z., Zhou, L., Liu, L., Hou, Y., Xiong, M., Yang, Y., Hu, J., and Chen, K. (2020). Single-cell RNA sequencing highlights the role of inflammatory cancer-associated fibroblasts in bladder urothelial carcinoma. Nat. Commun. *11*, 5077. 10.1038/s41467-020-18916-5.

98. Luo, Y., Tao, T., Tao, R., Huang, G., and Wu, S. (2022). Single-Cell Transcriptome Comparison of Bladder Cancer Reveals Its Ecosystem. Front. Oncol. *12*, 818147. 10.3389/fonc.2022.818147.

99. Xiao, Y., Jin, W., Qian, K., Wu, K., Wang, G., Jiang, W., Cao, R., Ju, L., Zhao, Y., Zheng, H., et al. (2021). Emergence of an adaptive epigenetic cell state in human bladder urothelial carcinoma evolution. bioRxiv, 2021.10.30.466556. 10.1101/2021.10.30.466556.

100. Choi, W., Porten, S., Kim, S., Willis, D., Plimack, E.R., Hoffman-Censits, J., Roth, B., Cheng, T., Tran, M., Lee, I.-L., et al. (2014). Identification of Distinct Basal and Luminal Subtypes of Muscle-Invasive Bladder Cancer with Different Sensitivities to Frontline Chemotherapy. Cancer Cell *25*, 152–165. 10.1016/j.ccr.2014.01.009.

101. Seiler, R., Ashab, H.A.D., Erho, N., van Rhijn, B.W.G., Winters, B., Douglas, J., Van Kessel, K.E., Fransen van de Putte, E.E., Sommerlad, M., Wang, N.Q., et al. (2017). Impact of Molecular Subtypes in Muscle-invasive Bladder Cancer on Predicting Response and Survival after Neoadjuvant Chemotherapy. Eur. Urol. *72*, 544–554. 10.1016/j.eururo.2017.03.030.

102. Sjödahl, G., Abrahamsson, J., Holmsten, K., Bernardo, C., Chebil, G., Eriksson, P., Johansson, I., Kollberg, P., Lindh, C., Lövgren, K., et al. (2021). Different Responses to Neoadjuvant Chemotherapy in Urothelial Carcinoma Molecular Subtypes. Eur. Urol., S0302283821021382. 10.1016/j.eururo.2021.10.035.

103. Taber, A., Christensen, E., Lamy, P., Nordentoft, I., Prip, F., Lindskrog, S.V., Birkenkamp-Demtröder, K., Okholm, T.L.H., Knudsen, M., Pedersen, J.S., et al. (2020). Molecular correlates of cisplatin-based chemotherapy response in muscle invasive bladder cancer by integrated multi-omics analysis. Nat. Commun. *11*, 4858. 10.1038/s41467-020-18640-0.

104. Jun, T., Anker, J., and Galsky, M.D. (2022). Biomarkers for therapy selection in metastatic urothelial cancer. J. Cancer Metastasis Treat. 10.20517/2394-4722.2021.171.

105. Li, Q., Damish, A.W., Frazier, Z., Liu, D., Reznichenko, E., Kamburov, A., Bell, A., Zhao, H., Jordan, E.J., Gao, S.P., et al. (2019). ERCC2 Helicase Domain Mutations Confer Nucleotide Excision Repair Deficiency and Drive Cisplatin Sensitivity in Muscle-Invasive Bladder Cancer. Clin. Cancer Res. Off. J. Am. Assoc. Cancer Res. *25*, 977–988. 10.1158/1078-0432.CCR-18-1001.

106. Urun, Y., Leow, J.J., Fay, A.P., Albiges, L., Choueiri, T.K., and Bellmunt, J. (2017). ERCC1 as a prognostic factor for survival in patients with advanced urothelial cancer treated with platinum based chemotherapy: A systematic review and meta-analysis. Crit. Rev. Oncol. Hematol. *120*, 120–126. 10.1016/j.critrevonc.2017.10.012.

107. Bai, R., Lv, Z., Xu, D., and Cui, J. (2020). Predictive biomarkers for cancer immunotherapy with immune checkpoint inhibitors. Biomark. Res. *8*, 34. 10.1186/s40364-020-00209-0.

108. Cabel, L., Proudhon, C., Romano, E., Girard, N., Lantz, O., Stern, M.-H., Pierga, J.-Y., and Bidard, F.-C. (2018). Clinical potential of circulating tumour DNA in patients receiving anticancer immunotherapy. Nat. Rev. Clin. Oncol. *15*, 639–650. 10.1038/s41571-018-0074-3.

109. Yarchoan, M., Hopkins, A., and Jaffee, E.M. (2017). Tumor Mutational Burden and Response Rate to PD-1 Inhibition. N. Engl. J. Med. *377*, 2500–2501. 10.1056/NEJMc1713444.

110. Anagnostou, V., Smith, K.N., Forde, P.M., Niknafs, N., Bhattacharya, R., White, J., Zhang, T., Adleff, V., Phallen, J., Wali, N., et al. (2017). Evolution of Neoantigen Landscape during Immune Checkpoint Blockade in Non-Small Cell Lung Cancer. Cancer Discov. *7*, 264–276. 10.1158/2159-8290.CD-16-0828.

111. Lemery, S., Keegan, P., and Pazdur, R. (2017). First FDA Approval Agnostic of Cancer Site — When a Biomarker Defines the Indication. N. Engl. J. Med. *377*, 1409–1412. 10.1056/NEJMp1709968.

112. Marabelle, A., Le, D.T., Ascierto, P.A., Di Giacomo, A.M., De Jesus-Acosta, A., Delord, J.-P., Geva, R., Gottfried, M., Penel, N., Hansen, A.R., et al. (2019). Efficacy of Pembrolizumab in Patients With Noncolorectal High Microsatellite Instability/Mismatch Repair–Deficient Cancer: Results From the Phase II KEYNOTE-158 Study. J. Clin. Oncol., JCO.19.02105. 10.1200/JCO.19.02105.

113. Hastings, K., Yu, H.A., Wei, W., Sanchez-Vega, F., DeVeaux, M., Choi, J., Rizvi, H., Lisberg, A., Truini, A., Lydon, C.A., et al. (2019). EGFR mutation subtypes and response to immune checkpoint

blockade treatment in non-small-cell lung cancer. Ann. Oncol. Off. J. Eur. Soc. Med. Oncol. *30*, 1311–1320. 10.1093/annonc/mdz141.

114. Rizvi, H., Sanchez-Vega, F., La, K., Chatila, W., Jonsson, P., Halpenny, D., Plodkowski, A., Long, N., Sauter, J.L., Rekhtman, N., et al. (2018). Molecular Determinants of Response to Anti-Programmed Cell Death (PD)-1 and Anti-Programmed Death-Ligand 1 (PD-L1) Blockade in Patients With Non-Small-Cell Lung Cancer Profiled With Targeted Next-Generation Sequencing. J. Clin. Oncol. Off. J. Am. Soc. Clin. Oncol. *36*, 633–641. 10.1200/JCO.2017.75.3384.

115. Gandhi, L., Rodríguez-Abreu, D., Gadgeel, S., Esteban, E., Felip, E., De Angelis, F., Domine, M., Clingan, P., Hochmair, M.J., Powell, S.F., et al. (2018). Pembrolizumab plus Chemotherapy in Metastatic Non-Small-Cell Lung Cancer. N. Engl. J. Med. *378*, 2078–2092. 10.1056/NEJMoa1801005.

116. Mittendorf, E.A., Philips, A.V., Meric-Bernstam, F., Qiao, N., Wu, Y., Harrington, S., Su, X., Wang, Y., Gonzalez-Angulo, A.M., Akcakanat, A., et al. (2014). PD-L1 expression in triple-negative breast cancer. Cancer Immunol. Res. *2*, 361–370. 10.1158/2326-6066.CIR-13-0127.

117. Tumeh, P.C., Harview, C.L., Yearley, J.H., Shintaku, I.P., Taylor, E.J.M., Robert, L., Chmielowski, B., Spasic, M., Henry, G., Ciobanu, V., et al. (2014). PD-1 blockade induces responses by inhibiting adaptive immune resistance. Nature *515*, 568–571. 10.1038/nature13954.

118. Mariathasan, S., Turley, S.J., Nickles, D., Castiglioni, A., Yuen, K., Wang, Y., Kadel, E.E., Koeppen, H., Astarita, J.L., Cubas, R., et al. (2018). TGF-β attenuates tumour response to PD-L1 blockade by contributing to exclusion of T cells. Nature *554*, 544–548. 10.1038/nature25501.

119. Valpione, S., Mundra, P.A., Galvani, E., Campana, L.G., Lorigan, P., De Rosa, F., Gupta, A., Weightman, J., Mills, S., Dhomen, N., et al. (2021). The T cell receptor repertoire of tumor infiltrating T cells is predictive and prognostic for cancer survival. Nat. Commun. *12*, 4098. 10.1038/s41467-021-24343-x.

120. Peranzoni, E., Ingangi, V., Masetto, E., Pinton, L., and Marigo, I. (2020). Myeloid Cells as Clinical Biomarkers for Immune Checkpoint Blockade. Front. Immunol. *11*, 1590. 10.3389/fimmu.2020.01590.

121. Luca, B.A., Steen, C.B., Matusiak, M., Azizi, A., Varma, S., Zhu, C., Przybyl, J., Espín-Pérez, A., Diehn, M., Alizadeh, A.A., et al. (2021). Atlas of clinically distinct cell states and ecosystems across human solid tumors. Cell *184*, 5482-5496.e28. 10.1016/j.cell.2021.09.014.

122. Goswami, S., Chen, Y., Anandhan, S., Szabo, P.M., Basu, S., Blando, J.M., Liu, W., Zhang, J., Natarajan, S.M., Xiong, L., et al. (2020). ARID1A mutation plus CXCL13 expression act as combinatorial biomarkers to predict responses to immune checkpoint therapy in mUCC. Sci. Transl. Med. *12*. 10.1126/scitranslmed.abc4220.

123. Necchi, A., Raggi, D., Gallina, A., Ross, J.S., Farè, E., Giannatempo, P., Marandino, L., Colecchia, M., Lucianò, R., Bianchi, M., et al. (2020). Impact of Molecular Subtyping and Immune Infiltration on Pathological Response and Outcome Following Neoadjuvant Pembrolizumab in Muscle-invasive Bladder Cancer. Eur. Urol. *77*, 701–710. 10.1016/j.eururo.2020.02.028.

124. Powles, T., and Morrison, L. (2018). Biomarker challenges for immune checkpoint inhibitors in urothelial carcinoma. Nat. Rev. Urol. *15*, 585–587. 10.1038/s41585-018-0056-3.

125. Powles, T., Kockx, M., Rodriguez-Vida, A., Duran, I., Crabb, S.J., Van Der Heijden, M.S., Szabados, B., Pous, A.F., Gravis, G., Herranz, U.A., et al. (2019). Clinical efficacy and biomarker

analysis of neoadjuvant atezolizumab in operable urothelial carcinoma in the ABACUS trial. Nat. Med. *25*, 1706–1714. 10.1038/s41591-019-0628-7.

126. Powles, T., Sridhar, S.S., Loriot, Y., Bellmunt, J., Mu, X.J., Ching, K.A., Pu, J., Sternberg, C.N., Petrylak, D.P., Tambaro, R., et al. (2021). Avelumab maintenance in advanced urothelial carcinoma: biomarker analysis of the phase 3 JAVELIN Bladder 100 trial. Nat. Med. *27*, 2200–2211. 10.1038/s41591-021-01579-0.

127. Yoshida, G.J. (2020). Applications of patient-derived tumor xenograft models and tumor organoids. J. Hematol. Oncol.J Hematol Oncol *13*, 4. 10.1186/s13045-019-0829-z.

128. Pan, C.-X., Zhang, H., Tepper, C.G., Lin, T., Davis, R.R., Keck, J., Ghosh, P.M., Gill, P., Airhart, S., Bult, C., et al. (2015). Development and Characterization of Bladder Cancer Patient-Derived Xenografts for Molecularly Guided Targeted Therapy. PloS One *10*, e0134346. 10.1371/journal.pone.0134346.

129. Jäger, W., Xue, H., Hayashi, T., Janssen, C., Awrey, S., Wyatt, A.W., Anderson, S., Moskalev, I., Haegert, A., Alshalalfa, M., et al. (2015). Patient-derived bladder cancer xenografts in the preclinical development of novel targeted therapies. Oncotarget *6*, 21522–21532. 10.18632/oncotarget.3974.

130. Tracey, A.T., Murray, K.S., Coleman, J.A., and Kim, K. (2020). Patient-Derived Xenograft Models in Urological Malignancies: Urothelial Cell Carcinoma and Renal Cell Carcinoma. Cancers *12*. 10.3390/cancers12020439.

131. Kim, K., Hu, W., Audenet, F., Almassi, N., Hanrahan, A.J., Murray, K., Bagrodia, A., Wong, N., Clinton, T.N., Dason, S., et al. (2020). Modeling biological and genetic diversity in upper tract urothelial carcinoma with patient derived xenografts. Nat. Commun. *11*, 1975. 10.1038/s41467-020-15885-7.

132. Choi, A., Jang, I., Han, H., Kim, M.-S., Choi, J., Lee, J., Cho, S.-Y., Jun, Y., Lee, C., Kim, J., et al. (2021). iCSDB: an integrated database of CRISPR screens. Nucleic Acids Res. *49*, D956–D961. 10.1093/nar/gkaa989.

133. Onishi, I., Yamamoto, K., Kinowaki, Y., Kitagawa, M., and Kurata, M. (2021). To Discover the Efficient and Novel Drug Targets in Human Cancers Using CRISPR/Cas Screening and Databases. Int. J. Mol. Sci. *22*, 12322. 10.3390/ijms222212322.

134. McFarland, J.M., Ho, Z.V., Kugener, G., Dempster, J.M., Montgomery, P.G., Bryan, J.G., Krill-Burger, J.M., Green, T.M., Vazquez, F., Boehm, J.S., et al. (2018). Improved estimation of cancer dependencies from large-scale RNAi screens using model-based normalization and data integration. Nat. Commun. *9*, 4610. 10.1038/s41467-018-06916-5.

135. Meyers, R.M., Bryan, J.G., McFarland, J.M., Weir, B.A., Sizemore, A.E., Xu, H., Dharia, N.V., Montgomery, P.G., Cowley, G.S., Pantel, S., et al. (2017). Computational correction of copy number effect improves specificity of CRISPR-Cas9 essentiality screens in cancer cells. Nat. Genet. *49*, 1779–1784. 10.1038/ng.3984.

136. Tsherniak, A., Vazquez, F., Montgomery, P.G., Weir, B.A., Kryukov, G., Cowley, G.S., Gill, S., Harrington, W.F., Pantel, S., Krill-Burger, J.M., et al. (2017). Defining a Cancer Dependency Map. Cell *170*, 564-576.e16. 10.1016/j.cell.2017.06.010.

137. Yu, C., Mannan, A.M., Yvone, G.M., Ross, K.N., Zhang, Y.-L., Marton, M.A., Taylor, B.R., Crenshaw, A., Gould, J.Z., Tamayo, P., et al. (2016). High-throughput identification of genotype-

specific cancer vulnerabilities in mixtures of barcoded tumor cell lines. Nat. Biotechnol. *34*, 419–423. 10.1038/nbt.3460.

138. Seashore-Ludlow, B., Rees, M.G., Cheah, J.H., Cokol, M., Price, E.V., Coletti, M.E., Jones, V., Bodycombe, N.E., Soule, C.K., Gould, J., et al. (2015). Harnessing Connectivity in a Large-Scale Small-Molecule Sensitivity Dataset. Cancer Discov. *5*, 1210–1223. 10.1158/2159-8290.CD-15-0235.

139. Annibaldi, A., Wicky John, S., Vanden Berghe, T., Swatek, K.N., Ruan, J., Liccardi, G., Bianchi, K., Elliott, P.R., Choi, S.M., Van Coillie, S., et al. (2018). Ubiquitin-Mediated Regulation of RIPK1 Kinase Activity Independent of IKK and MK2. Mol. Cell *69*, 566-580.e5. 10.1016/j.molcel.2018.01.027.

140. Bai, L., Smith, D.C., and Wang, S. (2014). Small-Molecule SMAC Mimetics as New Cancer Therapeutics. Pharmacol. Ther. *144*, 82–95. 10.1016/j.pharmthera.2014.05.007.

141. Chang, Y.-C., and Cheung, C.H.A. (2021). An Updated Review of Smac Mimetics, LCL161, Birinapant, and GDC-0152 in Cancer Treatment. Appl. Sci. *11*, 335. 10.3390/app11010335.

142. Benetatos, C.A., Mitsuuchi, Y., Burns, J.M., Neiman, E.M., Condon, S.M., Yu, G., Seipel, M.E., Kapoor, G.S., Laporte, M.G., Rippin, S.R., et al. (2014). Birinapant (TL32711), a bivalent SMAC mimetic, targets TRAF2-associated cIAPs, abrogates TNF-induced NF-κB activation, and is active in patient-derived xenograft models. Mol. Cancer Ther. *13*, 867–879. 10.1158/1535-7163.MCT-13-0798.

143. Guillen, K.P., Fujita, M., Butterfield, A.J., Scherer, S.D., Bailey, M.H., Chu, Z., DeRose, Y.S., Zhao, L., Cortes-Sanchez, E., Yang, C.-H., et al. (2022). A human breast cancer-derived xenograft and organoid platform for drug discovery and precision oncology. Nat. Cancer *3*, 232–250. 10.1038/s43018-022-00337-6.

144. Xie, X., Lee, J., Liu, H., Pearson, T., Lu, A.Y., Tripathy, D., Devi, G.R., Bartholomeusz, C., and Ueno, N.T. (2021). Birinapant Enhances Gemcitabine's Antitumor Efficacy in Triple-Negative Breast Cancer by Inducing Intrinsic Pathway-Dependent Apoptosis. Mol. Cancer Ther. *20*, 296–306. 10.1158/1535-7163.MCT-19-1160.

145. Hernandez, L.F., Dull, A.B., Korrapati, S., and Annunziata, C.M. (2021). Smac-mimetic enhances antitumor effect of standard chemotherapy in ovarian cancer models via Caspase 8-independent mechanism. Cell Death Discov. *7*, 134. 10.1038/s41420-021-00511-2.

146. Singh, T., Neal, A., Dibernardo, G., Raheseparian, N., Moatamed, N.A., and Memarzadeh, S. (2022). Efficacy of birinapant in combination with carboplatin in targeting platinum-resistant epithelial ovarian cancers. Int. J. Oncol. *60*, 35. 10.3892/ijo.2022.5325.

147. Zhu, D.L., and Shuai, L.Y. (2021). Effects of Birinapant on Proliferation and Invasion of MGC-803 Gastric Cancer Cells and Mechanism Underlying These Effects. Bull. Exp. Biol. Med. *171*, 56–61. 10.1007/s10517-021-05172-w.

148. McCann, C., Matveeva, A., McAllister, K., Van Schaeybroeck, S., Sessler, T., Fichtner, M., Carberry, S., Rehm, M., Prehn, J.H.M., and Longley, D.B. (2021). Development of a protein signature to enable clinical positioning of IAP inhibitors in colorectal cancer. FEBS J. *288*, 5374–5388. 10.1111/febs.15801.

149. Vallo, S., Stege, H., Berg, M., Michaelis, M., Winkelmann, R., Rothweiler, F., and Cinatl, J. (2020). Tumor necrosis factor-related apoptosis-inducing ligand as a therapeutic option in urothelial cancer cells with acquired resistance against first-line chemotherapy. Oncol. Rep. *43*, 1331–1337. 10.3892/or.2020.7487.

150. Ma, O., Cai, W.-W., Zender, L., Dayaram, T., Shen, J., Herron, A.J., Lowe, S.W., Man, T.-K., Lau, C.C., and Donehower, L.A. (2009). MMP13, Birc2 (cIAP1), and Birc3 (cIAP2), amplified on chromosome 9, collaborate with p53 deficiency in mouse osteosarcoma progression. Cancer Res. *69*, 2559–2567. 10.1158/0008-5472.CAN-08-2929.

151. Bardia, A., Parton, M., Kümmel, S., Estévez, L.G., Huang, C.-S., Cortés, J., Ruiz-Borrego, M., Telli, M.L., Martin-Martorell, P., López, R., et al. (2018). Paclitaxel With Inhibitor of Apoptosis Antagonist, LCL161, for Localized Triple-Negative Breast Cancer, Prospectively Stratified by Gene Signature in a Biomarker-Driven Neoadjuvant Trial. J. Clin. Oncol. Off. J. Am. Soc. Clin. Oncol., JCO2017748392. 10.1200/JCO.2017.74.8392.

152. Hu, H., Piotrowska, Z., Hare, P.J., Chen, H., Mulvey, H.E., Mayfield, A., Noeen, S., Kattermann, K., Greenberg, M., Williams, A., et al. (2021). Three subtypes of lung cancer fibroblasts define distinct therapeutic paradigms. Cancer Cell *39*, 1531-1547.e10. 10.1016/j.ccell.2021.09.003.

153. Cabrita, R., Lauss, M., Sanna, A., Donia, M., Skaarup Larsen, M., Mitra, S., Johansson, I., Phung, B., Harbst, K., Vallon-Christersson, J., et al. (2020). Tertiary lymphoid structures improve immunotherapy and survival in melanoma. Nature *577*, 561–565. 10.1038/s41586-019-1914-8.

154. Goubet, A.-G., Lordello, L., Alves Costa Silva, C., Peguillet, I., Gazzano, M., Mbogning-Fonkou, M.D., Thelemaque, C., Lebacle, C., Thibault, C., Audenet, F., et al. (2022). Escherichia coli-specific CXCL13-producing TFH are associated with clinical efficacy of neoadjuvant PD-1 blockade against muscle-invasive bladder cancer. Cancer Discov., CD-22-0201. 10.1158/2159-8290.CD-22-0201.

155. Hao, Y., Hao, S., Andersen-Nissen, E., Mauck, W.M., Zheng, S., Butler, A., Lee, M.J., Wilk, A.J., Darby, C., Zager, M., et al. (2021). Integrated analysis of multimodal single-cell data. Cell *184*, 3573-3587.e29. 10.1016/j.cell.2021.04.048.

156. Korsunsky, I., Millard, N., Fan, J., Slowikowski, K., Zhang, F., Wei, K., Baglaenko, Y., Brenner, M., Loh, P., and Raychaudhuri, S. (2019). Fast, sensitive and accurate integration of single-cell data with Harmony. Nat. Methods *16*, 1289–1296. 10.1038/s41592-019-0619-0.

157. Patil, N.S., Nabet, B.Y., Müller, S., Koeppen, H., Zou, W., Giltnane, J., Au-Yeung, A., Srivats, S., Cheng, J.H., Takahashi, C., et al. (2022). Intratumoral plasma cells predict outcomes to PD-L1 blockade in non-small cell lung cancer. Cancer Cell *40*, 289-300.e4. 10.1016/j.ccell.2022.02.002.

158. DepMap: The Cancer Dependency Map Project at Broad Institute https://depmap.org/portal/.

159. Christodoulou, E., Rashid, M., Pacini, C., Droop, A., Robertson, H., Groningen, T. van, Teunisse, A.F.A.S., Iorio, F., Jochemsen, A.G., Adams, D.J., et al. (2020). Analysis of CRISPR-Cas9 screens identifies genetic dependencies in melanoma. Pigment Cell Melanoma Res. 10.1111/pcmr.12919.

160. Laulumaa, S., and Varjosalo, M. (2021). Commander Complex-A Multifaceted Operator in Intracellular Signaling and Cargo. Cells *10*, 3447. 10.3390/cells10123447.

161. Vasconcelos-Nóbrega, C., Colaço, A., Lopes, C., and Oliveira, P.A. (2012). BBN as an urothelial carcinogen. In Vivo *26*, 727–739.

162. Jaitin, D.A., Weiner, A., Yofe, I., Lara-Astiaso, D., Keren-Shaul, H., David, E., Salame, T.M., Tanay, A., van Oudenaarden, A., and Amit, I. (2016). Dissecting Immune Circuits by Linking CRISPR-Pooled Screens with Single-Cell RNA-Seq. Cell *167*, 1883-1896.e15. 10.1016/j.cell.2016.11.039.

RÉSUMÉ

Le cancer de vessie est responsable de 212 536 décès en 2020 dans le monde. Il est constitué de tumeurs n'infiltrant pas le muscle (TVNIM, à risque de récidives locales), et infiltrant le muscle (TVIM, à risque de disséminations métastatiques et de décès). 95% sont des cancers urothéliaux alors que 5% sont des cancers épidermoïdes. Au niveau moléculaire, ces tumeurs sont caractérisées principalement par des tumeurs luminales (incluant des Luminales-papillaires) ou basales (Ba/Sq). Le traitement en 2022 est principalement basé, pour les stades avancés, sur la chimiothérapie (incluant les anticorps drogues conjugués), l'immunothérapie par inhibiteur de point de contrôle immunitaire (IPI, anticorps anti-PD-1/L1) et les inhibiteurs de FGFR en cas d'altérations génomiques *FGFR2/3*. Ces traitements ont néanmoins une efficacité modérée.

Les objectifs de cette thèse étaient dans les TVIM de rechercher des biomarqueurs de sensibilité ou de résistance aux traitements ainsi que de rechercher de nouvelles pistes thérapeutiques.
Concernant la recherche de biomarqueurs de réponse ou de résistance dans les TVIM nous avons pu montrer que :

- les structures lymphoïdes tertiaires, mesurées par l'expression du gène *CXCL13*, sont un biomarqueur prédictif majeur de réponse aux anticorps anti-PD-L1, et sont enrichies dans le type Ba/Sq, (étude réalisée via l'analyse de cohortes publiques comme IMVIGOR210) ;
- les cellules plasmatiques semblent également un biomarqueur de réponse aux IPI dans les TVIM métastatiques (conclusion basée sur des résultats préliminaires des données de séquençage de noyaux uniques de la cohorte MATCH-R avant et pendant le traitement par IPI) ;
- une combinaison thérapeutique par anti-FGFR (erdafitinib) + anti-EGFR (erlotinib) est efficace dans des PDXs (patient-derived xenografts) mutés pour *FGFR3*, cette efficacité étant probablement due à une surexpression d'*ERBB2-3* et d'*EGFR* sous inhibiteur de FGFR ;
- les tumeurs sarcomatoïdes présentaient une expression/activité plus faible d'EGFR et un switch vers FGFR1, responsable d'une moindre réponse à un inhibiteur d'EGFR par rapport aux autres TVIM Ba/Sq ;

Nous avons pu identifier de nouvelles pistes thérapeutiques dans les lignées cellulaires de cancers urothéliaux :

- RARy, partenaire de RXRα, cible identifiée dans la base publique de criblage par CRISPR-Cas9 de lignées cellulaires (DepMap). RARy est activé dans les TVIM en particulier dans les sous-types Ba/Sq et Luminales-papillaires, et son inhibition semble intéressante en particulier dans le sous type Ba/Sq.
- Le birinapant (XIAP/cIAP1/2 inhibiteur, Smac-mimétique) qui est efficace dans certaines lignées de cancer de vessie selon les données de DepMap. L'efficacité du birinapant a été confirmée *in vitro et in vivo* au laboratoire dans les lignées UMUC14 et SCaBER, avec comme biomarqueur de sensibilité potentiel l'amplification de *BIRC2* ou la surexpression de *RIPK1*.
- FGFR1 qui est une nouvelle piste thérapeutique dans les cancers de vessie de type sarcomatoïde.

MOTS CLÉS

Cancer de vessie ; Biomarqueurs ; RARG ; Birinapant ; CXCL13 ; structures lymphoïdes tertiaires

ABSTRACT

Bladder cancer is responsible for 212,536 deaths worldwide in 2020. It includes tumors that do not infiltrate the muscle (NMIBC, at risk of local recurrence), and tumors that infiltrate the muscle (MIBC, at risk of metastatic dissemination and death). 95% are urothelial cancers while 5% are squamous cell cancers. At the molecular level, these tumors are characterized mainly by luminal (including luminal-papillary) or basal (Ba/Sq) tumors. Treatment in 2022 is mainly based for advanced stages on chemotherapy (including antibody-drug conjugates), immune checkpoint inhibitor (ICI, anti-PD-1/L1 antibodies) and FGFR inhibitors in case of *FGFR2/3* genomic alterations. However, these treatments have a moderate efficacy.

The objectives of this thesis were to search for biomarkers of sensitivity or resistance to these treatments and to look for new therapeutic approaches.
Concerning the search for biomarkers of response or resistance in MIBC, we were able to show that :

- tertiary lymphoid structures, measured by the expression of the *CXCL13* gene, are a major predictive biomarker of response to anti-PD-L1 antibodies, and are enriched in the Ba/Sq type, (analysis of public cohorts such as IMVIGOR210);
- plasma cells also appear to be a biomarker of response to ICI in metastatic MIBC (conclusion based on preliminary results of single nuclei sequencing data from the MATCH-R cohort before and during ICI treatment);
- combination therapy with anti-FGFR (erdafitinib) + anti-EGFR (erlotinib) is effective in *FGFR3*-mutated PDXs (patient-derived xenografts), probably due to overexpression of *ERBB2-3* and *EGFR* under FGFR inhibitor;
- sarcomatoid tumors showed lower EGFR expression/activity and a switch to FGFR1, responsible for a lower response to an EGFR inhibitor compared to other Ba/Sq MIBC.

We were able to identify new therapeutic approaches in urothelial cancer cell lines:

- RARy, a partner of RXRα, a target identified in the public CRISPR-Cas9 screening cell line database (DepMap). RARy is activated in MIBC particularly in the Ba/Sq and Luminal-papillary subtypes, and its inhibition appears to be of interest particularly in the Ba/Sq subtype.
- Birinapant (XIAP/cIAP1/2 inhibitor, Smac-mimetic) which is effective in some urinary cancer lines according to DepMap data. The efficacy of birinapant has been confirmed *in vitro* and *in vivo* in UMUC14 and SCaBER cell lines, with *BIRC2* amplification or *RIPK1* overexpression as potential biomarkers of sensitivity.
- FGFR1 which is a new therapeutic lead in sarcomatoid bladder cancer.

KEYWORDS

Bladder cancer ; Biomarkers; RARG ; Birinapant ; CXCL13 ; tertiary lymphoid structures